CHAPTER 11

OTDRs and Backscatter Measurements

Josef Beller

OVERVIEW

The preceding chapter, 10, covered spatially resolved reflectometry that enables a view inside of optical waveguides and other components with sub-cm spatial resolution. This chapter covers direct-detection optical time-domain reflectometers (OTDRs) which are best-suited for medium and long-haul distance ranges with submeter resolution. These OTDRs are designed to not only provide information about reflections, but also about attenuation properties and loss of the fiber under test. This is accomplished by exploiting backscattered and backreflected light returning from the fiber when probing it with a short laser pulse. Backscattered light provides a signature from which information about signal strength is deduced, sometimes in an ambiguous manner. Interpretation of the OTDR measurement features is aided by knowledge of the fiber backscatter and reflection mechanisms together with familiarity of the measurement process.

This chapter begins with a close look at the single-pulse OTDR. This is the most successful commercial method due to both its inherent simplicity and excellent results. After describing the operational principle, its limitations and performance parameters, a short treatment of fiber-attenuation and loss-mechanisms follows. The succeeding section analyzes the backscattering signal as a function of pulsewidth, fiber-length, and fiber parameters. Then two sections focus on insertion-loss measurements with an analysis of the uncertainty on the measurement data due to superimposed noise, and on return-loss and reflectance measurements. Section 11.6 provides an overview on remote-fiber-testing and some of its applications.

11.1 INTRODUCTION

Most optical fiber parameters like core and cladding diameter, refractive index profile, NA (numerical aperture), or cutoff wavelength are unlikely to change after fiber manufacture and installation. Yet, experience shows that properties like fiber loss and attenuation are prone to alter through environmental influences like humidity, temperature, or physical stress. Fiber loss is of great importance for installed fiber links since fiber attenuation directly determines the total loss and thus the quality of a transmission system.

A direct method to measure insertion loss is the cut-back technique.[1,2] The power coming from an unconnectorized fiber end is measured. While keeping the launching condition fixed, a known length of fiber is then removed and the fiber power is remeasured. The difference in power measurements is the fiber loss. The cut-back technique provides accurate results but is a destructive measurement that requires access to both ends of the fiber. In general, installed fiber-optic cables can not be measured by this method. Another technique is the OTDR backscatter measurement that indirectly allows for determination of the fiber attenuation. It is a nondestrutrive technique capable of doing *in situ* measurements and requires access to only one end of the fiber. Furthermore it provides extra information about the fiber under test, like length dependence of the fiber attenuation, and insertion loss of defects, splices, bends, or connectors. The location and type of faults occurring in fiber fabrication, the homogeneity of fiber characteristics, and fiber length can all be tested.

In 1976 Barnsen and Jensen authored the first publications about backscatter in optical waveguides and provided proof for its suitability to fiber characterization.[3,4,5,6] OTDR analysis has evolved to a standard technique for testing of optical fibers links. The OTDR has become the primary instrument for single-ended characterization of optical fibers based on backscatter measurements.

OTDRs can be classified by several measurement techniques. Most instruments are based on time-domain techniques, such as single-pulse OTDRs and correlation OTDRs.[7,8,9] Frequency-domain OFDRs (Chapter 10), on the other hand, promise some advantages, especially in terms of highest resolution (sub-cm). OFDRs have yet to emerge from the laboratory state.[10,11,12] OTDRs can be further classified by with respect to the optical-detection technique. These are analogue direct detection using a photodetector, digital direct detection using photon counting,[13,14] and coherent detection with either homodyne or heterodyne methods.[15,16] The physical principle of backscatter measurements is the same independent of OTDR technique. For simplicity, the following text refers primarily to the standard single-pulse OTDR with many of the results applicable to other OTDRs.

11.2 PRINCIPLE OF OTDR OPERATION

OTDRs launch short duration light pulses into a fiber and then measure, as a function of time after the launch, the optical signal returned to the instrument. As the optical pulses propagate along the fiber, they encounter reflecting and scattering sites resulting in a fraction of the signal being reflected back in the opposite direction. Rayleigh scattering and

Fresnel reflections are physical causes for this behavior. By measuring the arrival time of the returning light, the locations and magnitudes of faults can be determined and the fiber link can be characterized.

A block diagram of a generic OTDR is shown in Figure 11.1. A pulse generator triggered by the signal-processing unit is used to modulate the intensity of a laser. While there are a few special designs using codes and correlation techniques,[9] the probe signal in conventional OTDRs is a single square-pulse. Pulse widths between 5 ns and 10 μs are used depending on the spatial resolution and sensitivity requirements of the measurement. Dual-wavelength OTDRs equipped with two laser diodes (typically 1310 nm and 1550 nm) combine the light sources via a wavelength-division-multiplexing (WDM) coupler. In order to prevent the laser signal from saturating the receiver, the source is coupled into the fiber under test by a directional coupler with sufficient isolation between ports A and B.

The most common coupler type is a 3 dB-fusion type fiber coupler with low polarization sensitivity and a split ratio near 50:50 at the measurement wavelengths. This keeps the round-trip loss to the receiver close to the minimum of 6 dB. In principle, beam splitters, circulators, polarizing prisms, or lithium-niobate acousto-optical switches can perform the same function as the fused directional coupler with potentially higher performance at a higher cost.

The directional-coupler guides the returning signal to the photodetector that is either a p-i-n diode or an avalanche photo diode (APD) acting as current source for a low-noise transimpedance amplifier with high linearity. Signals covering several orders of magnitude are incident on the photodetector. This requires the receiver to have a high dynamic range together with high sensitivity. A flash type analog-to-digital-converter (ADC)

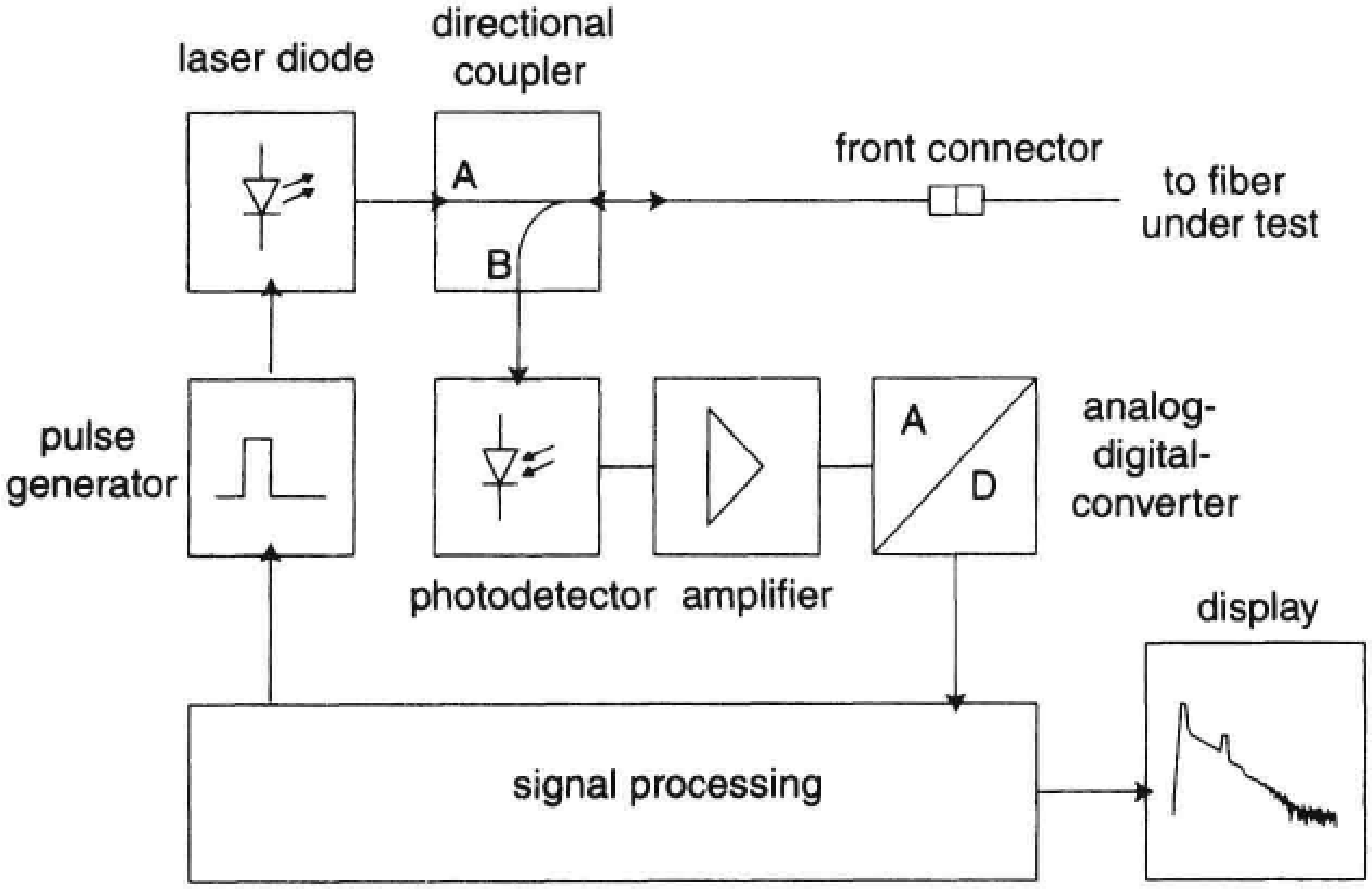

Figure 11.1 Block diagram of a single-pulse OTDR.

forms the interface to the digital data world where the measurement data is processed and the fiber signature is computed. The ADC sampling rate determines the spatial separation of adjacent data samples. Short-distance fiber links require spatial resolutions far smaller than those achievable by direct data acquisition. A sampling rate of 50 MHz corresponds to a data spacing of approximately 2 m.[17] It is not practical to increase the resolution by increasing the data sampling rate. OTDRs commonly use an interleaved processing scheme to improve spatial resolution down to the centimeter region.

The result of an interleaved measurement is the composition of individual measurement shots delayed by a varying fraction of the ADCs sampling time, as depicted in Figure 11.2. The delay is always referenced to the launched laser pulse. Depending on the de-

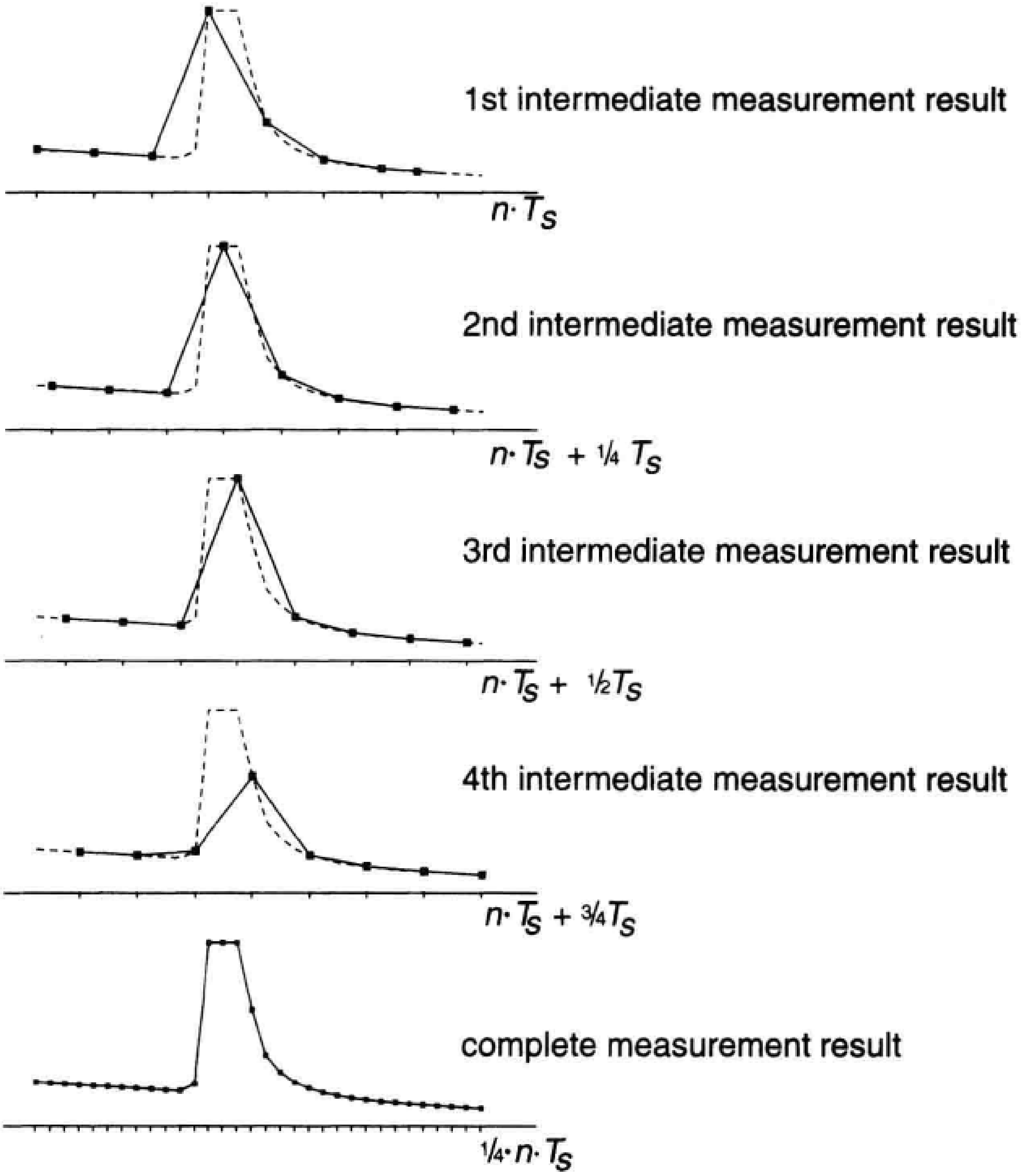

Figure 11.2 Improving spatial resolution by interleaved data acquisition.

sired resolution, the number of individual measurement shots can double, quadruple, or in general multiply as a power of two, compared to a noninterleaved measurement. The example above shows a four-fold improvement in sample spacing, at the expense of four times the measurement time. Taking full advantage of even higher interleaving rates requires a sufficiently high bandwidth in the signal-processing path to avoid smoothing of the final result.

Because the backscattered signal typically is very weak, it is often covered by noise. To overcome this problem, the process of sending a pulse and receiving the echo is repeated many times to improve the signal-to-noise ratio (SNR) by averaging.[17]

11.2.1 OTDR Fiber Signature

The main objective of an OTDR measurement is to determine the backscattering impulse response of the fiber under test. The OTDR's pulses approximate an ideal delta-function impulse rather than being a perfect copy of it. The fiber response is the result of a convolution with a finite width pulse, leading to a smoothed version of the impulse response.

Figure 11.3 illustrates a typical OTDR measurement display. The vertical scale is the reflected signal level on a logarithmic scale (in dB). The horizontal axis corresponds to the distance between the instrument and a location in the fiber under test. Because an OTDR can only measure time, it translates the time base to fiber distance by using a conversion factor which approximately equals 10μs/km, the round-trip propagation delay of light in fiber. Horizontal scale accuracy not only depends on the exact timing, but also on the fiber's group index, and on the fiber's cabling factor (a loose-buffered fiber is longer

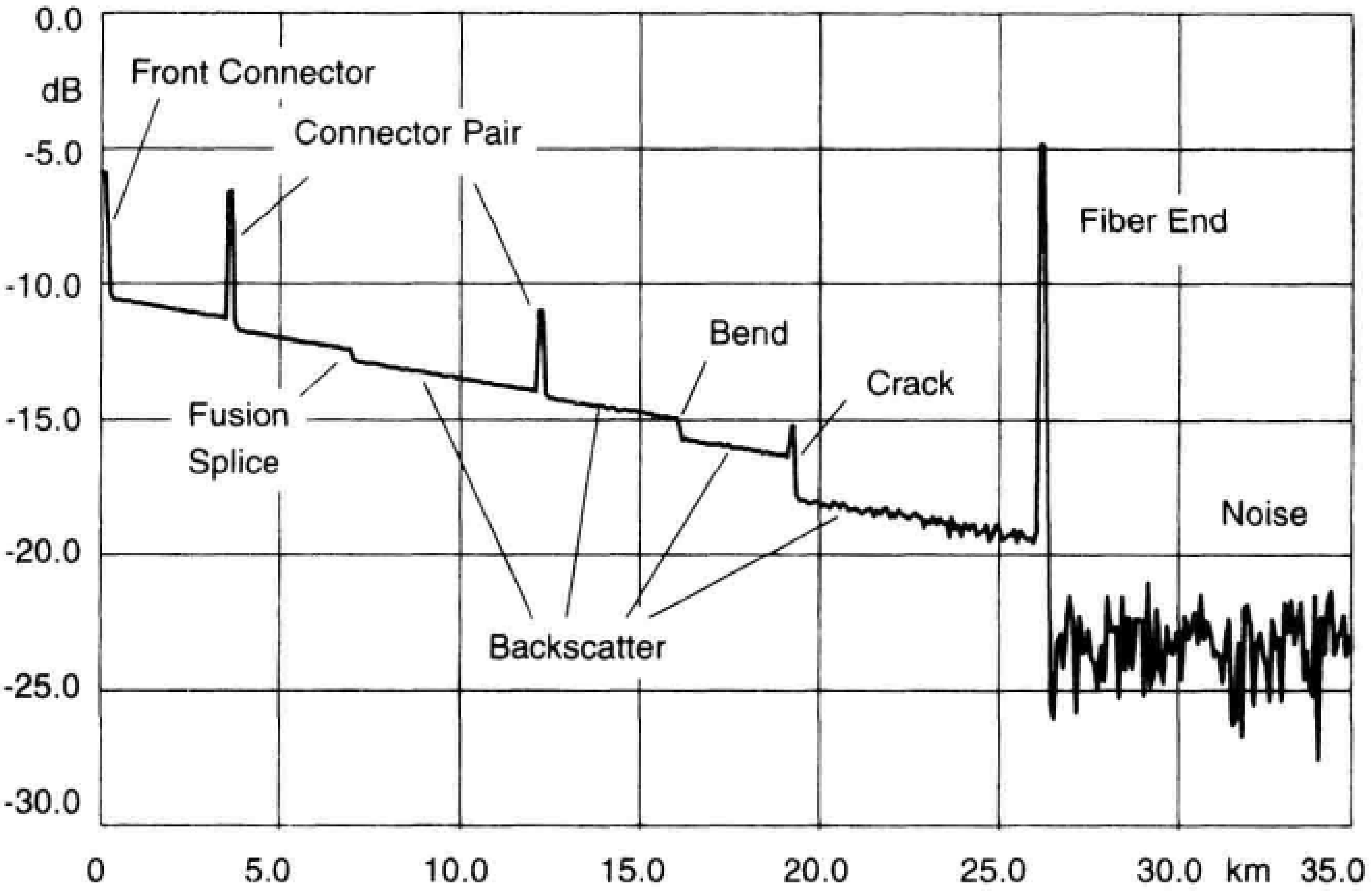

Figure 11.3 Typical OTDR trace.

than a tightly buffered one). With a typical time-base accuracy better than 0.01%, in practice, both the index of refraction and the cabling factor always are the limiting factors to overall distance accuracy.

An OTDR measures round-trip loss. Light captured by the OTDR moves in the opposite direction to the launched pulse. By traveling forward and backward to the OTDR it experiences a two-fold fiber attenuation and it needs twice the time it takes to reach a distinct location on the fiber. This is why traces are scaled by a factor of two on the display in both the vertical ($5 \cdot \log$ instead of $10 \cdot \log$) and horizontal direction, the so called one-way representation.

The measured response typically exhibits three types of features: straight lines caused by distributed Rayleigh backscattering, positive spikes caused by discrete reflections, and finally steps that can either be positive or negative depending on physical fiber properties.

The first event that can be seen on an OTDR trace is the reflection of the front connector that mates the OTDR to the fiber under test. As this reflection covers the near-end measurement zone, it is an undesirable event hiding information about the fiber to be tested. A clean high-quality connector with low reflectance is mandatory to achieve best results. A bad connector not only decreases launch power by its insertion loss, but also causes the returning light to be re-reflected back into the fiber under test again generating multiple echoes or ghost patterns. Connector care is an important part of OTDR operation (see Appendix C).

As the trace is plotted as power vs. distance, the slope of the straight lines gives the fiber attenuation in dB/km. Fusion splices cause a sudden drop in the backscatter level. The step size corresponds to the insertion loss only if the two mated fibers are identical. Otherwise the true insertion loss can only be determined by the average of two measurements from both fiber ends.[18] A similar signature on an OTDR display is caused by a stressed curve in the fiber. This is called a bend, and results in light reflecting out through the cladding, instead of continuing on down the fiber. Fusion splices and bends show only insertion loss without a reflection. They are called nonreflective events. A mismatch in the refractive index causes Fresnel reflections leading to spikes superimposed on the backscatter signal (see Equation 11.26 for details). Mechanical splices, connectors, and cracks in general show a tiny air gap which reflects light rather than scatters it. They belong to reflective events. An open nonterminated fiber end can cause a strong reflection depending on the condition of the fiber end surface. At a glass-to-air transition, up to 4% of the optical power can be reflected back to the OTDR. Behind the fiber end no optical signal can be detected and the curve drops to the receiver noise which ultimately limits the detectable power level.

11.2.2 Level Diagram

The level diagram in Figure 11.4 illustrates the range of powers that an OTDR has to work with. At a glance, both the highest and the lowest signal levels that return from the fiber, either because of reflections or because of backscatter, can be seen. This is useful information for an OTDR design with a certain required dynamic range. For example, the

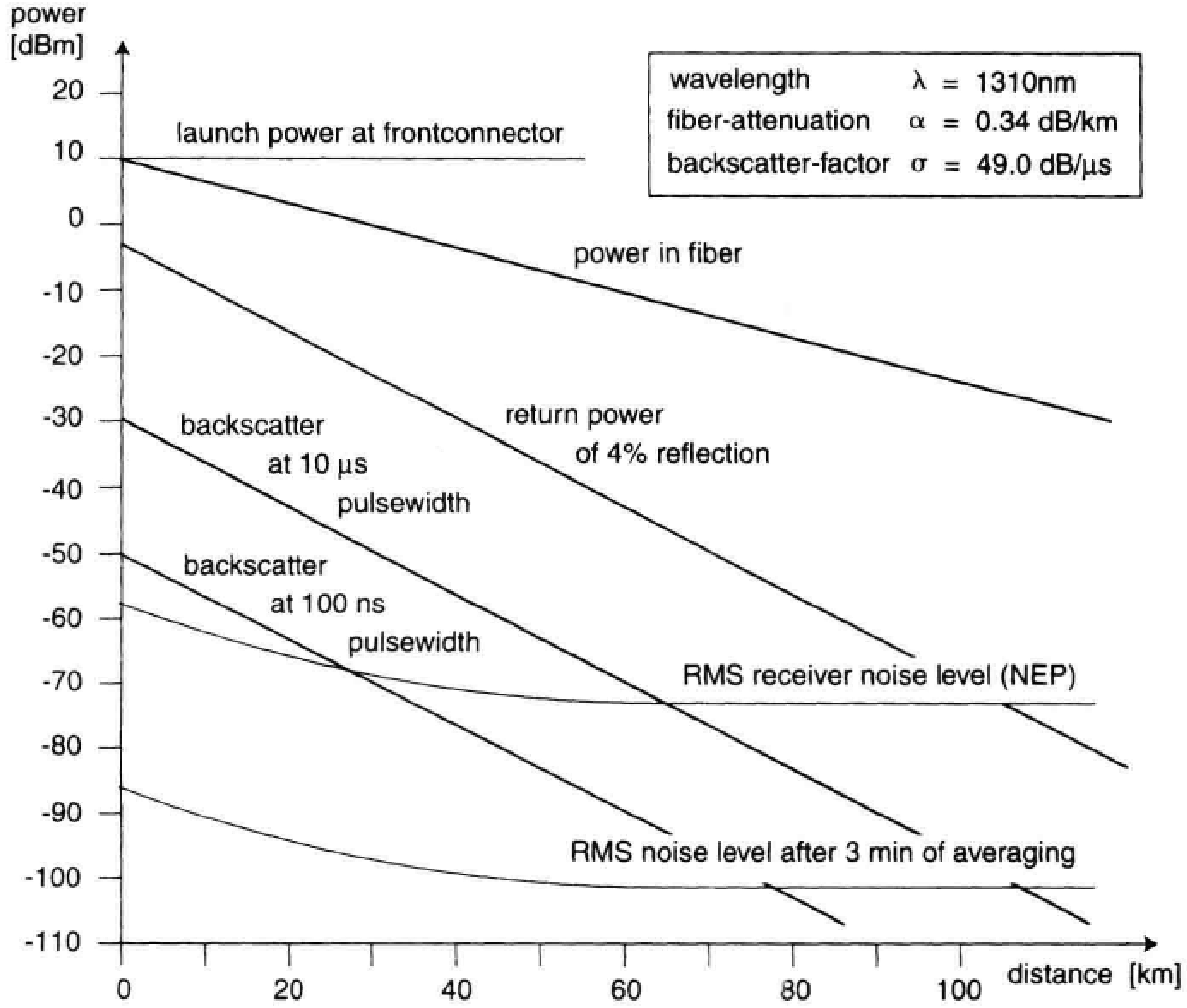

Figure 11.4 OTDR level diagram.

necessary noise equivalent power (NEP) that the receiver must not exceed to achieve the desired dynamic range performance can easily be determined.

To calculate the maximum power levels of reflected and backscattered light we assume an OTDR laser-source with a peak pulse power of +13 dBm. Then the launch power at the front-connector is about +10 dBm because of the 3 dB-coupler loss.

In case of a noncontact front panel connector, the resulting 4% reflection of a glass-to-air transition at the near end corresponds to a reflected light pulse approximately 14 dB below the incident pulse, in other words, –4 dBm. For a singlemode fiber at $\lambda = 1310$ nm, the backscatter power level is roughly 49 dB/µs below peak power (see Equation 11.23). This yields about –30 dBm backscatter power level for 10 µs pulsewidth, and –50 dBm for 100 ns, respectively. Light scattered and reflected back from a remote location in the fiber under test is exposed to twice the fiber loss as is indicated in Figure 11.4 by the slopes of the corresponding lines. Taking the fiber attenuation into account, the backscatter signal weakens with increasing distance, and eventually dips into the receiver noise. Often the receiver's bandwidth is adapted to the chosen measurement span to provide optimal resolution and dynamic range as well. This leads to a higher NEP at short-distance ranges. A wider pulse with its higher energy enables the OTDR to look deeper into the fiber. Also, receiver sensitivity can be improved with signal averaging. Depending on fiber length, laser pulse repetition rate, and processing speed, up to 25 to 30 dB of noise reduction within a 3 min measurement time can be achieved.[17] As the fiber's attenuation is considerably lower at $\lambda = 1550$ nm, the level diagram at this wavelength would reveal a much longer distance before the backscatter curves hit the noise level.

Example

A 20 km fiber link is being tested with an OTDR. Determine the noise reduction that can be achieved by signal averaging compared to a single measurement shot:

a. within the first second,
b. within a 3 min measurement time,
under the assumption that 10% of the time is needed for processing overhead.

Solution

With a time-distance conversion factor of approximately 10 μs/km, the round-trip time T_{RT} for a 20 km link length is:

$$T_{RT} = 10\,\frac{\mu s}{km} \times 20\,km = 200\,\mu s$$

This corresponds to N_{1s} and $N_{3\text{min}}$ measurement shots in 1 s and 3 min measurement time, respectively, where:

$$N_{1s} = \frac{1}{200 \cdot 10^{-6}} \times 90\% = 5000 \times 0.9 = 4500$$

$$N_{3\text{min}} = N_{1s} \times 180 = 810{,}000$$

The noise reduction is proportional to the square-root of N. Thus, the (two-way) SNR improvement is:

$$\Delta SNR_{1s} = 10 \times \log(\sqrt{N_{1s}}) = 5 \times \log(4500) = 18.3\text{ dB}$$

$$\Delta SNR_{3\text{min}} = 10 \times \log(\sqrt{N_{3\text{min}}}) = 5 \times \log(810{,}000) = 29.5\text{ dB}$$

Obviously the major part of the noise reduction is achieved within the very first second of the measurement. Keep in mind that OTDRs display one-way dBs, in other words, after 3 min the noise level on the screen decreases by (29.5 − 18.3)/2 dB = 5.6 dB compared to the first display update after a 1 s measurement time.

11.2.3 Performance Parameters

The performance of an OTDR is specified by a set of parameters that describe the quality of the measurement and allow the user to understand how much the instrument fits the application needs. Generic requirements for OTDRs are proposed in Reference 19. Figures 11.5 to 11.7 depict the key parameters: dynamic range, measurement range, attenuation deadzone, event deadzone, and resolution.

Dynamic Range and Measurement Range. Dynamic range is an important parameter, as it is often used to rank an OTDR among a particular performance class. It provides information not only on the maximum fiber loss that can be measured, but also on

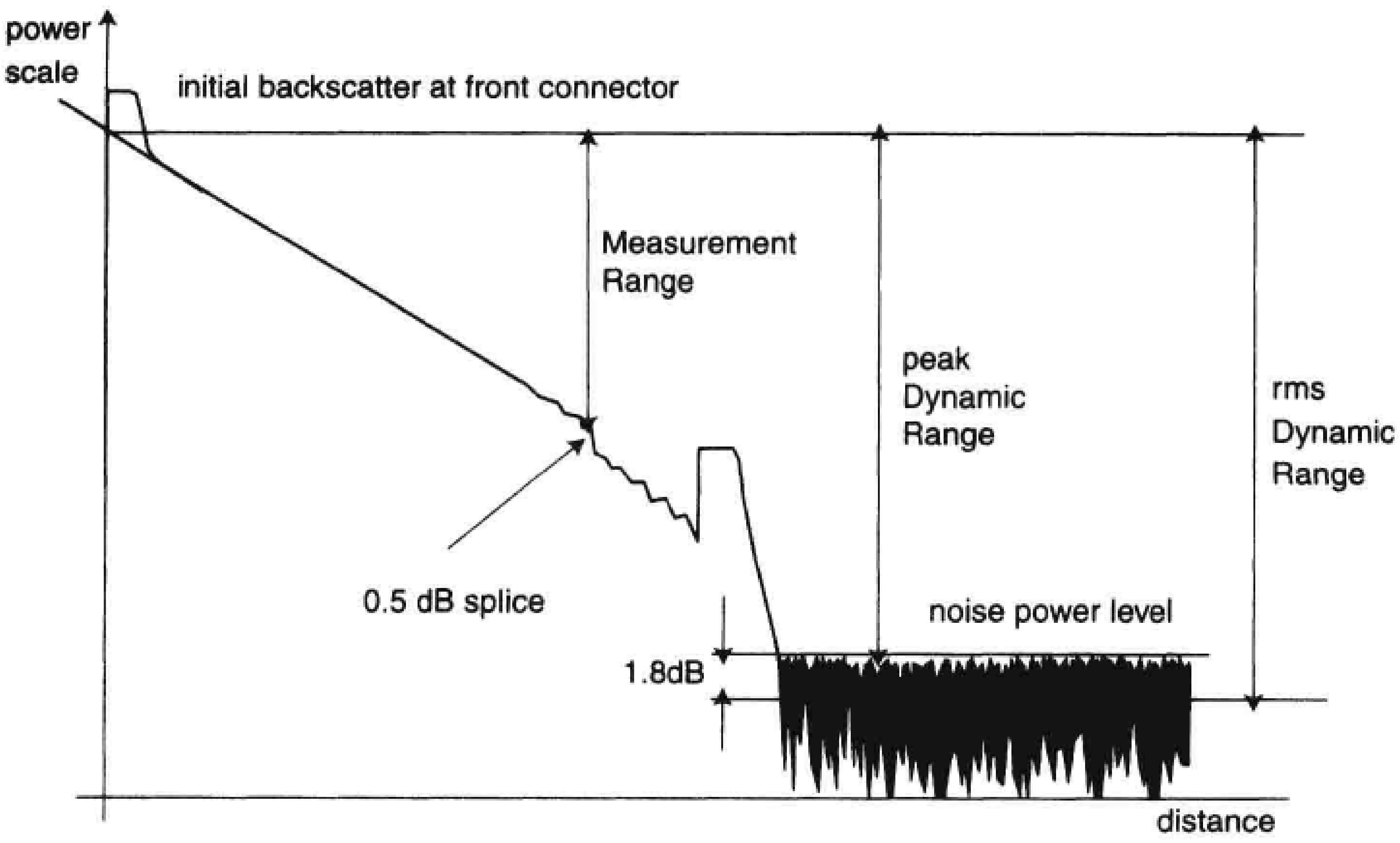

Figure 11.5 Dynamic range and measurement range.

the measurement time required for a given fiber loss. Dynamic range is defined as the difference between the initial backscatter level and the noise level after 3 min of measurement time, expressed in decibels of one-way fiber loss. The noise level either can be defined as rms (SNR = 1), or 98% peak noise level. Assuming purely Gaussian noise distribution, 98% of all noise samples are covered within approximately 2.4 times the standard deviation. This corresponds to a 1.8 dB increase if referring to the rms value rather than to the 98% peak level. As the reference condition SNR = 1 is the one giving the maximum value for the dynamic range, it is often used in the literature.

Measurement range deals with identification of events. The measurement range is defined as the maximum attenuation that can be inserted between the OTDR and an event for which the OTDR is still able to accurately measure the event.[19] Commonly a 0.5 dB splice is chosen as the event to be identified.

As the accuracy of a loss measurement made with an OTDR primarily depends on the SNR at that point, instruments with a high dynamic range are highly valued. Software algorithms to identify patterns in a noisy environment have great impact on measurement range performance.[20]

Dead Zones. Dead zones are always related to the presence of reflections. Dead zones occur when the reflected signal saturates the OTDR receiver. The receiver is slow to recover its sensitivity after the saturation resulting in the loss of information. If the receiver saturates because of strong signals, it will take some time to recover from this overload condition. As a consequence, the measured fiber response is superimposed by the receiver's overload behavior, yielding a distinct fiber segment covered by an exponentially

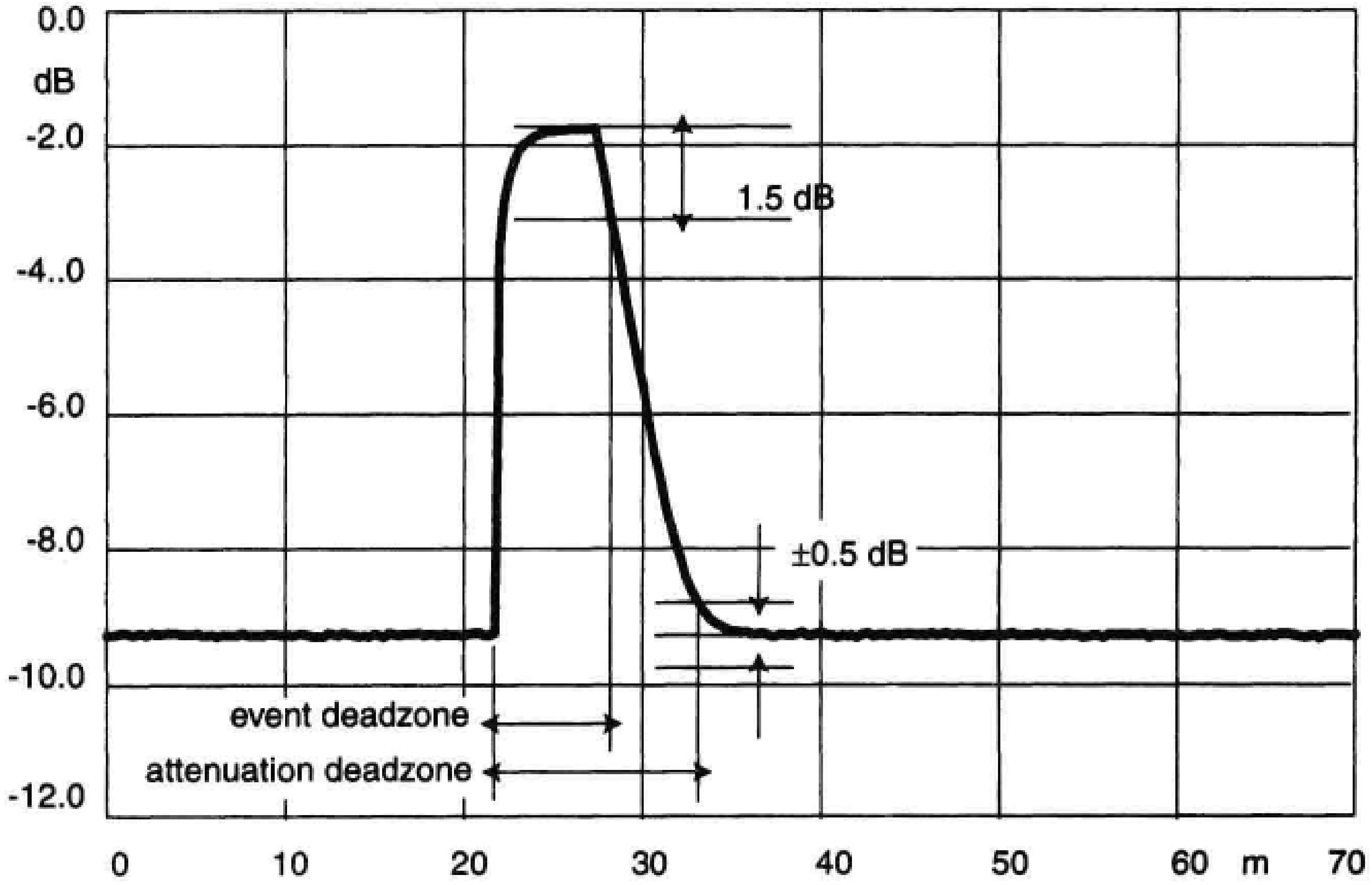

Figure 11.6 Attenuation and event dead zone.

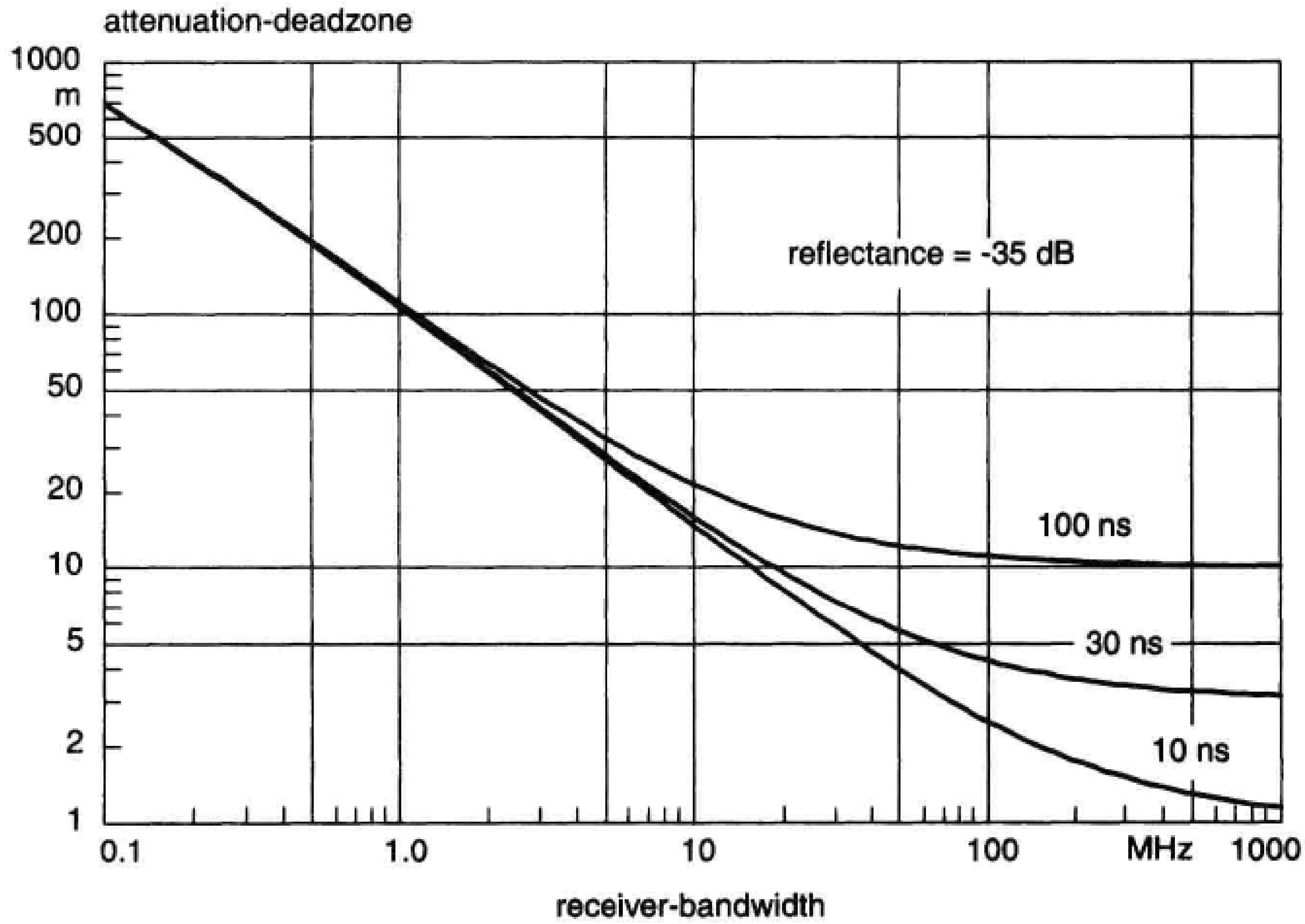

Figure 11.7 Minimum attenuation dead zone as function of OTDR receiver-bandwidth.

diminishing tail. Two different kinds of dead zones are usually specified. The OTDR's event dead zone is the distance between the beginning of a reflection and the −1.5 dB point on the falling edge of the reflection as indicated in Figure 11.6. After the event dead zone, an adjacent reflective event could clearly be recognized.

The attenuation dead zone is defined as the distance from the start of a reflection to the point where the receiver has recovered to within a ±0.5 dB margin around the settled backscatter trace. It depends on pulsewidth, wavelength (backscatter factor σ), the receiver bandwidth, and reflectance. The purpose of dead-zone terminology is to quantify the distance over which information is lost after a large reflection. Commonly a 35 dB reflection is used for dead zone specifications, in other words, about 0.03% of optical power at this point is reflected and superimposes with backscattered light, the power level of which is a function of the chosen pulsewidth. Therefore the actual height seen on the OTDR display depends on both reflectance and pulsewidth for a given fiber (see Figure 11.20 and Equation 11.29 for details). Note that very short pulsewidths do not necessarily lead to shorter attenuation dead zones. This is because as the pulse gets narrower, the difference between the backscatter level and the top of the reflection increases. With a finite receiver bandwidth, the exponential tail of the falling edge adds significantly to the dead zone. APDs also have inherent tailing effects at low signal levels. Short pulse widths also lower SNR. Therefore, OTDR specifications for attenuation dead zone are often given at a pulsewidth next to the shortest one. In Figure 11.7 the minimum-achievable attenuation dead zones for three different pulsewidths as a function of receiver-bandwidth are compared. The plot is calculated for a 35 dB reflection on a typical singlemode fiber at λ = 1310 nm, using a first-order low-pass model for the ideal receiver. Typical singlemode OTDRs have receiver bandwidths in the 1 to 10 MHz region where the curves start to overlap towards the low frequencies. In terms of attenuation dead zone, this indicates a bandwidth-limitation rather than a pulsewidth-limitation. At 10 MHz receiver-bandwidth, the dead-zone values for 10 ns and 30 ns lie close together. Hence the +2.4 dB SNR improvement with the wider pulse has a real advantage, as this corresponds to nearly a tenfold gain in measurement speed. When aiming at 5 m dead zone with a singlemode OTDR, the required receiver-bandwidth is about 50 MHz.

Spatial Resolution. Spatial resolution indicates the instrument's ability to resolve two adjacent events; one of them might be slightly reflective. Near-end resolution simply takes the instrument front-panel connector reflection as the first event and characterizes how close a nonreflective event (for example, a splice) can be spaced to the instrument and accurately measured.[19] Single-event resolution is also specified. For a splice with less than 1 dB, the single event resolution is defined as the 10% to 90% step width. For a discrete reflection, the 50% width is used as the reference.[21]

11.2.4 Tradeoff between Dynamic Range and Resolution

A fundamental limitation for any conventional OTDR is the tradeoff between dynamic range and resolution. The received signal $s(t)$ can be expressed as the convolution ($\otimes$) of $p(t)$, the probing pulse, $f(t)$, the backscattering impulse response of the fiber, and $r(t)$, the impulse response of the receiver.

$$s(t) = p(t) \otimes f(t) \otimes r(t) \tag{11.1}$$

The achievable resolution is therefore limited by the receiver response and the geometrical width of the probe signal. For high-spatial resolution, the probe pulsewidth has to be as small as possible with a correspondingly wide receiver bandwidth. This leads to a reduced SNR. Increasing the strength of the received signal by using longer probe pulses and low noise (low bandwidth) receivers leads to improved sensitivity with correspondingly less resolution. This tradeoff of pulse width and sensitivity is shown in Figure 11.8. Two reflective events spaced about 100 m apart have been measured with a pulsewidth of 1 μs as well as 100 ns. Though the upper trace shows a smoother backscatter than the lower one, the drawback of insufficient spatial resolution is evident.

Increasing the laser output power also maximizes the backscatter level at a given pulsewidth. Unfortunately, the use of very high-power sources is normally precluded in a practical system because of reliability, cost, safety regulations, availability, or nonlinear scattering phenomena. Spread-spectrum techniques such as correlation[22] overcome this limitation and offer the possibility of improving the SNR without sacrificing resolution. Such techniques are commonly used in radar[23,24] and other peak-power limited systems. In OTDRs, however, this principle has only limited success, mainly because even small nonlinearities in the analog hardware lead to spurious signals that disturb the measurement results.

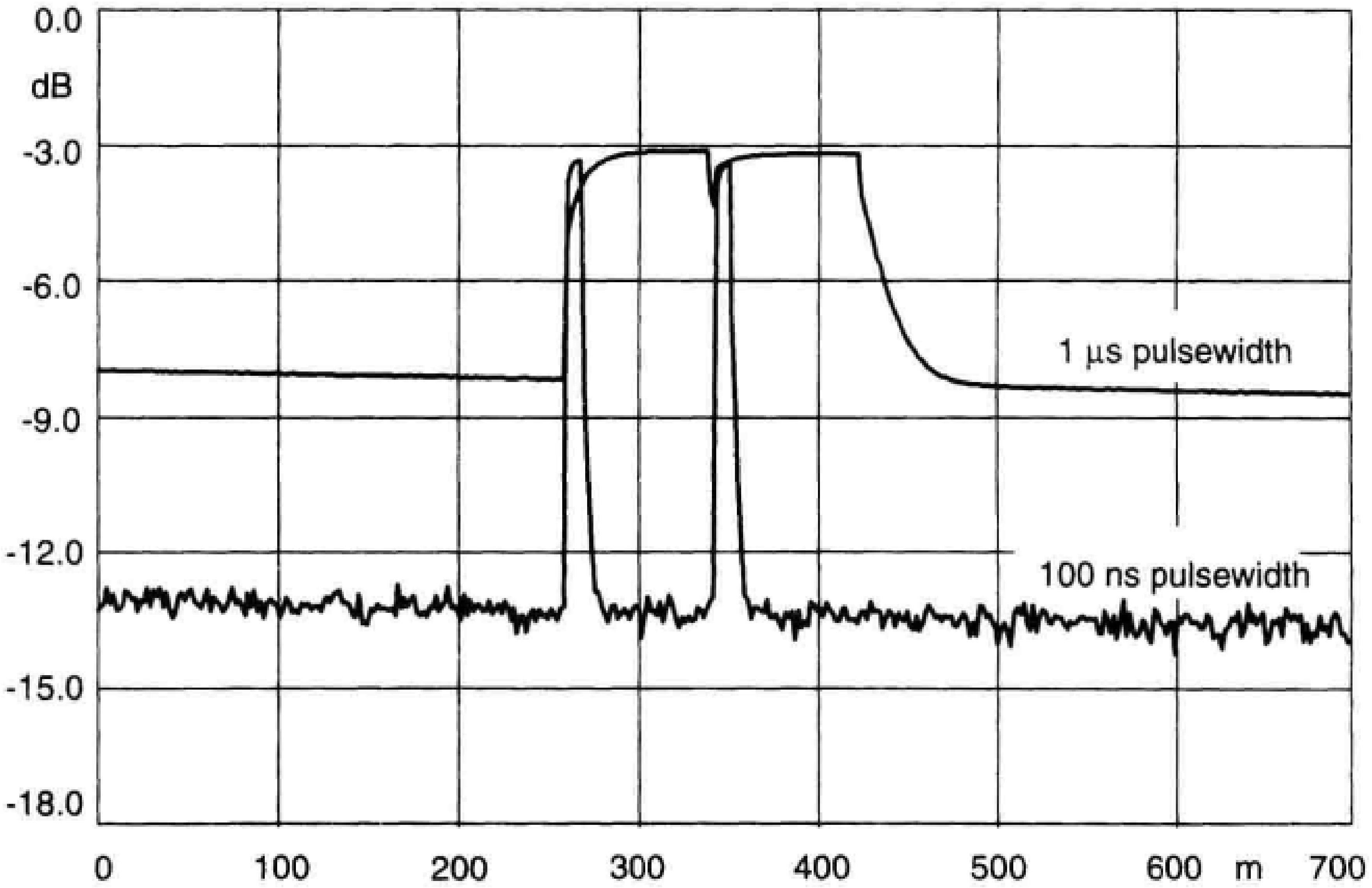

Figure 11.8 Differences in resolution and SNR caused by different pulsewidths.

11.2.5 Ghost Features Caused by Multiple Reflections

Sometimes the reflectometry trace includes "ghost" features. If the fiber under test contains connectors that reflect strongly, echoes generated by multiple reflections can produce spikes at false locations. The only solution for (real) ghosts is to avoid high reflectivity connections. Figure 11.9 shows a measurement setup with an OTDR and two connected fiber spools. Even in case of physical contact, ordinary connectors show discrete spikes on the OTDR display. Any echo pulse returning from the DUT to the OTDR is partially reflected back at the front-panel connector, acting like an additional delayed probe pulse. For well-maintained connectors, the echo amplitude is too small to generate a visible (and delayed) ghost picture.

Dirty or scratched connectors, however, can reflect a big part of a pulse's energy. In this case, a visible ghost spike can appear at a location l_{ghost} which can be calculated as

$$l_{\text{ghost}} = 2 \cdot l_2 - l_1 \tag{11.2}$$

with l_1 and l_2 being the location of the two reflections involved. In the example above $l_1 = 0$, yielding $l_{\text{ghost}} = 2\, l_2$.

In contrast to real ghosts, an OTDR can create ghost patterns if the repetition rate of the laser pulses is too fast and not adapted to the fiber under test. If the OTDR emits a sec-

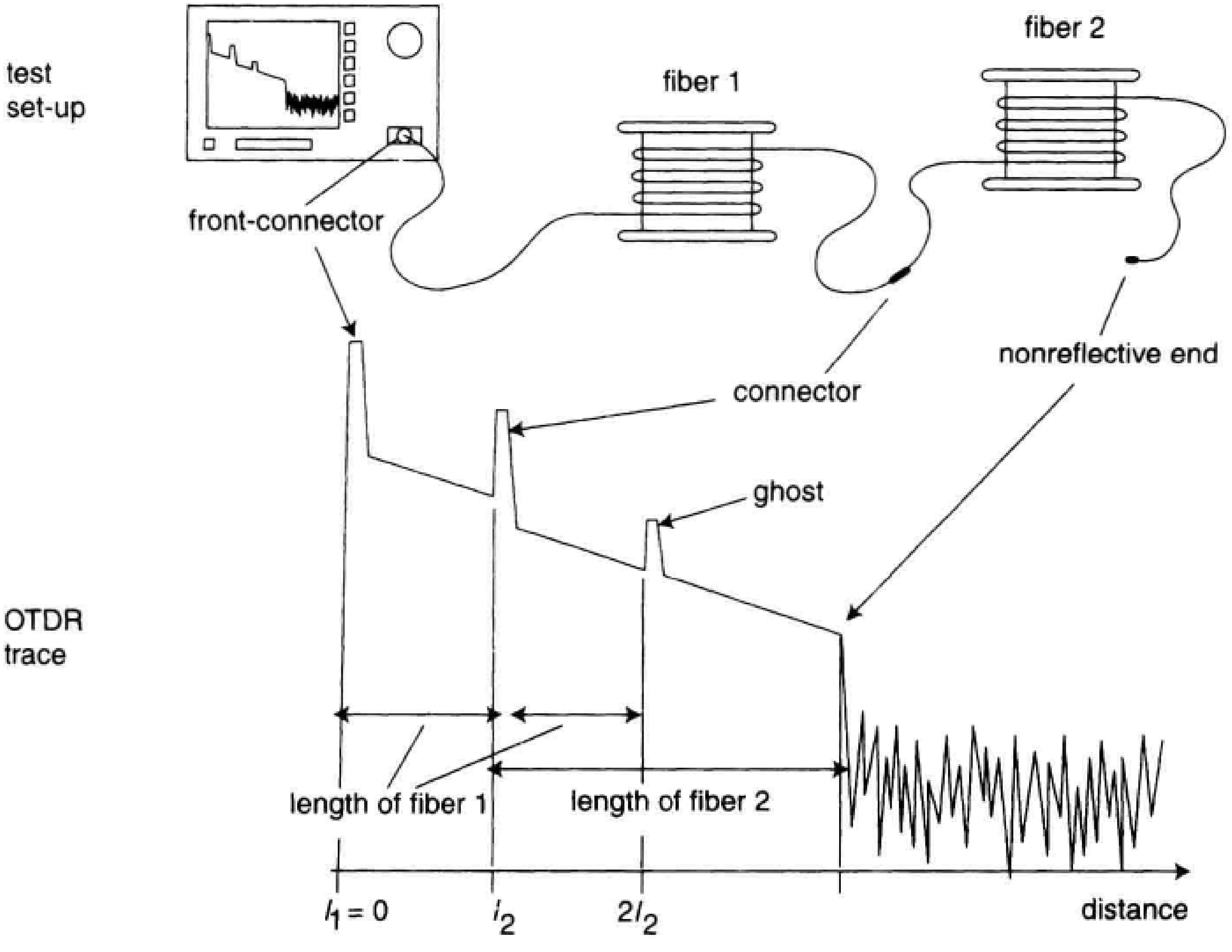

Figure 11.9 Example of a ghost generated by multiple reflections.

ond light pulse and starts data acquisition before the response of the previous one has been completely received, echoes from both pulses will overlap, leading to erroneous measurement results.

11.3 FIBER LOSS, SCATTER, AND BACKSCATTER

11.3.1 Loss in Fiber

Fiber loss is one of the most important properties of an optical fiber. It largely determines the maximum repeaterless span for an optical communication link. Absorption, scattering, and bending are the three major loss mechanisms in fused silica glass (SiO_2) fibers. Intrinsic absorption is extraordinarily low in the commercially used wavelength-window between the ultraviolet and the infrared region and is at short wavelengths negligible compared to scattering loss. Above 1700 nm, glass starts absorbing light energy because of vibrational transitions of the Si–O bond.[25] Figure 11.10 shows the typical tub-shaped total loss in optical silica fibers with its minimum attenuation around 1600 nm.

The dominant extrinsic absorption factor is the presence of impurities in the fiber material, for example, metal ions or water (OH^-) ions.[26,27] OH^- absorption can be used to monitor undersea links for the tiniest water penetration. Overtones of the fundamental absorption wavelength of water at 2.7 μm reside near the wavelength regions of commercial interest, for example, 1383 nm, 1250 nm, or 950 nm, respectively. The absorption lines

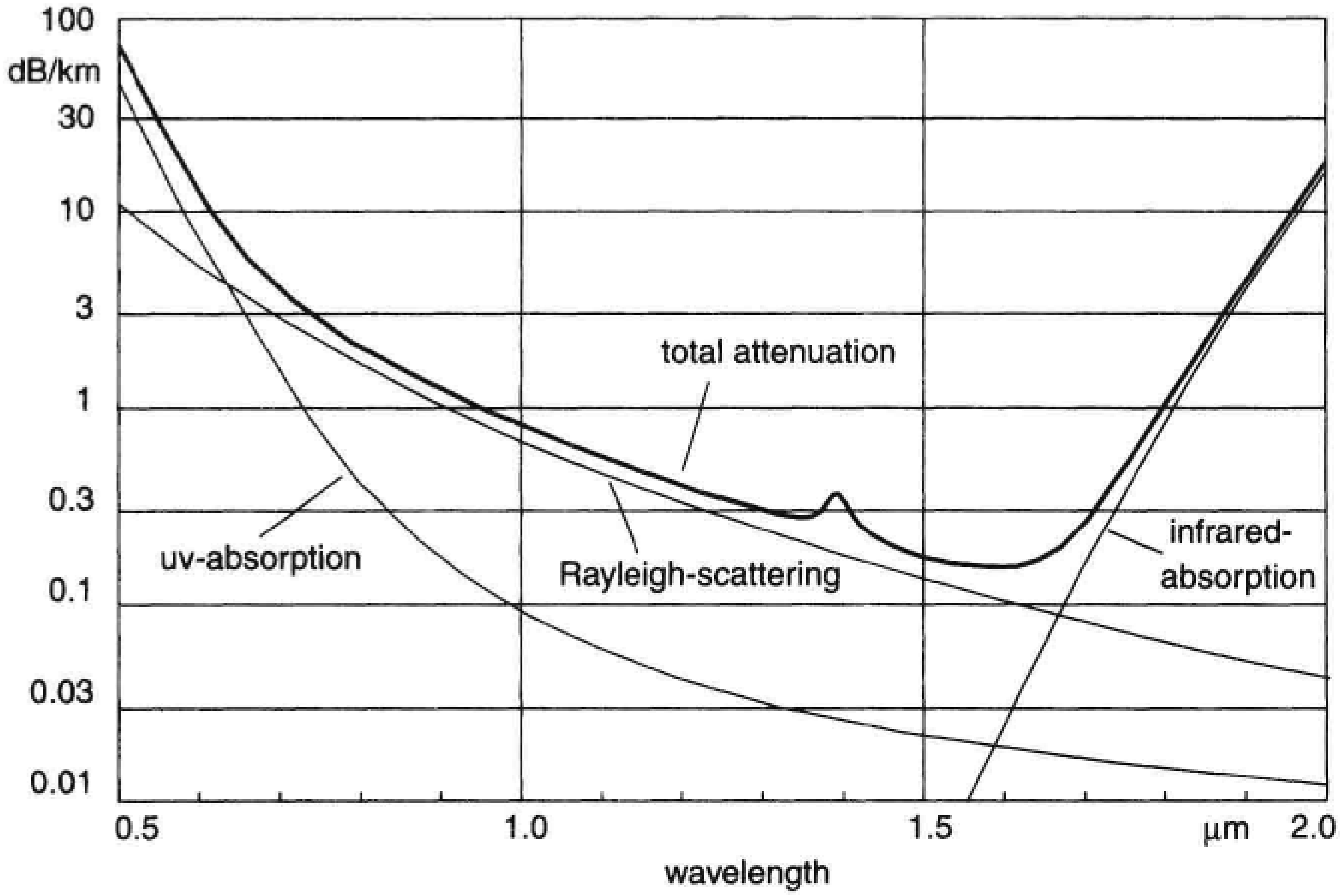

Figure 11.10 Wavelength dependence of silica-glass fiber attenuation α.

cover very narrow spectral widths. The locations and magnitudes of these absorption peaks in the earlier fiber manufacturing are the prime reason for the three major transmission windows at 0.85 μm, 1.3 μm, and 1.55 μm. In typical GeO_2-doped fibers, the zero-point for chromatic dispersion is near 1310 nm. The third transmission window at 1.55 μm shows the minimum fiber attenuation of approximately 0.2 dB/km, or even lower.

Rayleigh-Scattering Phenoma Description. Scattering losses in glass arise from light interacting with density fluctuations in the fiber. Variations in material density and compositional fluctuations occurring during fiber manufacture create random inhomogeneities that give rise to refractive index variations. This isotropic phenomenon is termed Rayleigh scattering if the size of the defect is less than one-tenth of the wavelength of the incident light.[28,29] The mechanism does not cause elimination or conversion of optical energy but simply forces a part of the optical wave to escape from the waveguide. The scattered intensity is proportional to $1/\lambda,^4$ so that longer wavelengths in the standard transmission windows exhibit lower attenuation losses than shorter wavelengths. Equation 11.3 shows a simple empirical relation for the Rayleigh scattering loss α_s and the wavelength λ in germanium-doped silica fibers:[30]

$$\alpha_s = \frac{(0.76 + 0.51 \cdot \Delta n)}{(\lambda/\mu m)^4} \left[\frac{\mathrm{dB}}{\mathrm{km}}\right] \tag{11.3}$$

where Δn is the difference between the fiber core's refractive index and that of the fiber cladding. A further simplification replaces the denominator with the constant 0.8. This gives a formula that is sufficiently accurate in most cases and that can be simply held in memory.

Brillouin and Raman Scattering. There are two types of scattering that can cause additional loss because of interaction between incident photons and phonons of the material. Phonons, the quantized energy of vibrations, behave like particles, and therefore can interact with photons. Because of the Doppler effect, a frequency shift occurs during collision. Brillouin scatter is induced by acoustic waves and shows a frequency shift in the order of 10 GHz which depends on the angle under which scattering is measured.[31] This Doppler frequency shift is maximized in the backward direction. Different methods have been proposed for optical fiber sensors based on this effect. Brillouin frequency shift increases linearly with (longitudinal) strain and temperature.[32] The effect of Brillouin scattering can be reduced by using short-coherence length light sources.

Raman scattering on the other hand is caused by molecular vibrations of "optical" phonons which is generated by the interaction of a strong electric field of the optical wave and the quartz molecules. The resulting nonuniform spectrum exhibits the so-called Stokes-lines. These lines extend at low temperatures chiefly to longer wavelengths and approach a symmetrical shape with increasing temperatures. The spectral width extends to more than 10 THz. A description on how to take advantage of the Raman effect for distributed temperature sensing can be found in Dakin and co-workers.[33] Both the Brillouin and the Raman scattering phenomena are nonlinear effects that occur only at higher power levels.[34,35] They can be a limiting factor in high power systems[36] (also see the treatment in Appendix B).

Micro- and Macrobending. Bending is the third effect leading to increased fiber loss. Microbending is due to tiny imperfections in the geometry of the fiber caused either by the manufacturing process or by mechanical stress, such as pressure, tension, and twist. To overcome this problem, fibers are protected by either a loose or a tight buffer. Macrobending, on the other hand, occurs when the fiber is formed to a curvature with diameters on the order of centimeters. In this case, less-than-total internal reflection at the core-to-cladding boundary forces some of the light to leave the core.

11.3.2 Backscatter Signal Analysis

As a result of these attenuation effects, light traveling along a fiber exhibits an exponentially decreasing power level with the distance. The power transmission relation between incident light P_0 and transmitted power $P(z)$ at a distance z is

$$P(z) = P_0 \cdot e^{-\alpha z} \tag{11.4}$$

with the attenuation coefficient α measured in km^{-1} units. Since system losses in general are calculated in dB units, it is often more convenient to use the attenuation coefficient α_{dB} in dB/km units for loss calculations. Then

$$P(z) = P_0 \cdot 10^{\frac{-\alpha_{\mathrm{dB}}}{10} z} \tag{11.5}$$

with

$$\alpha_{\mathrm{dB}} = \frac{10}{\ln 10} \cdot \alpha \approx 4.34\,\alpha \tag{11.6}$$

To simplify matters, the total attenuation coefficient, α, is commonly composed of an absorption coefficient α_a and a scattering coefficient α_s

$$\alpha = \alpha_a + \alpha_s \tag{11.7}$$

It is obvious that the lower attenuation limit is bounded by α_s since $0 \leq \alpha_a << \alpha_s$.[37] Let's now focus on the effect of scattering and consider a laser pulse in a fiber with the temporal pulse duration τ. As the pulse propagates, light is scattered within a fiber element of length W, as depicted in Figure 11.11, with

$$W = \tau \cdot v_{gr} = \tau \frac{c}{n_{gr}} \tag{11.8}$$

where v_{gr} is the group velocity, c the speed of light in vacuum, and n_{gr} the group index of glass.

The scattered power dp_s at the position z within an infinitesimal small interval dz is proportional to the pulse power $P(z)$.[38]

$$dp_s = k \cdot P(z)\, dz \tag{11.9}$$

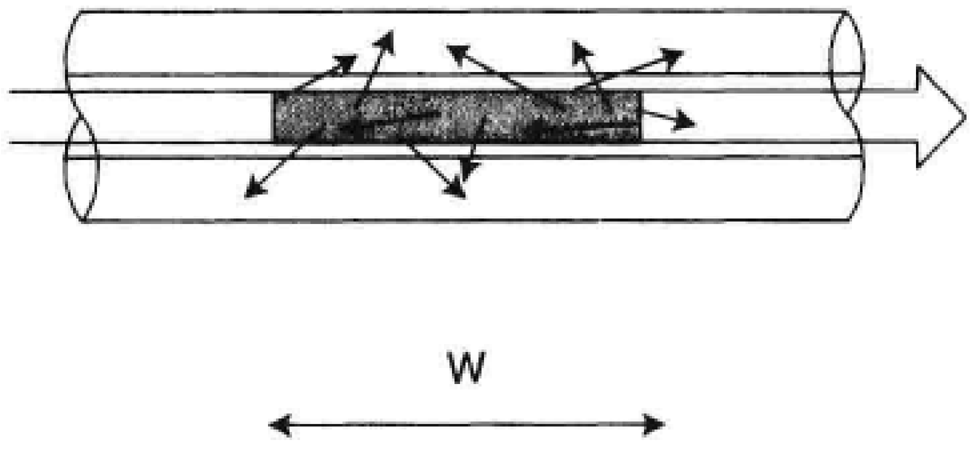

Figure 11.11 Scattering within a fiber element of width *W*.

with
$$k = S \cdot \alpha_s \tag{11.10}$$

and
$$\alpha_s = \text{scattering coefficient} \sim \frac{1}{\lambda^4}$$

S is the fraction of the light scattered in all directions that is captured by the fiber core and guided back to the OTDR. The backscattering capture coefficient *S* is given in Equation 11.11.

$$S = \left(\frac{NA}{n_0}\right)^2 \cdot \frac{1}{m} \tag{11.11}$$

where *NA* is the fiber's numerical aperture, n_o is the refractive index of the fiber core center and *m* depends on the refractive index profile. A detailed derivation of the context can be found in References 38, 39, and 40. For singlemode fibers a typical value for *m* is 4.55.[41,42]

To derive the backscatter response caused by a rectangular pulse, we first assume the leading edge of the pulse to be at a location $L = T \cdot v_{gr}$. Light scattered back from exactly this distance will arrive at $t = 2T$, the round-trip time, at the OTDR port again. This situation is depicted in Figure 11.12a. After a time, $t = T + \tau/2$, the trailing edge hits the distance $L - W/2$. The light scattered from this position needs $t = T - \tau/2$ to travel back to the beginning, summing up to the same round-trip time $t = 2T$ as can be seen in Figure 11.12b. We can generalize the condition for light that returns after $t = 2T$. Let's look at a short interval ΔW that is $2\Delta z$ behind the pulse's leading edge at $t = T + \Delta t$. Backtraveling light from this part arrives after $t = T - \Delta t$ yielding again the round-trip time $t = 2T$. This close inspection reveals the important fact that the backscatter power seen by the OTDR at a time $t = 2T$ is actually the integrated sum of backscatter from the locations $z = L - W/2$ to $z = L$ when probing the fiber with a pulse of geometrical width *W*.

Summing up the light power backscattered from infinitesimal short intervals *dz* from the whole pulse and taking the fiber attenuation into account, yields

$$P_s(L) = \int_0^W S \cdot \alpha_s \cdot P_0 \cdot \exp\left(-2\alpha\left(L + \frac{z}{2}\right)\right) dz \tag{11.12}$$

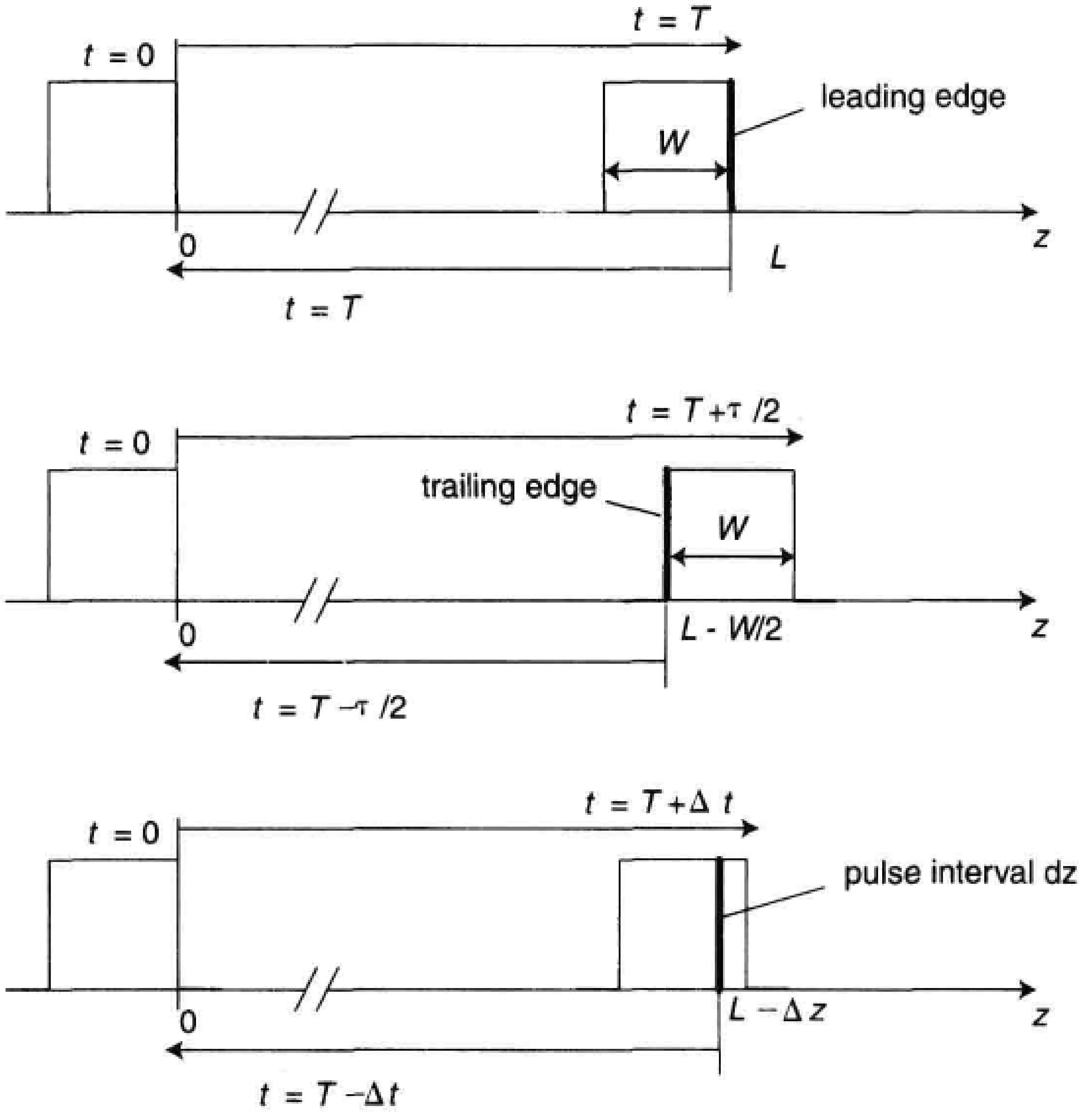

Figure 11.12 Backscatter round trip time $t = 2T$.

$$= S \cdot \frac{\alpha_s}{\alpha} \cdot P_0 \cdot e^{-2\alpha L}\,(1 - e^{-\alpha W}) \quad L \geqslant \frac{W}{2} \tag{11.13}$$

Equation 11.13 is valid only for $t \geq \tau/2$. For distances less than $W/2$, the lower integral limit has to be substituted by $W - 2L$. Then we get

$$P_s(L) = \int_{W-2L}^{W} S \cdot \alpha_s \cdot P_0 \cdot \exp\left(-2\alpha\left(L + \frac{z}{2}\right)\right) dz \tag{11.14}$$

$$= S \cdot \frac{\alpha_s}{\alpha} \cdot P_0 \cdot e^{-\alpha W}\,(1 - e^{-2\alpha L}) \quad 0 \leqslant L \leqslant \frac{W}{2} \tag{11.15}$$

An approximation for the initial value of the backscattered power P_{init} can be derived for $L = W/2$ from Equation 11.15 when developing the exponential functions into polynomials.

$$P_{\text{init}} = P_s\left(\frac{W}{2}\right) \approx S \cdot \alpha_s \cdot P_0 \cdot W \tag{11.16}$$

Likewise for short pulsewidth, $\alpha W << 1$, the last expression in parentheses in Equation 11.13 can be simplified to

$$\frac{1 - e^{-\alpha W}}{\alpha} = \frac{1}{\alpha} \cdot (1 - 1 + \alpha W) = W \tag{11.17}$$

Equation 11.13 then changes to

$$P_s(L) = S \cdot \alpha_s \cdot W \cdot P_0 \cdot e^{-2\alpha L} \tag{11.18}$$

The approximations in Equations 11.16 and 11.18 show the well-known fact that for narrow pulses, the backscattered power is proportional to the pulse duration τ. Equations 11.16 and 11.18 are widely used and provide sufficient accuracy when dealing with pulsewidths typical in OTDR applications.

Example

A 100 km fiber is probed with an OTDR having a peak output power of +13 dBm. The pulsewidth used is 10 μs.

a. Determine the power level of the backscattered light returning from the far end of the fiber assuming an attenuation coefficient α_{dB} of 0.33 dB/km, a scattering coefficient α_s of 0.3 dB/km, and a capture coefficient S of 10^{-3} at the wavelength $\lambda = 1310$ nm.

b. Calculate the corresponding number of photons if the acquired data samples are spaced 10 m apart.

Solution

a. The backscattered power can be calculated using Equation 11.18. From Equation 11.6 we get the conversion factor 0.23 to convert dB/km figures in 1/km. Equation 11.8 gives the length W as 2 km.

$$P_s(100\text{ km}) = 0.001 \times (0.3 \times 0.23) \times 2 \times 20\text{ mW} \times e^{-2\times(0.33\times0.23)\times100}$$

$$= 35.3 \times 10^{-12} \times 20\text{ mW} = 0.75\text{ pW} \cong -91.5\text{ dBm}$$

b. With a time-distance conversion factor of 10 μs/km, a data spacing of 10 m is equivalent to the time period T

$$T = 10 \cdot 10^{-6} \times 0.01 = 10^{-7}\,s$$

As power is energy per time, the following relation between optical power and number of photons Z can be derived:

$$P = \frac{1}{T} \cdot h \cdot v \cdot Z = \frac{1}{T} \cdot \frac{h \cdot c}{\lambda} \cdot Z$$

Hence the average number of photons within a 100 ns timeframe that corresponds to an optical power of 0.7 pW is

$$Z = \frac{10^{-7} \times 1.3 \cdot 10^{-6}}{6.626 \cdot 10^{-34} \times 2.998 \cdot 10^{8}} \times 0.705 \cdot 10^{-12} = 0.46$$

After 3 min averaging with approximately 160,000 repetitive measurement shots, Z sums up to a total of 74,000 photons.

Substituting distance L in Equation 11.18 by the corresponding term $t \cdot c/n$ yields a time-dependent relation for the backscatter signal which shows a first-order lowpass behavior such as given in Equation 11.19. This can be used to derive the backscatter bandwidth BW_{Bsc} of optical fibers which is helpful in calculating a fiber's backscatter response to an arbitrary data signal.

$$P_s(t) \sim e^{-2\pi BW_{Bsc} \cdot t} \tag{11.19}$$

$$BW_{Bsc} = \frac{\alpha \cdot c}{\pi \cdot n} \tag{11.20}$$

Solving Equation 11.20 gives 5 kHz and 3 kHz figures for typical fibers at 1310 nm or 1550 nm wavelength, respectively.

An interesting aspect in regard to return-loss calculations is the total backscattered power $P_{s,\text{total}}(L)$ of a piece of fiber with length L, if excited by a cw (continuous-wave) signal. This can be readily derived from Equation 11.18 when integrating $P_s(L)$ for small pulsewidths, dW, over the total length of the fiber. With the substituted integration variable z we get

$$P_{s,\text{total}}(L) = \int_0^L P s(z)\, dz \tag{11.21}$$

$$= S \cdot \alpha_s \cdot P_0 \int_0^L e^{-2\alpha z}\, dz$$

The result is

$$P_{s,\text{total}}(L) = \frac{1}{2 \cdot \alpha} \cdot S \cdot \alpha_s \cdot P_0 \cdot [1 - e^{-2\alpha L}] \tag{11.22}$$

The exponential term $e^{-2\alpha L}$ indicates that very long fibers return a power value that approaches a maximum limit which mainly depends on the capture coefficient S.

Optical fibers are characterized by a backscatter factor σ in dB for a given pulsewidth. It is an indicator for the backscattered power that returns to the OTDR receiver. For rectangular pulses with peak power P_0, the near-end backscatter level is σ dB below peak power.

$$\sigma = -10 \cdot \log\,(S \cdot \alpha_s \cdot W) \tag{11.23}$$

This model is valid as long as the fiber's attenuation during the geometrical width W is negligible. Typical values for singlemode and multimode fibers are listed in the Table 11.1 below. The backscatter parameter η, defined in equation (11.24) is also included in the table. This parameter is independent of the pulsewidth and is sometimes used instead of σ.

$$\eta = \frac{c}{2 \cdot N} \cdot \alpha_s \cdot S \tag{11.24}$$

Table 11.1 Backscatter parameters for different kinds of optical fibers.

λ [nm]	Fibertype	α_s [km^{-1}]	S	σ [dB/1 μs]	η [W/J]
850	MM-SI 50μ	$3.5 \cdot 10^{-1}$	$1.1 \cdot 10^{-2}$	31	385
1300	MM-GI 62.5μ	$6.5 \cdot 10^{-2}$	$1.0 \cdot 10^{-2}$	38	65
1300	MM-GI 50μ	$6.5 \cdot 10^{-2}$	$5.0 \cdot 10^{-3}$	41	32
1310	SM 9μ	$6.3 \cdot 10^{-2}$	$1.0 \cdot 10^{-3}$	49	6.3
1550	SM 9μ	$3.2 \cdot 10^{-2}$	$1.0 \cdot 10^{-3}$	52	3.2

11.4 MEASURING SPLICE LOSS AND CONNECTOR LOSS

Splices, (macro-) bending, as well as physical and geometrical variations of fibers and connectors cause insertion losses that add to the total loss of fiber links. OTDRs can be used to measure loss from these events. Differences between Rayleigh-backscatter coefficients before and after the event affect insertion-loss accuracy of the OTDR measurement.

11.4.1 Fusion Splice Loss

Local insertion loss can be caused by reflective and by nonreflective events. For both cases, it is basically the same procedure to determine the loss from the step-size of the displayed data. Thus we can focus on an event like that depicted in Figure 11.13. Ideally insertion loss is represented as a sharp step, however, the convolution of the fiber's impulse response with the probing pulse leads to a smoothed transition depending on the pulse width.

As illustrated in Figure 11.13, the splice loss is defined as the vertical distance between the two lines L_1 and L_2 representing the fiber's backscatter signal before and after the event. The width of the step is as a first approximation equal to half of the width W of the probing pulse, but can be broadened by a low receiver bandwidth. It is common practice to apply the LSA (least-square-approximation)[43] method to determine the slope and position of the two auxiliary lines L_1 and L_2. More sophisticated algorithms are based on pattern matching schemes, providing improved accuracy with noisy trace data.[20] If the lines L_1 and L_2 are not quite parallel, the loss depends on the evaluated splice position.[44] In this case, the accuracy of finding the splice location is also important for splice loss measurements. Modeling the splice loss with the receiver bandwidth and pulsewidth as parameters and deriving the position from the turning point is one possibility to determine the splice position. A much simpler approach is to determine the position where the curve dips at the right-sided end of L_1, by checking the deviation of the data samples to line L_1 until a given threshold is exceeded.

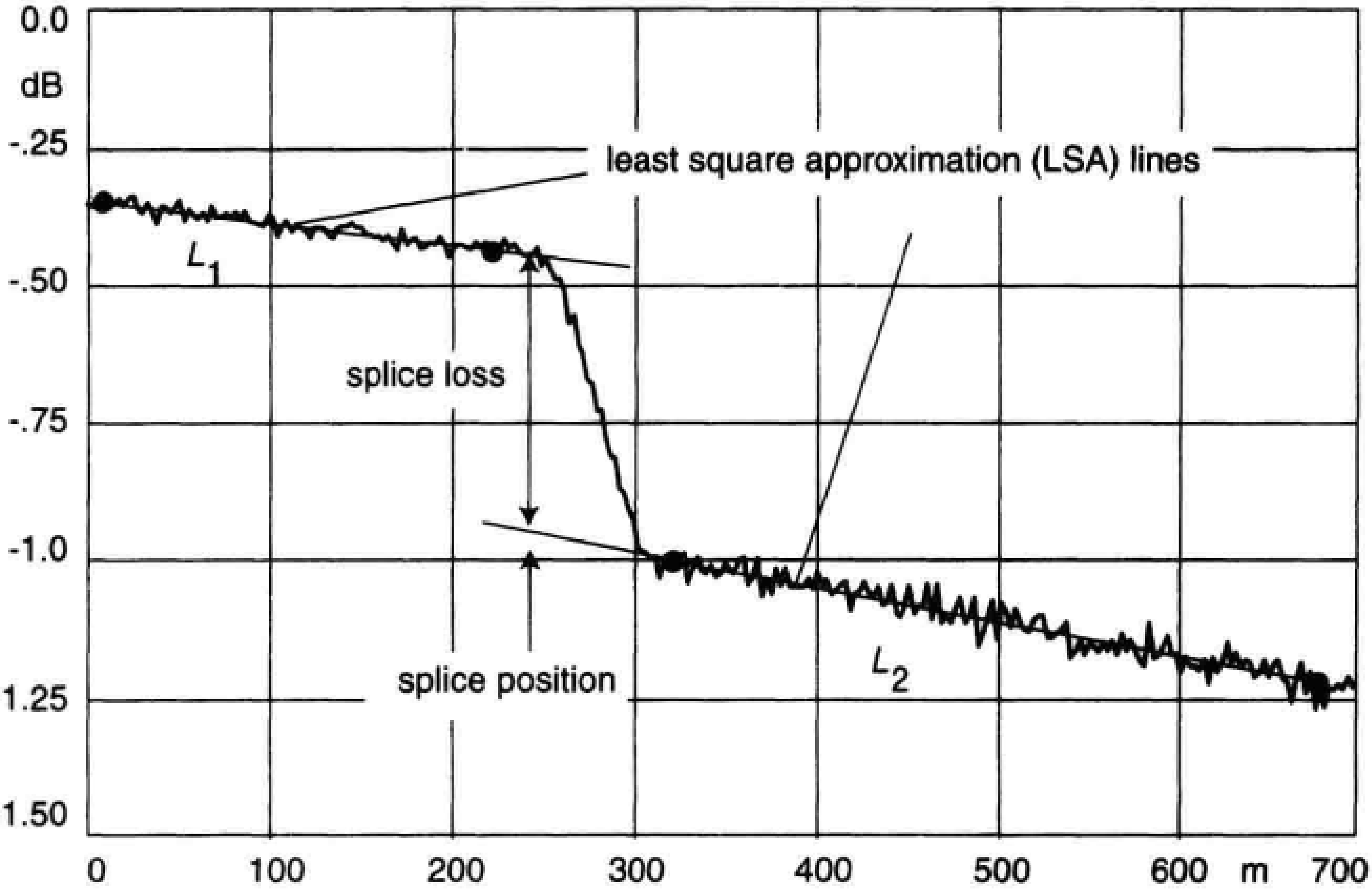

Figure 11.13 Nonreflective event (for example, fusion splice)—two different fibers spliced together.

11.4.2 Different Fibers

Different slopes of L_1 and L_2 occur if fibers with different attenuation coefficients are spliced together. If the backscatter after the loss event is higher than before the event, a "gainer" will occur. Figure 11.14 shows a gainer measurement. This example points out that backscatter information does not always precisely indicate what happens to a forward traveling signal as the light in the fiber certainly doesn't experience the gain. The OTDR calculates loss from differences in backscatter signals and not from the actual power in the fiber. Variations in fiber scatter coefficients α_s and backscatter capture coefficients S (differences in mode-field diameter on either side of a splice) affect the OTDR signal and can lead to ambiguity in the interpretation of data. If α_s and S of both fiber 1 and fiber 2 are known, then the true splice loss α_{splice} can be calculated according to Equation 11.25.[45]

$$\alpha_{\text{splice}} = 5 \cdot \log \frac{P_1}{P_2} - \alpha_2 \cdot \frac{W}{2} - 5 \cdot \log \frac{S_1 \alpha_1}{S_2 \alpha_2} \tag{11.25}$$

In this equation P_1 and P_2 are the left and right-sided backscatter signal levels, α_2 is the attenuation coefficient of fiber 2, and W the geometrical pulse-width. The term on the right corrects for the different backscatter properties.

Different backscattering behavior of spliced fibers cause OTDR splice-loss measurements to be directional. Hence, in general, splice-loss measurements depend on the direction of the OTDR measurement. Measuring the loss from each end of a link and av-

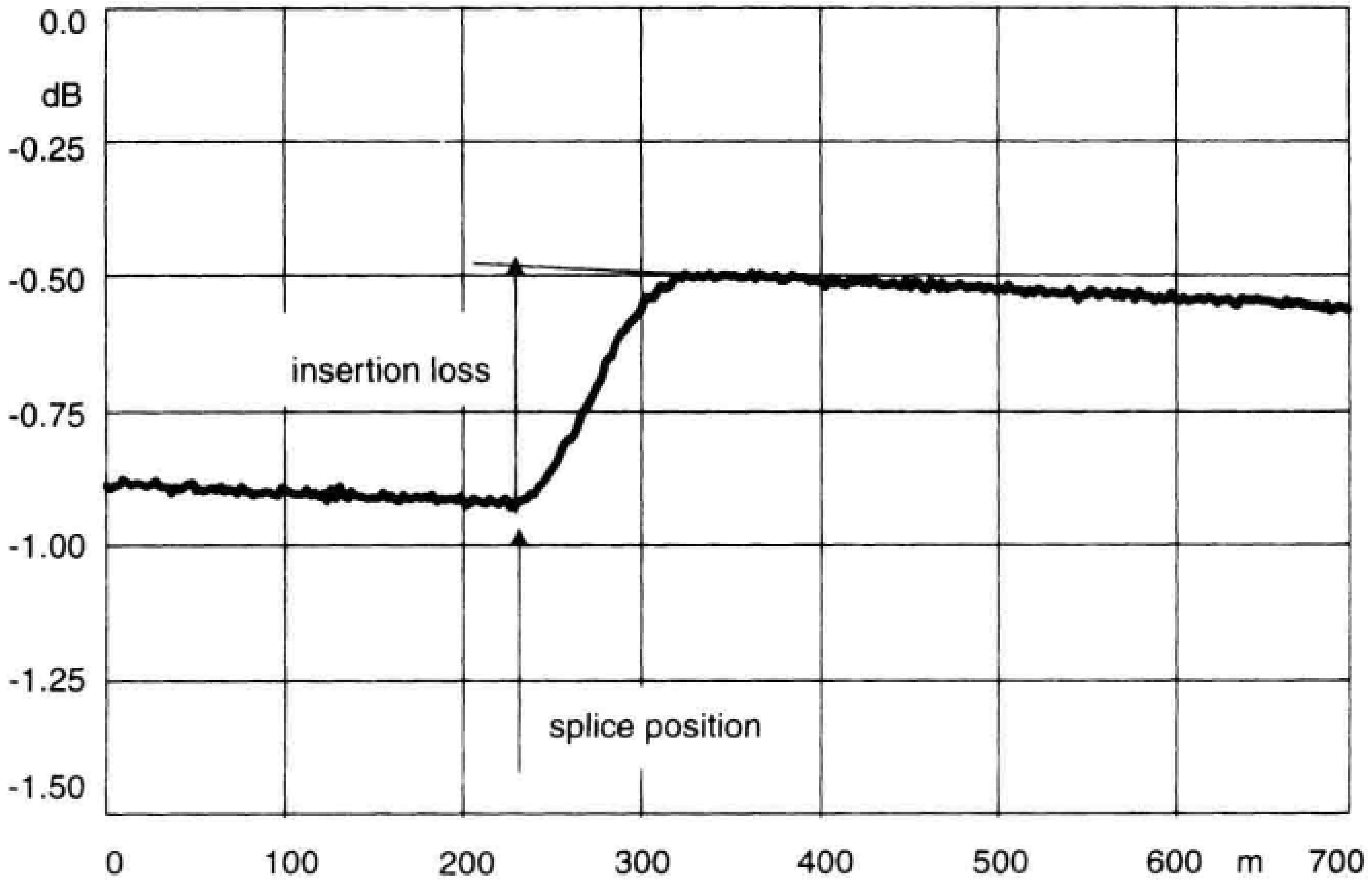

Figure 11.14 A gainer can occur when splicing two different fibers together.

eraging the results will remove the directionality effect.[18] Bidirectional OTDR measurements have shown good correlation with measurements made using the cutback technique.[46]

11.4.3 Insertion Loss of Reflective Events

An optical fiber can be perturbed by small changes of the refractive index. The air gap of a tiny crack, a mechanical splice, or connector are examples of such reflective events. Misalignment of connectors, mismatch in core diameter or NA, or nonconcentric fiber cores also induce additional loss. The OTDR display of a measured connector with low reflectance and an insertion loss of about 0.4dB is pictured in Figure 11.15. The slightly tilted roof of the pulse indicates that the shape is the sum of both the reflected rectangular signal and the transition of the backscattered signal (due to the insertion loss).

11.4.4 Bending Loss

Good fusion splices show very low variation of insertion loss with wavelength. Bending loss induced by a curvature however shows a strong dependence on wavelength. As the wavelength is increased, the mode becomes less confined to the higher doped core. The lower confinement can lead to higher radiation loss for bends induced in the fiber. In practice, loss induced by (macro-) bending is seen at $\lambda = 1550$ nm, and especially at $\lambda = 1625$ nm. An important application for the fiber's sensitivity to bending is to create a nonreflective termination. Wrapping a singlemode fiber several times around a mandrel (a

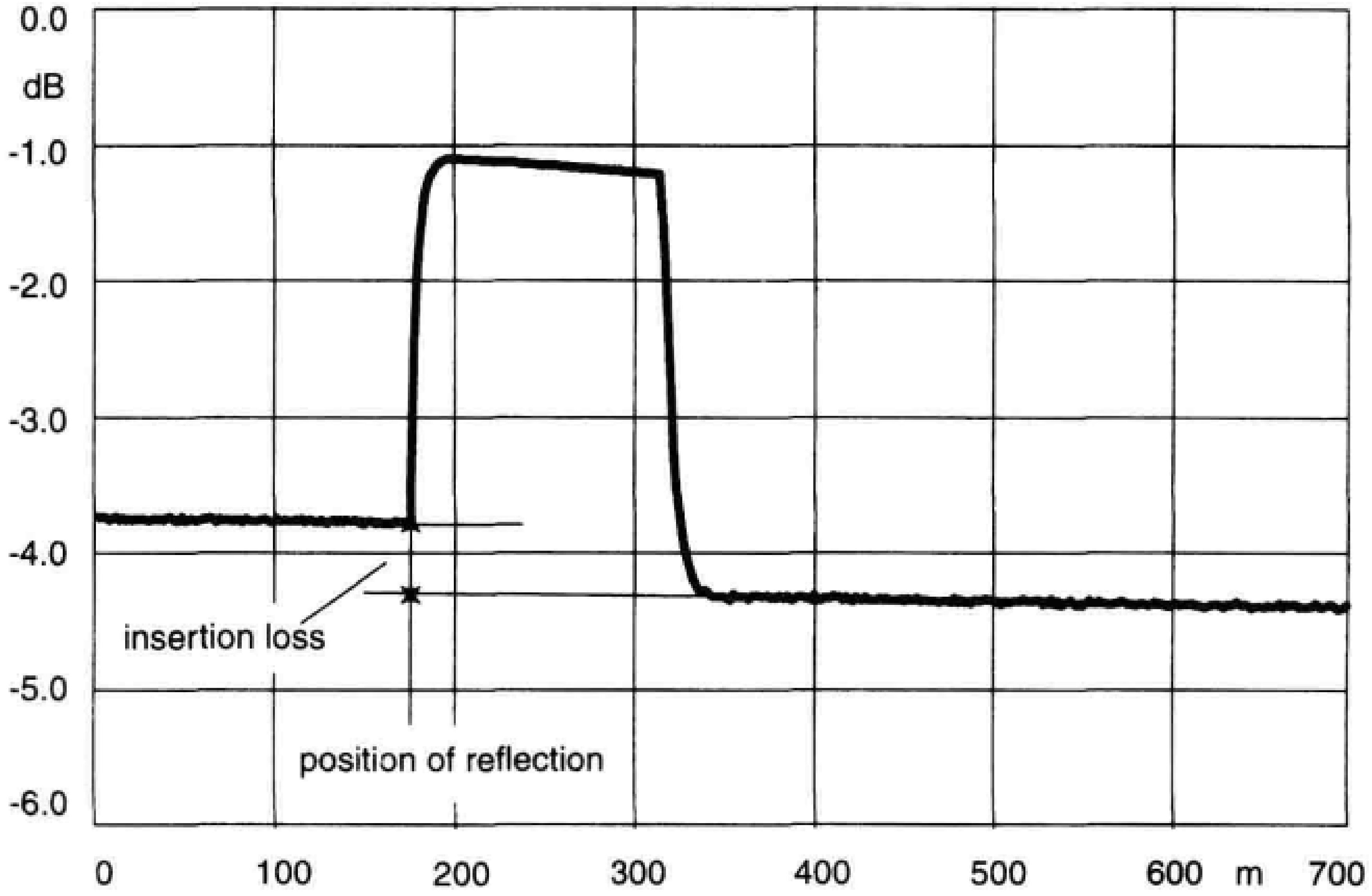

Figure 11.15 Reflective event (for example, a connector) with insertion loss.

small-diameter rod such as a pencil or a ballpoint pen) effectively attenuates the light in the order of 20 to 40 dB.

An example for induced bending-loss at different wavelengths by wrapping two turns of singlemode fiber around a mandrel with a diameter of 23 mm can be seen in Figure 11.16. For better comparison, the individual traces were aligned both horizontally and vertically. It is obvious that longer measurement wavelengths allow for easier detection of small fiber bends which can advantageously be used for security supervision of fiber optic networks.

11.4.5 Uncertainty of Loss Measurements

An important question is the accuracy of loss measurements made with OTDRs. The accuracy depends on the nonlinearity of electronic hardware and primarily on the SNR at a given point. Figure 11.17 shows measurement uncertainty plotted vs. the one-way rms SNR. The vertical axis gives the peak value of the uncertainty in terms of a 95% confidence interval. As an example, backscatter of an OTDR trace with 8 dB SNR shows a noise-ripple with a peak-amplitude that lies within ±0.1dB for 95 out of 100 trace samples.

In practice OTDR loss measurements surpass these results by applying curve fit algorithms to estimate the slope of the backscatter signal and improve the effective SNR shown in Figure 11.17 by several dBs.

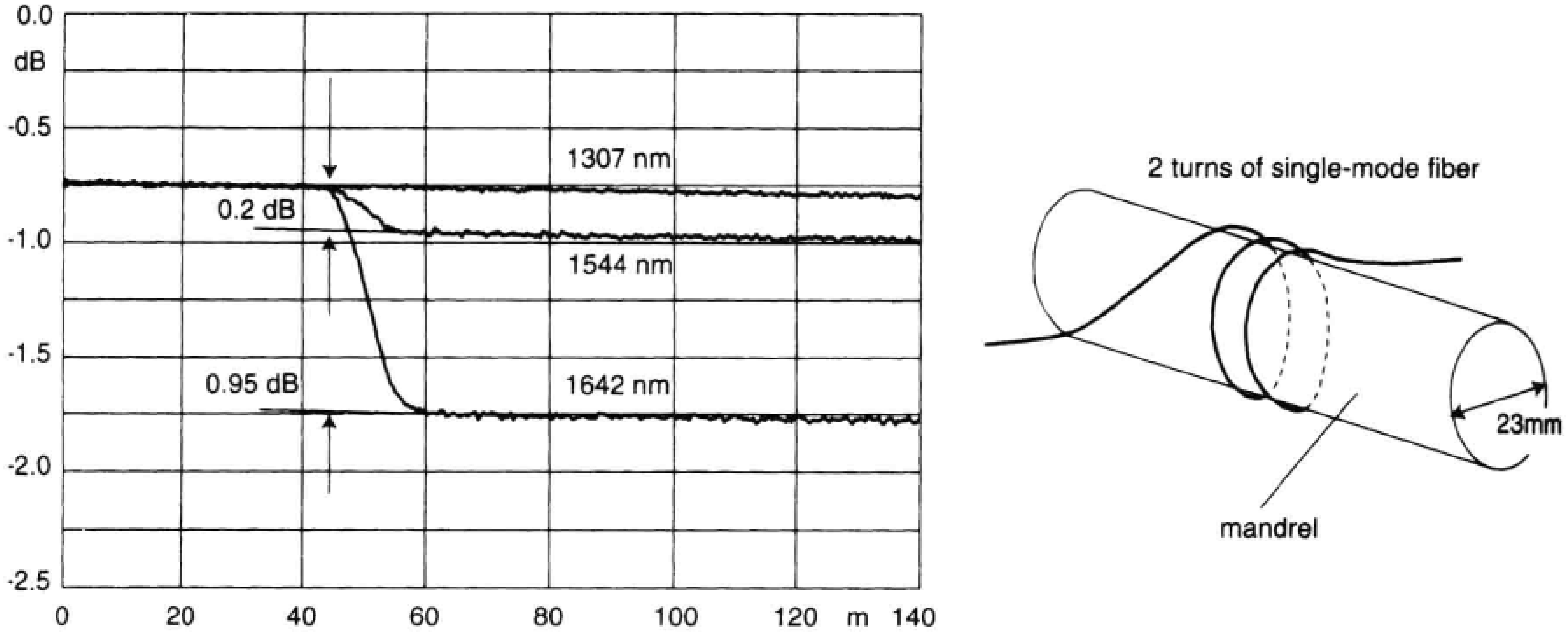

Figure 11.16 Bending-loss at various wavelengths measured with a pulsewidth of 100 ns.

Example

A 0.5 dB splice is located near the far end of a 50 km fiber. Which dynamic range is necessary to measure the event's insertion loss with ±0.05 dB accuracy assuming a fiber attenuation of $\alpha_{dB} = 0.33$ dB/km?

Solution

Figure 11.13 gives the necessary one-way SNR of 9.5 dB for ±0.05 dB measurement accuracy.

The total loss of the 50 km fiber is

$$\alpha_{\text{total}} = 0.33\frac{\text{dB}}{\text{km}} \times 50\ \text{km} = 16.5\ \text{dB}$$

Hence, the necessary OTDR dynamic range D is

$$D = 9.5\ \text{dB} + 16.5\ \text{dB} + 0.5\ \text{dB} = 26.5\ \text{dB}$$

The 0.5 dB insertion loss is added to the dynamic range because the noise that ultimately limits the achievable accuracy shows up after the event.

11.4.6 A Variable Splice-Loss Test Setup

So far, only simple nonbranched fibers were considered with OTDR measurements. An informative and very useful example of a branched fiber network will be discussed now. The ability to reliably produce a splice event with accurately adjustable insertion loss is of highest importance not only for the test of splice-loss uncertainty, but also for the development of measurement-range algorithms. A basic arrangement of a 3 dB coupler, an optical attenuator, and two fibers with different lengths L_1 and L_2, with $L_2 > L_1$, as shown in

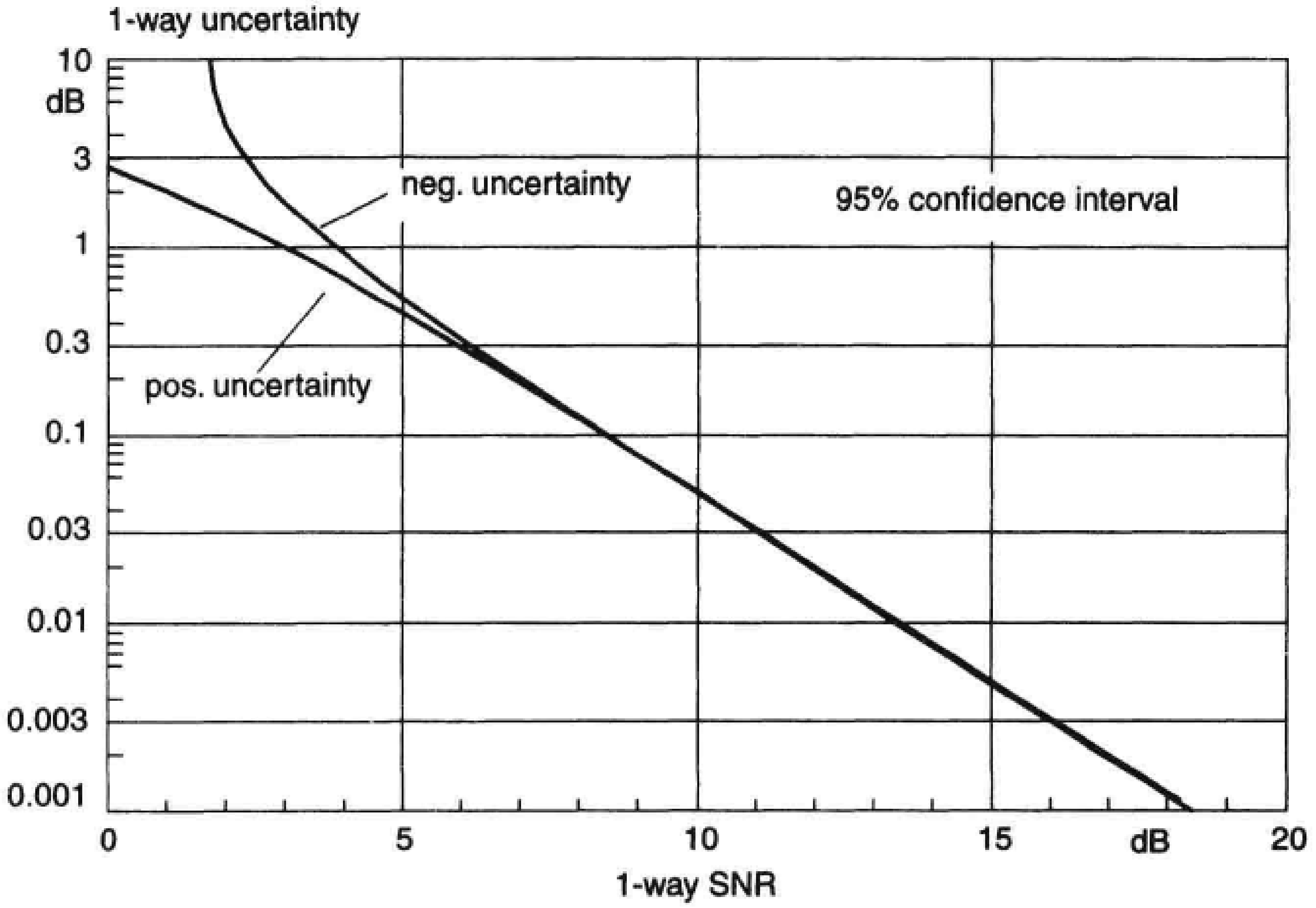

Figure 11.17 Uncertainty of OTDR loss measurements as a function of signal-to-noise ratio.

Figure 11.18, yields a variable step in the backscatter signal at a distance L_1 away from the position of the coupler.

This setup is a typical example where returning light from different paths overlap in the OTDR measurement result. When deriving the behavior of this setup, one should take into account that the OTDR actually measures the superimposed backscattered signals from both fibers. Assuming an attenuator with zero insertion loss and a perfect 50:50 coupling ratio, a 1.5 dB step could be measured both at the coupler itself and at a distance L_1. A simple train of thought reveals this number. At a distance L, with $L_1 < L < L_2$, the backscatter from the longest fiber only contributes to the signal seen by the OTDR. This signal is dampened twice by the 3 dB-coupler loss with the effect of a 3 dB total loss on the OTDR display (when omitting the fiber attenuation). At shorter distances $L < L_1$ the signal seen by the OTDR is twice as high as in the case before, since now both fibers contribute, leading to a one-way step of 1.5 dB at $L = L_1$. In reality, a finite insertion-loss of the attenuator decreases this step considerably. Bellcore recommends a 0.5 dB splice for measurement-range tests, therefore careful selection of attenuator and coupler is necessary to maintain the desired minimum 0.5 dB step for all measurement wavelengths applied. A slight deviation from the ideal 50:50 coupling ratio can be used to compensate partly for the attenuator's insertion loss if the low-loss path is connected to the attenuator. In principle, a more asymmetrical coupler, for example, with 80:20 coupling ratio, ensures even higher values for the achievable maximum splice-loss, however at the cost of an increasing total loss between OTDR and event. Last not least, a carefully terminated

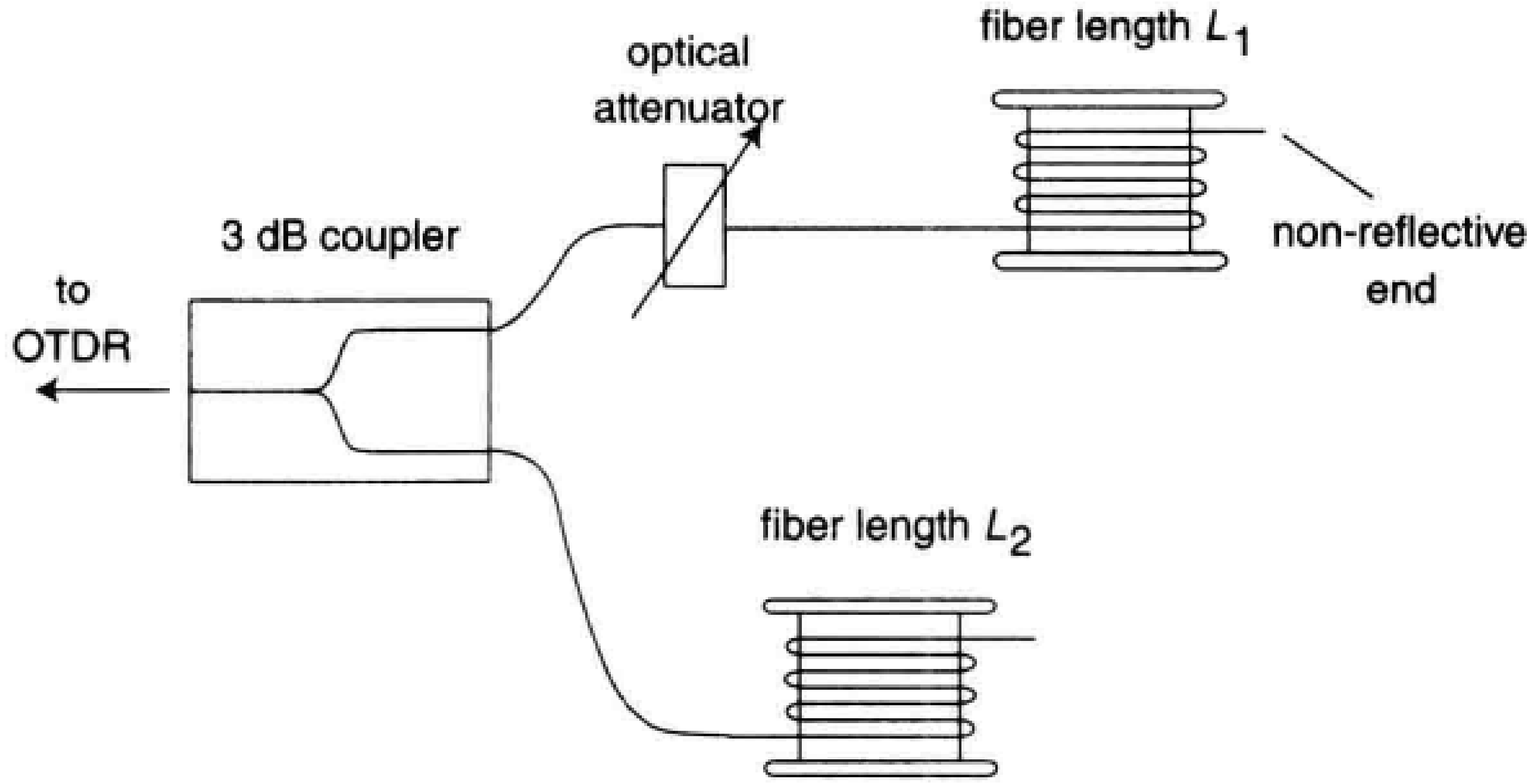

Figure 11.18 A variable splice-loss generator.

nonreflective fiber end at the short fiber is mandatory for a high-quality splice reproduction especially for measurements with short pulses.

Figure 11.19 depicts the splice-loss value as a function of attenuation achieved with a low-insertion loss attenuator and a 3 dB coupler with approximately 44:56% coupling ratio.

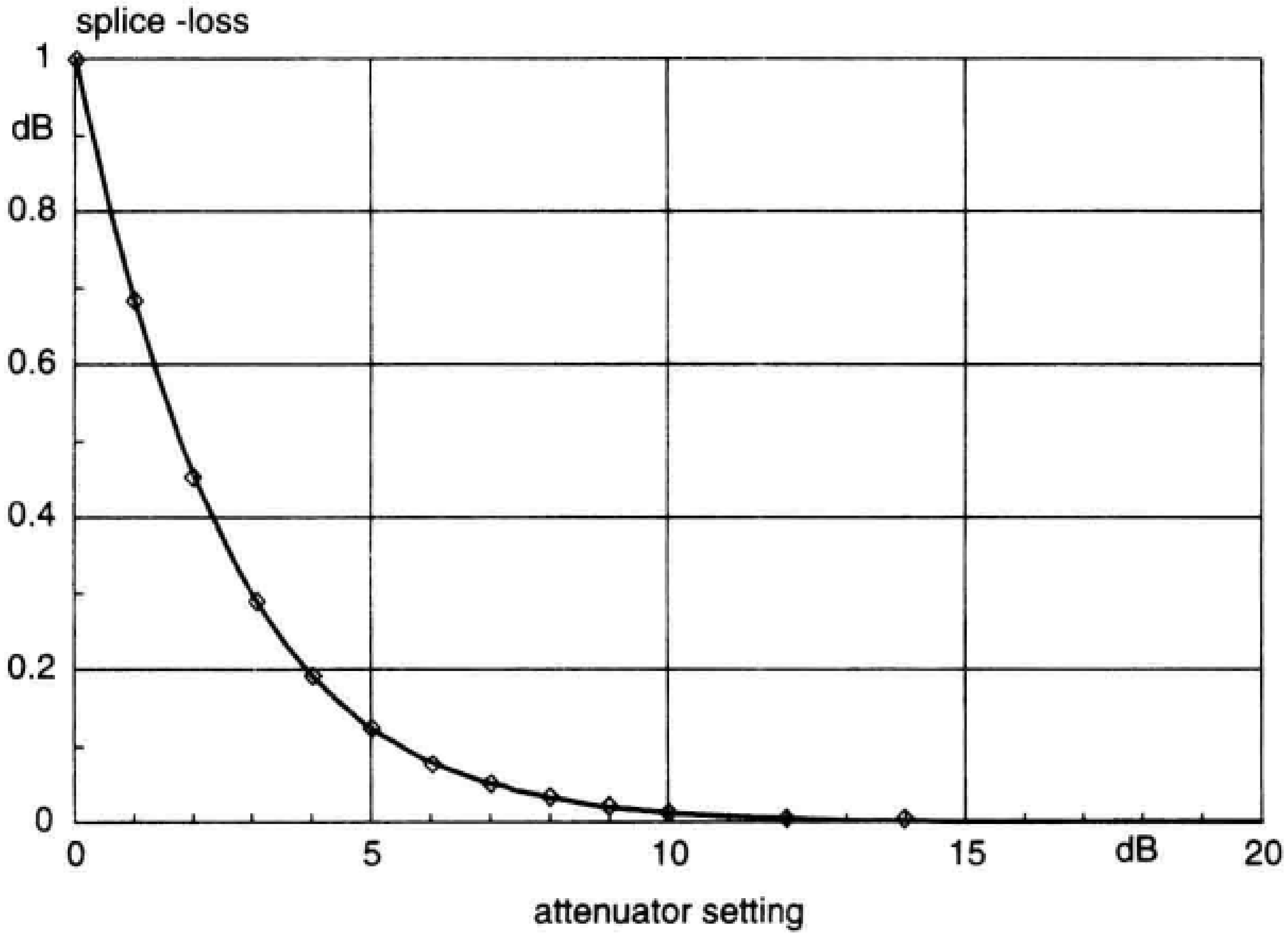

Figure 11.19 Splice loss vs. attenuator setting.

11.5 RETURN LOSS AND REFLECTANCE

At the boundary of two media with different refractive indices, reflection of light occurs. The reflectivity that results from an abrupt change in media can easily be calculated. The power reflection factor, r^2, at normal incidence is

$$r^2 = \frac{P_{\text{refl}}}{P_{\text{inc}}} = \left(\frac{n_1 - n_2}{n_1 + n_2}\right)^2 \leqslant 1 \qquad (11.26)$$

At a boundary between glass ($n_1 = 1.5$) and air ($n_2 = 1$), for example, $r^2 = 0.04$, so that 4% of the light is reflected. This is commonly referred to as a Fresnel reflection.

Common sources of reflections are glass-air interfaces at open fiber ends, mechanical splices, cracks, poorly mated connectors because of mud and dirt, and sometimes overpolished connectors. Reflections not only cause light returning back to the source, but also cause loss of optical power.

Reflections occurring in a fiber optic link can lead to performance degradation in high-speed systems.[47] Since any reflection causes a weak image of the transmitted pulse string, these ghost patterns return to the transmitter. In case of multiple reflections these echoes add to the traffic signal as a noise signal affecting bit-error-rate. With steadily increasing digital data rates and complex analog modulation schemes, this subject is going to be of more and more importance. Therefore it is common practice to test a fiber link for reflections at installation before system switch-on.

11.5.1 Return-Loss Measurements

There are two basic methods to measure the presence of reflections: return-loss-testing and reflectance-testing. (See Chapter 10 for further aspects on total return-loss methods.) Optical return loss (ORL) gives the ratio of incident light to total reflected light from an entire fiber optic span.

$$\text{ORL}\ (dB) = 10 \log \left(\frac{P_{\text{inc}}}{P_{\text{refl}}}\right) \geqslant 0 \qquad (11.27)$$

It applies to a series of components including fiber along a link and combines the effects of all reflective events in a transmission system. It is often used as part of an acceptance test. Either an optical-continuous-wave reflectometer (OCWR) or an OTDR with accumulative return-loss measurement capabilities is appropriate. Usually expressed as a positive dB value, ORL describes an optical system as a whole.

11.5.2 Reflectance Measurements

When knowledge of individual reflection magnitude and location is required as with system evaluation, then reflectance measurement is adequate. Reflectance is the term preferred for single components and is the ratio of reflected light at discrete point to light incident on that point. It can only be measured with OTDRs if the event is far away.

$$\text{refl} = 10 \log \left(\frac{P_{\text{refl}}}{P_{\text{inc}}}\right) \leqslant 0 \qquad (11.28)$$

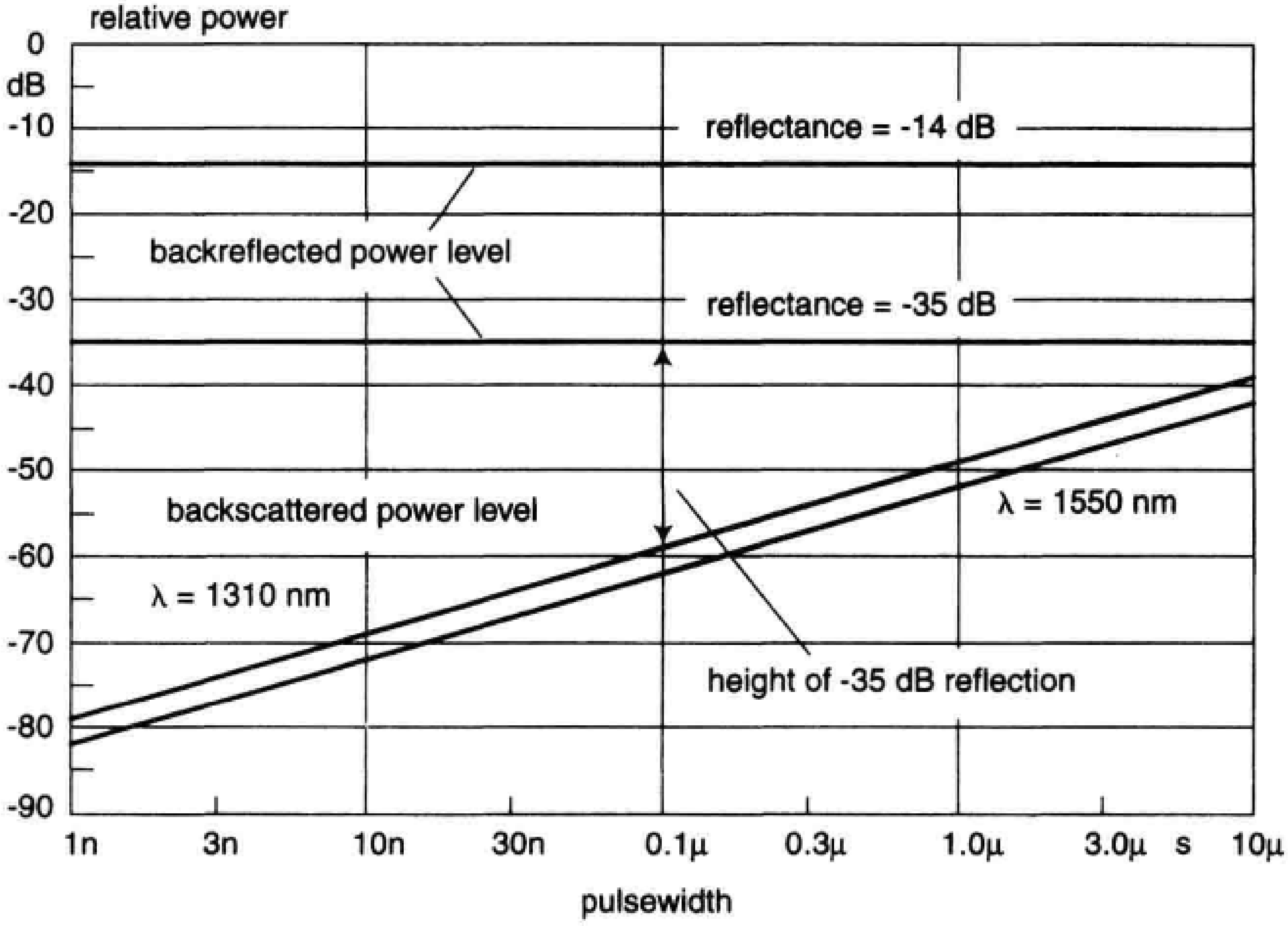

Figure 11.20 Reflected and backscattered power relative to the incident power in fiber.

The fact that the height of a reflection on an OTDR display does not exactly represent its reflectance, but rather is a relative indication for it, dependent on the selected pulsewidth, is depicted in Figure 11.20. There the power levels for both reflected and backscattered light relative to the incident power in the fiber are plotted vs. pulsewidth. It can clearly be seen that the reflected power is a function of reflectance only and independent of pulsewidth. The backscattered power is approximately proportional to the pulsewidth according to Equation 11.18. The proportionality is true only for short pulses where the fiber loss over the spatial pulse length is negligible. Also, backscatter power is wavelength dependent. This means that reflectance measurements with OTDRs is not quite straightforward, but in general the OTDR-firmware does the necessary calculations to correct for the pulsewidth and wavelength dependence.

The double-arrow gives the difference between the reflected power of a –35 dB reflection and the backscatter power measured with a pulsewidth $\tau = 100$ ns at $\lambda = 1310$ nm. As this graph is based on a 10 · log scale, an OTDR screen with its 5 · log scaling (see Section 11.2.1) would reveal such a reflection as a spike only half as high, in other words, approximately 12 dB. Another fact catches the eye when considering wide pulsewidths. There the backscattered power can reach or even exceed the power level caused by average Fresnel reflections, making it hard to discern the signature of standard connectors with about –40 dB reflectance.

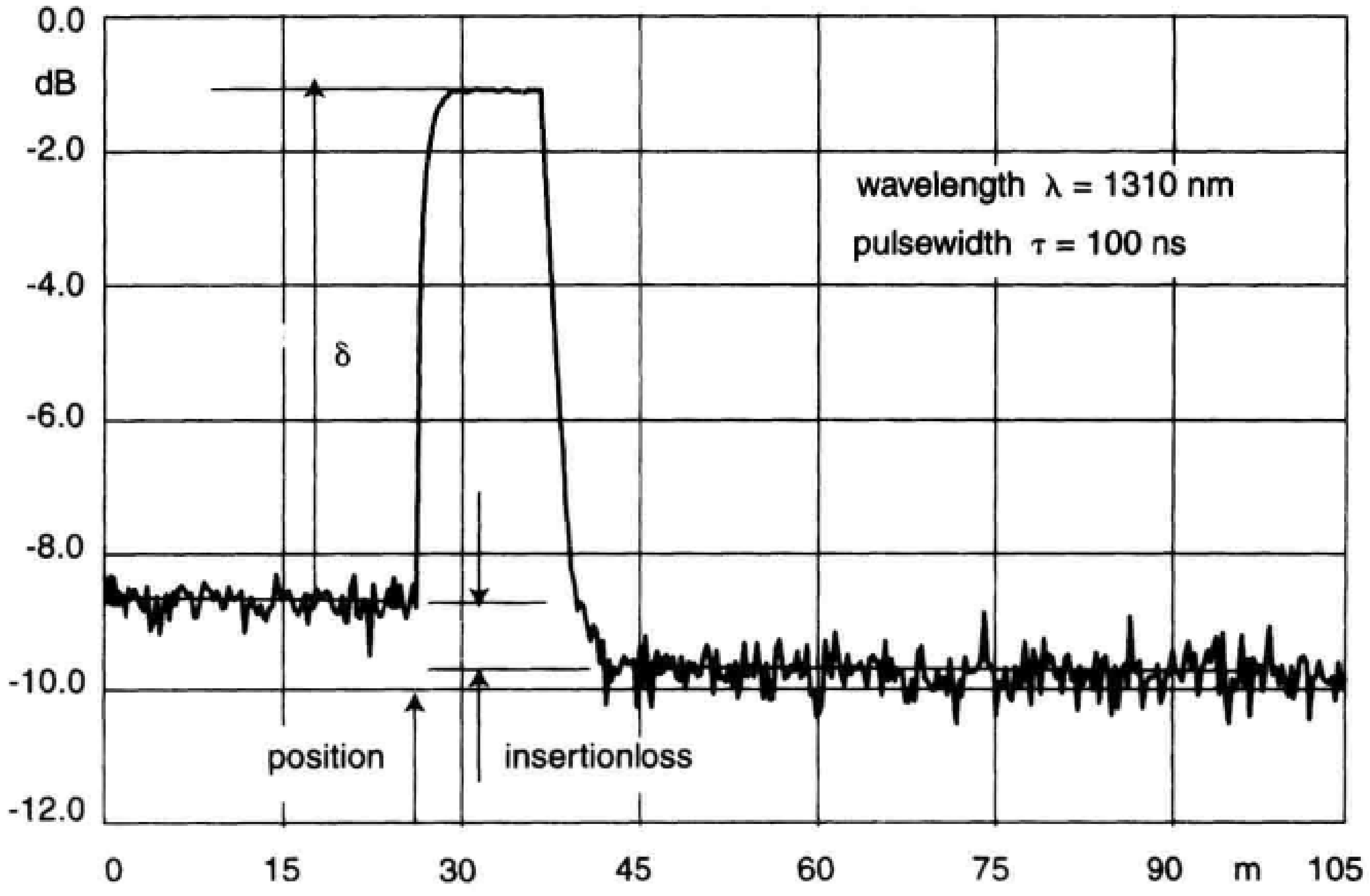

Figure 11.21 Example of reflectance measurement.

An example of a reflectance measurement of an isolated event can be seen in Figure 11.21. This plot shows a reflection with a noisy backscatter and auxiliary LSA (least-square-approximation) lines for backscatter level determination.

As an OTDR cannot directly measure incident power, this information is derived indirectly with the known (or estimated) backscatter factor σ. The relation between the measured pulse-height δ and the reflectance of an event is given in Equation 11.29 which can readily be derived from Equations 11.16, 11.23, and 11.28.

$$\text{refl}\,(dB) = -\sigma + 10 \cdot \log\,(10^{0.2 \cdot \delta} - 1) \tag{11.29}$$

σ is the backscatter factor for the pulsewidth used. The exponent 0.2 comes from the OTDR's one-way data representation.

Example 11.4

Calculate the reflectance of the event shown in Figure 11.21 which has been measured at a pulsewidth $\tau = 100$ ns and a wavelength of $\lambda = 1310$ nm.

Solution

Initially for using Equation 11.29 we need to determine the appropriate backscatter factor σ for the given pulsewidth. This may be derived from Equation 11.23 or Table 11.1.

$$\sigma = 49\,\frac{\text{dB}}{\mu s} + 10 \times \log\left(\frac{1\,\mu s}{100\text{ ns}}\right) = 49 + 10\text{ dB} = 59\text{ dB}$$

The reflection height δ can directly be obtained from the drawing, yielding $\delta = 7.4$ dB. Hence, the reflectance is

$$\text{refl} = -59 + 10 \times \log(10^{0.2\times 7.4} - 1) = -44.4\ dB$$

From Equation 11.29 and from Figure 11.20 we can see that reflectance values in the order of $-\sigma$ can't be measured precisely since the difference δ between backscatter and top of the pulse becomes very small. In this situation a smaller pulsewidth must be chosen, lowering the backscatter level and thus increasing δ. As the reflected signal is proportional to pulse power and the backscattered signal is proportional to pulse energy, it is obvious that small reflections can be measured better with shorter pulsewidths. A problem that could arise when using short pulses is the signal's limited slew rate due to a finite receiver bandwidth. Figure 11.22 shows an example for reflectance measurements with different receiver bandwidths. Clearly, as a rule of thumb, OTDRs suitable for accurate reflectance measurements have short pulsewidths and high receiver bandwidth at the same time.

With a finite receiver bandwidth, the limited slew rate prevents the signal from reaching its final peak value. Knowing the bandwidth *BW* of the OTDR receiver, a more accurate equation can be derived as given in Equation 11.30.

$$\text{refl} = -\sigma + 10 \cdot \log\left(\frac{10^{0.2\cdot\delta} - 1}{1 - \exp(-2\pi \cdot \tau \cdot BW)}\right) \tag{11.30}$$

This correction is not quite perfect since a simple first-order lowpass model was chosen for the approximation of the receiver transfer function. However, in regard to reflectance accuracy in OTDRs, this is a sufficiently precise formulation.

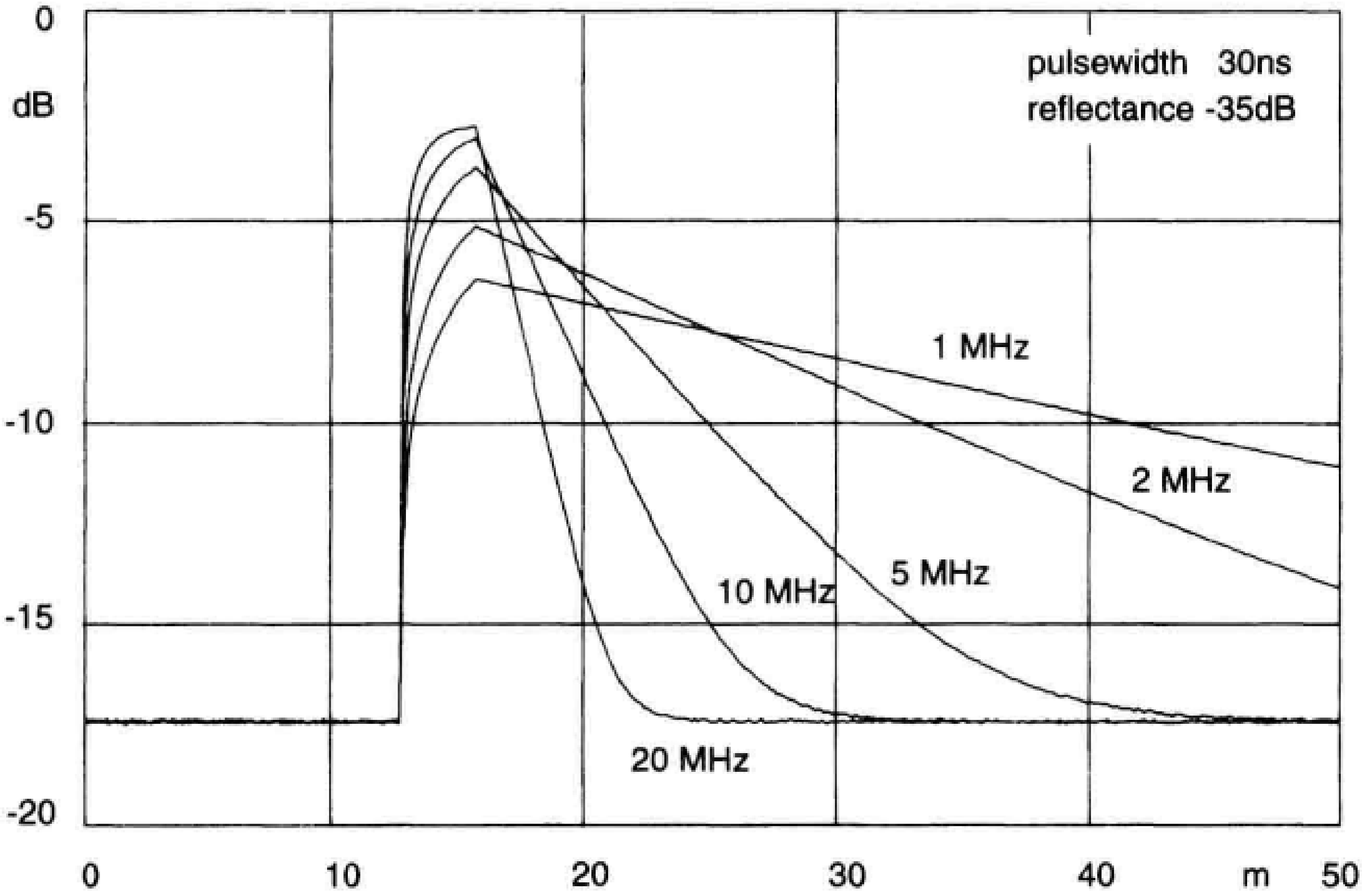

Figure 11.22 Influence of OTDR receiver bandwidth on reflection height (τ = 30 ns, refl . = −35 dB).

If one happens to have a device with known reflectance, it is possible to determine the backscatter factor σ of a fiber by simply measuring the pulse-height δ according to Figure 11.21 and solving Equation 11.29 for σ.

Example

An FC/PC connector pair gives a reading of 33.5 dB total return loss when measured with a cw reflectometer setup. The same connector pair shows a reflectance of –36 dB with an uncompensated OTDR measurement according to Equation 11.29 using a pulsewidth of 30 ns. Calculate the OTDR receiver bandwidth *BW*.

Solution

Subtracting Equation 11.29 and Equation 11.30 gives the error ϵ caused by a finite receiver bandwidth

$$\epsilon = 10 \cdot \log\left[1 - \exp(-2\pi \cdot \tau \cdot \mathrm{BW})\right] = 33.5\ \mathrm{dB} - 36\ \mathrm{dB} = -2.5\ \mathrm{dB}$$

Solving for *BW* yields

$$\begin{aligned}\mathrm{BW} &= -\frac{1}{2\pi \cdot \tau} \cdot \ln(1 - 10^{0.1\epsilon}) \\ &= -\frac{1}{2\pi \times 30 \cdot 10^{-9}} \times \ln(1 - 10^{-0.1 \times 2.5}) = 4.38\ \mathrm{MHz}\end{aligned}$$

11.5.3 Accumulative Return Loss

Some OTDRs can calculate the accumulative return loss vs. distance from a backscatter measurement. Omitting the backscatter information and displaying just the return loss of the fiber plus reflectances gives a clear and crisp overview of a fiber link. The total return loss of a link according to Equation 11.26 is given as the maximum value on the curve in Figure 11.23. This example of a 5 km fiber link measured at $\lambda = 1310$ nm demonstrates how the return loss increases monotonous with distance, showing distinct steps at positions of reflections. These are a –45 dB front-reflection, and two reflections with –40 dB and –36 dB reflectance at a distance of 2.0 km and 3.5 km, respectively. The total return loss (33dB) and the quality of reflective network components can be checked at a glance. For example, reliable OC_48 (2.5 Gb/s) data transmission requires a system return-loss of no more than 24 decibels with no individual reflectance exceeding –27 dB. A return-loss chart exactly reveals the information to check these two limits in a quick acceptance test.

From the total backscattered power $P_{s,\mathrm{total}}(L)$ in Equation (11.22), the total return loss of a pure fiber with length L can be calculated according to Equation 11.27.

$$\mathrm{ORL}(L) = -10 \log\left[S \frac{\alpha_s}{2\alpha}(1 - e^{-2\alpha L})\right] \tag{11.31}$$

For return loss measurements it is a valid approximation to equate α and α_s. On this basis the return loss can be simplified to

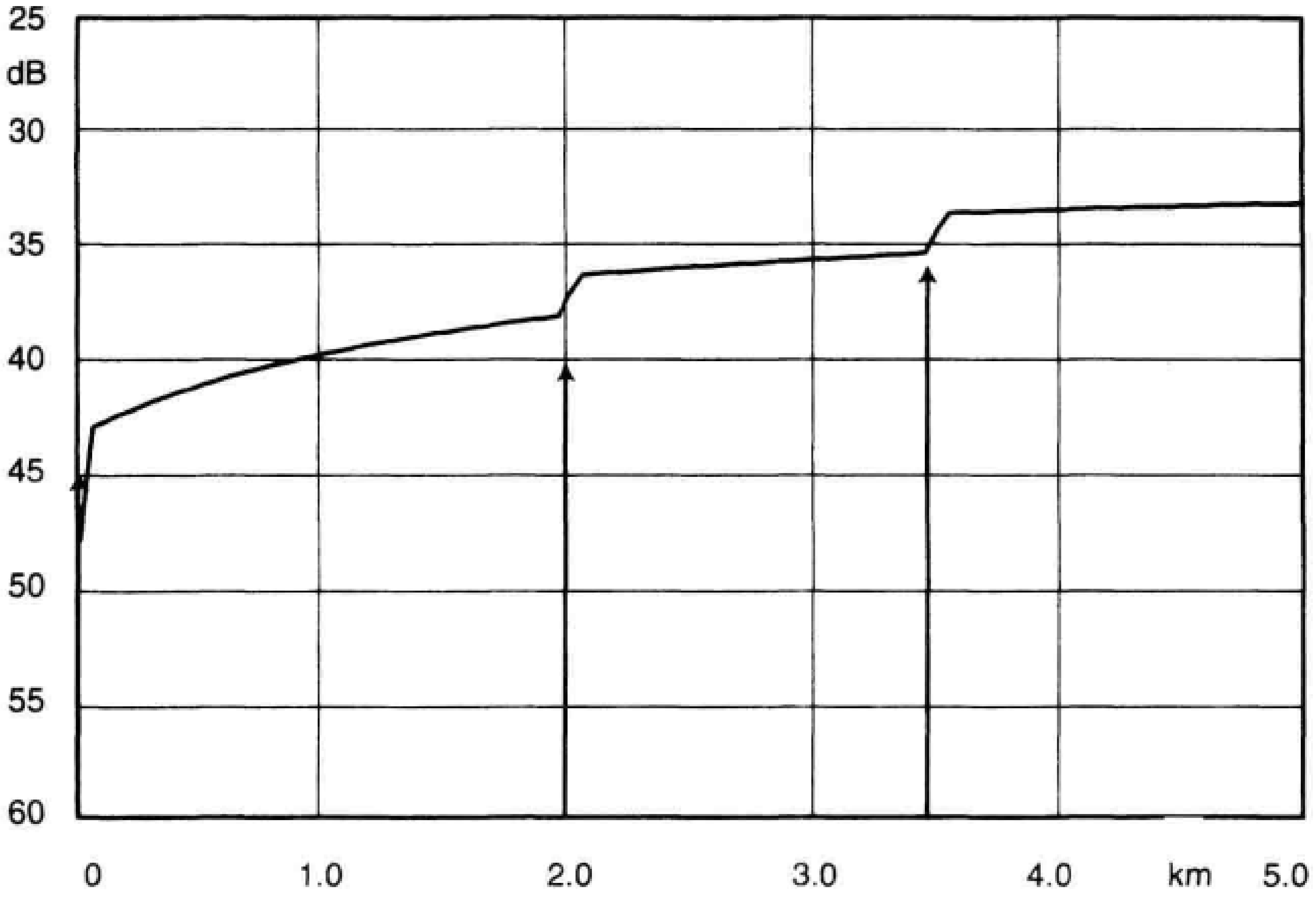

Figure 11.23 OTDR return-loss chart for a 5 km fiber at λ = 1310 nm.

$$\mathrm{ORL}(L) = -10\log\left[\frac{S}{2}(1-e^{-2\alpha L})\right] \tag{11.32}$$

This formula is particularly interesting because it suggests that S can be determined from Figure 11.23 if α is known. Or even both S and α can be determined either from measuring the return losses of different lengths of the same fiber, or from two different points on an accumulative return-loss chart.

A detailed report on return loss and reflectance measurements with OTDRs and with cw excitation can be found in Kapron and co-workers.[48] In Blanchard and co-workers,[49] further information about the calibration of OTDR return loss is given.

Example

Determine the total return loss for spans of singlemode fiber with lengths of 1 m, 1 km, 10 km, and 100 km and an attenuation coefficient of 0.19 dB/km, in other words, at a wavelength around λ = 1550 nm.

Solution

Using Equation 11.32, the total return loss as a function of fiber length L (in km) is

$$\mathrm{ORL}(L) = -10\times\log\left[\frac{0.001}{2}\times(1-e^{-2\times(0.19\times0.23)\times L})\right]$$

Hence, $\mathrm{ORL}(1\ m) = 73.6$ dB
$\mathrm{ORL}(1\ km) = 43.8$ dB
$\mathrm{ORL}(10\ km) = 35.4$ dB
$\mathrm{ORL}(100\ km) = 33.0$ dB

With increasing length L the total return loss approaches a limit which depends mainly on the fiber's capture coefficient S.

11.6 AUTOMATED REMOTE FIBER TESTING

OTDRs are currently used in installation and maintenance of optical fiber networks. To ensure the integrity of existing links, they are checked by a dispatched crew equipped with an OTDR. A typical fiber break takes more than 10 h to detect, locate, and repair.[50] With an increasing number of deployed fiber-optic cables, both practical and economical limitations arise with this kind of preventive maintenance. Since high transmission rates tie tens of thousands of subscribers to one fiber, network downtime is expensive in terms of lost revenue, customer satisfaction, reputation, and future business. Minimizing revenue loss from system downtime by quickly detecting, locating and then repairing breaks in operational cables, demands automated testing of the fiber plant. The significance of this issue is addressed by the Bellcore Generic Requirements for RFTS (Remote Fiber Test System).[51]

11.6.1 Link Loss Comparison

The typical test equipment for an RFTS consists of a remote test unit (RTU) together with its control unit, located at a central office. An optical test access unit (OTAU) (basically an optical switch) accomplishes direct access to the fiber optic network to share one test equipment with numerous fibers. The RFTS system is controlled by a computer with an operations system that encompasses databases and computing algorithms.

As the complexity of fiber optic network increases, maintenance cost becomes a significant issue. During network commissioning and installation, a reference file for each individual fiber of a cable is created and saved in the data base. A baseline OTDR measurement is made of the fiber link. As the test equipment remains permanently connected to the fibers, periodic testing with automatic analysis and trace comparison is performed as part of a proactive and preventive maintenance strategy.

A good indication for the onset of link degradation is a deviation in the end-to-end attenuation or total link loss. Link loss is defined as the difference between the initial backscatter level at the near end and the backscatter level at the far end. Calculating the link loss from an OTDR trace and comparing it to a reference value (recorded during commissioning of the fiber plant) as depicted in Figure 11.24 gives a first indication for a variation in the link characteristics.

If the deviation exceeds a given threshold level, the system responds with a detailed analysis providing a problem description, exact location, the nearest access point, the technical staff to be called and the task force's phone numbers. The repair process can start without delay.

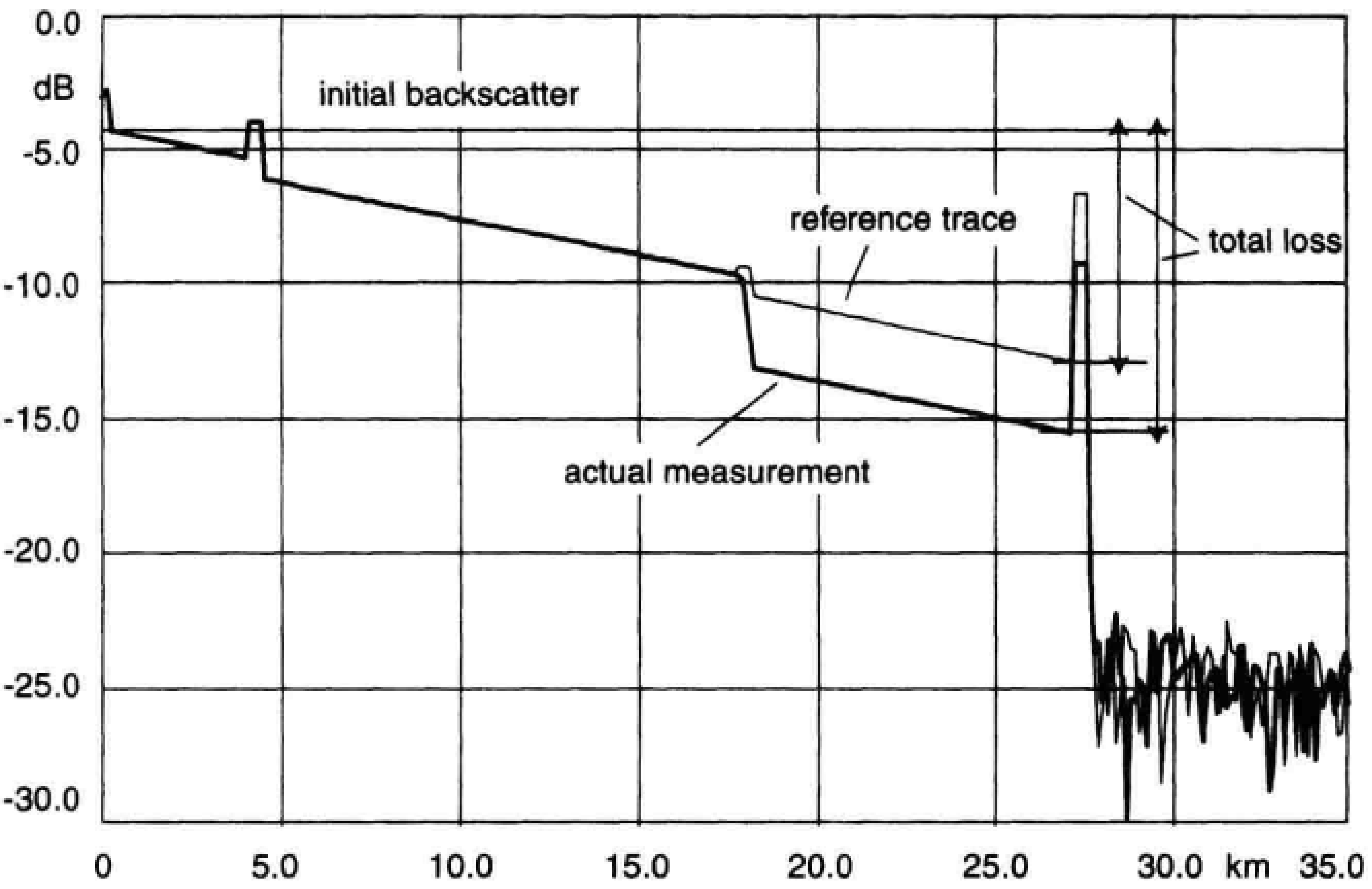

Figure 11.24 Comparison of the total link loss between reference trace and actual measurement.

11.6.2 Dark Fiber Testing

Many installed fiber cables contain spare fibers. These inactive fibers can be used for dark fiber testing. This allows OTDR measurements to be performed while traffic is carried on neighboring active fibers. Dark fiber testing has the advantage that no link modification is necessary and that the test wavelength can be identical to the transmission wavelength. A simple example of how this works is shown in Figure 11.25.

Justification for this practice is based on the assumption that if a critical failure occurs, most likely all fibers in the cable are affected by the breakdown. The percentage of detected failures with dark fiber testing is about 80%.[52]

11.6.3 Active Fiber Testing

If reliable fault coverage is mandatory, in-service or active fiber test is the measurement of choice. In contrast to dark fiber testing, this method uses the same fiber for test signal and data signal transmission.[53,54] WDM techniques are used to preserve the integrity of both live traffic and test signals. It is common practice to choose the test wavelength longer than the traffic wavelength. This ensures detection of all critical faults because longer wavelengths are more sensitive to physical abuse in the cable. With 1550 nm traffic, 1625 nm and 1650 nm have been established as test wavelengths. On 1310 nm data transmission links a 1550 nm test signal is often used. Commonly, measurement results at different wavelengths are not quite comparable, but especially at 1550 nm and 1625 nm, numerous fiber loss and splice loss measurements show similar loss results at both wave-

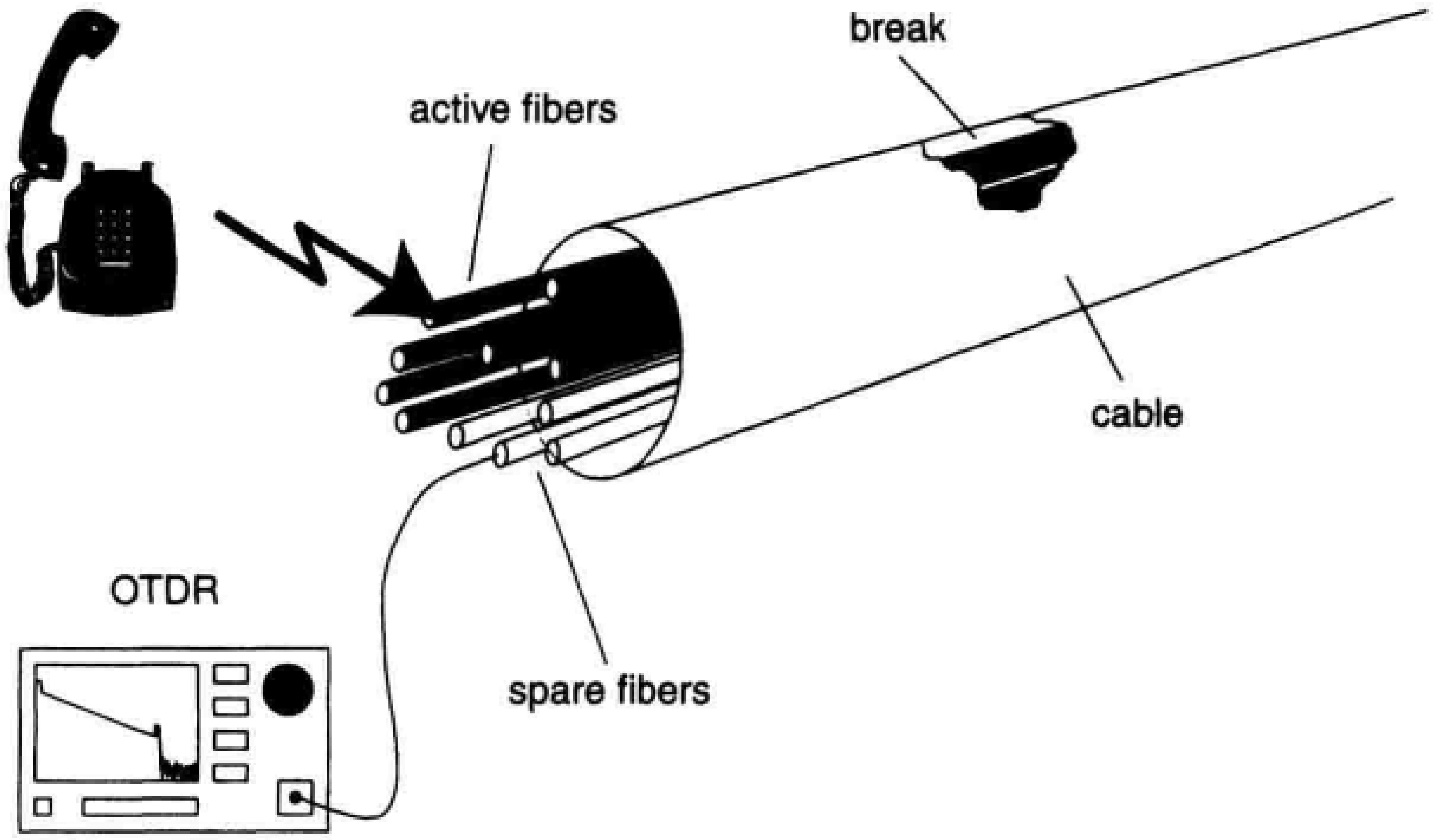

Figure 11.25 Dark fiber testing.

lengths.[55] Figure 11.26 depicts the way a 1625 nm OTDR can be connected with low loss via a WDM to a 1550 nm data link. There are two directions that the OTDR signal can be injected, toward the transmitter or toward the receiver. This example shows transmitter-side coupling. The WDM provides a low-loss test-signal path and isolates the transmitter from the OTDR test signal because of its directivity. Both the transmitter's signal and the OTDR test pulse together propagate towards the receiver. To ensure nonintrusive fiber testing, the OTDR test signal is removed from the traffic signal prior to reaching the receiver. This is accomplished by inserting a 1550 nm bandpass (filter F2) at the far end before the receiver, acting as a blocking filter at 1625 nm. The bandpass filter adds extra

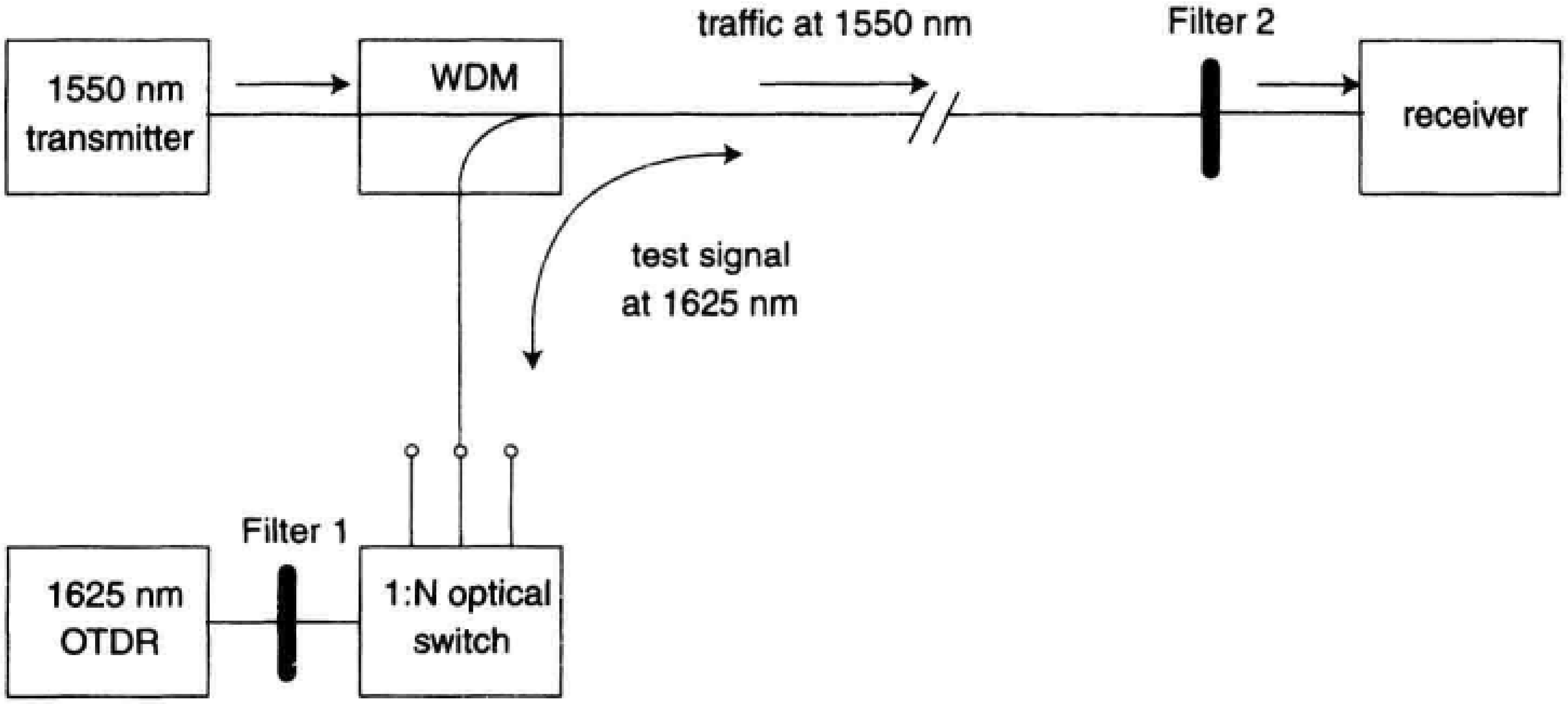

Figure 11.26 Out-of-band active fiber measurements at λ = 1625 nm.

loss to the traffic signal path. With higher transmitting power, the additional link loss can be compensated. This increase in transmitting power caused by active fiber testing is called power penalty.

At the OTDR side, filter F1 rejects any traffic crosstalk at 1550 nm, which could severely impair the OTDR test signal. The necessary 1550 nm isolation of filter F1 is determined by the power levels of the average traffic backscatter, the shot noise induced by it, and the residual rms backscatter at $\lambda = 1550$ nm. The more sensitive an OTDR is designed, the higher the susceptibility to interfering light. Any incident cw light superimposed on the weak backscatter signals causes shot noise that limits the achievable dynamic range. Another undesirable noise source is the residual rms portion of the traffic backscatter. An estimation of this interference magnitude can be done by taking the fiber's backscatter bandwidth, and the traffic's spectral distribution into account. The traffic's data stream can be approximated by a pseudorandom binary signal with a sin(x)/x-shaped spectra. The fiber's backscatter frequency transfer function is basically a first-order lowpass filter with a very low 3 dB corner frequency in the order of 3 kHz at a 1550 nm wavelength as is derived in Equation 11.20. A simple equation to estimate the suppression γ of the (random) traffic signal with data transfer rate *DR* when filtered through a first-order lowpass with bandwidth *BW* is given in Equation 11.33.

$$\gamma = 10 \cdot \log\left(2\,\frac{BW}{DR}\right) \tag{11.33}$$

The results are accurate within a couple of dBs if $DR > 10 \cdot BW$. With an improved out-of-band rejection of filter F1, the specified OTDR dynamic range could easily be maintained. Attention must be paid to any reflectivity that occurs on the fiber link. The interfering traffic noise level can increase drastically from these discrete reflections.

Example

Determine the necessary 1550 nm attenuation a_{1550} of filter F1 to avoid any noticeable interference between the traffic signal and the OTDR measurement result. The following parameters may be assumed: Average traffic transmitting power 0 dBm, data transmission rate $DR = 155$ Mbit/s, link length $L = 35$ km, attenuation coefficient $\alpha_{\mathrm{dB}} = 0.2$ dB/km, WDM selectivity 16 dB. The OTDR peak output power is + 12 dBm, the pulsewidth is $\tau = 100$ ns, the OTDR receiver bandwidth is $BW = 1$ MHz, the receiver clipping level is −50 dBm, and the NEP is −70 dBm with an APD gain of 10 A/W. For simplicity, the insertion loss of the WDM and the optical switch can be omitted.

Solution

This problem has to be tackled with a threefold approach. The first question deals with the maximum cw signal the OTDR can handle without running into overload. As a rule of thumb, for proper operation, any incident cw power level should be at least 20 dB below OTDR clipping level. From Equation 11.22 the average backscatter signal generated by the 1550 nm traffic can be derived with the simplification $\alpha_{dB} = \alpha_s$:

$$P_{s,cw} = \frac{0.001}{2} \times 1\text{ mW} \times [1 - e^{-2\times(0.2\times0.23)\times35}] = 480\text{ nW} \cong -33\text{ dBm}$$

The WDM's selectivity attenuates this signal typically by 16 dB, yielding

$$P_{s,cw} = -33 - 16\ dBm = -49\text{ dBm}$$

The requirement for the cw power level at the OTDR input to be lower than −70 dBm leads to the filter attenuation value:

$$a_{1550} = -49 - 70\ dB = 21\text{ dB}$$

The second issue is related to the shot-noise which is generated by the −70 dBm (= 0.1 nW) cw signal. The corresponding photocurrent i_{ph} in the APD is

$$i_{ph} = 0.1\ nW \times 10\frac{A}{W} = 1.0\ nA$$

which leads to a rms shot noise of

$$\bar{i}_s = \sqrt{2 \times 1.6\cdot10^{-19} \times 1.5\cdot10^{6} \times 1\cdot10^{-9}} = 21.9\ pA$$

assuming an equivalent noise bandwidth of 1.5 times the 3 dB receiver bandwidth. This is equivalent to an optical input power of

$$P_{\text{equiv}} = 10 \times \log\left(\frac{21.9\cdot10^{-12} \times 10^{3}}{10}\right) = -86.6\text{ dBm}$$

For the sake of simplicity, the calculation of the shot noise neglects the APD's excessive noise behavior which actually leads to a somewhat higher noise level. However, even with a 5 dB penalty increase the resulting shot noise is sufficiently below the receiver's NEP. Obviously the additional shot noise does not interfere noticeably with the measurement.

Finally the direct traffic crosstalk must be estimated. From Equation 11.33 we get the suppression γ of the (random) traffic signal when filtered through a lowpass

$$\gamma = 10 \times \log\left(2 \times \frac{3\cdot10^{3}}{155\cdot10^{6}}\right) = -44\text{ dB}$$

Hence the rms noise level P_x due to traffic crosstalk is

$$P_x = 0 - 44 - 33 - 16 - 11\text{ dBm} = -104\text{ dBm}$$

This number takes the additional attenuation through backscattering, WDM, and filter F1 into account and is far below the receiver noise level. In the end, the most dominant factor for the filter F1 specification a_{1550} is the resulting cw power level at the OTDR input.

11.7 OUTLOOK

Though OTDR development has evolved over nearly two decades, the emerging changes in optical transmission technology and network topology, constantly give rise to new challenges. OTDRs primarily are suitable for ordinary point-to-point links. Point-to-multi-point links will soon gain importance. In addition to the ongoing and expected improvements in the standard performance parameters like dynamic- and measurement range, resolution, and deadzones, there remain at least three growing areas which need to be addressed with dedicated OTDRs and appropriate measurement methods. These are

1. Links equipped with optical fiber amplifiers;
2. Network structures with multiple branches, for example PONs (passive optical network), subscriber loop links, or LANs;
3. WDM-equipped multiple wavelengths links.

Convenient solutions will most likely be found in a combination of appropriately designed networks plus adapted test equipment, rather than in a single OTDR alone.

Another interesting area for derivatives of standard OTDRs develops in distributed fiber sensor applications which is, however, beyond the scope of this book. Not only temperature and strain, but even magnetic field and electrical current have been measured by use of Brillouin optical time-domain reflectometer (BOTDR) and polarization optical time-domain reflectometer (POTDR), respectively.

REFERENCES

1. CCITT Comité Consultatif International Télégraphique et Téléphonique-Recommendation G.652 "Characteristics of a Single-Mode Optical Fibre Cable".
2. TIA/EIA, Electronic Industries Association, Washington, DC, Fiber Optic Test Procedure FOTP-78 for singlemode fiber.
3. Barnoski, M.K. and S.M. Jensen. 1976. Fiber waveguides: a novel technique for investigating attenuation characteristics. *Appl. Optics* 15: 2112–2115.
4. Personik, S.D. 1977. Photon probe—an optical time domain reflectometer. *Bell Syst. Techn. J.* 56: 355–366.
5. Costa, B. and B. Sordo. 1977. Backscattering technique for investigating attenuation characteristics of optical fibers: a new experimental approach. *CSELT Rapporti Tecnici.* V.
6. Barnoski, M.K. et al. 1977. Optical time domain reflectometer. *Appl. Optics 16:* 2375–2379.
7. Zoboli, M. and Bassi, P., 1983. High spatial resolution OTDR attenuation measurements by a correlation technique. *Appl. Optics,* 22 (23), 3680–3681.
8. Newton, S.A. 1987. A new technique in optical time domain reflectometry. RF & Microwave Symposium and Exhibition. Hewlett-Packard.
9. Nazarathy, M. et al. 1989. Real-time long range complementary correlation optical time domain reflectometer. *J. Lightwave Tech.* 7 (1): 24–37.
10. Dolfi, D.W., and M. Nazarathy. 1989. Optical frequency domain reflectometer with high sensitivity and resolution using optical synchronous detection with coded modulators. *Electronics Lett.* 25 (2), 160–161.
11. Tsuji, K., K. Shimizu, T. Horiguchi, and Y. Koyamada. 1995. Coherent optical frequency domain reflectometry for a long singlemode optical fiber using a coherent lightwave source and an external phase modulator. *IEEE Photon. Technol. Lett.* 7.

12. Eickoff, W., R. Ulrich. 1981. Optical frequency domain reflectometry in singlemode fibre. *Appl. Phys. Lett.* 39, 693–695.
13. Bethea, C.G., B.F. Levine, L. Marchut, V.D. Mattera, and L.J. Peticolas. 1986. Photon counting optical time domain reflectometer using a planar InGaAsP avalanche detector. *Electron. Letters.* 22(6): 302–303.
14. Lacaita, A.L., P.A. Francese, and S. D. Cova. 1993. Single-photon optical-time-domain reflectometry at 1.3 μm with 5 cm resolution and high sensitivity. *Opt. Lett.* 18,
15. King, J.P., D.F. Smith, K. Richards, P. Timson, R.E. Epworth, S. Wright. 1987. Development of a Coherent OTDR Instrument. *Journ. Lightwave Techn.* LT-5(4), 616–623.
16. Horiuchi, Y. et al. 1990. Novel coherent heterodyne optical time domain reflectometry for fault localization of optical amplifier submarine cable systems. *Photon Technol. Lett.* 2(4):
17. Beller, J. 1993. A high performance digital signal processing system for the HP8146A OTDR. *Hewlett-Packard J.,* 63–68.
18. DiVita, P., and U. Rossi. 1980. The backscattering technique: its field of applicability in fibre diagnostic and attenuation measurements. *Opt. Quant. Elec.* 11(17): 17–22.
19. Generic Requirements for Optical Time Domain Reflectometer (OTDR) Type Equipment. Bellcore (Bell Communications Research) GR-196-CORE, Issue 1, 1995.
20. Anderson, D., and D. Judge. 1994. A pattern matching algorithm for remote systems that measures the distance and loss of fusion splices with high precision, NFOEC '94, San Diego, 139–154.
21. Caviglia, F. and P.G. Ricaldone. 1995. *OTDR performance specifications.* 3rd Optical Fiber Measurement Conference, OFMC '95, Liège 1995, paper VIII.1.
22. Healy, P. 1986. Instrumentation principles for optical time domain reflectometry. *J. Phys. E: Sci. Instrum.* 19, 334–341.
23. Gold, M.P. 1985. Design of long-range singlemode OTDR. *J. Lightwave Tech.* 3, 39–46.
24. Rihaczek, A.W. 1967. *Principles of high resolution radar.* NY: McGraw Hill Book Company.
25. Keiser, G. 1985. *Optical fiber communications.* NY:McGraw-Hill.
26. Stone, J., and C.A. Burrus. 1980. Reduction of the 1.38μm water peak in optical fibers by deuterium-hydrogen exchange. *Bell Syst. Techn. J.* 59.
27. Noguchi, N., N. Shibata, N. Uesugi, and Y. Negishi. 1985. Loss increase in optical fibers exposed to hydrogen atmosphere. *J. Lightwave Techn.* LT-3, 236–243.
28. Kerker, M. 1969. *The scattering of light and other electromagnetic radiation.* Academic Press.
29. Born, M., and E. Wolf. 1964. *Principles of optics.* Oxford: Pergamon Press.
30. Izawa, T. and S. Sudo. 1987. Optical fibers: material and fabrication, KTK Scient. Publ., Tokyo, p. 35.
31. Cotter, D. 1983. Stimulated Brillouin scattering in monomode optical fiber. *J. Opt. Comm.* 4(1), 10–19.
32. Horiguchi, T., K. Shimizu, T. Kurashima, M. Tateda, and Y. Koyamada. 1995. Development of a Distributed Sensing Technique Using Brillouin Scattering. *J. Lightwave Techn.,* 13(7), 1296–1302.
33. Dakin, J.P., D.J. Pratt, G.W. Bibby, and J.N. Ross. 1985. Distributed optical fiber Raman temperature sensor using a semiconductor light source and detector. *Electron. Lett.* 21(13), 569–570.
34. Koyamada, Y., H. Nakamoto, and N. Ohta. 1992. High performance coherent OTDR enhanced with erbium doped amplifiers. *Journ. Opt. Commun.* 13, 127–133.

35. Izumita, H., Y. Koyamada, S. Furakawa, and I. Sankawa. 1994. The performance limit of coherent OTDR enhanced with optical amplifiers due to optical nonlinear phenomena. *IEEE J. Lightwave Technol.* 12, p. 1230.
36. Stolen, R.H. 1980. Nonlinearity in fiber transmission. *Proc. IEEE* 68(10), 1232–1236.
37. Li, T. 1980. Structures, parameters, and transmission properties of optical fibers. *Proc. IEEE* 68(10), 1175–1180.
38. Neumann, E.G. 1980. Analysis of the backscattering method for testing optical fiber cables. AEÜ, Band 34, Heft 4, 157–160.
39. Brinkmeyer, E. 1980. Backscattering in singlemode fibers. Electronics Lett. 16(9), 329–330.
40. Nakazawa, M. 1983. Rayleigh backscattering theory for singlemode optical fibers. *Journ. Opt. Soc. Am.* 73.
41. Hentschel, C. 1989. *Fiber optic handbook.* Hewlett-Packard.
42. Danielson, D.L. 1981. *Backscatter measurements on optical fibers.* NBD Technical Note 1034, U.S. Department of Commerce.
43. Meyer, P.L. 1970. *Introductory probability and statistical applications.* 2nd ed. Addison-Wesley Publishing Company, Inc.
44. Hentschel, C. and J. Beller. 1995. *Taking the Guesswork out of OTDR Measurements.* Metrology for the Americas, Miami, November 1995.
45. Schickedanz, D. 1980. Theorie der Rückstreumessung bei Glasfasern. Siemens Forschungs- und Entwicklungsberichte, Springer-Verlag, Bd.9, 1980, Nr. 4, 242–248.
46. Costa, B. 1979. *Comparison between various fibre characterization techniques.* Opt. Commun. Conf. Proc., Amsterdam, II-1 - II-5.
47. Sasaki, S., H. Nakano, and M. Maeda. 1986. *Bit-error-rate characteristics with optical feedback in 1.5* μm *DFB semiconductor laser.* Proc. Euro. Conf. Opt. Commun. ECOC '86, Barcelona, 1986.
48. Kapron, F.P., B.P. Adams, E.A. Thomas, and J.W. Peters. 1989. Fiber-optic reflection measurements using OCWR and OTDR techniques. *J. Lightwave Techn.* 7(9), 1234–1241.
49. Blanchard, P., P.H. Zongo, and P. Facq. 1990. Accurate reflectance and optical backscatter parameter measurement using an OTDR. *Electr. Lett.* 26(25).
50. Hou, V.T. 1991. Update on interim results of fiber optic system filed failure analysis. NFOEC '91, 539–548.
51. Bellcore: Generic Requirements for Remote Fiber Testing Systems (RFTS). TA-NWT-001295, Issue 2, 1993.
52. Davé, R. 1994. Next Generation FITL Remote Fiber Test Systems. NFOEC '94, 357–371.
53. Lee, N., D. Suarez. 1993. Active fiber monitoring using remote OTDR technology. NFOEC '93, 369–376.
54. Davé, R. 1993. Comparison of automated fiber maintenance technologies. NFOEC '93, 385–403.
55. Furukawa, S., Y. Koyamada, T. Horiguchi, and I. Sankawa. 1994. 1.65 μm optical surveillance and test system for subscriber lines and ultra-long span trunk. OFC '94, San Jose.

CHAPTER

12

Dispersion Measurements

Paul Hernday

12.1 INTRODUCTION

All forms of dispersion degrade the modulation-phase relationships of lightwave signals, reducing information-carrying capacity through pulse-broadening in digital networks and distortion in analog systems. Designers of optical fiber transmission systems must cope with three basic forms of fiber dispersion, illustrated schematically in Figure 12.1. Intermodal dispersion, which limits data rates in systems using multimode fiber, results from the splitting of the signal into multiple modes that travel slightly different distances. Chromatic dispersion, which occurs in both singlemode and multimode fiber, results from a variation in propagation delay with wavelength that is shaped, in turn, by the interplay of fiber materials and dimensions. Polarization-mode dispersion, caused by the splitting of a polarized signal into orthogonal polarization modes with different speeds of propagation, becomes a limiting factor in singlemode fiber when chromatic dispersion is sufficiently reduced. This chapter deals with the dispersion characteristics of the physical layer of a telecommunications system—the fiber, components, and installed transmission paths—providing a brief introduction to the causes of dispersion and a sampling of measurement methods. Measurement approaches to these critical attributes take many forms; some of the methods described here are widely used commercial methods, and others are presented simply because they provide good insight into the dispersive phenomena. The detail with which the methods are discussed reflects, to some extent, the author's experience with the methods. Measurement methods for many fiber, component, and system attributes are developed by standards groups such as Telecommunications Industry Association and its international counterparts. Guidance in the measurement of dispersive effects is provided by formal fiber optic test procedures (FOTPs), referenced herein.

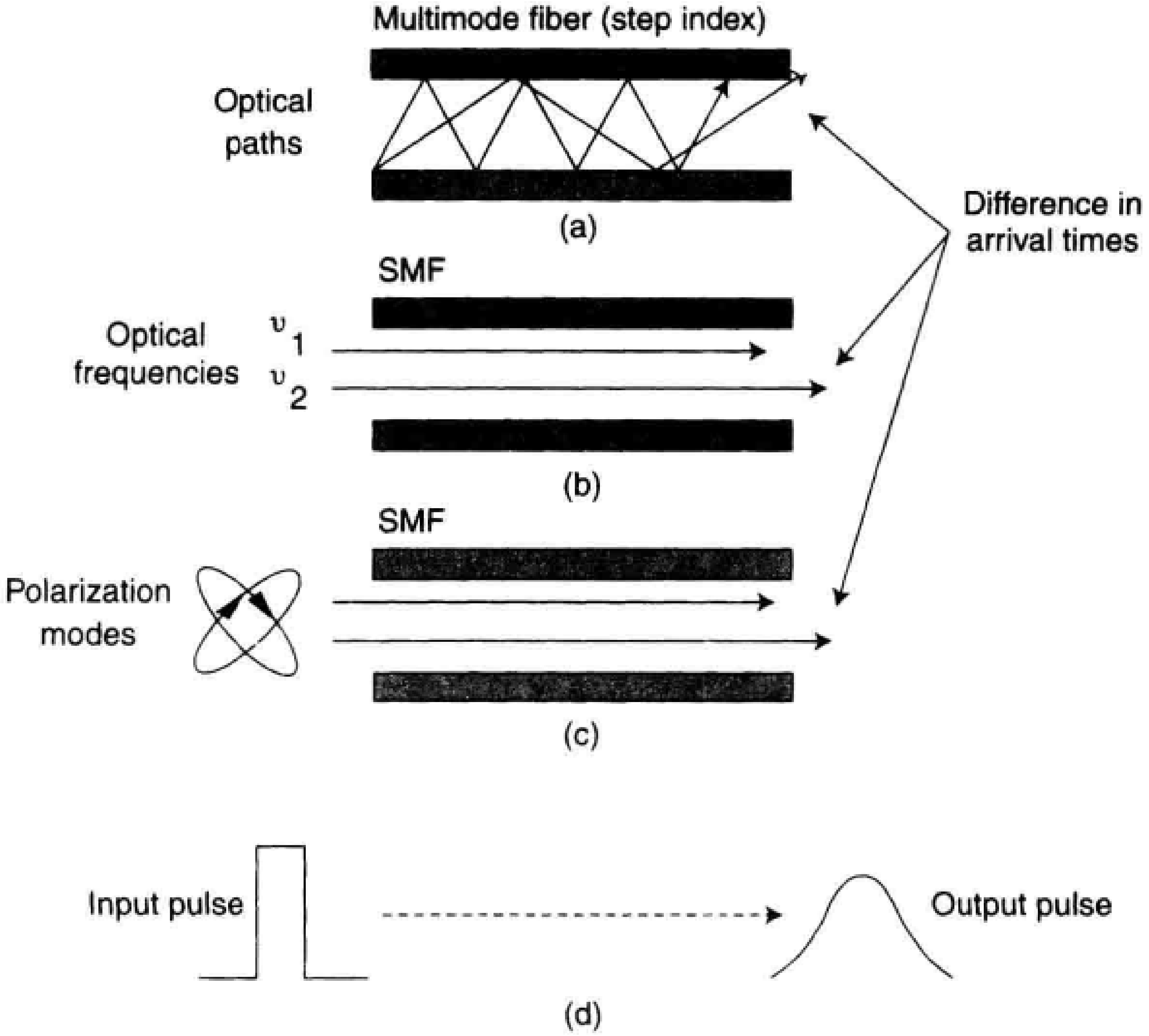

Figure 12.1 Schematic representations of fiber dispersion. (a) Intermodal dispersion. (b) Chromatic dispersion. (c) Polarization-mode dispersion. (d) Typical effect of dispersion on a transmitted pulse.

12.2 MEASUREMENT OF INTERMODAL DISPERSION

12.2.1 Introduction

Singlemode fiber supports the propagation of a single guided wave, or mode. In contrast, multimode fiber supports hundreds of modes, and this characteristic produces the phenomenon called intermodal dispersion. Because the modes travel slightly different distances, as indicated in Figure 12.1a, the modulation envelopes of light in the various modes become increasingly out of phase as the signal travels along the fiber. In the case of a digital system, each mode delivers a pulse, but the distribution of arrival times caused by the different propagation times causes the transmitted pulse to broaden in time and to drop in peak amplitude. Intermodal dispersion typically limits multimode fiber to transmission distances of less than 1 km and bit rates less than 1 Gb/s. For measurement purposes, intermodal dispersion is typically expressed as the lowest modulation frequency at which the baseband AM response of the fiber has rolled off by 3 dB. The following section discuss two common methods for measuring multimode fiber bandwidth.

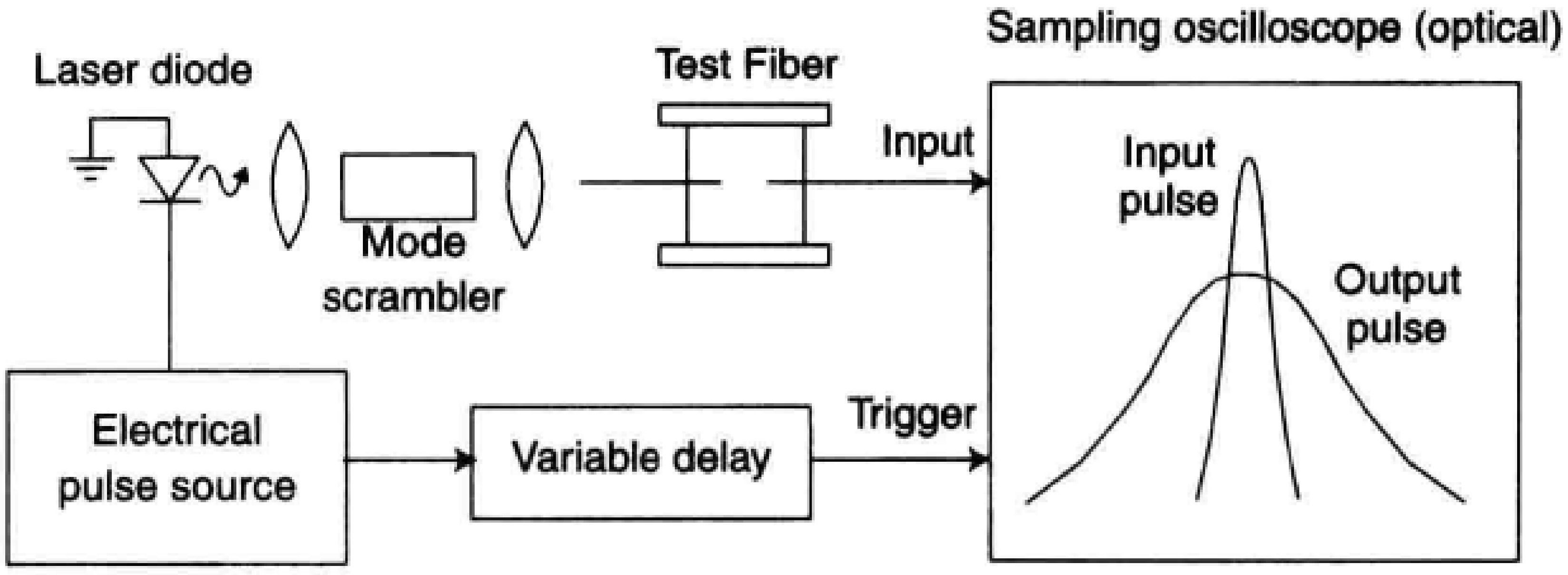

Figure 12.2 Measurement of multimode fiber bandwidth by the pulse distortion method.

12.2.2 The Pulse Distortion Method

The most common method for measuring multimode fiber bandwidth, illustrated in Figure 12.2, is based on measurement of the impulse response.[1] A pulsed laser source is coupled through a mode scrambler to the input of the test fiber. The source spectrum must be narrow enough that the results are not significantly influenced by chromatic dispersion. The output of the fiber is measured by a sampling oscilloscope with built-in optical receiver. A horizontal trigger is supplied through a variable delay to offset the difference in delay between a short reference fiber and the fiber to be tested. The reference fiber is typically a few meters in length. In operation, a fast pulse is launched into the test fiber and the output pulse is digitized, including leading and trailing edges down to 1% of the peak amplitude. Next, the input pulse is measured in the same way, using a short reference path in place of the test fiber. The reference fiber can be a short length cut from the input of the test fiber, or a short length of fiber having similar optical characteristics. The transfer function of the test fiber is given by

$$H(f) = \frac{B(f)}{A(f)} \tag{12.1}$$

where $B(f)$ and $A(f)$ are the Fourier transforms of the output and input pulses, respectively. Fiber bandwidth is defined as the lowest frequency for which $|H(f)| = 0.5$.

Multimode fiber bandwidth measurements are sensitive to optical launch conditions and the deployment of the test sample. For stable, repeatable measurements, a mode-scrambling device should be inserted ahead of the test device to assure excitation of a large number of modes. In addition, cladding light should be removed. In some cases, the fiber coating dissipates cladding modes. Alternatively, cladding mode strippers can be used at both ends of the test fiber.

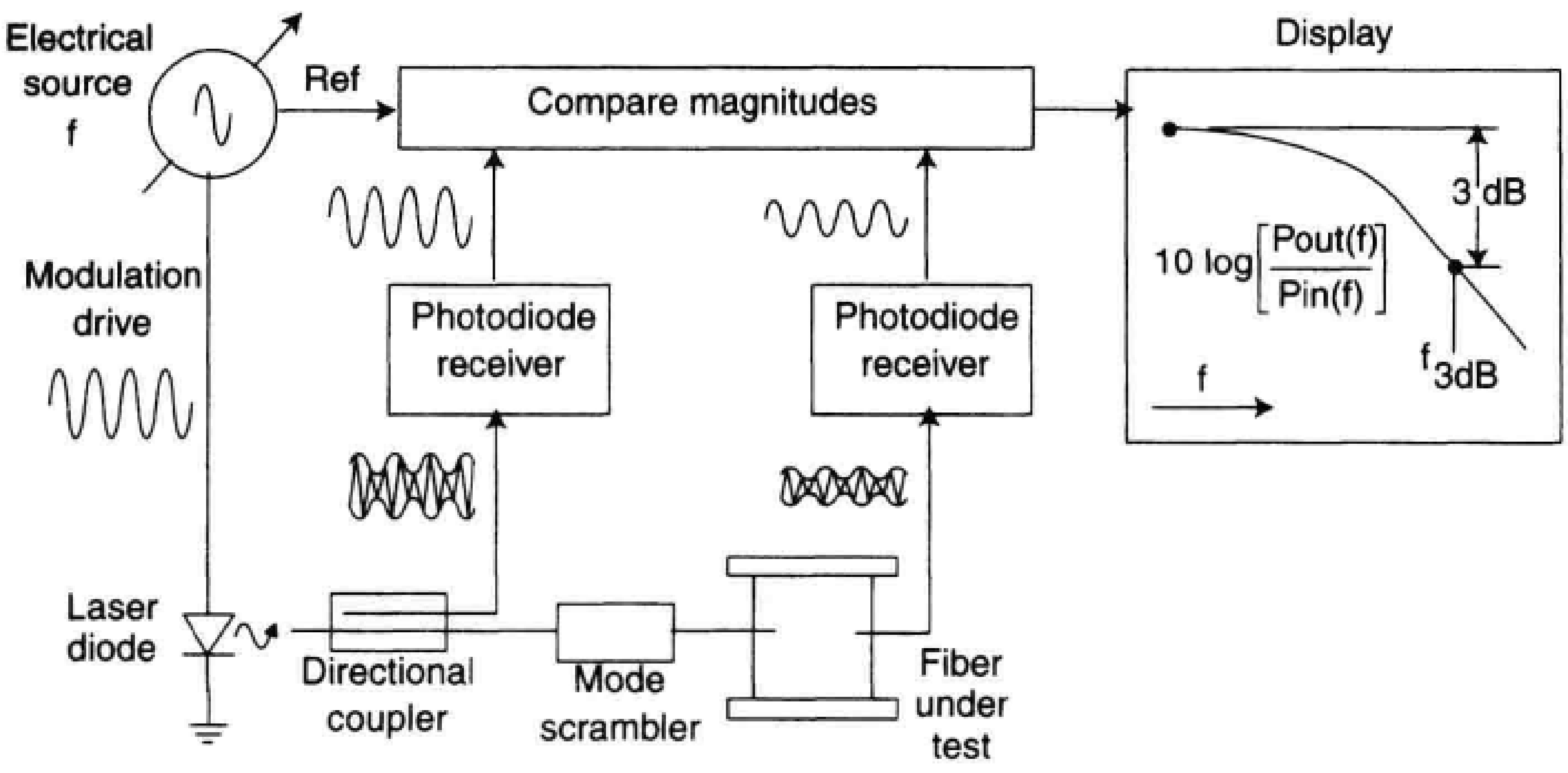

Figure 12.3 Measurement of multimode fiber bandwidth by the frequency domain method.

12.2.3 The Frequency Domain Method

An alternative method for the measurement of multimode fiber bandwidth is the baseband AM response method[2] shown in Figure 12.3. A narrowband cw optical carrier is sinusoidally intensity modulated by a swept-frequency RF or microwave signal source and coupled through a mode scrambler to the test fiber. Cladding mode strippers may also be needed. The modulation is detected by a photodiode receiver. The instrumentation records the received optical power as a function of modulation frequency. In operation, the test fiber is generally measured first, resulting in the measurement $P_{out}(f.)$ The input signal is then determined by measuring again with a short reference fiber. As in the pulse method, the reference fiber can be a short length cut from the input of the test fiber, or a short length of fiber having similar optical characteristics. The reference measurement yields the function $P_{in}(f)$. The frequency response in optical power is given by

$$H(f) = \log_{10}\left[\frac{P_{out}(f)}{P_{in}(f)}\right]. \tag{12.2}$$

Fiber bandwidth is defined as the lowest frequency at which $H(f)$ has decreased by 3 dB from its zero-frequency value.

For convenience, source and receiver functions may be performed using a lightwave component analyzer or a network analyzer with appropriate transducers. In either case, sweeping of the modulation frequency, subtraction of the calibration values and display of the resulting transmission response are performed automatically. When an electrical network analyzer is used with external laser source and photodiode receiver, care must be taken to properly interpret the frequency response. Because an electrical network analyzer measures RF power and the photodetector produces a current that is proportional to optical power, the network analyzer will indicate a 6 dB change for a 3 dB change in optical level.

12.3 MEASUREMENT OF CHROMATIC DISPERSION

12.3.1 Introduction

Chromatic dispersion is simply a variation in the speed of propagation of a lightwave signal with wavelength. The optical source in a high-speed communication system is typically a single-line diode laser with nonzero spectral width. Pulse modulation increases the spectral width. Each wavelength component of the signal travels at a slightly different speed, resulting in the pulse broadening illustrated in Figure 12.1d. This section provides an introduction to chromatic dispersion, the primary dispersive mechanism in singlemode fiber, and describes several chromatic dispersion measurement methods appropriate to singlemode fiber. Chromatic dispersion is also an important parameter of multimode fiber.[3,4]

12.3.2 Causes of Chromatic Dispersion

In singlemode fiber, chromatic dispersion results from the interplay of two underlying effects—material dispersion and waveguide dispersion.[5] Material dispersion results from the nonlinear dependence upon wavelength of the refractive index, and the corresponding group velocity, of doped silica. Waveguide dispersion is rooted in the wavelength-dependent relationships of the group velocity to the core diameter and the difference in index between the core and the cladding. A third component, called second-order PMD or differential group delay dispersion, arises from the details of fiber PMD and produces an effect which is identical to chromatic dispersion.[5–7] Second-order PMD sets the ultimate limit to which a transmission path can be compensated for chromatic dispersion.

The information-carrying capacity of a fiber optic system is highest when the group delay is flat with wavelength. In dispersion-unshifted singlemode fiber, the zero-dispersion wavelength λ_0 is near 1300 nm, where the two main underlying mechanisms, material dispersion and waveguide dispersion, naturally cancel one another. Control of the refractive index profile can place λ_0 anywhere in the 1300/1550 nm wavelength range. In dispersion shifted fiber, λ_0 is set to approximately 1550 nm.

12.3.3 Definitions and Relationships

The discussion will make use of several specialized terms, defined in Table 12.1

An example of the chromatic dispersion of a disperson-shifted singlemode fiber in the region of 1550 nm is shown in Figure 12.4. The upper curve shows the typical wavelength dependence of the relative group delay. The chromatic dispersion coefficient D, shown in the lower curve, is the attribute used to estimate pulse broadening. Its value at a particular wavelength is determined by differentiating the relative group delay curve with respect to wavelength and dividing by the length of the transmission path

$$D_\lambda = \frac{1}{L}\frac{d\tau_g}{d\lambda} \tag{12.3}$$

where τ_g is the group delay in ps, L is the path length in km, and λ is the wavelength in nm. To a first approximation, the broadening T of a pulse is given by

Table 12.1 Definitions for Chromatic Dispersion.

Attribute	Units	Definition
V_g	m/s	The propagation speed of the modulation envelope of a lighwave signal.
τ_g or τ—Group delay	ps	The time required for a modulated signal to travel along the transmission path; also called the envelope delay.
$\frac{d\tau}{d\lambda}$—Chromatic dispersion	ps/nm	The slope of the group delay wavelength versus curve.
D—Dispersion coefficient	ps/nm-km	The chromatic dispersion of a path divided by the path length.
λ_0—Lambda-zero	nm	The wavelength at which chromatic dispersion is zero.
S_0—Slope at λ_0	ps/nm^{2}km	The slope of the dispersion curve at λ_0.

$$T = D\,\Delta\lambda\,L, \tag{12.4}$$

where T is in ps, D is the dispersion in ps/nm-km, and $\Delta\lambda$ is the spectral width of the modulated lightwave signal in nm. For a given value of chromatic dispersion, the pulse becomes broader with increase in the path length or the spectral width of the signal.

A narrowband signal centered at λ_0 can propagate for great distances with minimal degradation from chromatic dispersion. Away from λ_0, dispersion increases according to

$$D(\lambda) = S_0(\lambda - \lambda_0) \tag{12.5}$$

where S_0 in ps/nm^{2}km is the slope at λ_0. Knowledge of the slope of the dispersion curve at λ_0 allows system designers to estimate the dispersion at nearby wavelengths.

The zero dispersion wavelength of singlemode fiber is a function of temperature. The temperature dependence of λ_0 is approximately +0.03 nm/C for dispersion-shifted fiber and +0.025 nm/C for dispersion-unshifted fiber. Depending on the application, it may be appropriate to record the temperature of the fiber under test. The dispersion slope does not change appreciably with temperature.

12.3.4 Control of Chromatic Dispersion

Control of the total chromatic dispersion of transmission paths is critical to the design and construction of long-haul, high-speed telecommunications systems. The first objective is to reduce the total dispersion to the point where its contribution to the error rate of the system is acceptable. A system consists of many spans of fiber from different manufacturing runs, each with its own zero-dispersion wavelength and dispersion slope at lambda-zero. The dispersion of a single-channel system can be controlled by concatenating fibers of differing dispersion such that the total dispersion is near zero. Alternately, dispersion

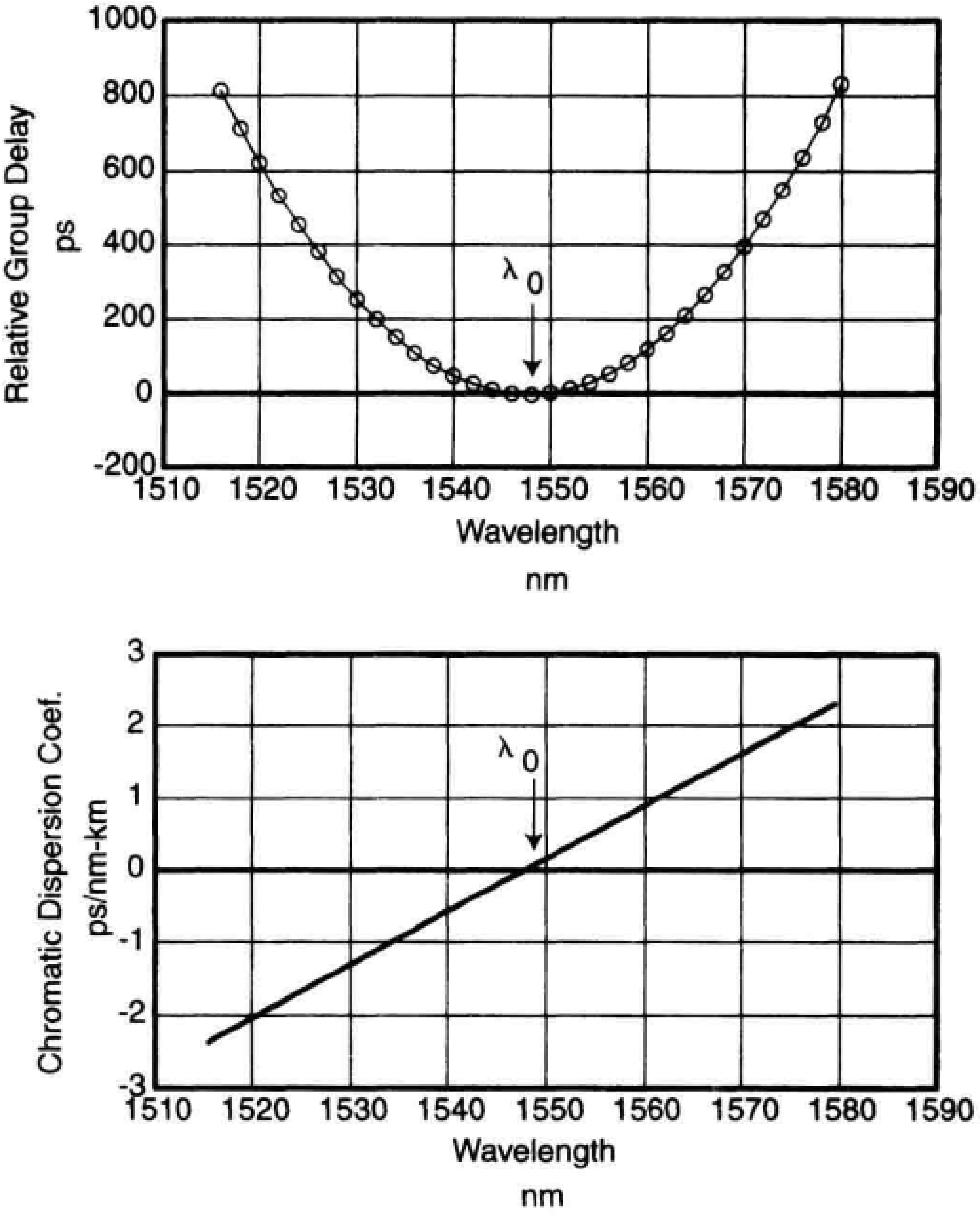

Figure 12.4 Chromatic dispersion measurement of dispersion-shifted fiber. (a) Relative group delay. (b) Dispersion coefficient.

may be allowed to accumulate along the path and then compensated at the output of the system. For example, if an installed dispersion-shifted fiber system exhibits negative dispersion at the chosen operating wavelength, it can be compensated with a relatively short length of dispersion-unshifted fiber, which has a large, positive dispersion coefficient at 1550 nm. Dispersion can also be compensated with chirped fiber Bragg gratings, made by exposing specially doped fiber to an interference pattern of intense ultraviolet light. Chirping refers to an increase in the period of the index variation as a function of distance along the fiber. Dispersion compensation is more complex in dense WDM systems.

The output power of erbium-doped fiber amplifiers (EDFAs) is sufficient to produce nonlinear effects in singlemode fiber. The second objective of chromatic dispersion compensation is to limit the impairments caused by these nonlinearities. For example, four-wave mixing can be controlled by maintaining a small negative dispersion in those portions of a span that are exposed to high power levels. (Another approach to this problem, in wavelength multiplexed systems, is to space the channels in unequal wavelength increments). In summary, in high-speed, long-haul systems, chromatic dispersion must be compensated on a system end-to-end basis to minimize ordinary pulse broadening, but must be maintained at some small but nonzero level in regions where the optical power is extremely high.

Chromatic dispersion measurements are performed by fiber and cable researchers and manufacturers, and by system integrators. Increasingly, chromatic dispersion measurements are also performed during the design, manufacture, and incoming inspection of system components, particularly chromatic dispersion compensators and wavelength division multiplexing components. In the field, chromatic dispersion is measured in connection with the installation of new systems or the upgrade of existing routes to higher bit rates. Some types of measurement systems require local access to both ends of the test fiber, making them more appropriate for factory and laboratory testing and special cases in which it is practical to measure installed fiber in a loop-back arrangement. Some types of measurement systems can be split between remote ends of the fiber.

Having defined the basic terms and measurement applications, we next examine the phase shift and differential phase shift chromatic dispersion measurement methods. Two additional methods, the interferometric method and the pulse delay method, will not be discussed. The interferometric method is useful for measurement of fibers in the length range of several meters. Unfortunately, fiber manufacturing processes are such that the behavior of a long span cannot be projected with accuracy from measurements of a short sample. The pulse delay method is a classic measurement based on the change in pulse arrival time over a series of wavelengths. This method is used for measurement of single-mode and multimode fibers and is discussed in connection with measurement of multimode fiber bandwidth in Section 12.2.2.

12.3.5 The Modulation Phase-Shift Method

A chromatic dispersion measurement apparatus based on modulation phase shift[8,9] is shown in Figure 12.5. In operation, the output of a narrowband, tunable optical source is intensity modulated and applied to the fiber under test. The transmitted signal is detected and the phase of its modulation is measured relative to the electrical modulation source. The phase measurement is repeated at intervals across the wavelength range of interest. From measurements at any two adjacent wavelengths, the change in group delay, in ps, corresponding to the wavelength interval $\Delta\lambda$ is

$$\Delta\tau_\lambda = -\frac{\phi_{\lambda+\frac{\Delta\lambda}{2}} - \phi_{\lambda-\frac{\Delta\lambda}{2}}}{360\, f_m} \times 10^{12} \tag{12.6}$$

where λ is the center of the wavelength interval, f_m is the modulation frequency in Hz, and ϕ is the phase of the recovered modulation relative to the electrical modulation source, in degrees. Wavelengths are in nm. The curve of relative group delay shown in Figure 12.4 is constructed by accumulating these changes in group delay across the measurement

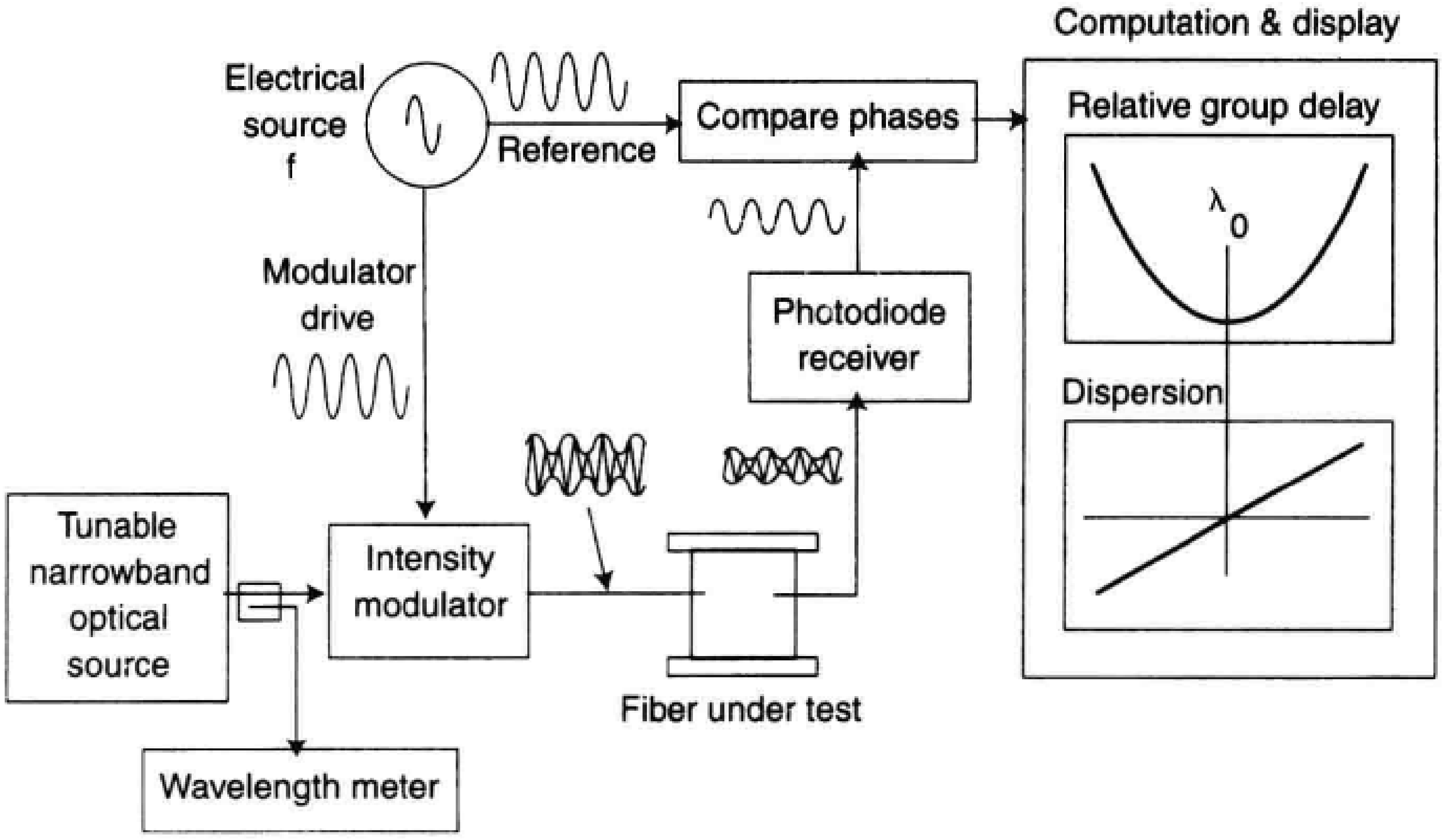

Figure 12.5 Measurement of chromatic dispersion by the modulation phase-shift method.

wavelength range. The vertical axis is labeled "relative" because measurement of dispersion does not require determination of absolute delay, although this same set of instrumentation can measure absolute delay with a change in measurement flow and computation. For convenience of interpretation, the relative group delay curve is typically offset vertically to bring the minimum value to zero.

As mentioned earlier, chromatic dispersion is defined as the rate of change of the group delay with wavelength. The result is also valid if change in relative group delay is used. Equation 12.3 becomes

$$D_\lambda = \frac{1}{L}\frac{d\Delta\tau}{d\lambda} \tag{12.7}$$

where D is the dispersion coefficient in ps/nm/km, $\Delta\tau$ is the relative group delay in ps, and L is the path length in km. If the physical characteristics of the fiber are consistent along its length, the total chromatic dispersion, in ps/nm, scales linearly with fiber length.

Curve Fitting to Improve Measurement Precision. The precision of chromatic dispersion measurements is greatly improved by fitting an appropriate model equation to the measured relative group delay data. Because direct differentiation of the raw group delay data tends to amplify the effect of noise, the values of λ_0, S_0, and $D(\lambda)$, the value of dispersion at any particular wavelength, are calculated from the fitted curve. The model equation is chosen according to the type of fiber being measured. The three-term Sellmeier is commonly used for dispersion-unshifted fiber, in which material dispersion plays the major role. It has the form

$$\tau(\lambda) = A\lambda^2 + B + C\lambda^{-2}. \tag{12.8}$$

The quadratic equation is commonly used for dispersion-shifted fiber, in which waveguide dispersion is dominant. It has the form

$$\tau(\lambda) = A\lambda^2 + B\lambda + C. \tag{12.9}$$

Other equations are available for special cases. The five-term Sellmeier has the form

$$\tau(\lambda) = A\lambda^4 + B\lambda^2 + C + D\lambda^{-2} + E\lambda^{-4}. \tag{12.10}$$

The five-term Sellmeier provides more degrees of freedom but is more sensitively affected by noise and instabilities in the measurement path. Incidentally, the association of *A*, *B*, etc., with the particular λ terms is quite variable in the chromatic dispersion literature.

Optimizing Measurement Accuracy. The precision and accuracy of chromatic dispersion measurements is dependent upon test equipment design. The impact of phase instability and phase measurement resolution depends upon the modulation frequency. For a given wavelength step, a higher modulation frequency will produce a phase change that is larger in comparison with a given phase measurement uncertainty.

Phase-detection equipment can generally measure phase unambiguously only over a ±180 degree range. If the combination of wavelength step, modulation frequency, and device dispersion produces a phase change that exceeds the phase-detector range, the apparent phase will simply fold back within the measurable range and produce a $N \times 360$ degree error, where N represents the number of full cycles of phase that escaped notice of the instrumentation. For unambiguous phase measurements, the wavelength step must be limited so that the phase change produced by a wavelength step falls within the ±180 degree range of the phase detector. Some chromatic dispersion measurement systems provide automatic, real-time optimization of the modulation frequency, selecting as high a modulation frequency as possible without exceeding the range of the phase detector.

Wavelength accuracy is important because the actual phase shift is proportional to the wavelength step. Depending upon measurement objectives, the inherent wavelength accuracy of a tunable laser or filtered broadband optical source, for example, 0.1 nm, may be sufficient. When high precision is called for, as in high-speed, long-haul applications, a tunable external cavity laser and wavelength meter are commonly employed. Measurement of narrowband devices such as fiber Bragg gratings and wavelength division multiplexers demands both the high wavelength resolution of a tunable laser and the accuracy of a wavelength meter to faithfully reveal the fine structure of the relative group delay curve.

Thermal transients in the measurement setup and the fiber under test can contribute significant measurement error. Spools of fiber are very effective thermometers. A change in temperature produces a change in length and a corresponding change in group delay $\Delta\tau$ according to

$$\Delta\tau = \frac{\Delta L}{L}\tau \tag{12.11}$$

where τ is the absolute group delay through the path under test, L is the path length, and ΔL is the temperature-induced change in path length. Because the modulation phase-shift method does not instantly step across the measurement wavelength range, temperature-induced changes in group delay can accumulate throughout a measurement and distort the final results. To minimize temperature effects, the device under test (DUT) can be allowed to stabilize in the ambient air before starting the measurement. The test device can be covered with a physical baffle such as a spool cover or a cloth blanket to block the flow of air currents across the spool. Baffling should also be used when the spool being measured is inside of a circulating air type of thermal chamber.

The effects of thermal drift in both instrumentation and test device can be reduced by alternating the phase measurement between the test wavelengths and a fixed reference wavelength. Changes in the reference wavelength phase are caused only by temperature effects, and this information can be used to correct the phase measurements performed at the test wavelengths. Use of the reference wavelength trades off measurement speed for increased measurement accuracy.

12.3.6 The Differential Phase-Shift Method

The differential phase-shift method[10] determines the value of chromatic dispersion at a selected wavelength directly from measurement of the change in group delay across a small wavelength interval. The resulting chromatic dispersion can be assumed to be the average dispersion over the wavelength interval if the interval is sufficiently small. A reference fiber and test fiber are measured using the same wavelength increment. The chromatic dispersion in ps/nm·hm at each wavelength λ_i is given by

$$D_{\lambda_i} = \frac{\Delta\phi_{\lambda_i} - \Delta\phi'_{\lambda_i}}{360 f_m L \Delta\lambda} \times 10^{12} \tag{12.12}$$

where $\Delta\lambda$ is the wavelength interval centered about $\lambda_{i,}$ $\Delta\phi_{\lambda_i}$ is the measured phase change with the test fiber in the path, $\Delta\phi'_{\lambda_i}$ is the measured phase change with only a calibration fiber in the path, and f_m is the modulating frequency in Hz. If the test-fiber measurement is performed without the calibration fiber in the path, L is the length of the test fiber minus the length of the calibration fiber, in km. Wavelength is in nm and phase is in degrees. Dispersion is measured as a function of wavelength by repeating the process at a sequence of wavelengths. A model equation can be fitted to the curve to improve the precision with which $\lambda_{0,}$ D, and S_0 can be determined.

The differential phase-shift measurement can be performed using several different equipment setups.[8] All of the methods require modulation of the optical test signal, but the approaches differ in other ways. Test wavelength may be controlled by switching among different laser diodes, filtering light from an EELED, or modulating the wavelength of an external cavity laser. The reference required for phase measurements is derived from the same electrical signal source used to modulate the optical source. The reference path may be a direct connection to the phase meter in the case of laboratory measurements, or a fiber link in the case of field measurements. In addition, the various implementations of the differential phase-shift method differ in the details of signal pro-

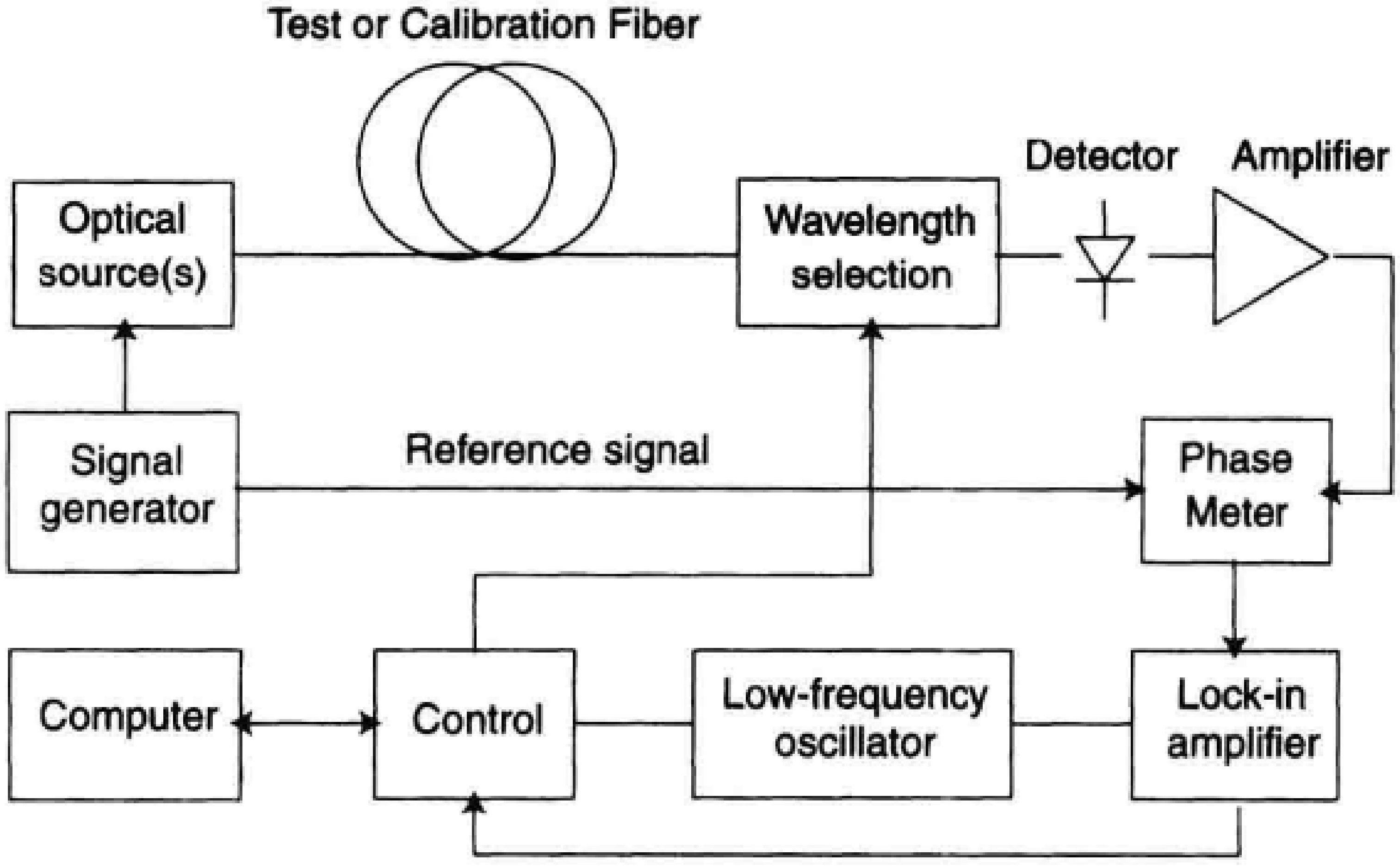

Figure 12.6 Setup for measurement of chromatic dispersion by the differential phase-shift method.

cessing. One method, referred to as the double demodulation method, is shown in Figure 12.6. Wavelength is changed at a high enough rate to avoid the 1/*f* noise of the electronics and to reduce the impact of drift of the instrumentation and the test device.

12.3.7 The Baseband AM Response Method

Chromatic dispersion changes the relative phase of the sidebands of modulated signals. In the case of a simple intensity modulated signal, chromatic dispersion converts amplitude modulation (AM) to frequency modulation (FM). The effect gives the AM response a characteristic shape which can be analyzed to determine the dispersion coefficient at the operating wavelength.[11,12] The setup shown in Figure 12.7 is based on a lightwave component analyzer (LCA). A tunable laser with narrow spectral width is tuned to the wavelength at which dispersion is to be determined. The light is intensity modulated by a lithium niobate Mach-Zehnder modulator. As the modulation frequency is swept, the baseband AM response exhibits a series of nulls. The null frequencies in GHz are predicted by

$$f_m = \sqrt{\frac{500\, c\, (1 + 2N)}{D\, L\, \lambda_0^2}} \tag{12.13}$$

where $N = 0,1,2 \ldots$ is the index of the null, D is the chromatic dispersion in ps/nm-km, L is the length of the fiber in km, and λ_0 is the wavelength in nm. At 1550 nm, for a 20 km fiber with a dispersion coefficient of 17 ps/nm-km dispersion and a wavelength of 1550 nm, the first null occurs at 13.55 GHz. The chromatic dispersion of the test fiber at the first null is given by

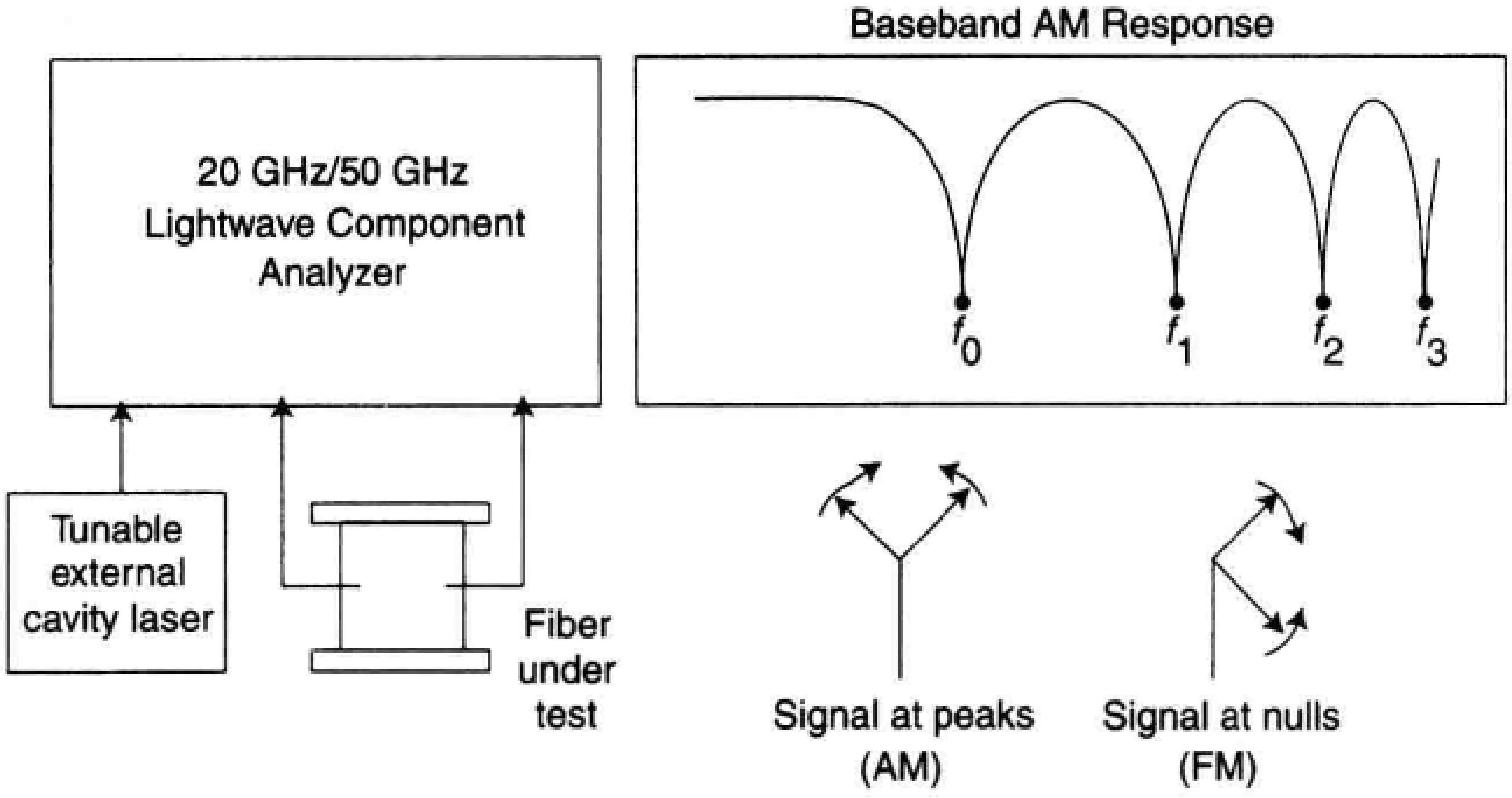

Figure 12.7 Measurement of chromatic dispersion by the baseband AM response method.

$$D_0 = \frac{500\, c}{f_m^2\, L\, \lambda_0^2} \tag{12.14}$$

As will be apparent from inspection of the example following Equation 12.13, this method is most applicable to measurement of relatively large values of dispersion, that is, well away from the zero dispersion wavelength.

12.4 POLARIZATION-MODE DISPERSION

12.4.1 Introduction

Polarization-mode dispersion, or PMD, is a fundamental property of singlemode optical fiber and components in which signal energy at a given wavelength is resolved into two orthogonal polarization modes of slightly different propagation velocity.[13] The resulting difference in propagation time between polarization modes is called the differential group delay, commonly symbolized as $\Delta\tau_g$, or simply $\Delta\tau$. PMD causes a number of serious capacity impairments,[14–16] including pulse broadening. In this respect, its effects resemble those of chromatic dispersion, but there is an important difference. Chromatic dispersion is a relatively stable phenomenon. The total chromatic dispersion of a telecommunications system can be calculated from the sum of its parts, and the location and value of dispersion compensators can be planned in advance. In contrast, the PMD of singlemode optical fiber at any given signal wavelength is not stable, forcing system designers to make statistical predictions of the effects of PMD and making passive compensation impossible. The effect of PMD on a digital transmission system is shown in Figure 12.8.

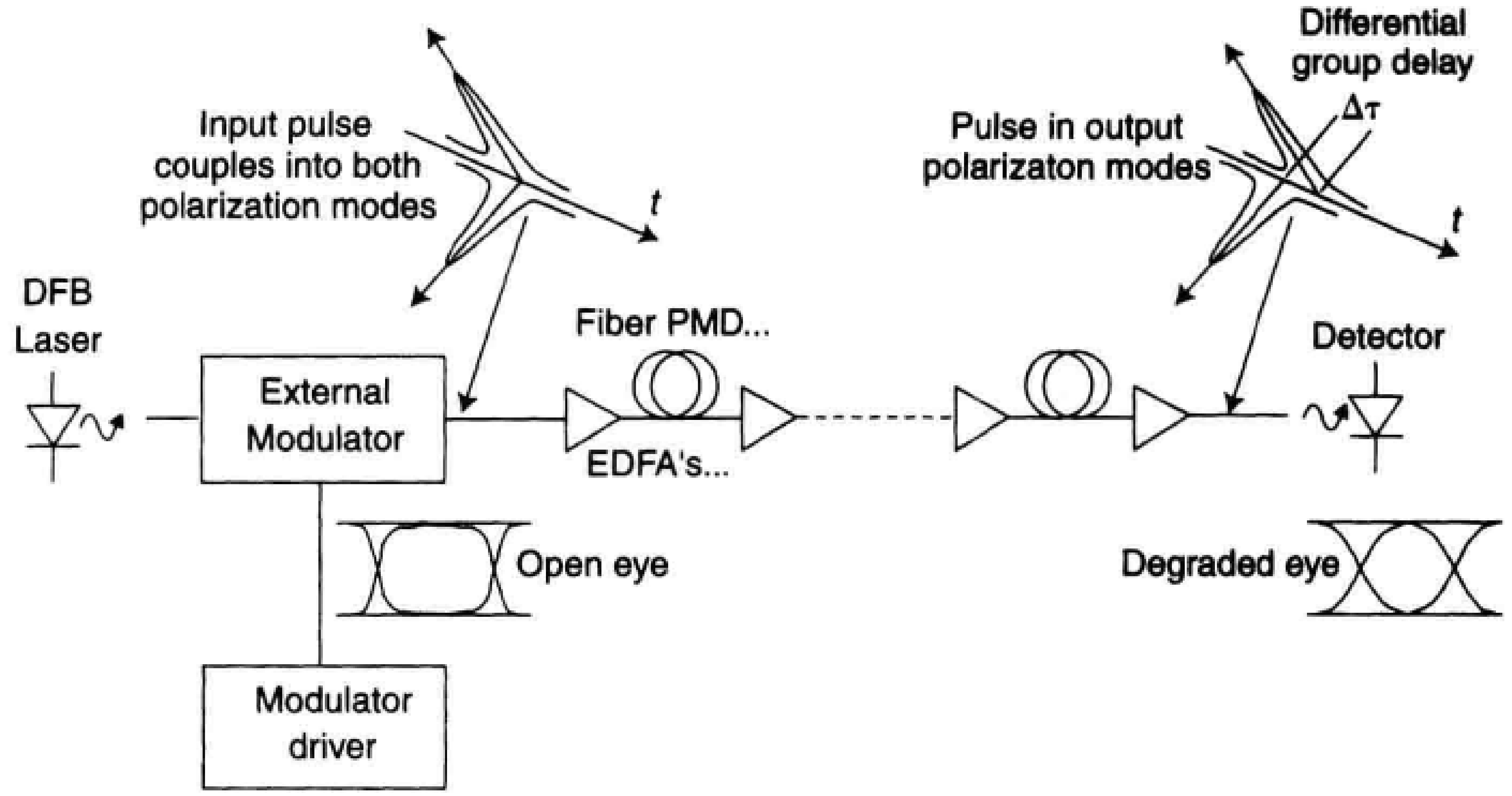

Figure 12.8 The effect of polarization mode dispersion in a digital communication system.

PMD can also affect the performance of high channel-capacity fiber optic CATV systems as shown in Figure 12.9. Direct intensity modulation of the DFB laser in the transmitter produces a signal of fixed state of polarization and chirped wavelength. In other words, the optical frequency is modulated to some extent by the changing laser current. Fiber PMD transforms each signal frequency component differently, adding a polarization modulation component to the signal. The final damage is done by the polarization-

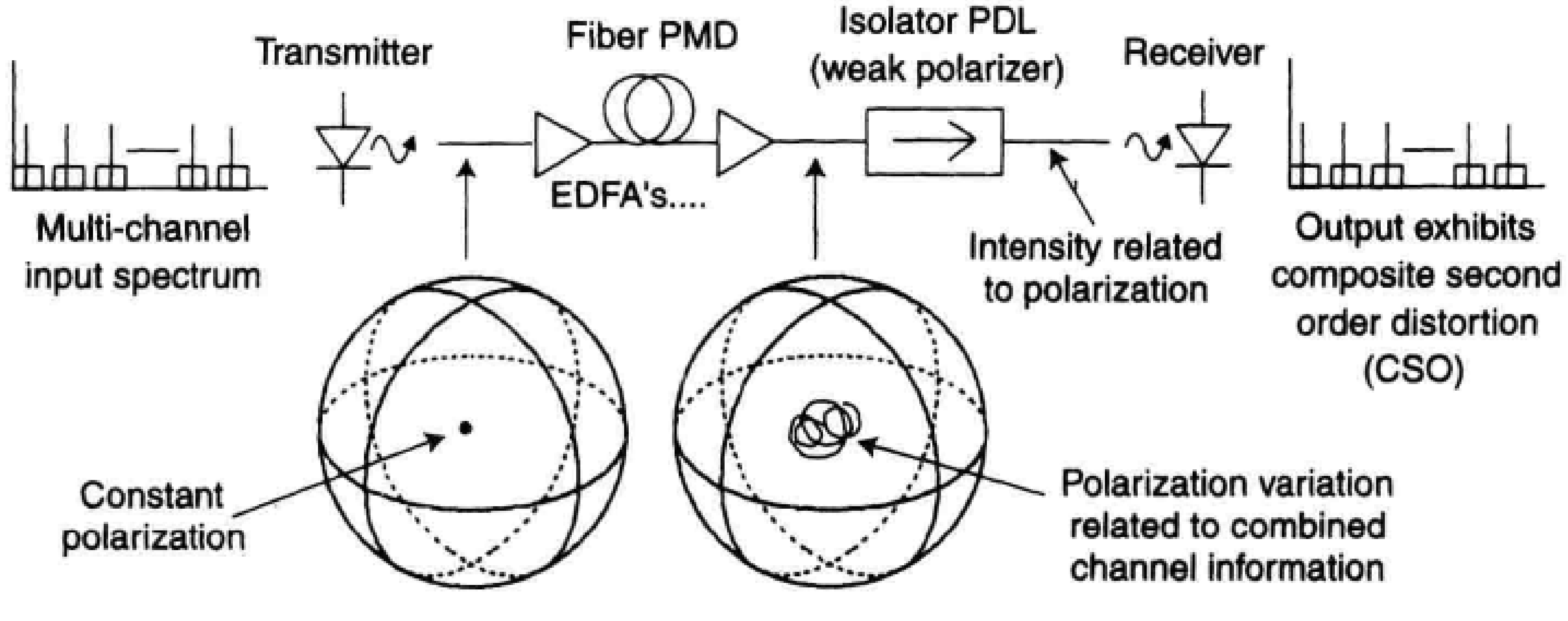

Figure 12.9 The effect of polarization-mode dispersion in a CATV distribution system.

dependent loss (PDL) of components. By attenuating polarization states selectively, PDL discriminates the changing polarization into an intensity component that is detected along with the desired signal, producing composite second-order distortion (CSO).[14]

System designers minimize the impact of PMD by specifying low PMD in fiber and components and by minimizing the PDL of components. PMD of some older installed fibers may be much higher than recently manufactured fibers, and system operators often measure these installed fibers as they plan to upgrade their systems to higher bit rates.

12.4.2 Causes of PMD

Optical fiber and fiber-optic components typically exhibit a small difference in refractive index for a particular pair of orthogonal polarization states, a property called birefringence. The index difference results in a difference in the propagation time—the differential group delay—for waves traveling in these polarization modes, as shown for the case of pulse transmission in Figure 12.10a. In singlemode fiber, birefringence originates from non-circularity, or ovality, of the fiber core in two ways: an oval waveguide is inherently birefringent, and the mechanical stress field set up by the oval core induces additional birefringence. The waveguide effect generally dominates in low PMD fiber. The phenomenon of mode coupling, to be discussed in the next section, complicates the picture, making the differential group delay a function of wavelength and of environmental conditions.

The birefringence of crystalline materials such as quartz is produced by the regular structure of the crystal. PMD in optical components may be caused by the birefringence of its sub-components, which may include quartz elements, for example, or segments of asymmetric fiber. Propagation of a signal along parallel paths of slightly different optical length, where the splitting is a function of polarization, also produces differential group delay. Certain types of optical isolators owe their PMD to this parallel-path mechanism. Components for state-of-the-art communication systems are typically specified at less than 0.05 ps of differential group delay.

Polarization maintaining fiber (PM or hi-bi fiber) is an extreme example of stress-induced birefringence. Elements of dissimilar glass embedded in the cladding assure that the core is exposed to an asymmetric stress field that is uniform along the fiber's length. When polarized light is coupled into a section of PM fiber, as illustrated in Figure 12.10a, the electric field of the input light resolves into two orthogonal polarization modes with slightly different speeds of propagation. The polarization modes are maintained along the fiber and energy does not couple between the modes. As indicated earlier, the difference in propagation time between these orthogonal polarization modes is called the differential group delay. The polarization modes and the differential group delay of a simple, linearly birefringent device are independent of wavelength. The degree of birefringence that PM fiber exhibits is often expressed as beat length, defined as the length of fiber over which the fast and slow waves change relative phase by 360 degrees. The beat length is typically a few millimeters in PM fiber.

Fiber birefringence is also induced by bending. Through the photoelastic effect, bending produces an asymmetry of the index of refraction. This is the basis of the common fiber polarization adjuster, discussed in Chapter 6. Bend-induced birefringence is not

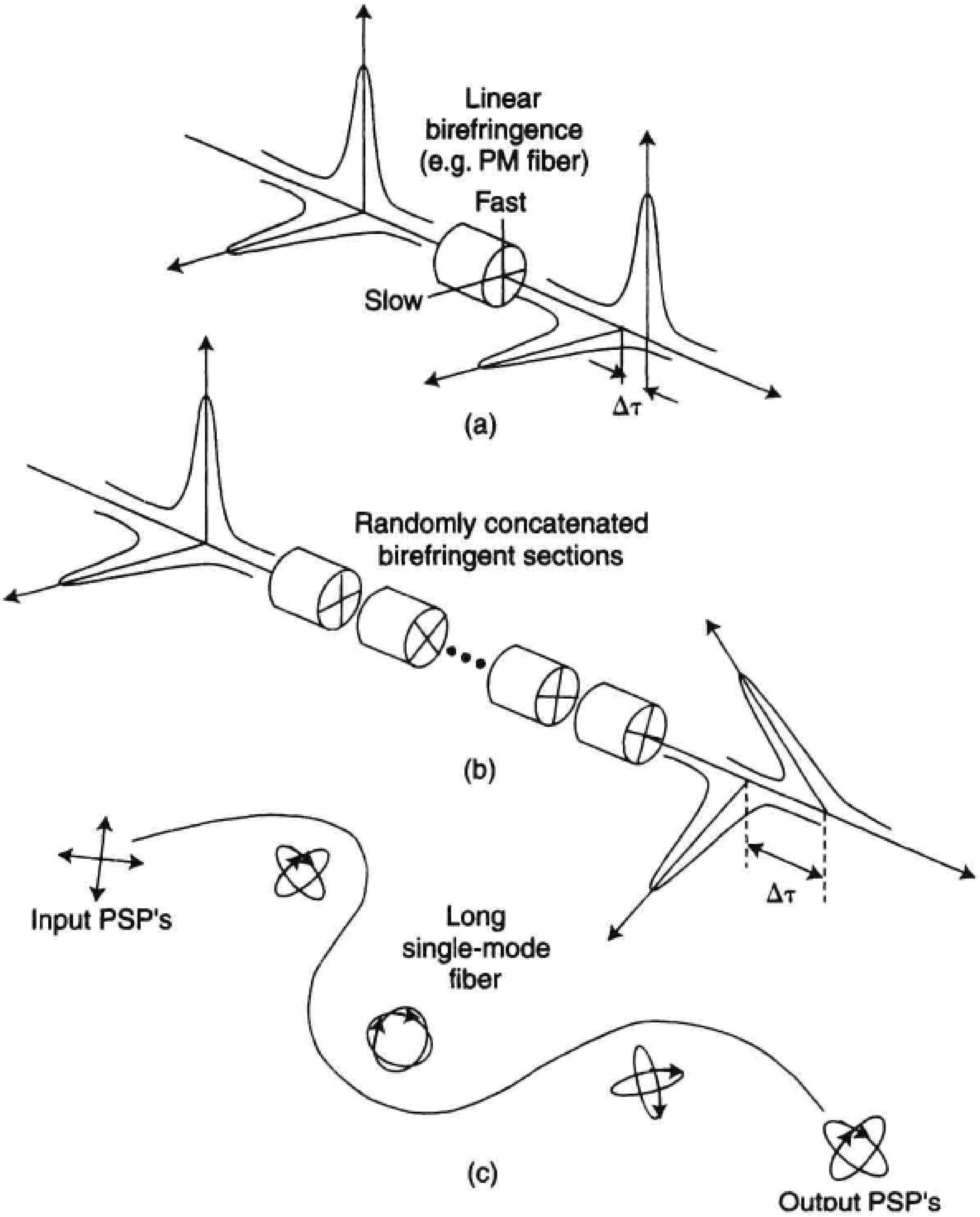

Figure 12.10 Conceptual model of PMD. (a) A simple birefringent device. (b) Randomly concatenated birefringences. (c) Input and output principal states of polarization.

in itself a significant cause of PMD, although by modifying the extent of mode coupling along a fiber, it can cause a difference in measured PMD between spooled, cabled, and installed fiber.[17]

12.4.3 Mode Coupling and the Principal States of Polarization

The birefringence of singlemode fiber varies along its length, an artifact of variation in the drawing and cabling processes. A detailed statistical model of PMD has been developed from the basis of accumulated local birefringences, and has been experimentally confirmed.[18–20] A long fiber is represented in Figure 12.10b as a series of random length, birefringent segments of random rotations. Each segment exhibits fast and slow polarization modes, generally with some of the signal light propagating in each. The electric field emerging from each segment is projected onto the polarization modes of the following segment, a process called mode coupling. It is repeated many times along a fiber span or communication link, and it is this mechanism that causes the differential group delay of most installed fiber systems to show a dependence upon wavelength and upon environmental conditions.

Fastest and slowest propagation through a fiber span can be related to orthogonal input polarization states particular to the fiber span and the environmental conditions. These relationships are most easily described using the Poincaré sphere. In general, the output polarization of an optical component or fiber will trace out an irregular path on the Poincaré sphere as wavelength is changed.[21] Over a small wavelength interval, any portion of this path can be represented as an arc of a circle. The center of the circle, projected normal to the plane of the circle to the surfaces of the sphere, locates two states that are diametrically opposed and therefore orthogonal. These states are called the principal states of polarization.[13] The defining characteristic of the principal states is that over a narrow wavelength interval, they locate the axis of the sphere about which the output state of polarization rotates as wavelength is changed. Figure 12.11 shows two examples. In the

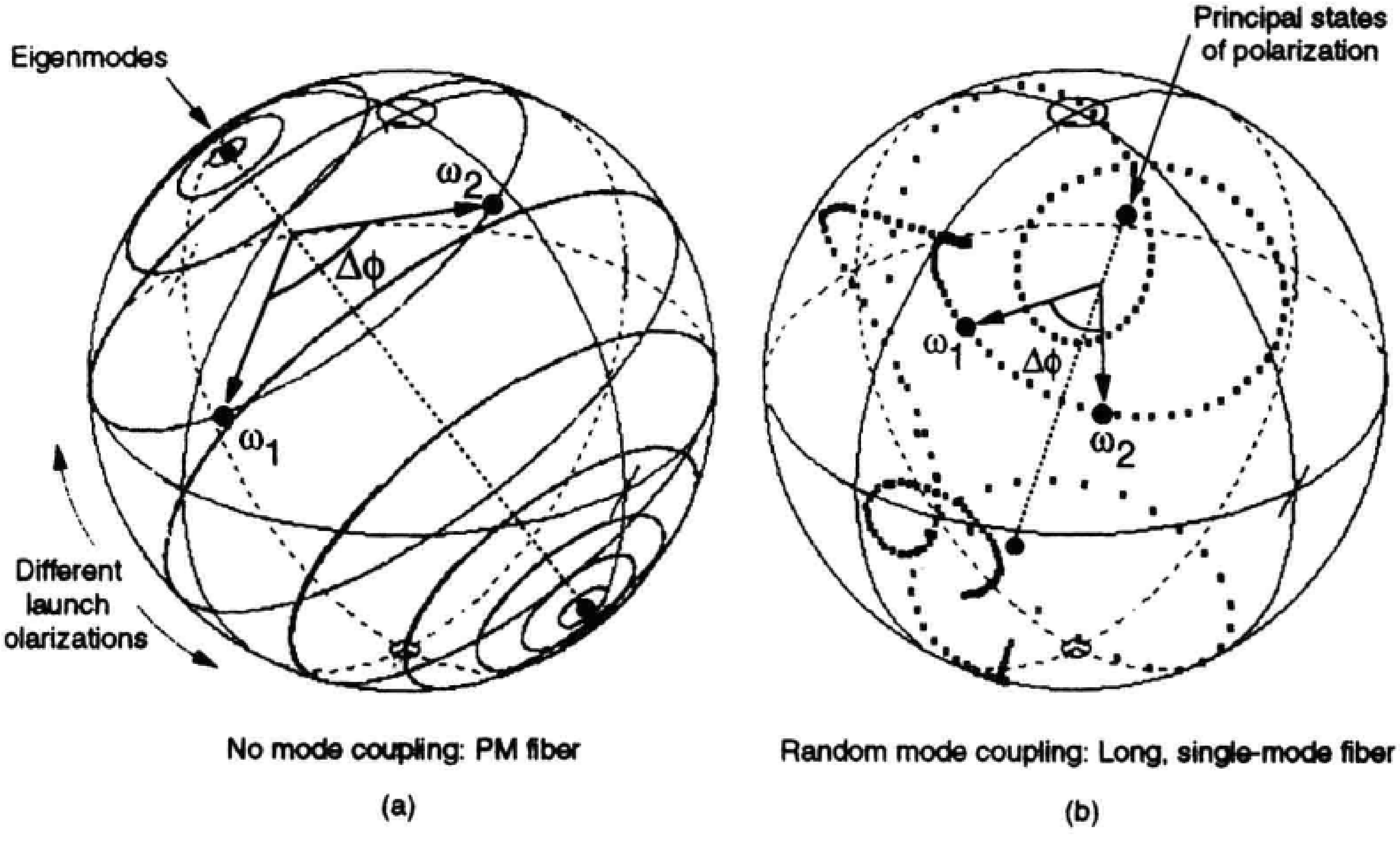

Figure 12.11 Variation of output polarization with wavelength. (a) Simple birefringent device; no mode coupling. (b) Long singlemode fiber; random mode coupling.

absence of mode coupling, the typical case for optical components, the principal states are fixed; as wavelength changes, the output state of polarization orbits regularly around the principal states axis of the sphere as shown in Figure 12.11a. In the general case of long, singlemode fiber paths, the principal states move randomly about the sphere as a function of wavelength, as shown in Figure 12.11b, and can be considered fixed only over narrow wavelength intervals.

A rigorous description of the PMD of a particular fiber at a given time requires specification of both the differential group delay and the principal states as functions of wavelength. Although only the mean or rms differential group delay is actually specified for commercial applications, the behavior of the principal states is of great interest to researchers and cable manufacturers.

12.4.4 Definitions and Relationships

The term PMD is used to denote the physical phenomenon in general and the mean, or expected, value of the differential group delay in particular. The attributes that define PMD are the differential group delay $\Delta\tau(\lambda)$ and the principal states of polarization $PSP_{1,2}(\lambda)$. Both are generally functions of wavelength in singlemode fiber systems. The principal states exist in orthogonal pairs. Some of the more common PMD terminology is defined in Table 12.2.

For a given transmission path, the difference in propagation time experienced by the two polarization modes at a given wavelength is called the differential group delay (DGD) $\Delta\tau_g$, or simply $\Delta\tau$. In fibers that exhibit random coupling, PMD scales with the square root of fiber length. For minimal effect on the eye diagram in an intensity-modulated NRZ system, the mean value of PMD should be kept below one-tenth of a bit period, or 10 ps for a 10 Gb/s system. To put PMD in perspective, components for such a system may exhibit only tenths of picoseconds of differential group delay, and fiber may be limited to a few tenths of picoseconds per root kilometer. In a system with N individual sources of PMD, the total PMD can be estimated from the following relation:

Table 12.2 Definitions for Polarization-Mode Dispersion.

Attribute	Units	Definition
$PSP_{1,2}(\lambda)$—Principal states of polarization	(Diametrically opposed points on the Poincaré sphere.)	Orthogonal polarization states corresponding to fastest and slowest propagation.
$\Delta\tau_g$ (or $\Delta\tau$)—Differential group delay	ps	The difference in propagation time between the principal states.
$<\Delta\tau>$, $<\Delta\tau>_\lambda$, $<\Delta\tau>_t$	ps	Mean value of DGD; over wavelength, time. Also called the expected value.
$[\Delta\tau]/\sqrt{L}$	ps/$\sqrt{\text{km}}$	PMD coefficient; the "PMD" of randomly mode-coupled fiber

$$\text{Mean total DGD} \approx \sqrt{<\Delta\tau_1>^2 + <\Delta\tau_2>^2 + \ldots + <\Delta\tau_N>^2}. \quad (12.15)$$

A powerful and intuitively meaningful representation of PMD, defined in the same real, three-dimensional space as the Poincaré sphere, is provided by the polarization dispersion vector[22] $\mathbf{\Omega}$, illustrated in Figure 12.12. This vector originates at the center of the Poincaré sphere and points toward the principal state of polarization about which the output states of polarization rotate in a counterclockwise sense with increasing optical frequency ω.

The length of $\mathbf{\Omega}$, or $|\mathbf{\Omega}|$, is the differential group delay. When the output state of polarization is expressed as a three-dimensional vector **s** composed of normalized Stokes parameters locating the state of polarization on the sphere, the rotation about the principal states of polarization axis can be written as a cross product relation:

$$\frac{d\mathbf{s}}{d\omega} = \mathbf{\Omega} \times \mathbf{s}. \quad (12.16)$$

In the most general case, typical for spans of singlemode fiber, $\mathbf{\Omega}$ is a function of optical frequency.

The rate of rotation of the output state of polarization about the principal states axis is a measure of the differential group delay of the device. This is true regardless of the degree of mode coupling, although in highly mode-coupled devices the relationship must be evaluated over wavelength increments small enough that the principal state remains fixed. Differential group delay is given by

$$\Delta\tau = \frac{\Delta\theta}{\Delta\omega} \quad (12.17)$$

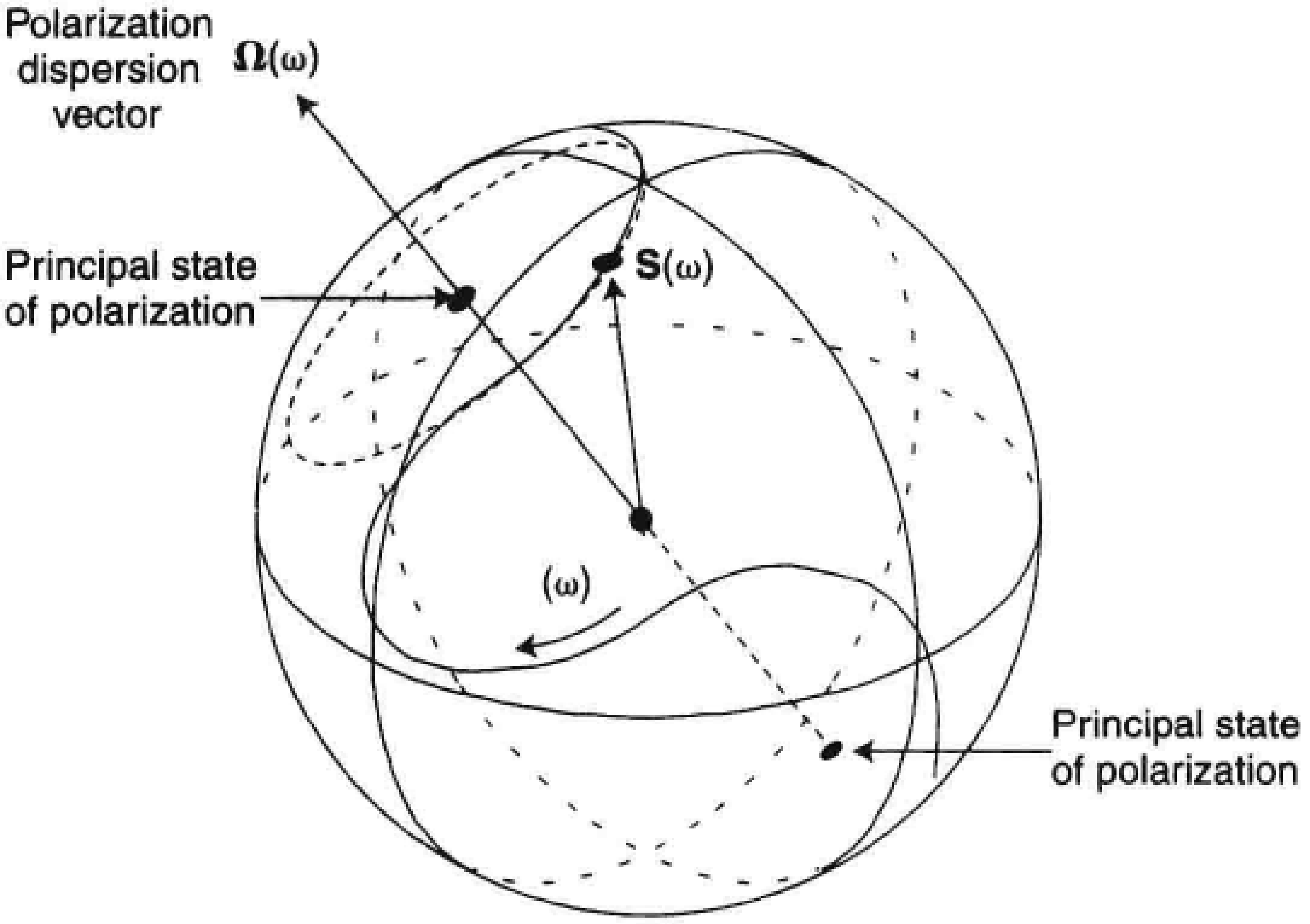

Figure 12.12 Dispersion vector representation of PMD.

where $\Delta\tau$ is the differential group delay in seconds, $\Delta\theta$ is the rotation about the principal states axis in radians, and $\Delta\omega$ is the optical frequency change that produced the arc, in radians/seconds. This relationship is a key element of the principal states model and the basis of a number of PMD measurement methods, most directly the Poincaré arc method described in Section 12.4.10 and shown in Figure 12.22.

12.4.5 Statistical Characterization of PMD in Mode-Coupled Fiber

The designers of undersea telecommunications systems predict the impact of PMD from the distribution of $\Delta\tau$, the differential group delay; it is this parameter which determines pulse broadening. We have discussed the variability of $\Delta\tau$ as a function of wavelength and the environmental conditions. It has been shown that in the random mode-coupled or "long fiber" regime, $\Delta\tau$ follows a Maxwell distribution.[14] That is, the distribution of values of $\Delta\tau$ measured over a wide wavelength range will be Maxwellian. The same distribution will result over time at a fixed wavelength, if the path is acted upon by a changing environment. As a result of this variability, the PMD of a path is expressed statistically, as either the mean or the rms differential group delay, related by

$$<\Delta\tau^2>^{1/2} = \sqrt{\frac{3\pi}{8}} <\Delta\tau> . \tag{12.18}$$

It is interesting to note the relationship of the Maxwell distribution to the dispersion vector $\mathbf{\Omega}$ discussed earlier. At a given wavelength, the direction of $\mathbf{\Omega}$ locates the principal states of polarization on the sphere's surface, and its length gives the magnitude of the differential group delay. The dispersion vector can be decomposed into three orthogonal vectors along the axes of the sphere. Because each of these components stems from cascaded, random birefringences, each is a normal independent random variable with zero mean and can be described statistically by the Gaussian distribution, of the form

$$f(x) = \frac{1}{\sqrt{2\pi\sigma^2}} e^{\frac{-x}{2\sigma^2}} \tag{12.19}$$

The magnitude of the polarization dispersion vector is given by the square root of the sum of the squares of the orthogonal components. As it happens, the square root of the sum of the squares of three normal, independent random variables with zero mean is described by the Maxwellian distribution, given by

$$f(x) = \frac{1}{\sqrt{2\pi\alpha^2}} e^{\frac{-x}{2\alpha^2}} \tag{12.20}$$

The shape of Gaussian and Maxwell distributions are shown in Figure 12.13. The rms and mean values of the Maxwellian data set are given by

$$\text{rms:} \quad \sqrt{3}\,\alpha \qquad \text{mean:} \sqrt{\frac{8}{\pi}}\,\alpha. \tag{12.21}$$

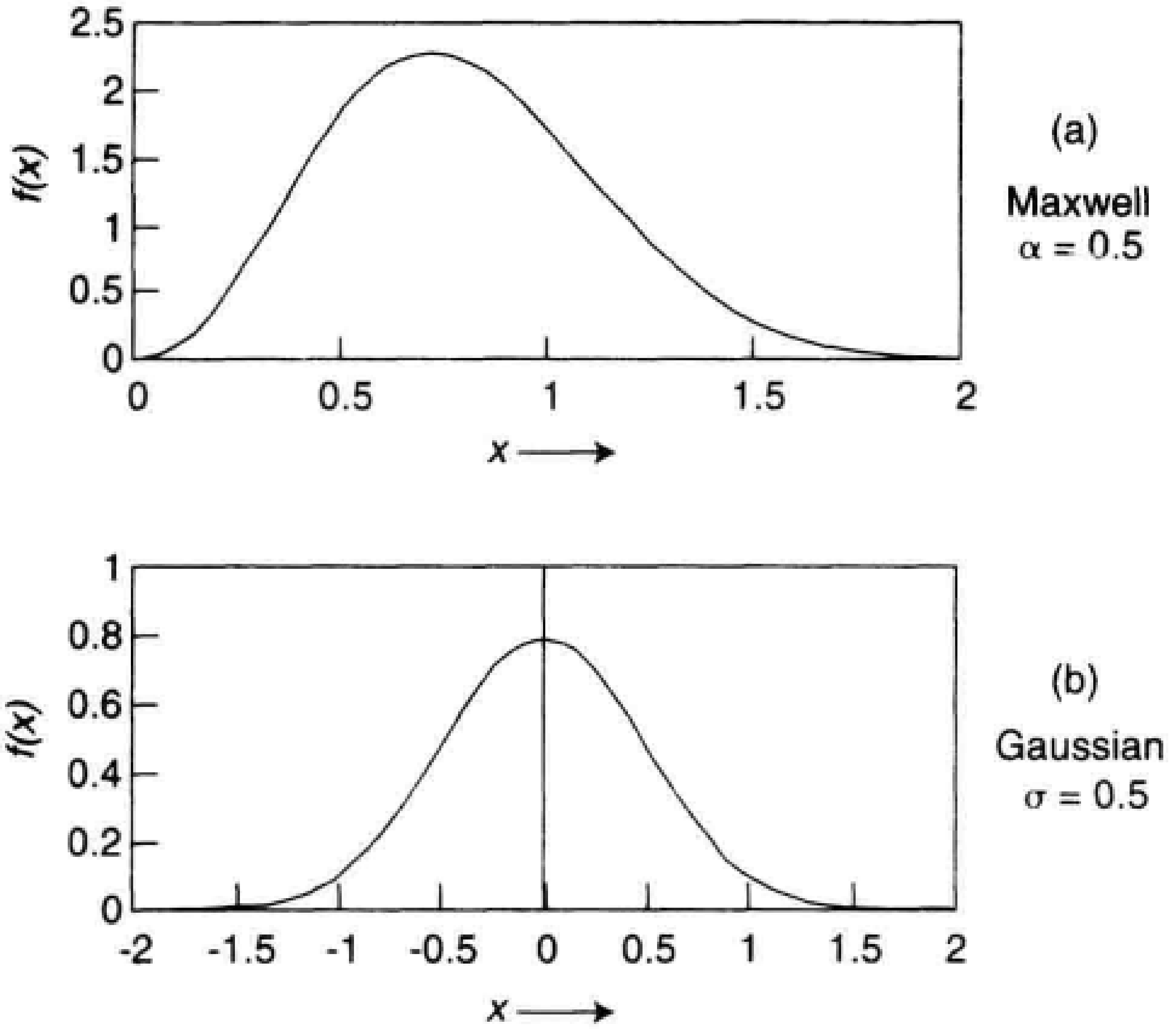

(a)
Maxwell
$\alpha = 0.5$

(b)
Gaussian
$\sigma = 0.5$

Figure 12.13 Gaussian and Maxwell distributions.

12.4.6 A Brief Summary of PMD Measurement Methods

The PMD problem has inspired the development of many measurement methods, most of which are summarized in Table 12.3.

The following discussion will focus on the first six methods. The first three are in wide commercial use. The Poincaré arc, or SOP (for state of polarization) method will be of interest to owners of polarimeters and has been submitted for standardization. The modulation phase-shift method is a useful application of a lightwave component analyzer or a network analyzer with electrical-to-optical and optical-to-electrical transducers. The pulse delay method is discussed for the insight that it offers into the phenomenon of PMD.

12.4.7 The Fixed-Analyzer Method

In the fixed analyzer PMD measurement method,[23] the mean differential group delay is determined statistically from the number of peaks and valleys in the optical power transmission through a polarizer as wavelength is scanned.[24,25] A polarizer placed directly before a detector is referred to as an "analyzer," hence the name of the method (it is also referred to as the wavelength-scanning method).

The output state of polarization of fibers and fiber optic devices generally trace out paths on the Poincaré sphere as wavelength is changed. In the case of components that exhibit simple birefringence, the path is a circle described by a ray sweeping about the principal states axis, as shown in Figure 12.11a. The diameter of the circle depends upon the balance of energy in the principal states of polarization. The circle collapses to a point at the principal states. In contrast, the output polarization of randomly mode-coupled, singlemode fibers moves irregularly about the sphere, reflecting the wavelength dependence of both the principal states and the differential group delay. This case is shown in Figure 12.11b.

Table 12.3 A Sampling of PMD Measurement Methods.

Method	Determines differential group delay from . . .
Fixed analyzer[23] (also called wavelength scanning)	. . . the random evolution of the output state of polarization as wavelength is scanned.
Jones matrix eigenanalysis[28]	. . . the change in the Jones matrix across wavelength intervals.
Interferometry[34]	. . . an interferogram obtained by placing device in low-coherence interferometer.
Poincaré arc (also called SOP)	. . . the rate of rotation of the output state of polarization about the principal states axis.
Modulation phase shift	. . . the phase change of an intensity modulation envelope between the two principal states.
Pulse delay	. . . a sampling scope measurement of the difference in time of flight between pulses in the two principal states.
Baseband curve fit	. . . a mathematical model in which a curve is fit to the microwave AM response of the fiber.

Although the variation of output polarization in the case of randomly mode-coupled fibers is erratic, at any particular wavelength, a pair of principle states of polarization exist that describe a sphere diameter about which the output polarization will rotate over a sufficiently small wavelength scan. As pointed out in the discussion of the dispersion vector, differential group delay $\Delta\tau$ can be calculated from the relation

$$\Delta\tau = \frac{\Delta\theta}{\Delta\omega} \tag{12.22}$$

where $\Delta\theta$ is the radian angle of the arc and $\Delta\omega$ is the incremental change in radian optical frequency that produced the arc. The radius of the arc does not figure into the calculation. Repeating this measurement at a series of wavelengths yields $\Delta\tau(\lambda)$, the differential group delay as a function of wavelength (this technique, a valid way of measuring PMD, will be discussed later in the chapter). Intuitively, the fixed analyzer method employs this same principle. It determines rate of rotation from the number of peaks and valleys in the transmission through a polarizer over a relatively large wavelength scan. It accounts for the movement of the principal states with a well-understood correction factor.

Measurement Setup and Process. Several alternative hardware configurations of the fixed analyzer method are shown in Figure 12.14 (polarimetric detection is shown in Figure 12.16). The setups differ in the type of light source and the means of defining spectral width and tuning the wavelength.

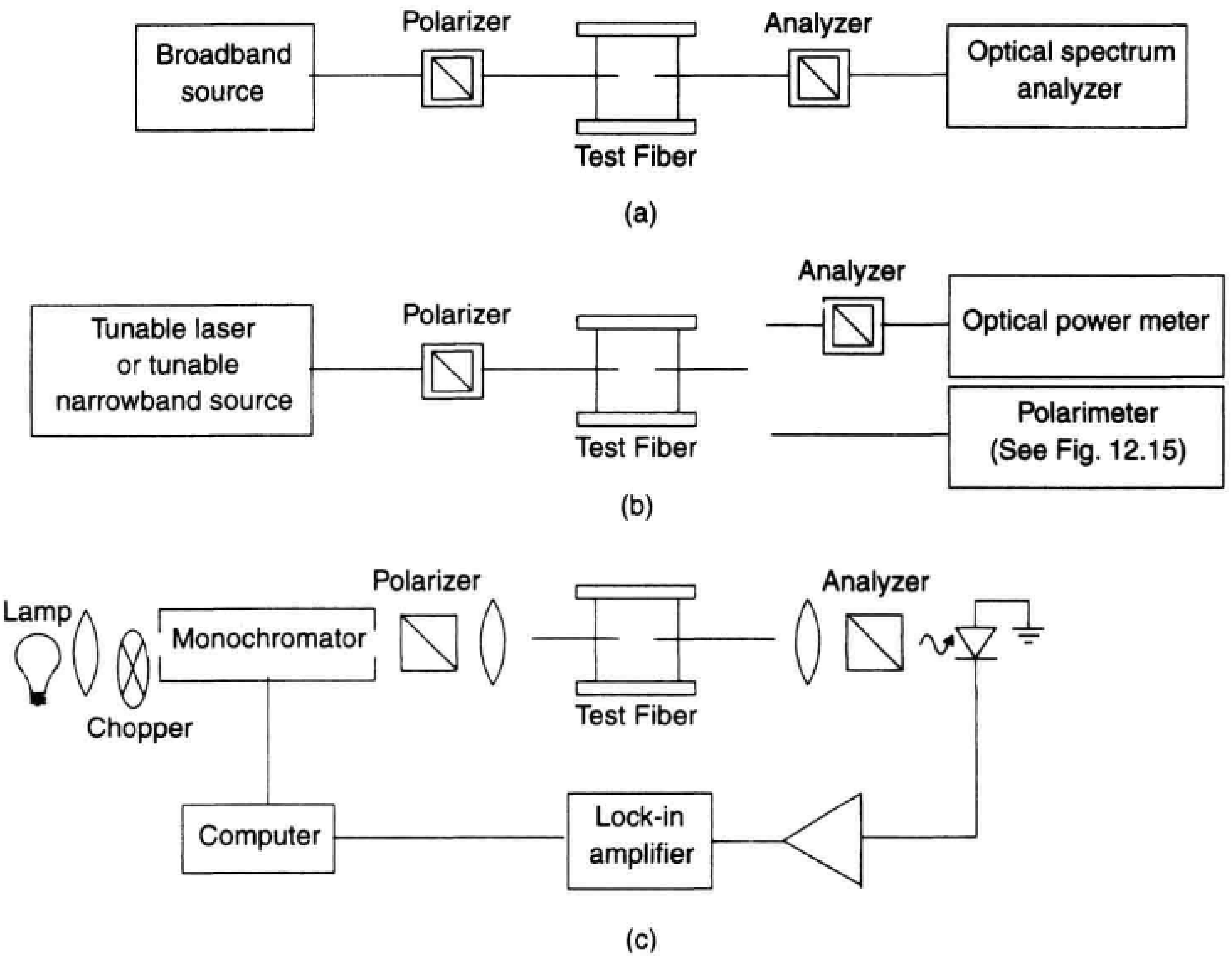

Figure 12.14 Alternative setups for the fixed analyzer PMD measurement.

A typical fixed-analyzer response is shown in Figure 12.15. To allow for adequate resolution of the features of the response, the spectral resolution of the setup should satisfy the requirement[23]

$$\frac{\Delta\lambda}{\lambda} < \frac{1}{8\,\upsilon\,\Delta\tau} \tag{12.23}$$

where $\Delta\lambda$ is the spectral width of the source or the resolution bandwidth of the receiver, λ is the nominal measurement wavelength, υ is the optical frequency in Hz and $\Delta\tau$ is the differential group delay of the test device in seconds. Wavelengths are in meters. In the region of 1550 nm, the requirement is approximated by

$$\Delta\lambda(\mathrm{nm}) < \frac{1}{\Delta\tau(\mathrm{ps})}\,. \tag{12.24}$$

Measurement data is collected while sweeping or stepping the wavelength of the source (or receiver, depending upon the setup). Typically, a reference measurement is taken with

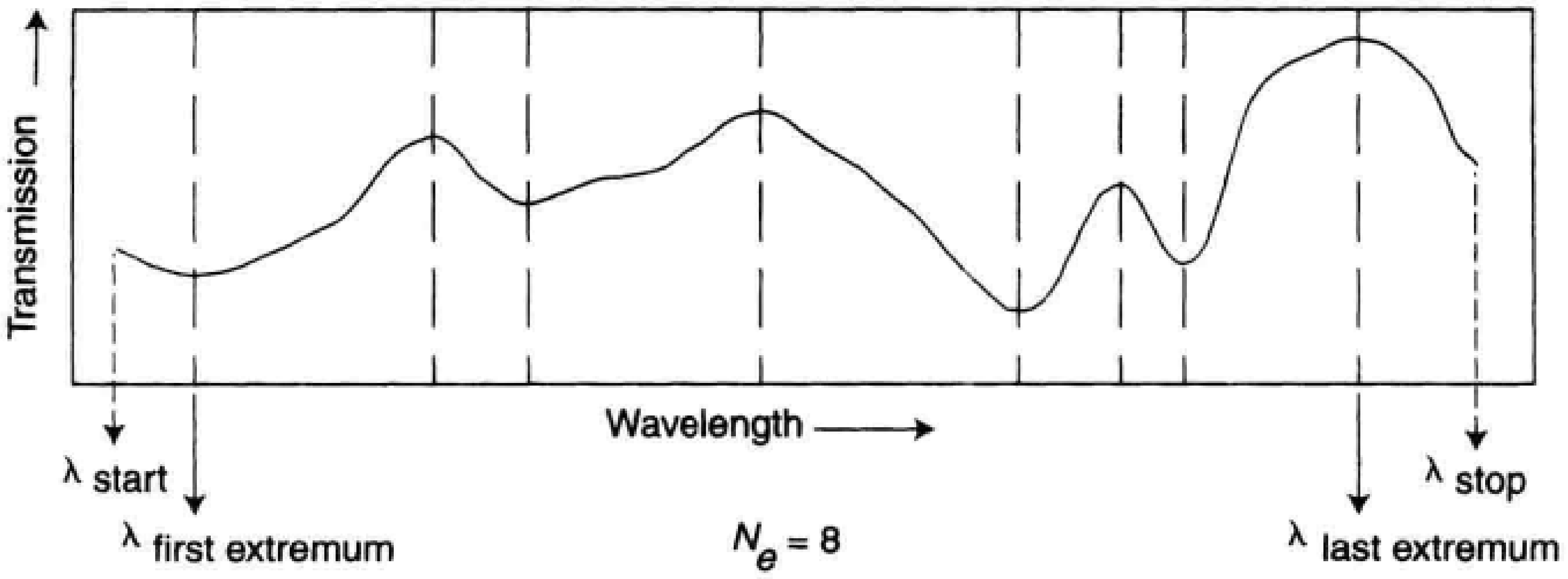

Figure 12.15 A typical fixed analyzer PMD measurement response.

the analyzer removed for correction of the actual measurement for the dependence of source power and device insertion loss upon wavelength. Alternatively, the reference measurement can be made with the analyzer rotated 90 degrees. A typical corrected measurement is shown in Figure 12.15.

Analysis of the Fixed Analyzer Response by Extrema Counting. An automatic means is generally used to extract the PMD information from the resulting measurement trace. The methods generally used are extrema counting and Fourier analysis. The mean differential group delay $<\Delta\tau>$ of the test device can be determined by extrema counting from[23]

$$<\Delta\tau>_\lambda = \frac{k\,N_e\,\lambda_{\text{start}}\,\lambda_{\text{stop}}}{2(\lambda_{\text{stop}} - \lambda_{\text{start}})c} \tag{12.25}$$

where λ_{start} and λ_{stop} are the ends of the wavelength sweep in meters, N_e represents the number of transmission extrema (peaks and valleys) that occur across the scan, and c is the speed of light. The unitless factor k statistically accounts for the effects of the wavelength dependence of the principal states of polarization. It is called the mode-coupling factor and its value is 0.824 for randomly mode-coupled fibers and 1.0 for nonmode-coupled fibers and devices.[25] The λ subscript of the expected value $<\Delta\tau>$ indicates that the quantity is determined over a wavelength span.

An alternative form of Equation 12.25 replaces the start and stop wavelengths of the span with the wavelengths of the first and last extremum, respectively. Note that the number of extrema is reduced by one count to account for the change in wavelength endpoints.

$$<\Delta\tau>_\lambda = \frac{(N_e - 1)\,k\,\lambda_{\text{first extremum}}\,\lambda_{\text{last extremum}}}{2(\lambda_{\text{last extremum}} - \lambda_{\text{first extremum}})c} \tag{12.26}$$

When the number of extrema is large, the difference in mean differential group delay resulting from the two equations is small. However, many users prefer to let the test device determine the analysis wavelengths. This point is easier to see when we realize that the start and stop wavelengths can generally be changed up or down to some degree without changing the number of extrema.

If the test device shows no mode coupling, the analysis is based upon the first and last extremum and the mode coupling factor is set to unity.

$$\Delta\tau = \frac{(N_e - 1)\,\lambda_{\text{first extremum}}\,\lambda_{\text{last extremum}}}{2\,(\lambda_{\text{last extremum}} - \lambda_{\text{first extremum}})c} \tag{12.27}$$

This formula should be used for measurements of polarization maintaining fiber and optical components such as isolators and waveplates.

False peaks and valleys can be caused by wavelength dependence of the optical source output power or the test path insertion loss. A reference measurement is generally needed. If the optical power is repeatable over wavelength, false peaks can be avoided by ratioing the measurement to a second scan performed with the output analyzer removed. Alternatively, the second scan may be taken with the output analyzer rotated 90 degrees. Note that these precautions do not correct for short-term fluctuations of optical source level or optical coupling. Polarimetric detection, discussed in a following section, is insensitive to these power variations.

The wavelength range over which the fixed analyzer PMD measurement is performed should be great enough to produce a statistically significant number of extrema. For optical components without mode coupling, a basic measurement can be based on a single cycle of amplitude change, or even a single peak and valley pair. Near 1550 nm, the wavelength change required to span two peaks in the fixed analyzer response for a component, such as an optical isolator, is approximated by

$$\Delta\lambda_{\text{between peaks}}\,(\text{nm}) = \frac{7.8\,(\text{ps-nm})}{\Delta\tau\,(\text{ps})} \tag{12.28}$$

A component with 1 ps average differential group-delay produces peaks which are spaced an average of 7.8 nm apart. For random mode-coupled devices, the relationship is

$$\Delta\lambda_{\text{between peaks, average}}\,(\text{nm}) = \frac{6.5\,(\text{ps-nm})}{\Delta\tau\,(\text{ps})} \tag{12.29}$$

A 70 km fiber with 0.08 ps per root kilometer has an average differential group delay of 0.669 ps, requiring a scan width of 97 nm to produce approximately 10 cycles of wavelength scanning response. In singlemode fiber measurements, accuracy improves as the cycle count increases, although it may not be cost effective to extend the measurement beyond 10 or 20 cycles.

In the case of singlemode fiber, some variation in the measured PMD will occur over different launch polarizations. This is unavoidable, but a more central value can be obtained by repeating the measurement with different orientations of the input and output polarizers, or with a different lay of the input and output pigtails of the test device. Polarimetric detection, discussed later, reduces the effect of launch state and eliminates the effect of output polarizer orientation. In the case of optical components, the number of extrema is generally stable with polarizer orientation but it may be necessary to adjust the polarizers to obtain good interference between light in the two polarization modes.

Polarimetric Detection of the Output Polarization. In the fixed analyzer method, variation of the output state of polarization with wavelength is determined from the transmission through a fixed polarizer, called an analyzer in this application. Viewed in terms of the Poincaré sphere, the analyzer can be represented as a single point on the sphere. Each closest approach of the output state of polarization to this point corresponds to a peak in transmission through the analyzer.

Detection of the output polarization with a fast polarimeter, as shown in Figure 12.16, provides several advantages over the use of a single analyzer. (See Chapter 6 for a discussion of polarimeters.) The three normalized Stokes parameter traces provide a full description of output polarization over wavelength. Each trace is analyzed by extrema counting or Fourier analysis, and the resulting three mean differential group delays are av-

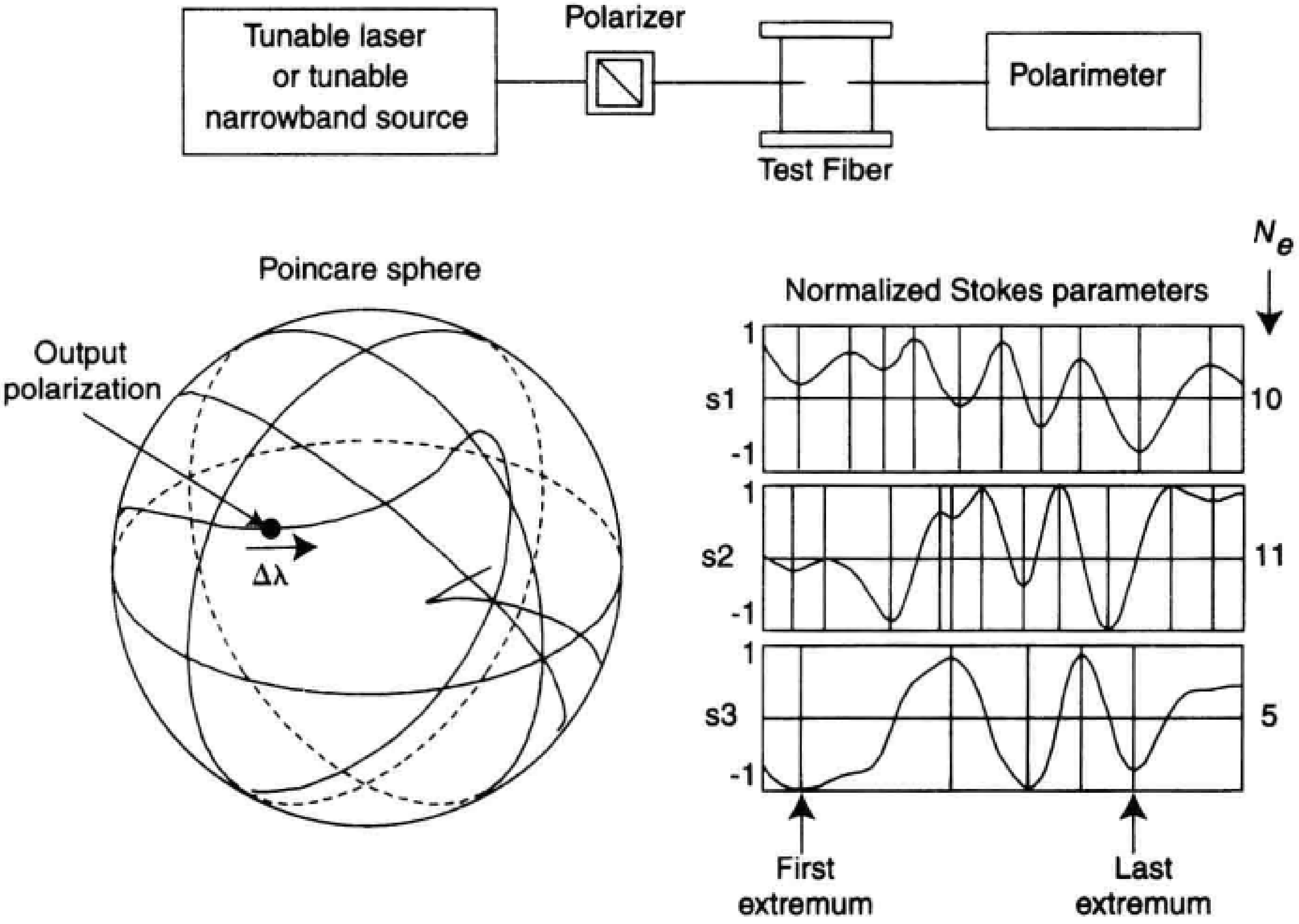

Figure 12.16 Fixed analyzer measurement of PMD using a polarimeter.

eraged. As a result of this completeness, fixed analyzer measurements taken with the polarimeter are less dependent upon launch polarization and less affected by the positions of the pigtails. A second advantage of polarimetric detection is that the normalized Stokes parameters are immune to changes of optical power. A reference or calibration measurement scan is not required and the absolute power level may vary during the measurement without affecting accuracy. The polarimeter also allows the user to view the output state of polarization on the Poincaré sphere for a sensitive indication of the stability of the test device. This is useful because the fixed analyzer response of a long fiber is sensitive to mechanical movement and temperature.

Fourier Analysis of the Fixed Analyzer Response. Analysis of the fixed analyzer response can be shifted to the time domain by taking the Fourier transform of the frequency domain data.[23] The resulting spectrum, which is functionally equivalent to the interferometric measurement response shown in Figure 12.21d, is of Gaussian shape in the case of randomly mode-coupled fiber. The value of PMD is determined from the response by fitting a Gaussian to the data, or by the second moment calculation described in Section 12.4.9 in connection with the interferometric method. Evaluation of the fixed analyzer response by Fourier analysis has the advantage of giving a graphical indication of the mode coupling characteristics of the sample. In addition, Fourier analysis allows filtering out high-frequency features, induced by noise or vibration, that would be detected as peaks and valleys by the extrema-counting method of analysis.

Measurement of Short, Low-PMD Fibers. Although fiber is drawn in continuous lengths of tens of kilometers, finished cable products for terrestrial applications are often only a few kilometers in length. Short lengths of fiber exhibit correspondingly small values of differential group delay and require a large wavelength range to produce a significant number of peaks. Short fibers also have low insertion loss, making the white light source or edge-emitting light-emitting diode (EELED) array and optical spectrum analyzer (OSA) or monochromator a reasonable PMD test solution. See Figure 12.14a, c. The broadband light source provides sufficient power and the tunable filter provides adequate wavelength selectivity. The measurement dynamic range achievable with the OSA or monochromator configuration is a function of the bandwidth of the tunable filter. Low-PMD devices typically exhibit very mild wavelength-dependence, allowing the use of larger filter bandwidth for higher signal level.

Measurement of Amplified Systems. The fixed analyzer method is not commonly used to characterize EDFAs for undersea applications because the differential group delay is so low that extremely large wavelength-tuning range is required. However, the method is quite applicable to the measurement of long, multiamplifier systems. The most extreme requirements are posed by transoceanic paths which may contain over 100 amplifiers. The cascading effect reduces system bandwidth to a few nanometers, limiting the span over which the fixed analyzer response can be measured and typically forcing the use of a spectrally narrow optical source or narrow receiver bandwidth. In one approach, an amplified spontaneous emission (ASE) source is polarized and applied to the first amplifier of the chain, driving it and subsequent amplifiers into saturation. The output of the system is measured through a fixed analyzer using a spectrum analyzer. Although the system bandwidth is narrow, there are typically enough peaks to allow an estimate of PMD. The combination of tunable laser source and polarimeter is another effective approach.

The Impact of Movement in the Test Path. Mechanical perturbation of the test path can affect the output polarization, adding spurious peaks and valleys to the fixed analyzer response. The test path includes the DUT and all fiber connecting the device to the instrument. In practice, the fiber path to and from the test device is always moving, if only microscopically. Measurement accuracy suffers when polarization changes caused by the environment are larger than the detection threshold of the instrumentation. It is good practice to constrain the motion of the pigtails that connect the measurement system and the DUT, and to avoid coupling severe mechanical vibrations into the spool of fiber being measured. The stability of the path can be checked by measuring the output polarization for a period of time at a fixed wavelength.

12.4.8 The Jones-Matrix-Eigenanalysis Method

The Jones matrix eigenanalysis (JME) method directly determines the difference in group delay between the principal states of polarization as a function of wavelength.[26] The analysis is based upon measurement of the transmission matrix of the test device at a series of wavelengths. The method can be applied to short and long fibers, regardless of the degree of mode coupling. It is applicable to the measurement of linear, time-invariant devices. The restriction of linearity precludes optical devices that generate new optical frequencies. The restriction of time invariance applies only to the polarization transformation caused by the device, and does not include the absolute optical-phase delay.

In the Jones calculus,[27] a polarized signal is expressed as a Jones vector, a complex, two-element column matrix. The Jones vector completely describes the amplitude and polarization state of the signal. The transmission path is represented by the Jones matrix, a complex two-by-two matrix. Input and output Jones vectors are related by the Jones matrix.

Measurement of the Jones matrix (discussed in Chapter 6) requires the application of three known states of linearly polarized light to the device or fiber under test. In the process described below, linear states oriented at 0, 45, and 90 degrees are used, as described by Jones, although the mathematics may be generalized to other input states. The Jones matrix is computed from the relationship of the measured output states to the known, applied input states. The resulting matrix describes the polarization transforming characteristic of the two-port device to within a complex constant that represents the absolute propagation delay. Absolute delay is not involved in the determination of differential group delay.

Measurement Setup and Process. The measurement setup for the JME method is shown in Figure 12.17. Key elements are a tunable narrowband optical source, a

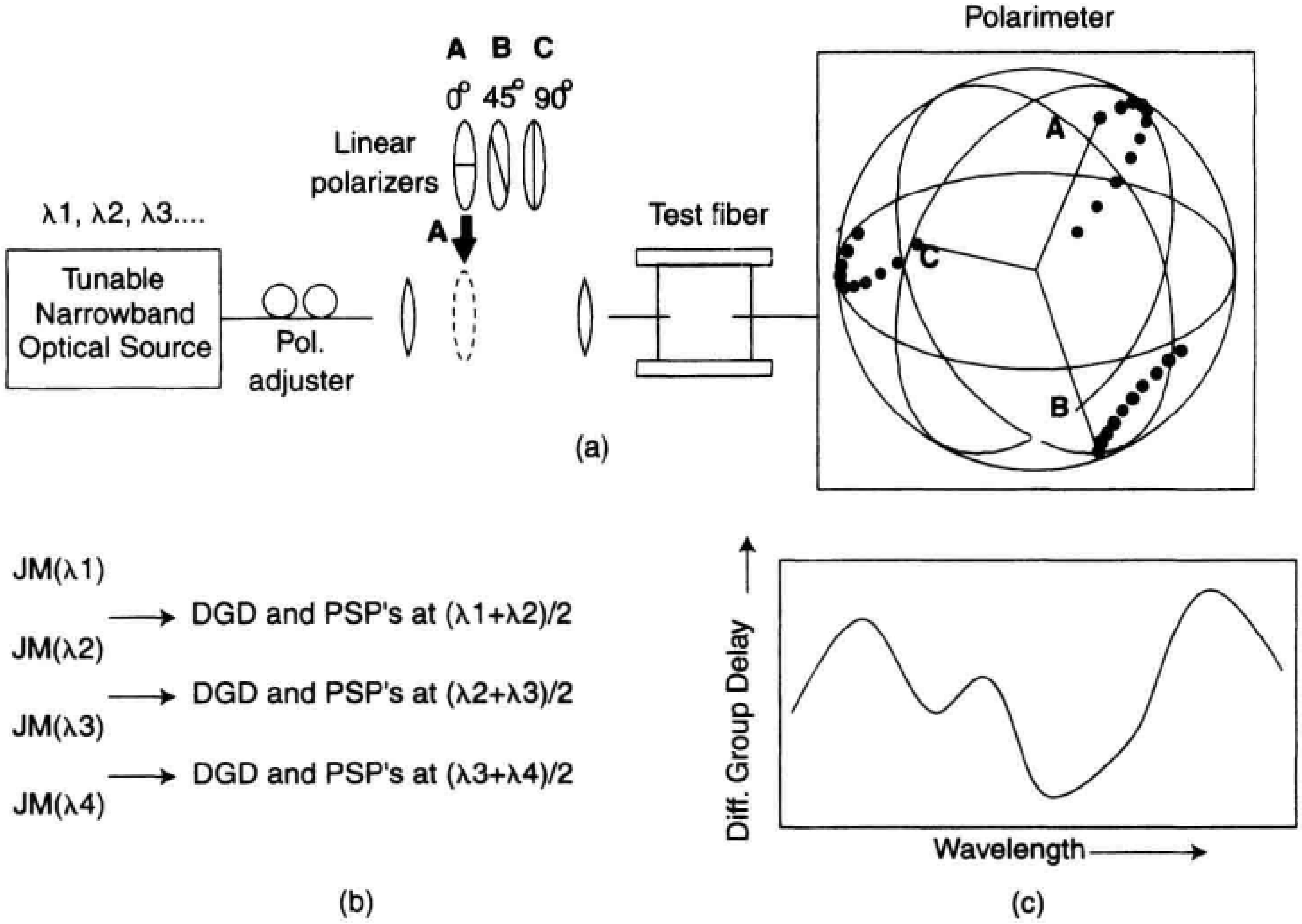

Figure 12.17 PMD measurement by the JME method. (a) Setup. (b) Measured attributes. (c) Differential group delay as a function of wavelength.

switchable polarizer for generating three linear polarization states, a fast polarimeter, and a computer for control of the hardware and processing of measurement results. Source polarization is adjusted to an approximately circular state to allow transmission through each polarizer. The Jones matrix of the path from the polarizers to the polarimeter is measured at a series of discrete wavelengths. A value of differential group delay $\Delta\tau$ at any wavelength λ_i is computed from a pair of Jones matrices measured at two wavelengths equally spaced about λ_i. The resulting series of $\Delta\tau$ values are displayed graphically to reveal the wavelength dependence, and are averaged to find the mean differential group delay $<\Delta\tau>_\lambda$. Fiber pigtails from the polarizer to the device and from the device to the polarimeter typically contribute less than 0.005 ps each to the measurement result.

The optical source used in the JME method must be tunable and sufficiently narrow-band to avoid depolarization by the test device. A tunable external cavity diode laser is commonly used.

Computing the Differential Group Delay. Differential group delay $\Delta\tau$ is computed from a pair of Jones matrices separated by a small wavelength step as follows[26,28]

$$\Delta\tau = |\tau_{g,1} - \tau_{g,2}| = \left| \frac{\operatorname{Arg}\left(\frac{\rho_1}{\rho_2}\right)}{\Delta\omega} \right| , \tag{12.30}$$

where $\tau_{g,1}$ and $\tau_{g,2}$ are the group delays associated with the principal states of polarization, $\Delta\omega$ is the change in optical frequency in rad/s corresponding to the wavelength interval, ρ_1 and ρ_2 are the eigenvalues of the following expression involving the measured Jones matrices **T**:

$$\mathbf{T}(\omega + \Delta\omega)\mathbf{T}^{-1}(\omega) , \tag{12.31}$$

and Arg denotes the argument function where $\operatorname{Arg} \alpha\epsilon^{j\theta} = \theta$. Determination of the differential group delay $\Delta\tau$ does not require knowledge of $\tau_{g,1}$ and $\tau_{g,2}$ individually.

Selecting the Wavelength Range and Wavelength Interval. The accuracy of the JME method is influenced by stray birefringences in the test path, test path stability, optical source incremental wavelength accuracy, polarimeter accuracy, and the repeatability of the stimulus polarizations. Larger wavelength steps generally provide better accuracy. However, in order to unambiguously measure the polarization change produced by the step, the rotation of the output state about the principal states axis on the Poincaré sphere produced by any single wavelength step must not exceed 180 degrees. In the region of 1550 nm, this "alias limit" translates into[28]

$$\Delta\tau(\text{ps})\ \Delta\lambda(\text{nm}) \leq 4.0\ (\text{ps-nm}) \tag{12.32}$$

For example, the maximum differential group delay that is measurable with a 0.1 nm wavelength change at 1550 nm is 40 ps. Very small wavelength steps, less than 0.1 nm or even 0.01 nm, may be required for measuring narrowband devices and devices that have extremely high PMD and/or strong variation of differential group delay with wavelength. In these cases, it may be necessary to improve the wavelength accuracy by adding a wavelength meter (see Chapter 4) to the system.

The effect of wavelength step size on the measurement of a 44 km spool of single-mode fiber is shown in Figure 12.18. Thirteen consecutive measurements were performed across the 1470 to 1570 nm wavelength range using different wavelength intervals. The average differential group delay is nearly independent of wavelength interval over a wide range. All of the curves roll off at the high end as aliasing occurs. Taking the maximum differential group delay to be 1.25 ps, aliasing is expected to occur above 3.2 nm according to Equation 12.32. The increase in the maximum values at low step size is related to laser tuning linearity and the repeatability of the insertable polarizers.

The wavelength range over which the measurement is performed can be selected according to the type of test device. The differential group delay of a broadband component such as an optical isolator is often independent of wavelength and a short series of 1 to 5 nm-steps will produce an accurate measurement. A single step may be sufficient, but a series of steps provides the benefit of averaging. Long, highly mode-coupled fibers, because of the statistical nature of PMD, require a broader wavelength range—typically the

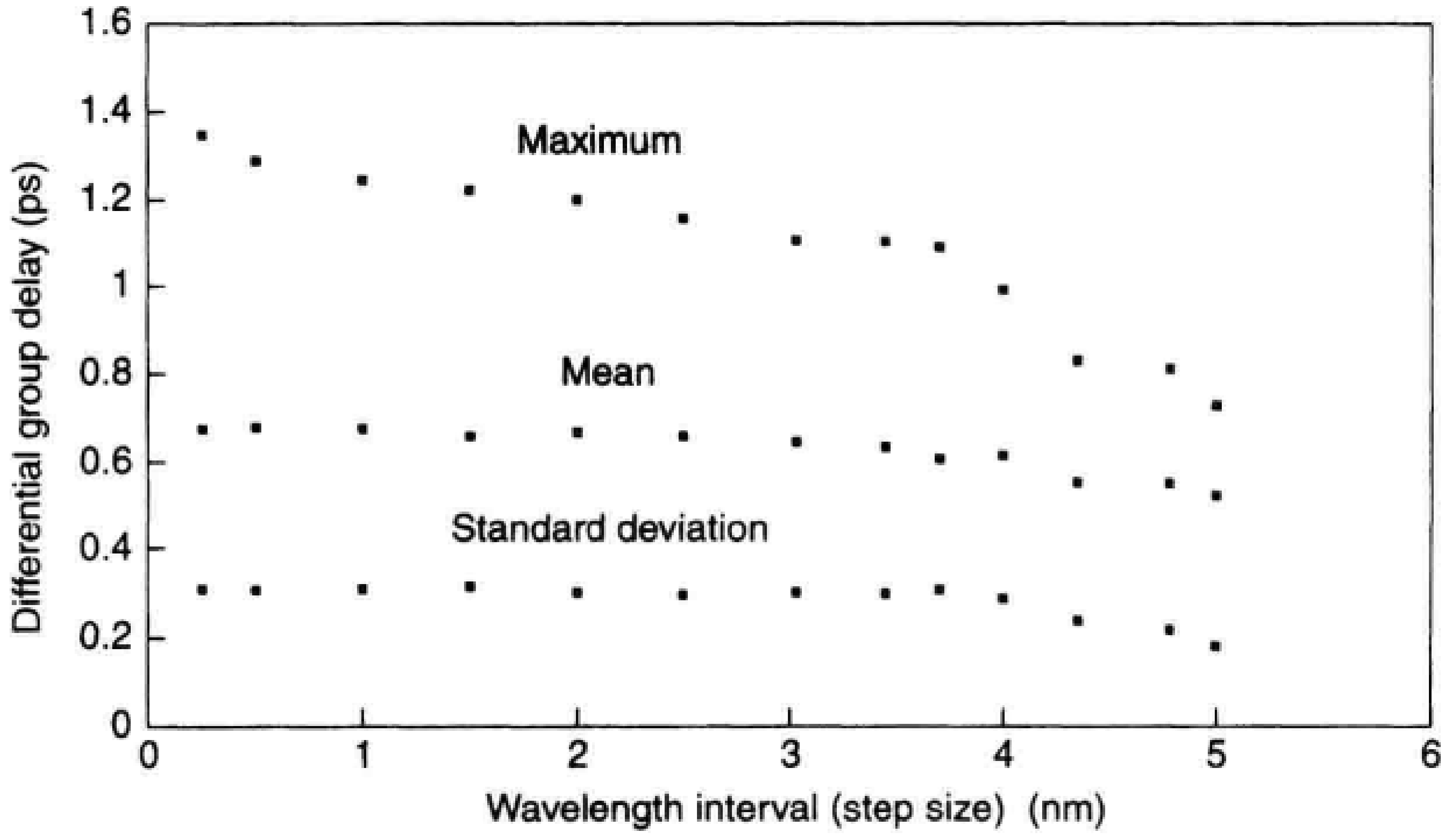

Figure 12.18 JME measurements of the DGD of a randomly mode-coupled fiber, as a function of wavelength step size.

full available tunable laser range—and a step size small enough to reveal the variation of differential group delay with wavelength. Measurement of the PMD of submeter length fibers[29] can be performed using a single step between the wavelengths of 1300 and 1550 nm. For fibers shorter than the mode-coupling length, PMD is not expected to vary significantly over the wavelength range in which the fiber remains singlemode.[17]

Statistical Characterization of Fiber PMD. The JME method is well-suited to measuring the distribution of differential group delay over wavelength, temperature, or time. Differential group delay values from individual wavelength steps of a single measurement can be displayed in a histogram as shown in Figure 12.19a. Comparison of the distribution to an ideal Maxwell distribution indicates the extent to which the variability of differential group delay has been sampled. The Maxwell curve is specified by the single parameter α, which can be determined for a particular data set using the maximum likelihood estimation, defined for an expected Maxwell distribution by[28]

$$\alpha^2 = \frac{1}{3N} \Sigma\, \Delta\tau_i^2 \tag{12.33}$$

where $\Delta\tau_i$ are the differential group delay values measured across N wavelenth intervals. A reasonably complete Maxwellian distribution assures that the fiber is adequately characterized and that the mean or rms values can be computed with good confidence. A poor Maxwell fit may result from measuring the fiber across too narrow a wavelength range, or from measuring a fiber sample that is not randomly mode-coupled. If the measurement

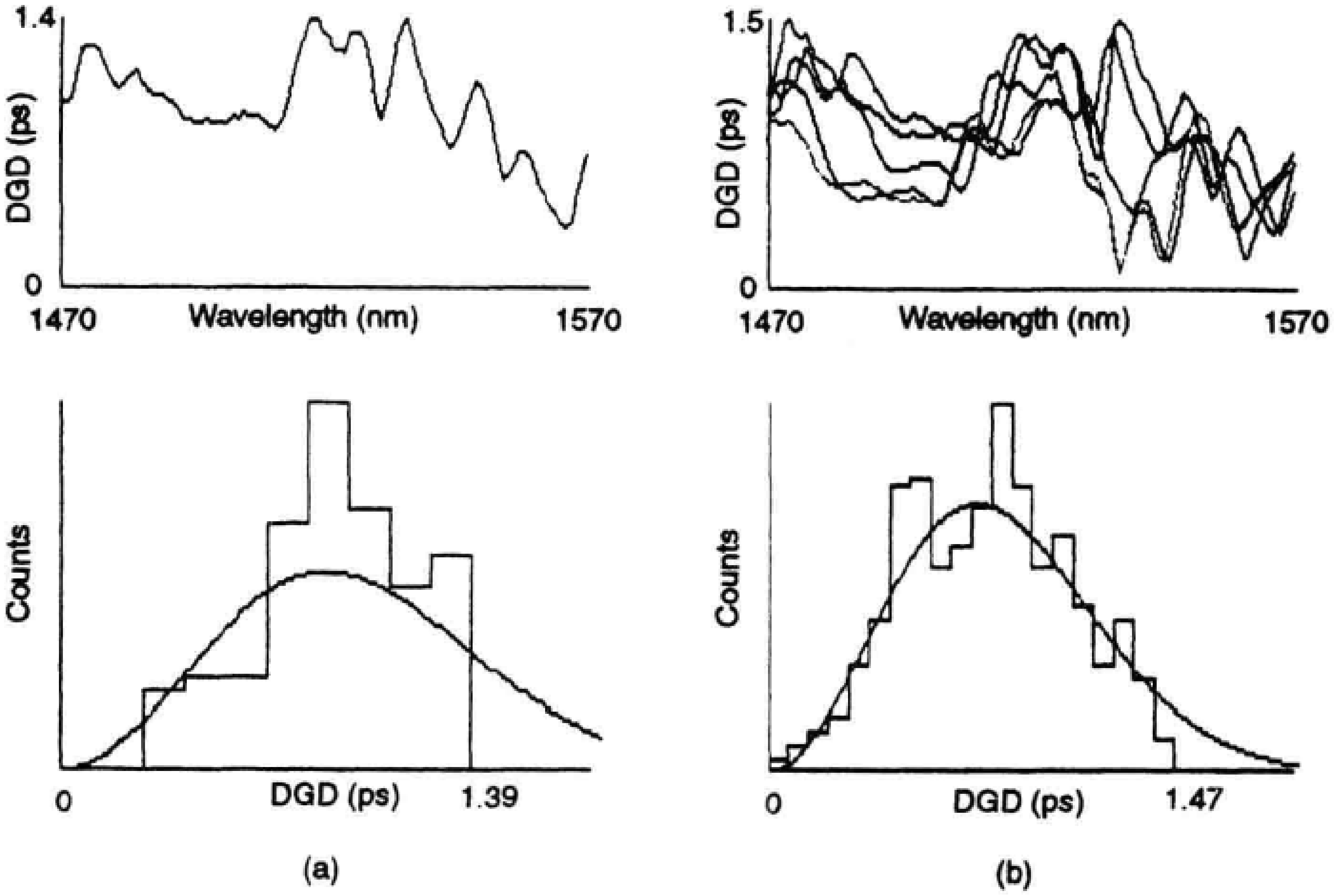

Figure 12.19 Distributions of DGD values from measurement of a 44 km fiber. (a) Single measurement. (b) Multiple measurements at different temperatures.

wavelength range is not sufficient to obtain a good distribution, it may be repeated at a series of temperatures, as shown in Figure 12.19b. For large-scale devices such as large coils of undersea cable, measurements can be made several times during the daily temperature cycle. It is sometimes possible to heat the fibers in a cable by running a current through a central metal wire.

Measurement of Amplifiers and Amplified Systems. The degree of polarization of the output of an EDFA is influenced by the power and degree of polarization of the input signal and the unpolarized SE output of the amplifier. When the signal wavelength does not coincide with the gain peak, the output degree of polarization decreases. The JME method is quite effective in these applications by virtue of the polarimeter's ability to measure the polarized component of a signal. A degree of polarization of 50% or higher produces good results and useable measurements have been performed with as low as 25% degree of polarization. In long telecommunication systems, EDFAs are operated in saturation, generally providing a large enough output signal to maintain better than 90% degree of polarization within the system passband.

The Impact of Movement in the Test Path. The JME method is valid when the PMD-related characteristics of the path under test are time invariant. The test path includes the DUT and all fiber connecting the device to the instrument. In principle, the test path is always moving, if only microscopically. Measurement accuracy suffers only when the movements are large enough to produce an output polarization change that is significant compared to the change produced by the wavelength step. The JME measurement method is particularly vulnerable to movement for test devices with less than 0.1 ps of differential group delay or when measuring with a small wavelength step. It is good practice to constrain the motion of the pigtails that connect the measurement system and the DUT, and to avoid coupling severe mechanical vibrations into the spool of fiber being measured.

The most demanding application of the method, from the standpoint of path movement, is the measurement of suspended or undersea cables. The varying output polarization can be displayed on the Poincaré sphere. If the variation of output polarization observed in the measurement time required for a pair of Jones matrix measurements is small relative to the changes produced by the wavelength interval, the method will yield useful measurements. The curve of differential group delay versus wavelength will be considerably less smooth because of the movement, but the mean value of differential group delay across a wavelength range will be statistically meaningful.

A simple, qualitative experiment was performed in our laboratory to see whether useful measurements could be obtained over a fiber path that is in motion. The DUT was connected to the instrumentation through a 13 m suspended span of unjacketed fiber. The span drooped about 1 m at the center and was caused to sway in a ½ m arc at the midpoint. This movement caused the output polarization state to move in a pattern 3 to 6 degrees peak-to-peak on the Poincaré sphere. Tests were performed over 1500 to 1550 nm with 1 nm step. The measurements shown in Figure 12.20a and b were taken on a component with 0.218 ps differential group delay. Although movement introduced noise, the average differential group delay values were reasonably consistent. In addition, it was found that doubling the wavelength step nearly halved the amplitude of the movement-induced peaks. The component was replaced with a 44 km spool of singlemode fiber to obtain the measurements shown in Figure 12.20c and d. Measurement results showed better agreement in this case because the test fiber's high PMD allowed the wavelength-induced polarization changes to dominate the movement induced changes.

12.4.9 The Interferometric Method

The interferometric PMD measurement method[30,31] is based upon measurement of the electric-field autocorrelation, or mutual coherence, of two signals derived from the same wideband source. Like the pulse delay and differential phase-shift methods, it is based on direct measurement of a time delay. The measurement is illustrated in Figure 12.21. Consider first the basic Michelson interferometer with no test device inserted in the detector path, shown in Figure 12.21a. Light from the broadband LED or white light source is coupled into both arms of the interferometer and light from the moving mirror and fixed mirror arms is superimposed at the detector. Interference occurs when the lengths of the two arms differ by less than the coherence length of the source. Maximum visibility occurs when the path lengths are perfectly matched. The width of the response is inversely proportional to the source spectral width. The amplitude of the photocurrent envelope is dis-

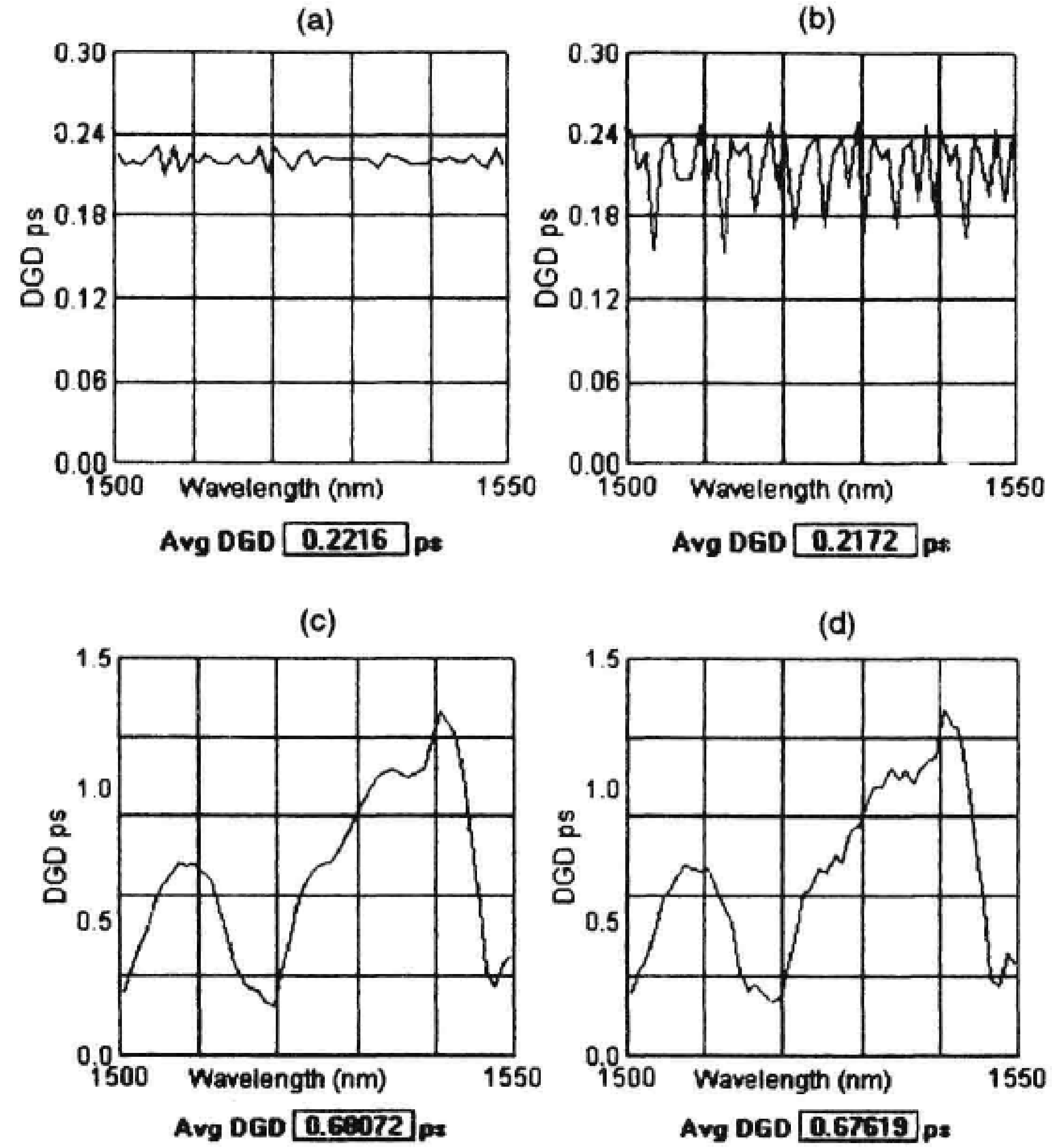

Figure 12.20 The effect of fiber movement on JME PMD measurement results. (a) Isolator, stationary fiber. (b) Isolator, moving fiber. (c) Fiber spool, stationary fiber. (d) Fiber spool, moving fiber.

played as a function of the time delay introduced by the moving mirror. The time delay Δt is given by

$$\Delta t = \frac{2\Delta x}{c} \tag{12.34}$$

where Δx is the distance of the mirror from balance, in other words, from the point where both paths are of equal length. Refer to Chapter 10 for a detailed discussion of this type of interferometry.

A basic interferometric PMD measurement setup requires the addition of polarizers at the optical source and photodetector. The setup shown in Figure 12.21b, although slightly more complex, allows adjustment for maximum visibility of a particular response peak. In this setup, the arms of the interferometer are orthogonally polarized. Mirror movement creates a delay between the orthogonally polarized incident waves. The polarizer before the detector, called an "analyzer" in this application, allows interference by

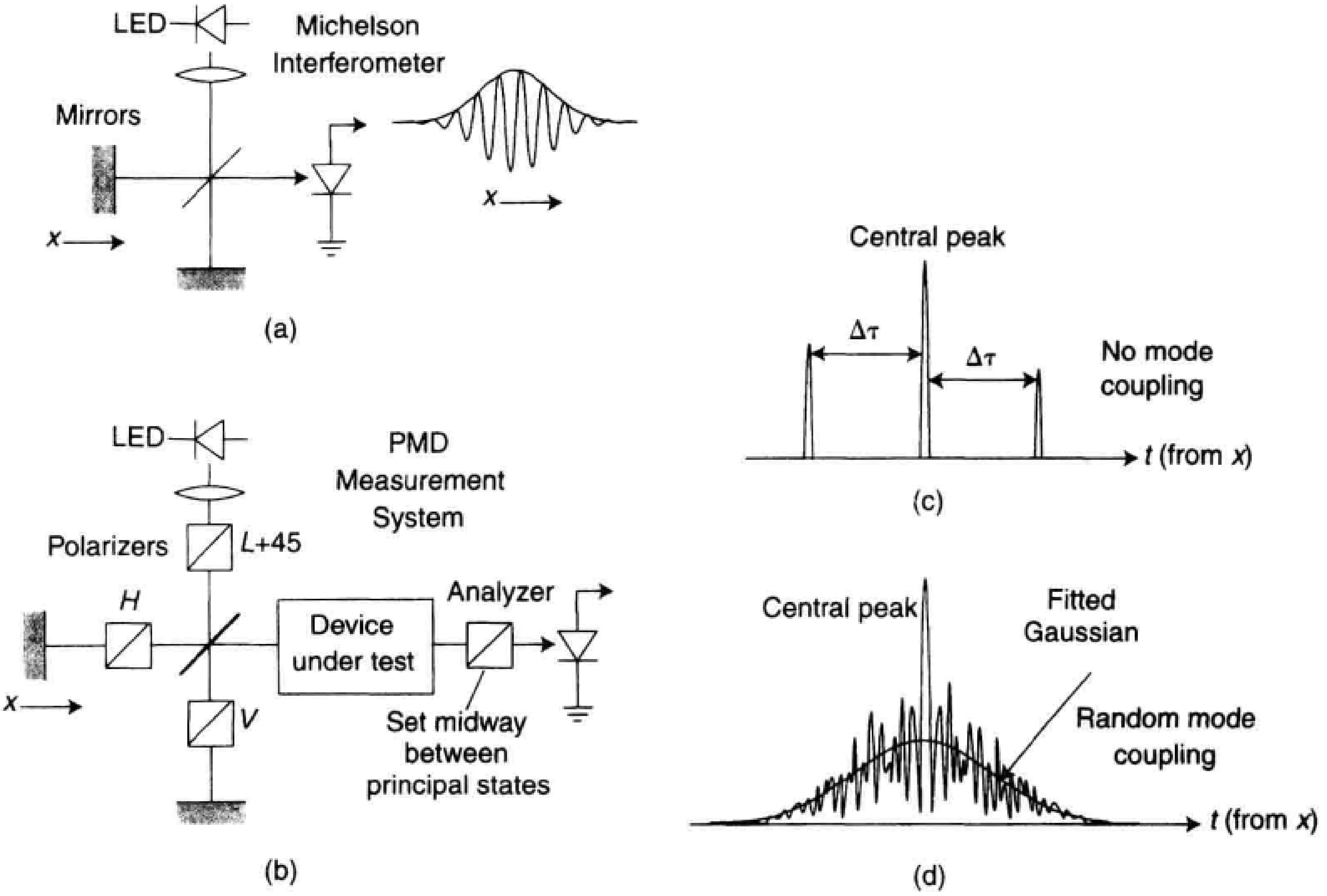

Figure 12.21 Interferometric PMD measurement. (a) Basic interferometer. (b) Example of a setup for testing PMD. (c) Response for simple birefringent device. (d) Response for random mode-coupled device.

coupling light from each of the output eigenmodes of the test device onto the photodetector with common polarization.

The interferometric method is applicable to optical components with well-defined eigenmodes, and to optical fiber in the "long-fiber" regime, where the principal states are strong functions of wavelength. The resulting interferograms, however, are quite different.

Consider first the case of a non-mode-coupled device. Referring to Figure 12.21b, the test device is placed in the optical beam and the mirror position is scanned. The response is as shown in Figure 12.21c. Both interferometer polarizations decompose into both eigenmodes of the test device. The central peak occurs when the interferometer arms are of equal length. The outlying peaks occur when the movable mirror introduces a delay equal to the differential group delay of the test device. One outlying peak is produced by interference between slow-mode light originating in the fixed mirror path and fast-mode light delayed by the movable mirror. The other outlying peak is produced by interference between fast-mode light originating in the fixed-mirror path and slow-mode light advanced by an identical movement of the mirror in the opposite direction. The time separation of the central and either of the outer peaks is the differential group delay of the device. The relative intensity of the peaks depends upon the orientations of the DUT and the analyzer.

The interferometric response for highly mode-coupled singlemode fibers with PMD much greater than the coherence time of the source is shown in Figure 12.21d. The photocurrent envelope is Gaussian in form, having a width determined by the PMD of the test fiber. The random detail is caused by coherence effects and has little impact on the calculation of PMD in the case of random mode coupling. PMD is determined from the photocurrent using one of two methods—direct fitting of a Gaussian curve, or computation of the second moment. It has been shown that for an ideal data set, a fitted Gaussian curve is related to the differential group delay by[32]

$$\text{rms DGD:} \quad \langle \Delta\tau^2 \rangle^{1/2} = \sqrt{\frac{3}{4}}\,\sigma \tag{12.35}$$

$$\text{mean DGD:} \quad \langle \Delta\tau \rangle = \sqrt{\frac{2}{\pi}}\,\sigma \tag{12.36}$$

where σ is the standard deviation of the Gaussian curve that would best fit the interferogram, excluding the central peak, if it were possible to measure the interferogram in the absence of instrumentation noise. (The traditional view has been that the rms differential group delay is equal to σ. The statistical nature of long-fiber PMD and the differences in signal processing between various PMD measurement methods has allowed the distinction between the 1:1 relationship and Equation 12.35 to remain undemonstrated until recently[32,33]).

More commonly, PMD is determined using an algorithm based upon the square root of the second moment of the photocurrent response.[34] The second moment is given by

$$\sqrt{\frac{\int I(t)t^2\,dt}{\int I(t)dt}} \tag{12.37}$$

where $I(t)$ represents the photocurrent. In practice, the algorithm involves amplitude-shifting of the response to reduce the effect of noise, removal of the central autocorrelation peak, truncation of the interferogram, computation of the second moment of the truncated interferogram, and determination of a Gaussian which, when substituted for the photocurrent and integrated over the same limits, produces the same value for the second moment. The rms differential group delay is determined from the value σ produced by this process, according to[34]

$$\langle \Delta\tau^2 \rangle^{1/2} = \sqrt{\frac{3}{4}}\,\sigma. \tag{12.38}$$

Alternately, PMD can be found from the second moment σ_ϵ without substituting the Gaussian. Assuming all other steps of the algorithm are followed, σ_ϵ relates to σ as

$$\sigma_\epsilon \approx \sqrt{\frac{3}{4}}\,\sigma \tag{12.39}$$

The rms differential group delay is given, to within a few percent, by:

$$<\Delta\tau^2> \approx \sigma_\epsilon. \tag{12.40}$$

The value of σ_ϵ is assigned to the rms differential group delay by some interferometric PMD measurement instruments.

The above discussion has assumed test devices with large values of PMD in relation to the coherence time of the source. For lower values of PMD, or specifically low-PMD source-width products, the PMD measured by interferometry depends upon the exact spectral shape of the optical source.[32]

In some of the PMD literature, it has been suggested measurements of small values of PMD can be corrected for the effect of the source autocorrelation peak according to

$$\sigma^2_{\text{device}} = \sigma^2_{\text{Meas}} - \sigma^2_{\text{Source}}\,. \tag{12.41}$$

However, it has been pointed out that this relation is not valid and that we do not yet have a rigorous method of correcting for optical source spectral width.[35] This reference provides several other excellent techniques for more accurately extracting the PMD value from the measured response.

The interferometric method is tolerant of movement along the fiber path during the measurement. Movement changes the details of the interferogram, but not the overall shape. Because interferometry measures large values of PMD quickly and interferometric setup is easily split into source and receiver units, the method also lends itself to measurement of high-PMD, installed fiber. Using modulation techniques, it is also possible to measure EDFAs using interferometry.[36]

12.4.10 The Poincaré Arc Method

The fixed analyzer, JME, and Poincaré arc (or SOP) methods are considered frequency-domain methods because they derive information from the change in output polarization state of the test device as wavelength is changed. Poincaré arc measurement results for a non-mode-coupled and a randomly mode-coupled test device are shown in Figure 12.22. The traces are generated by coupling polarized light from a tunable narrowband optical source partly into each of the input principal states of polarization of the test device. As the wavelength is adjusted incrementally, an arc is traced out on the Poincaré sphere by a ray perpendicular to the principal states axis. The differential group delay over the wavelength increment is computed from

$$\Delta\tau = \frac{\Delta\theta}{\Delta\omega} \tag{12.42}$$

where $\Delta\tau$ is the differential group delay in seconds, $\Delta\theta$ is the rotation about the principal states axis in radians, and ω is the radian optical frequency change that produced the arc.

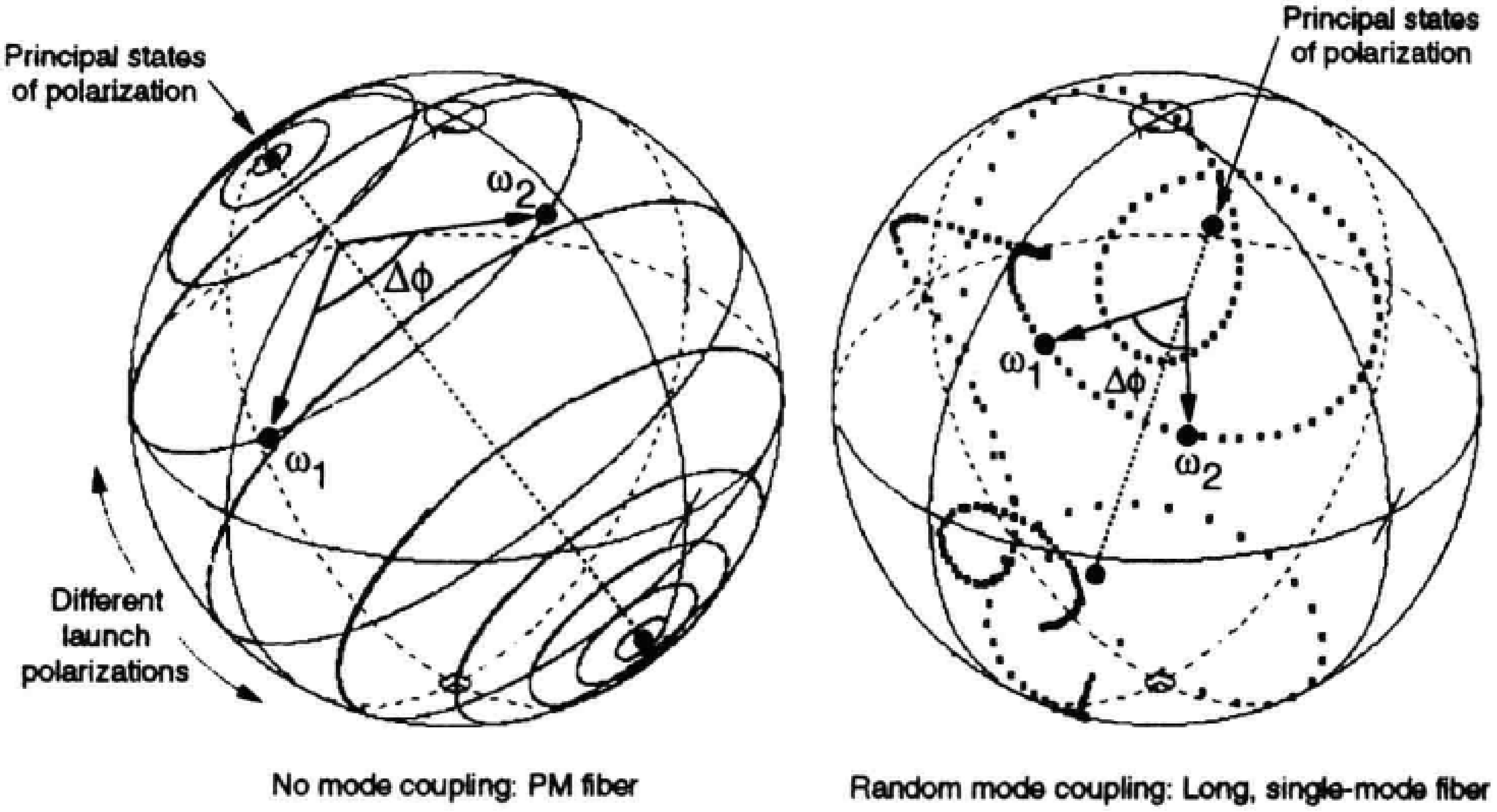

Figure 12.22 PMD measurement by the Poincaré arc (SOP) method. (a) Simple birefringent device. (b) Spool of fiber.

Although the Poincaré arc method is applicable to both component and randomly mode-coupled fiber measurements, the strong wavelength dependence of the principal states in randomly mode-coupled fiber may require readjustment of the launch polarization to maintain a reasonable amount of light in each of the two principal states of polarization.

12.4.11 The Modulation Phase-Shift Method

The modulation phase-shift method determines differential group delay from the difference in modulation phase between the principal states of polarization. The setup is shown in Figure 12.23. An intensity-modulated lightwave is coupled into the test fiber. The output signal is detected and the modulation phase is measured relative to either the electrical modulation source or a detected sample of the light incident on the test device. A network analyzer or lightwave component analyzer is typically used in this setup because it provides the microwave source, phase detection, phase normalization, and display functions. The phase response for an arbitrary input polarization is captured in memory and excess phase is removed electronically. The resulting trace is a flat line. The input polarization is then varied to produce maximum and minimum excursions of phase. Differential group delay is computed from the phase difference at a particular modulation frequency according to

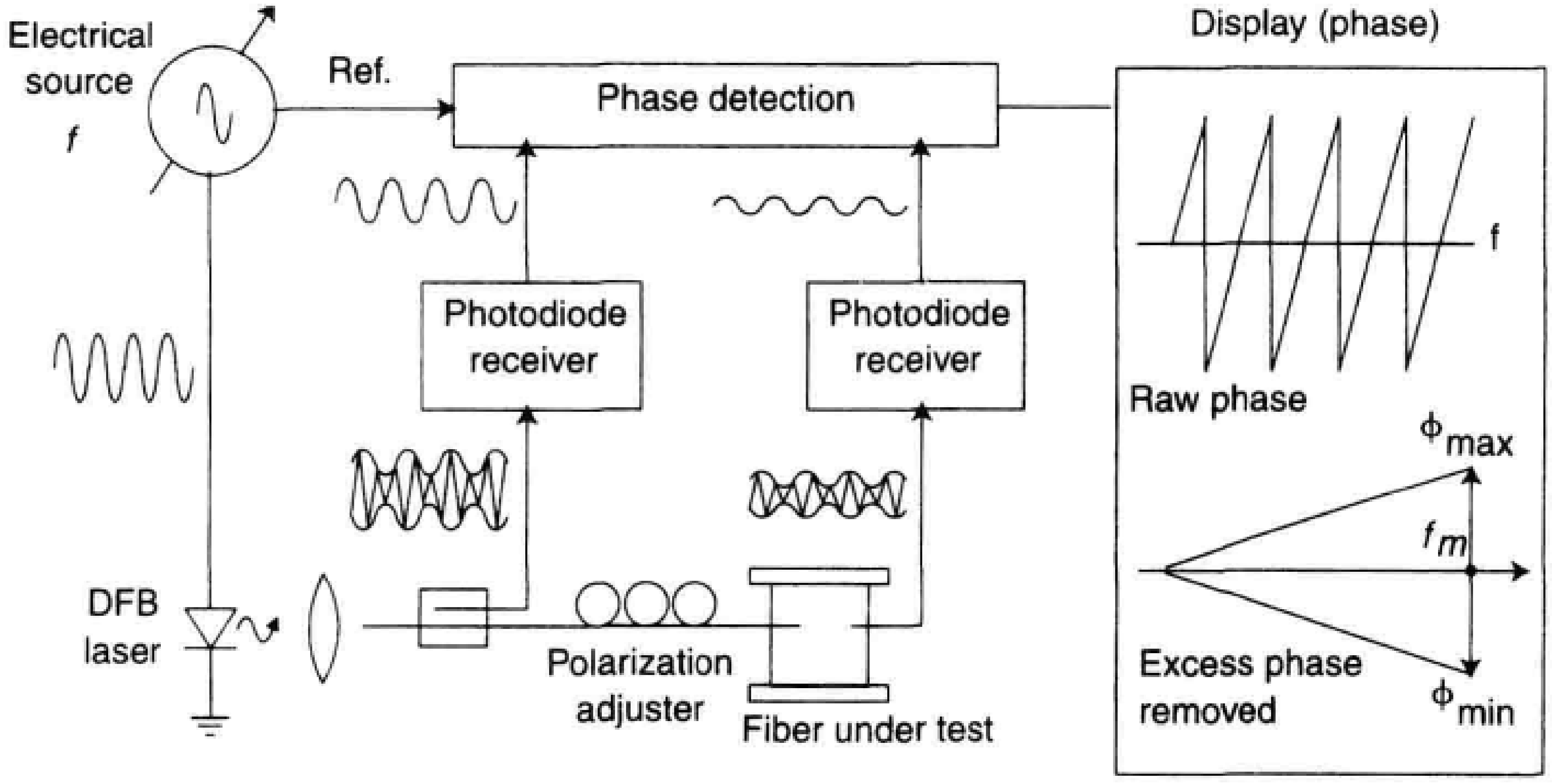

Figure 12.23 PMD measurement by the modulation phase-shift method.

$$\Delta\tau = \frac{\phi_{max} - \phi_{min}}{360 \times f_m}. \tag{12.43}$$

This technique is simple and intuitive but requires experimentally selecting the principal states of polarization. It also requires a stable operating temperature and isolation from mechanical vibrations.

12.4.12 The Pulse-Delay Method

One of the earliest and conceptually simplest methods of measuring differential group delay at a given wavelength involves sequentially launching very short pulses of light into the fast and slow polarization modes (input principal states) of the fiber and measuring the difference in arrival time of the pulses emerging from the corresponding output principal states. The setup is shown in Figure 12.24.

The differential group delay exhibited by spans of singlemode fiber, including fibers of newer and older technologies, range from less than 0.1 ps to several tens of picoseconds. An ultra-short-pulse source and high-speed detector are required. Pulses of 0.1 ps width have been produced by a demonstration EDFA pulse source at Hewlett-Packard Laboratories. Nonlinear crystal-autocorrelation techniques could be used to work around photodetector response limitations. In addition, since the principal states are measured sequentially, the instrumentation must be extremely stable.

The pulse-delay setup allows direct observation of the impact of PMD upon a fast pulse. Maximum broadening is observed when the polarized light couples equally to the input principal states of polarization.

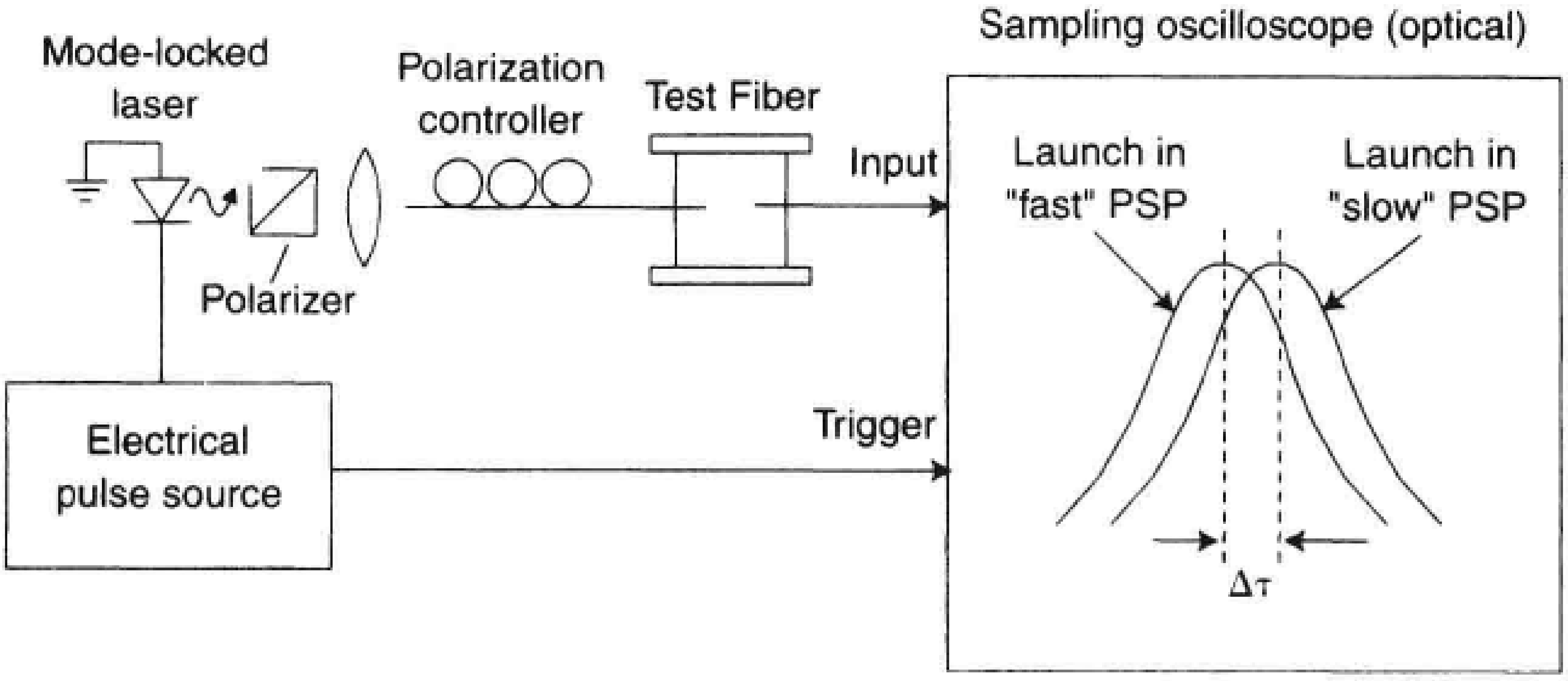

Figure 12.24 PMD measurement by the pulse-delay method.

12.4.13 Agreement between PMD Measurement Methods

As a result of the probabilistic character of PMD and the diversity of models, definitions, and measurement methods, the topic of numerical agreement between the methods has received a great deal of attention. Interest centers on the "long-fiber" regime, where mode coupling is random and the PMD coefficient is defined and has meaning. In this class of fiber, measurements of PMD coefficient commonly differ by 15 to 20%, with better agreement at higher values of PMD, worse at lower values. In contrast, for devices with simple birefringence, where the device is characterized by a single value of differential group delay, the methods agree to within a few percent.

The less impressive agreement observed for highly mode-coupled fibers is caused by a number of factors. First among these is that PMD is generally a function of temperature and mechanical stresses and thus is a less than ideal test device for inter-method comparisons. A second factor is the wavelength range, which is limited by instrumentation or by the bandwidth of the test device (for example, the narrowed passband of a long, amplified fiber link). This factor affects all of the measurement methods. For example, the fixed analyzer response of a fiber contains fewer peaks as the wavelength range is reduced, allowing a change of one count to more heavily influence the result. Closely linked is a third factor, the orientation of the launch polarization and output analyzer relative to the principal states of polarization. This is a factor in the interferometric and fixed analyzer techniques, particularly when measuring small values of PMD or using a narrow optical spectrum for the measurement. Taking the fixed analyzer as an example, rearrangement of the pigtails of the test fiber transforms the input and output polarizations and can change the extrema count.

A fourth factor bearing on measurement agreement involves the details of the instrument design and algorithms. These include filtering, thresholding, and the mathematical steps of extracting PMD from the conditioned data. A final aspect of measurement agreement is the conceptual model of PMD within which the measurement results are evaluated. The principal-states model describes PMD in terms of the wavelength-dependent differential group delay and principal states of polarization. It assumes narrowband light and considers the interference effects. An alternative model views PMD in terms of the repeated, random splitting of input pulses that are much shorter than the differential group delay. Splitting produces a distribution of pulse arrival times.[37] The PMD material presented in this chapter is based upon the principal-states model for three reasons. The high-speed telecommunications systems that are affected by PMD use narrowband light. Extremely short pulses, much shorter than the differential group delay, have wide spectra which suffer more severely from chromatic dispersion. Secondly, the pulse-splitting or incoherent light model can produce unexpected results in the intermediate mode-coupling regime because of the unaccounted-for coherent effects of the modeled, time-distributed output pulses. Finally, the principal-states model is directly verifiable by physical measurements.

12.5 SUMMARY

All forms of dispersion limit the capacity of systems to carry information. Degradation of the modulation phase relationships of lightwave signals causes pulse broadening in digital systems and equally serious distortion in analog systems. Intermodal dispersion, which limits data rates in systems using multimode fiber, is caused by the existence of multiple spatial modes of differing path lengths. Chromatic dispersion results from a variation in propagation delay with wavelength caused by the interplay of fiber materials and dimensions. PMD, caused by the division of signal energy into orthogonal polarization modes with different speeds of propagation, becomes a limiting factor after chromatic dispersion has been sufficiently reduced.

Chromatic dispersion is a relatively stable phenomenon. The total chromatic dispersion of a telecommunications system can be calculated from the sum of its parts. The location and value of dispersion compensators can be planned in advance. In contrast, the PMD of singlemode optical fiber at any given signal wavelength is not stable, forcing system designers to make statistical predictions of the effects of PMD and making passive compensation impossible.

The main chromatic dispersion measurement methods discussed in this chapter are based upon measurement of the variation of modulation phase with signal wavelength. The modulation phase-shift method measures the change in group delay over a series of wavelength intervals and determines the attributes of chromatic dispersion directly from a curve fit to the data. The differential phase-shift method measures the dispersion coefficient directly by stepping or sweeping between closely spaced wavelengths. Repeating the measurement at a series of wavelengths allows calculation of the remaining attributes. A method based on the conversion of AM to FM by the dispersion of the test device is also discussed.

The problem of PMD has inspired the development of many measurement methods, several of which were discussed. The fixed analyzer method determines a single value of

PMD from measurement of the transmission through a polarizer over wavelength. The fixed analyzer response may be Fourier transformed to yield a spectrum that gives insight into the degree of mode coupling and allows calculation of PMD from a Gaussian fit or from the second-moment algorithm. The JME method determines the differential group delay and principal states as functions of wavelength from measurements of the transmission matrix at a series of wavelengths. The interferometric method determines PMD from the electric field autocorrelation function using a broadband source. The value of PMD is computed with an algorithm based on the second moment. The Poincaré arc, or SOP (state of polarization) method uses a polarimeter to capture the arc traced out on the Poincaré sphere by the output polarization of the test device over a series of wavelength increments. The modulation-phase and pulse-delay methods determine PMD from measurements of the change in modulation phase and the change in pulse arrival time, respectively, between the principal states of polarization.

The reader is reminded that detailed measurement methods for many fiber, component and system parameters, or attributes, in the field of fiber optic communications are developed and published by standards committees under the auspices of the Telecommunications Industry Association and its international counterparts. Dispersion measurement technique is described in detail in EIA/TIA fiber optic test procedures (FOTPs), some of which are referenced herein.

REFERENCES

Intermodal Dispersion

1. TIA/EIA FOTP-51. 1991. *Pulse distortion measurement of multimode glass optical fiber information transmission capacity.* Washington, DC: Telecommunications Industry Association.
2. TIA/EIA FOTP-30. 1991. *Frequency domain measurement of multimode optical fiber information transmission capacity.* Washington, DC: Telecommunications Industry Association.

Chromatic Dispersion

3. Hackert, M.J. 1992. Development of chromatic dispersion measurement on multimode fiber using the relative time of flight measurement technique. *IEEE Photonics Technology Letters,* 4(2): 198–200.
4. EIA/TIA FOTP-168. 1992. *Chromatic dispersion measurement of multimode graded-index and singlemode optical fibers by spectral group delay measurement in the time domain.* Washington, DC: Telecommunications Industry Association.
5. Cohen, Leonard G. 1985. Comparison of singlemode fiber dispersion measurement techniques. *Journal of Lightwave Technology,* LT-3 (5): 958–966.
6. Heffner, B.L. 1993. Accurate, automated measurement of differential group delay dispersion and principal state variation using Jones matrix eigenanalysis. *IEEE Photonics Technology Letters,* 5(7), 814–817.
7. Poole, C.D. and C.R. Giles. 1988. Polarization-dependent pulse compression and broadening due to polarization dispersion in dispersion-shifted fiber. *Optics Letters,* 13: 155–157.

8. EIA/TIA FOTP-169. 1992. *Chromatic dispersion measurement of singlemode optical fibers by the phase shift method.* Washington, DC: Telecommunications Industry Association.
9. Costa, B., D. Mazzoni, M. Puleo, and E. Vezzoni. 1982. Phase shift technique for the measurement of chromatic dispersion in optical fibers using LED's. *IEEE Journal of Quantum Electronics,* QE-18 (10): 1509–1515.
10. TIA/EIA FOTP-175. 1992. *Chromatic dispersion measurement of singlemode optical fibers by the differential phase shift method.* Washington, DC: Telecommunications Industry Association.
11. Christensen, B., J. Mark, G. Jacobsen, and E. Bodtker. 1993. Simple dispersion measurement technique with high resolution. *Electronics Letters,* 29(1): 132–134.
12. Rosher, P.A., M.K. Compton, and A.D. Georgiou. Dispersive considerations in microwave optical system.

Polarization-Mode Dispersion

13. Poole, C.D. and R.E. Wagner. 1986. Phenomenological approach to polarization dispersion in long singlemode fibers. *Electronics Letters,* 22: 1029–1030.
14. Darcie, T.E. and C.D. Poole. 1992. Polarization-induced performance variables. *Communications Engineering and Design.*
15. Bahsoun, S., J. Nagel, and C. Poole, 1990. *Measurements of temporal variations in fiber transfer characteristics to 20 GHz due to polarization-mode dispersion.* Proc. 16th European Conf. Opt. Comm., Amsterdam: 1003–1006.
16. Poole, C.D., R.W. Tkach, A.R. Chraplyvy, and D.A. Fishman. 1991. Fading in lightwave systems due to polarization-mode dispersion. *IEEE Photonics Technology Letters,* 3: 68–70.
17. Poole, C.D. 1988. *Optics Letters.* 13: 687.
18. Poole, C.D., J.H. Winters, and N.A. Nagel. 1991. Dynamical equation for polarization mode dispersion. *Optics Letters,* 16: 372–374.
19. Foschini, G.J. and C.D. Poole. 1991. Statistical theory of polarization dispersion in singlemode fibers. *Journal of Lightwave Technology,* LT-9: 1439–1456.
20. Gisin, N. and J.P. Pellaux. 1992. Polarization mode dispersion: time versus frequency domains. *Optics Communications,* 89: 316–323.
21. Born, M. and E. Wolf. 1980. *Principles of optics. 6th ed.* Pergamon.
22. Bergano, N.S., C.D. Poole, and R.E. Wagner. 1987. Investigation of polarization dispersion in long lengths of singlemode fiber using multi-longitudinal mode lasers. *Journal of Lightwave Technology,* LT-5:1618–1622.

The Fixed Analyzer PMD Measurement Method

23. TIA/EIA FOTP-113. 1997. *Polarization-mode dispersion measurement for singlemode optical fibers by the fixed analyzer method.* Washington, DC: Telecommunications Industry Association.
24. Poole, C.D. 1989. Mesurement of polarization-mode dispersion in singlemode fibers with random mode coupling. *Optics Letters,* 14: 523.
25. Poole, C.D. and D.L. Favin. 1994. Polarization-mode dispersion measurements based on transmission spectra through a polarizer. *Journal of Lightwave Technology,* LT-12: 917–929.

The Jones Matrix Eigenanalysis PMD Measurement Method

26. Heffner, B.L. 1992. Automated measurement of polarization mode dispersion using Jones matrix eigenanalysis. *IEEE Photonics Technology Letters* 4:1066.
27. Jones, R.C. 1947. A new calculus for the treatment of optical systems. VI: Experimental determination of the matrix. *Journal of the Optical Society of America,* 37:110–112.
28. TIA/EIA FOTP-122, 1996. *Polarization-mode dispersion measurement for singlemode optical fibers by Jones matrix eigenanalysis,* Washington, DC: Telecommunications Industry Association.
29. Heffner, B.L. 1993. Attosecond-resolution measurement of polarization mode dispersion in short sections of optical fiber. *Optics Letters,* 18 (24):2102–2104.

The Interferometric PMD Measurement Method

30. Mochizuki, K., Y. Namihira, and H. Wakabayashi. 1981. Polarization mode dispersion measurements in long singlemode fibers. *Electronics Letters,*17:153–154.
31. Gisin, N., J-P Von der Weid, and J-P Pellaux. 1991. Polarization mode dispersion of short and long singlemode fibers. *Journal of Lightwave Technology* LT-9:821–827 and references therein.
32. Heffner, B.L. 1985. Analysis of interferometric PMD measurements: Relation to principal states model for highly mode-coupled fibers. *Technical Digest—Optical Fibre Measurement Conference.* Liege, Belgium, September.
33. Williams, P.A. and P.R. Hernday. 1995. Anomalous relation between time and frequency domain PMD measurements. *Technical Digest—Optical Fibre Measurement Conference.* Liege, Belgium, September.
34. TIA/EIA FOTP-124. *Polarization-mode dispersion measurement for singlemode optical fibers by the interferometric method,* Telecommunications Industry Association.
35. Williams, P.A. 1996. Accuracy issues in comparisons of time- and frequency-domain polarization mode dispersion measurements. *Technical Digest—Symposium on Optical Fiber measurements.* NIST Special Publication 905: 125–129.
36. Namihira, Y., K. Nakajima, and T. Kawazawa. 1993. *Electronics Letters,* 29:1649.
37. Gisin, N., R. Passy, and J.P. Von der Weid. 1994. *IEEE Photonics Technology Letters* 6: 730–732.

CHAPTER 13

Characterization of Erbium-Doped Fiber Amplifiers

Douglas M. Baney

INTRODUCTION

This chapter presents several commonly used methods for optical amplifier gain and noise figure measurement. The methods are often modified in various ways depending on the instrumentation selected for the testing as well as the specifics of the measurement results obtained. With this in mind, the principle goal of this chapter is to convey enough information about the basic measurement methods so that the reader can make informed decisions on measurement procedures, experimental apparatus, and possible further improvements to the measurement techniques. As characterization methods are optimized, often the physics of the optical amplifier influences the measurement technique. For this reason, a working knowledge of the amplifier is useful to understand the basis for the measurement techniques.

Some of the amplifier properties that affect the communications systems are the optical gain, gain flatness, noise, temporal response, and polarization dependence.[1–5] These characteristics have a bearing on the methods employed for testing optical amplifiers. This chapter will be focused primarily on the erbium-doped fiber amplifier (EDFA), which has had a significant impact on lightwave telecommunications and the field of optics in general. A discussion of the various noise processes caused by optical amplification and interference effects[6,7] is also presented. This will be useful in understanding the origin of the noise figure of an optical amplifier.

The organization of the chapter is as follows. A discussion of basic fiber amplifier characteristics is presented in Section 13.1. Section 13.2 discusses the concept of optical gain. The noise processes that contribute to signal-to-noise ratio (SNR) degradation are introduced in Section 13.3. Noise figure definition is discussed in Section 13.4. Section

13.5 deals with measurement of gain and noise figure using both optical and electrical methods. Section 13.6 discusses other types of optical amplifiers which may impact future telecommunications systems. Section 13.7 highlights the most significant sources of measurement uncertainty in gain and noise figure measurements. Section 13.8 provides useful constants for noise figure calculations, and Section 13.9 provides a brief summary of this chapter.

13.1 FIBER AMPLIFIERS

The history of the rare-earth doped fiber amplifier dates back to the early 1960s with the demonstration of optical gain in neodymium-doped glass fiber at a wavelength of 1.06 μm.[8,9] Years later, the convergence of singlemode glass fiber drawing and semiconductor laser technologies set the stage for the 1.55 μm fiber optic amplifier. The optical propagation loss in silica glass fiber is lowest at 1.55 μm (~0.2 dB/km) making this wavelength region important for long-haul telecommunications. The demonstration, in 1986, of an erbium-doped silica fiber laser, and an EDFA in 1987[10,11] showed the great potential of fiber optic amplifiers. Soon after these initial results, telecommunications laboratories around the world began research and development efforts aimed at applying the EDFA towards optical communications systems.

The EDFA has a number of characteristics which make it an excellent amplifier for optical communications including: polarization-independent gain, low interchannel crosstalk, wide optical bandwidth and low-noise generation. In brief, the EDFA offers a nearly ideal way to compensate for signal propagation losses along high-speed singlemode fiber-optic links.

13.1.1 Basic Concepts

The basic *black-box* characteristics of an optical amplifier are shown in Figure 13.1. The incident optical signal is amplified after traversing the optical amplifier. In addition to providing for optical gain, the amplifier also adds other optical powers to the input and output optical fiber. These added optical powers include:

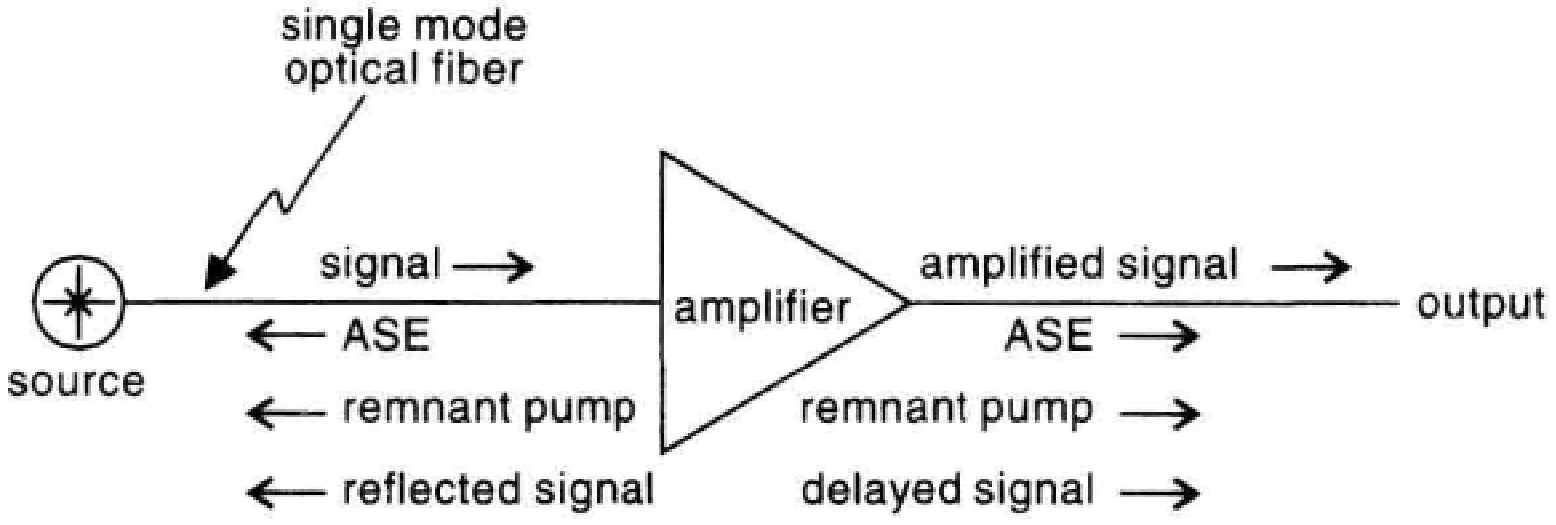

Figure 13.1 In addition to signal amplification in the forward direction, the amplifier adds other powers to the optical network.

- Amplified spontaneous emission (ASE);
- Remnant power from the pump laser;
- Time-delayed scaled-replicas of the signal power.

The degree to which these added powers are significant depends on the design of the EDFA.

The essential components of the EDFA are shown in Figure 13.2. These components are the laser pump, the wavelength division multiplexer (WDM), the optical isolators, and the erbium-doped fiber. With these basic components, many different amplifier topologies are possible.[12] To obtain gain, optical energy must be provided to the erbium-doped fiber. The energy source is called the pump. It delivers optical power at a wavelength of 980 nm or 1480 nm. The pump power is typically in the range of ~10 mW to ~400 mW. The WDM serves to efficiently couple signal and pump light into, or away from, the rare-earth doped fiber. Isolators reduce any light reflected from the system back to the amplifier to an acceptable level. Without an isolator, optical reflections may degrade the amplifier gain performance and increase noise generation. In Figure 13.2, the pump light is traveling along the fiber in a direction opposite that of the signal. This type of pumping is referred to as counter-directionally pumped, or counter-propagating, or simply counter-pumped. Codirectionally or copropagating-pumped amplifiers have the laser pump on the input end of the amplifying fiber. Sometimes multistage amplifiers are used with an isolator separating two erbium-doped fiber (EDF) gain sections. This design allows for improved amplifier noise and output power performance. Fiber Bragg gratings[13] are also used for flattening the EDFA gain variation with wavelength. This improves the amplifier performance in WDM applications as well as reducing optical noise.

The erbium ions are located in the central core region of the EDF as shown in Figure 13.3[14] The central core region (diameter ~5 μm) of the EDF is where the pump and signal wave intensities are the highest. Placement of the erbium ions in this region provides maximum overlap of pump and signal energy to the ions, resulting in better amplification. A lower index glass cladding layer surrounds the core region to complete the waveguide structure and provides for increased mechanical strength. A protective coating is added to the fiber bringing the total diameter to 250 μm. This coating, with its increased refractive index with respect to the cladding also serves to remove any nondesired light (higher order spatial modes) propagating within the cladding. Apart from the erbium dopant, this fiber construction is the same as standard singlemode telecommunications

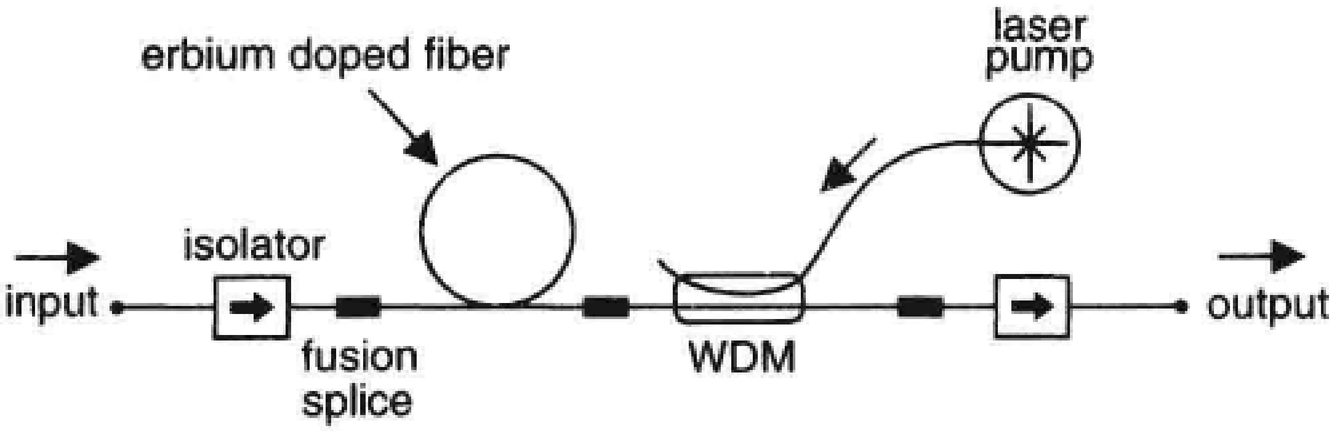

Figure 13.2 An EDFA design showing the essential components. WDM: wavelength division multiplexier.

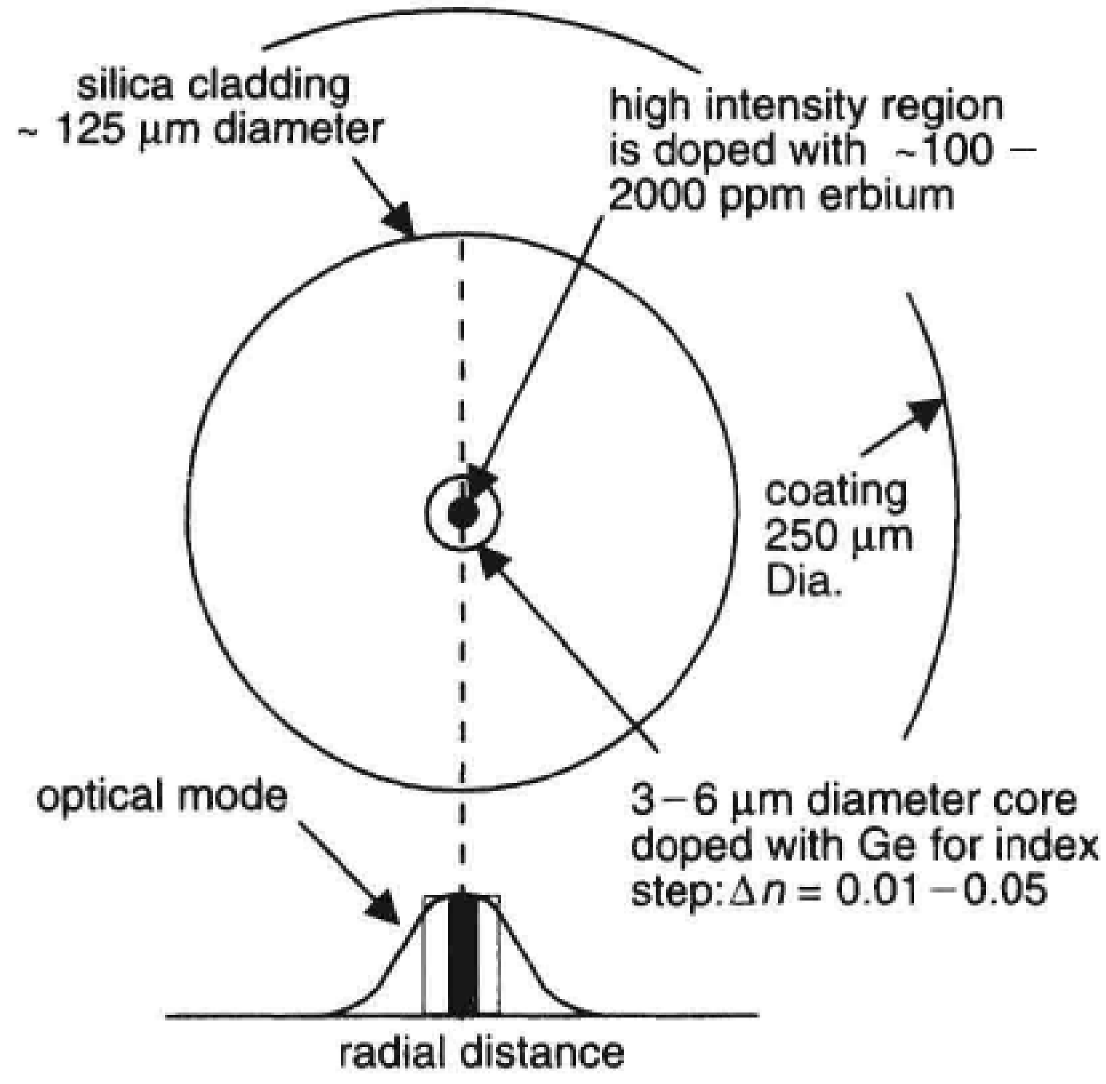

Figure 13.3 Erbium-doped fiber core geometry.

fiber. The important characteristics for the EDF are its loss/gain per unit length at the pump and signal wavelengths. This information is often given in terms of emission and absorption cross-sections, and the confinement factors for the signal and pump light.

Energy Levels. The trivalent erbium atoms (Er^{3+}) are the active elements in the amplifier responsible for optical gain. The relevant optical transitions are shown in Figure 13.4.[15] The approximate wavelengths of the transitions are indicated with respect to the ground state. The designations on the right side are the commonly used quantum numbers assigned to each transition. These numbers are of the form $^{2S+1}L_j$ where S is the spin quantum number, L is the orbital angular momentum, and J is the total $(L + S)$ angular momentum. L is equal to one of: 0, 1, 2, 3, 4, 5, 6 . . . which is designated by the letters S, P, D, F, G, H, I. This *LSJ* scheme is used in the literature to indicate the ion energy levels.[16,17] The "local crystalline" fields perturb the ion energy structure resulting in splitting of each LSJ energy level into multiple levels. This splitting is referred to as Stark splitting (Stark effect). As a result of randomness in the glass molecular structure, each ion experiences a different field strength and orientation, resulting in different Stark-splitting. This splitting is responsible for the large gain bandwidth of rare-earth doped amplifiers. Within the *LSJ* description for the ion energy structure, the number of Stark-split lines is $(2J + 1)/2$ for each level. Thus the $^4I_{13/2}$ and $^4I_{15/2}$ levels would have 7 and 8 Stark lines respectively, resulting in 56 possible transitions between them spread out across the 1.55 μm band.

In Figure 13.4, absorption of pump laser photons excites the ion to higher energy states as shown by the upward arrows. The ion can dissipate energy with either the radiation of a photon, or by converting the energy into lattice phonons (heat). The tendency to radiate a photon when transitioning to a lower energy level increases with the energy gap.

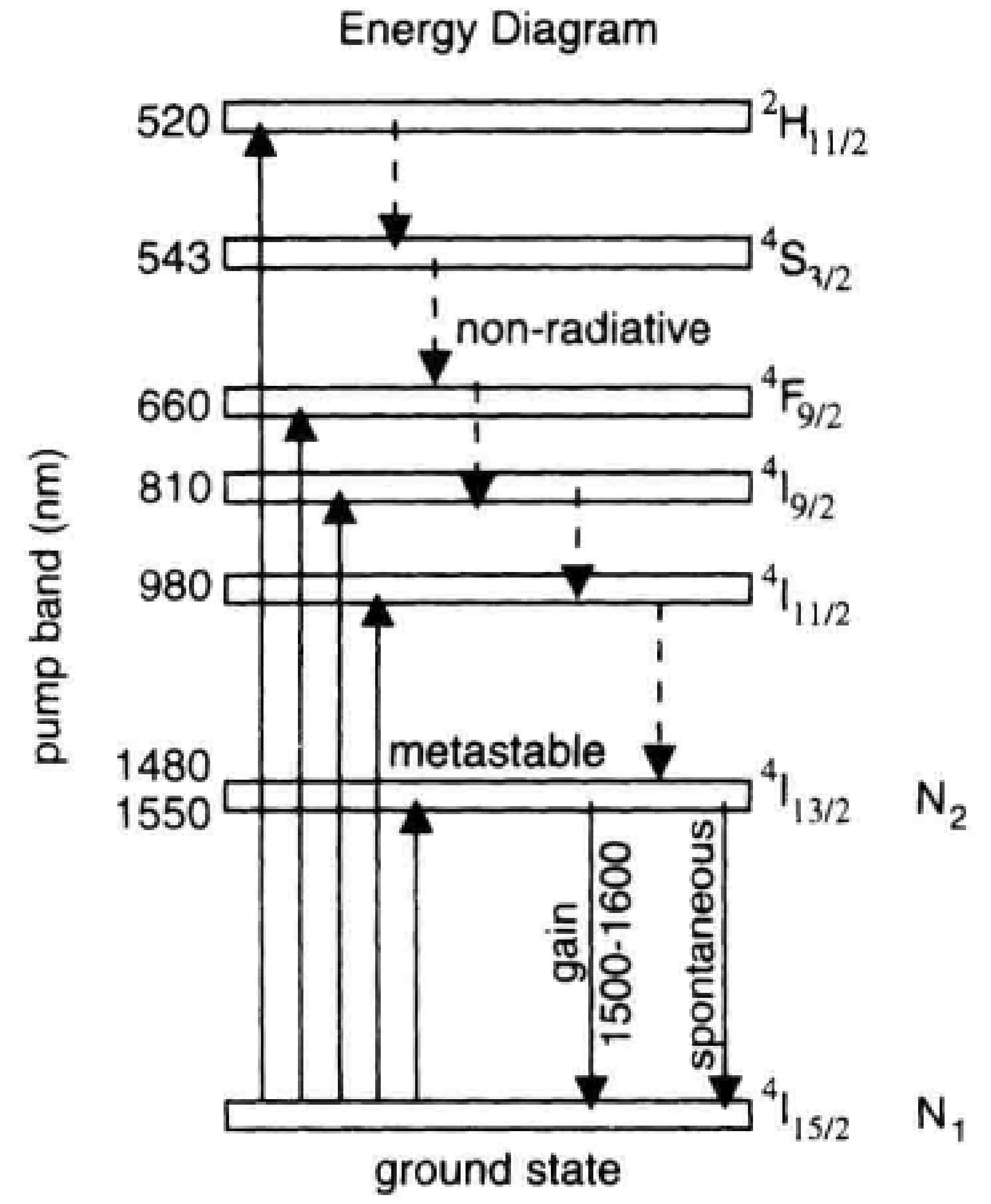

Figure 13.4 Partial energy diagram for the trivalent erbium ion.

Fortunately the $^4I_{13/2}$ – $^4I_{15/2}$ transition is predominantly radiative in silica-based glasses resulting in excellent amplification characteristics in the 1.5 μm to 1.6 μm wavelength region.

The different transitions between the various energy levels result in detailed absorption and fluorescence spectrums from visible wavelengths to the infrared as seen in Figure 13.5.[18,19] The precise shape of the absorption characteristic and the magnitude of the fluorescence depends on the codopants added to the glass structure which modifies the ion energy structure. The choice of glass hosts with low phonon (vibration) energies, such as ZBLAN fluoride glass, will allow rare-earth ions to have strong fluorescence (light emission) between energy levels which normally undergo non-radiative decay in a silica glass host. In Figure 13.5a, a strong fluorescence in the 1.55 μm region is evident for erbium ions in silica glass.

The absorption characteristic, shown in Figure 13.5b is also useful to investigate potential wavelengths for pumping the erbium ion. From the figure, the wavelengths of 1480 nm, 980 nm, 800 nm, 670 nm, and 521 nm should permit excitation of the erbium ion. All of these wavelengths have been successfully used to pump EDFAs.[20,21] The addition of other codopants such as ytterbium allows for pumping at other wavelengths.

The 1480 nm pump wavelength is used in EDFAs for a number of reasons including: (1) the availability of high pump power from semiconductor laser diodes operating at this wavelength; (2) good power efficiency since there is a small energy difference between 1480 nm and 1550 nm; (3) lower attenuation in optical fiber for remotely pumped EDFAs; (4) the broad absorption spectrum places less stringent demands on pump laser wavelength accuracy.

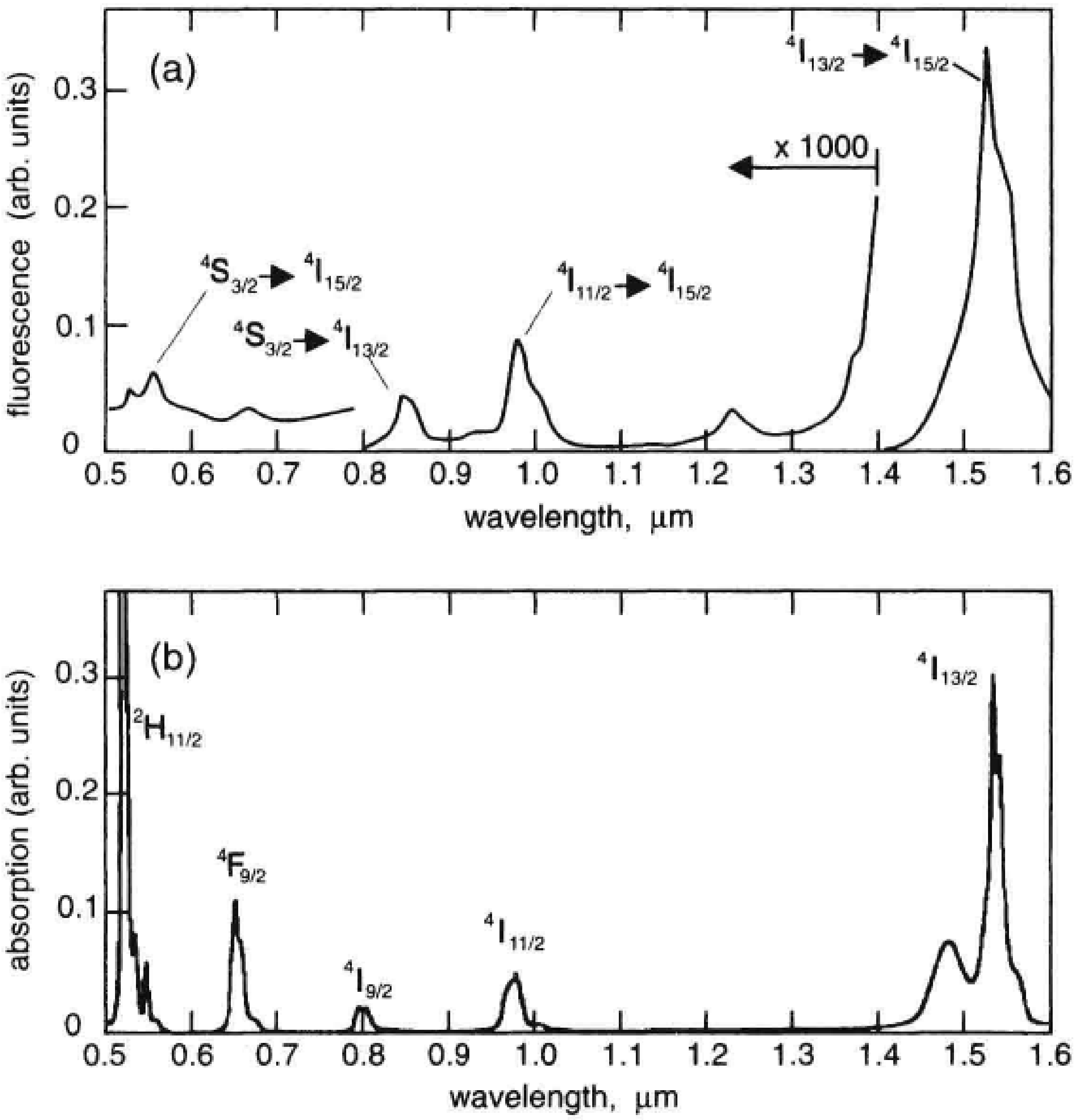

Figure 13.5 (a) Fluorescence intensity and (b) absorption characteristic for two different erbium doped silica fibers. [With permission after ref. [18], [19] ©1988 IEEE, ©1991 IEEE.]

The 980 nm pump band offers the best EDFA noise performance but also requires tighter pump wavelength accuracy to align to the narrow absorption band about 976 nm. The advent of the fiber Bragg-grating (FBG) has alleviated this problem by providing wavelength selective feedback to the pump laser to insure operation at the proper wavelength. FBGs are constructed by radiating a Ge-doped silica fiber core laterally with UV light to create periodic refractive index perturbations along a short length (~1 cm) of fiber.[13] This forms a wavelength-selectable narrow band (0.1 nm ~ 10 nm) reflective grating. A small reflection between approximately 1 to 10% provides feedback to lock the pump wavelength to the peak of the erbium absorption characteristic.

Two-, Three-, and Four-Level Systems. Optical amplifiers are classified as two-, three-, or four-level laser systems. An EDFA pumped into the $^4I_{13/2}$ band as shown in Figure 13.4 ($\lambda_p = 1480$ nm) is often approximated as a two-level system, since the pump and signal transitions are between the same energy bands. Pumping at 980 nm constitutes a three-level system where the ion energy quickly decays (~2 μs) nonradiatively from the $^4I_{11/2}$ level to the long-lived $^4I_{13/2}$ metastable state. Amplifiers based on two- or three-level systems must be designed properly to limit reabsorption of the signal due to the presence of ground-state absorption at the signal wavelength. A four-level system is an extension of the three-level where there is an additional energy level below the lower level of the gain transition. Four-level systems do not have the ground-state signal reabsorption which can degrade the performance of amplifiers based on three-level systems.

Stimulated Emission, Spontaneous Emission. When the erbium ion (Er^{3+}) is excited from the ground state through absorption of pump light, it will decay nonradiatively from the higher lying energy levels until it reaches the metastable state ($^4I_{13/2}$ state). The incident signal light (see Figure 13.2) arrives at the excited erbium atoms distributed along the optical fiber core. Stimulated emission occurs creating additional photons with the same optical phase and direction as the incident signal, thus amplification is achieved. Excited ions that don't interact with the incident light spontaneously decay to the ground state with a time constant of approximately 10 ms. The captured spontaneous emission (SE) has a random phase and direction. Typically less than 1% of the SE is captured by the optical fiber mode and becomes a source of optical noise. This noise gets amplified resulting in amplified spontaneous emission (ASE). Once in the ground state, absorption of a pump photon activates the erbium ion again and the process repeats itself. The presence of ASE causes degradation of the SNR of signals passing through the amplifier. Proper design of the amplifier will minimize the SNR degradation.

Table 13.1 gives a quick overview of the capabilities of EDFAs in terms of ranges of values for key performance characteristics.

13.2 GAIN

Gain is the most fundamental parameter of an optical amplifier. In addition to optical gain, the amplifier produces ASE. The optical amplifier gain, *G*, is defined as

$$G = (P_{\text{out}} - P_{ASE})/P_s \tag{13.1}$$

Table 13.1 EDFA Characteristics

Specification	Value	Units
gain	0 – ~ 50	dB
power output	1 –> 4000	mW
noise figure	3.5 – 12	dB
wavelength range	1520 ~ 1570	nm

where P_s and P_{out} are the amplifier input and output signal powers and P_{ASE} is the noise power generated by the amplifier which lies within the optical bandwidth of the measurement.

Predicting the gain is complicated by the distributed bidirectional nature of the amplifier, this often requires a numerical solution. An understanding of the net amplifier gain, G, can be derived from an analysis of the gain from individual "slices" along the fiber. A simplified analysis is presented here. Once the concepts are understood, the equations can be readily generalized to create a more realistic amplifier model.[17,22] An ASE-free two-level approximation is assumed. An EDFA is actually a concatenation of many amplifiers of incremental length Δz as illustrated in Figure 13.6. The net gain, G, is composed of the contributions of all the gain elements, $g(z)$ along the amplifier fiber:

$$G = \lim_{\Delta Z \to 0} \{e^{g(z_1)\Delta z} \times e^{g(z_2)\Delta z} \times \ldots e^{g(z_n = L)\Delta z}\} = \exp\left(\int_0^L g(z)\, dz\right) \tag{13.2}$$

The incremental signal gain, $g(z)$ for a photon propagating down the fiber is dependent on the metastable state population density, N_2, (see Figure 13.4), the ground-state population, N_1, the stimulated emission cross-section, σ_e, the absorption cross-section, σ_a, and the confinement (overlap) factor, Γ_s, between the signal field and the erbium-ion population. Γ_s can vary from zero to unity. A typical value is 0.3. The emission and absorption cross-sections represent the strength of the transition in other words, the ability to produce gain or absorption respectively. The gain coefficient is the difference between the upper and lower ion populations with a weighting taking into account their transition strengths:

$$g(z) = \Gamma_s[\sigma_{e,s} N_2(z) - \sigma_{a,s} N_1(z)] \tag{13.3}$$

In the discussion, subscripts s and p refer to signal and pump respectively. Similarly, the pump loss in a slice of fiber is given as

$$\alpha_p(z) = \Gamma_p[\sigma_{e,p} N_2(z) - \sigma_{a,p} N_1(z)] \tag{13.4}$$

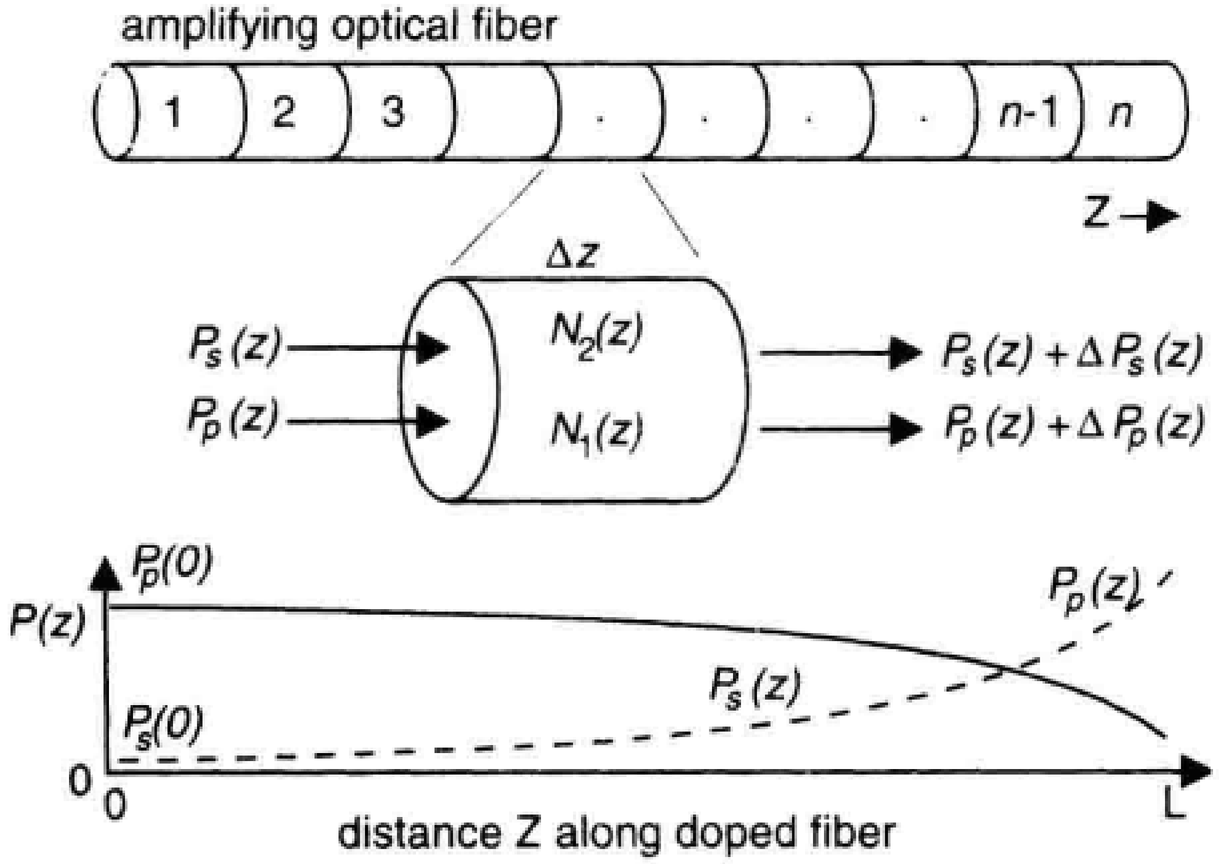

Figure 13.6 Fiber amplifier represented as a series of individual gain slices causing signal and pump power gain and absorption along the active fiber.

To achieve gain in a slice of doped fiber, the relationship $\sigma_{e,s}N_2 > \sigma_{a,s}N_1$ must be satisfied within the slice. The cross-sections can be determined experimentally from measurements of fluorescence and absorption of a short section of fiber. Experimental data, from which the cross-sections are derived is shown in Figure 13.7 for erbium in an Al and Ge co-doped silica glass.[22] Note the peak in the absorption and emission cross-sections near 1530 nm and the shift in the absorption spectrum toward shorter wavelengths. The shift towards shorter wavelengths is typical of the rare-earths. This is due to the thermal distribution of energy within each group of Stark-split energy levels favoring the lower energy levels. The addition of the Al codopant tends to broaden the gain peak near 1533 nm and reduce the amplifier gain difference between the 1533 nm and 1550 nm bands. The glass host may also be changed to improve the amplification characteristics of EDFAs. Changing from a silica host to fluorozirconate or fluorophosphate glass has been shown to substantially flatten the overall amplifier gain spectrum.[23,24] Broadband amplification from 1530 nm to 1610 nm using a tellurite glass host has also been demonstrated.[25]

The populations N_1 and N_2 are derived from the solution to the rate equation. The rate equation for the metastable state contains the contributions of pump light absorption, stimulated emission and SE.

$$\underset{(\mathrm{N_2\ change})}{\frac{dN_2}{dt}} = \underset{(\mathrm{pump\ absorption})}{\frac{P_p\sigma_{a,p}N_1}{Ah\nu_p}} - \underset{(\mathrm{stimulated\ emission})}{\frac{P_s\sigma_{e,s}N_2}{Ah\nu_s}} - \underset{(\mathrm{spontaneous\ emission})}{\frac{N_2}{\tau_{sp}}} \tag{13.5}$$

where P_p/A and P_s/A are the pump and signal intensities, $h\nu_p$, $h\nu_s$ are the pump and signal photon energies and τ_{sp} is the spontaneous decay time. From Equation 13.5, any change in the upper level, N_2 is due to a change in the relative values of pump absorption, stimulated emission or SE.

In the energy two-level approximation, conservation of the erbium ion population requires that

$$N_t = N_1 + N_2 \tag{13.6}$$

where N_t is the total ion population. The incremental gain, $g(z)$ is related to the power change across a differential slice of fiber. The simplest case occurs when the pump light

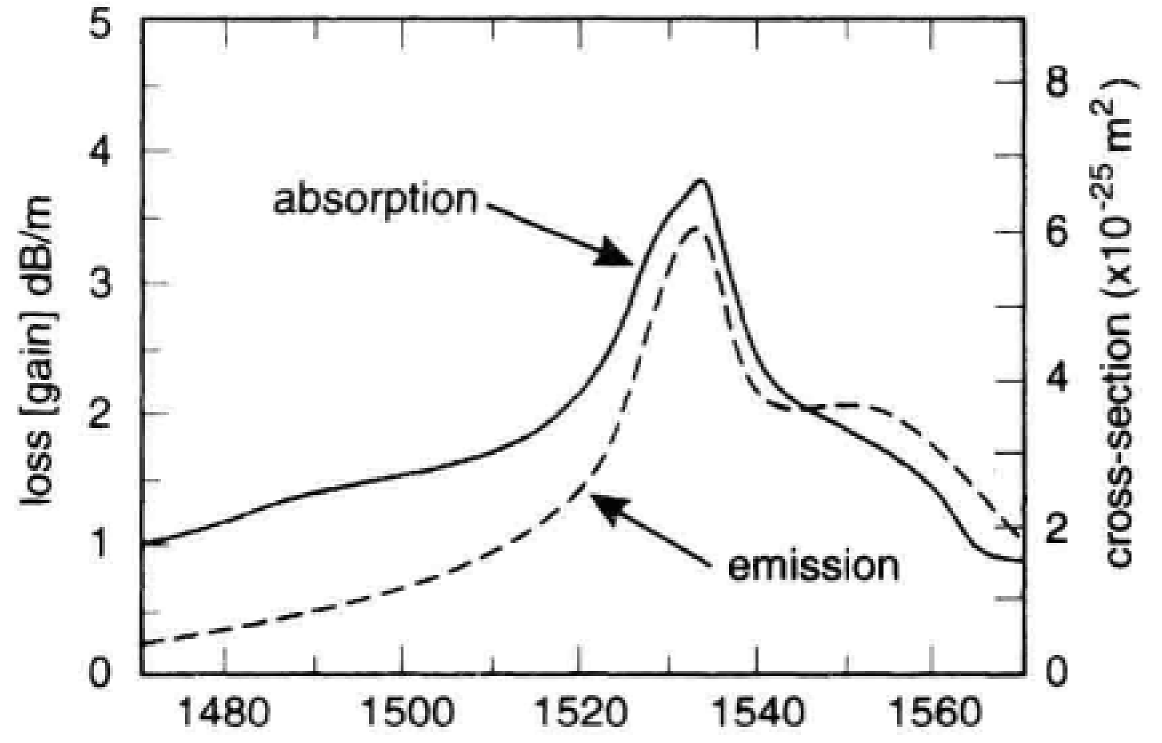

Figure 13.7 Measured absorption and gain characteristics along with calculated absorption and emission cross-sections for Al and Ge codoped EDF [With permission after ref. [22] ©1991 IEEE.]

and signal light propagate in the same direction along the fiber and amplified spontaneous emission is ignored (low gain approximation). The changes in pump and signal powers after passage through a slice of doped fiber are

$$\frac{dP_s}{dz} = g(z)\, P_s(z) \tag{13.7}$$

$$\frac{dP_p}{dz} = \alpha_p(z)\, P_p(z) \tag{13.8}$$

As the magnitude of the signal increases along the fiber, the upper-state population is reduced according to Equation 13.5. This results in increased pump absorption in the increment of fiber as indicated in Equation 13.4. These equations can be integrated numerically to solve for the signal and pump power as a function of length along the doped fiber.

The net amplifier gain is found from Equations 13.2 and 13.3. It depends on the average inversion level of the erbium ion population:

$$G = \exp\{\Gamma_s[\sigma_e\,[N_2] - \sigma_a\,[N_1]]L\} \tag{13.9}$$

The average inversion level is set by the pump and signal power levels. The gain dependency on pump power is a figure of merit for different EDFs. Figure 13.8 plots the gain versus pump power for an EDFA for two input powers. The amplifier gain coefficient in units of dB/mW is the maximum slope of the tangent to the curve that passes through the origin. Given the large emission and absorption cross-sections near 1530 nm, the highest gain coefficient is expected (from Equation 13.9) at this wavelength, provided the amplifier is highly inverted. The importance of the overlap factor is also expressed by

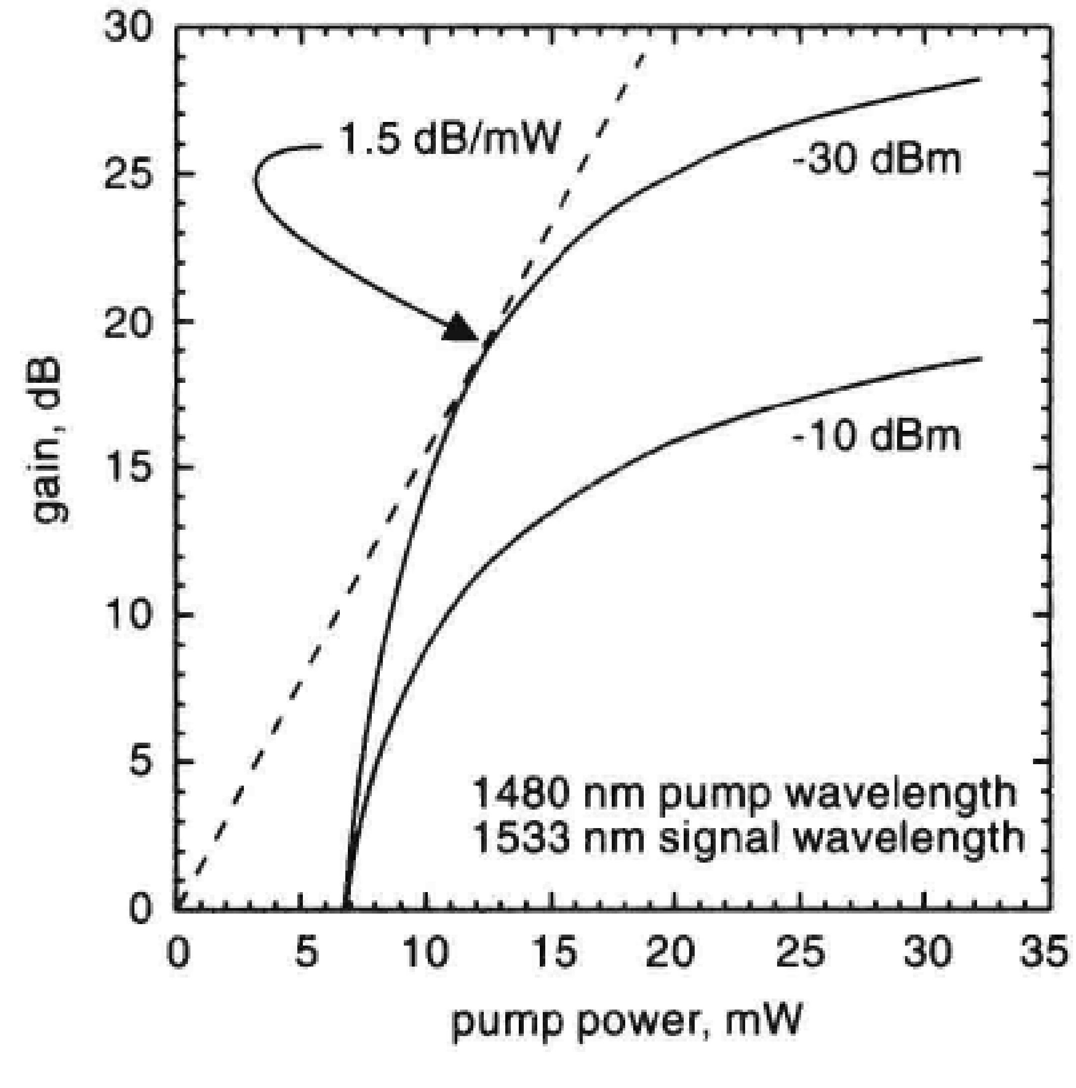

Figure 13.8 Measurement of gain dependence on EDFA pump power.

Equation 13.9. Increasing the fiber numerical aperture increases the overlap factor Γ_s resulting in improvement to the small-signal gain. For this reason, amplifiers designed to obtain the maximum gain per milliwatt of pump power tend to have fibers with high numerical apertures. Values for EDF numerical aperture typically range between 0.2 and 0.4.

13.2.1 Small-Signal Gain

The small-signal region corresponds to input power levels where the signal amplification does not reduce, appreciably, the gain of the amplifier. For the purposes of defining the small-signal gain region, it is useful to estimate the effective input noise $P_{\text{noise, eff}}$ of the amplifier.

$$P_{\text{noise, eff}} \approx 2h\nu B_o \sim 30\ \text{nW/nm for } \lambda = 1.5\ \mu\text{m} \tag{13.10}$$

where $h\nu$ is the photon energy (J) and B_o is the optical bandwidth (Hz) of the amplifier. The effective input noise multiplied by the amplifier gain yields the output noise power of the amplifier. As the input signal power becomes significant relative to the input noise power, it plays a larger role in determining the inversion level, N_2. Changes in N_2 result in changes in gain. As long as the input power is small compared to $P_{\text{noise,eff}}$, its affect on the amplifier will be insignificant and the amplifier will be in small signal operation. The amplifier gain can be plotted as a function of input power as shown in Figure 13.9. This type of curve can help identify the small signal input power region. Even at very low input power levels, a reduction in signal gain can occur.

As an example, an amplifier with 10 nm optical bandwidth about 1.55 μm has an effective input noise of ~ 0.3 μW. Therefore, the input signal probe should be less than 30 nW, or –45 dBm, to avoid affecting the amplifier gain. The small-signal gain is sometimes defined as the gain corresponding to a small, but practical input level, (for example, –30 dBm) with the understanding that compression effects may have already occurred to some degree.

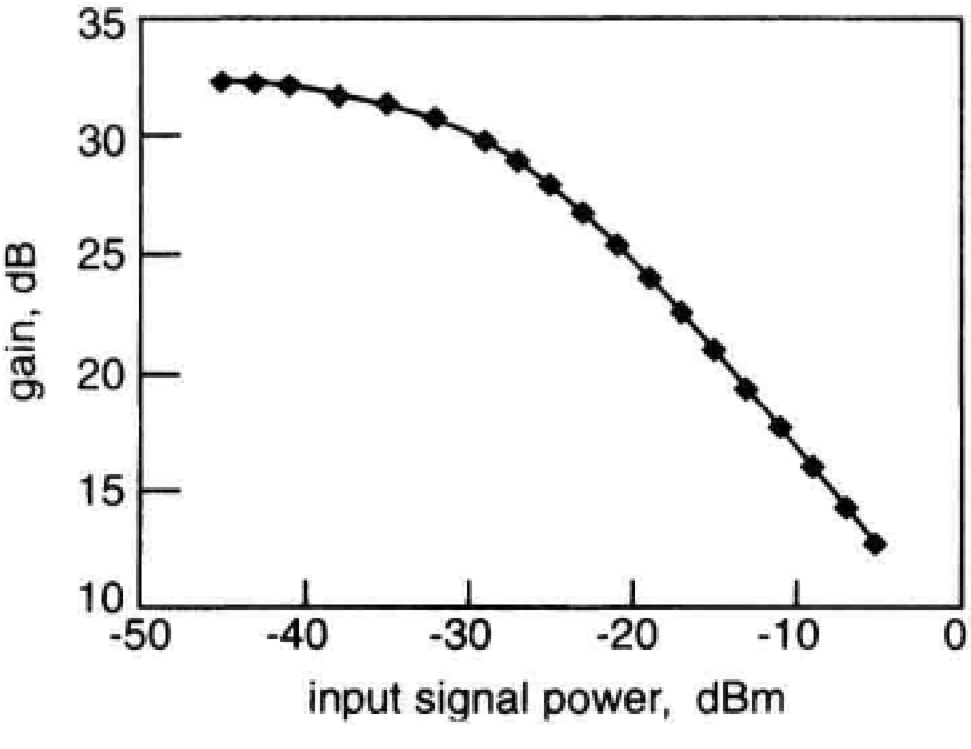

Figure 13.9 EDFA gain dependence on input signal power.

13.2.2 Saturated Gain

The EDFA is usually operated at input signal levels large enough to cause saturation of the amplifier gain. Gain saturation is observed in Figure 13.9 as a reduction in gain with an increase in signal power. The amplifier gain in an ASE-free model can be written implicitly as a function of the ratio of the output power, P_{out} to the saturation power, P_{sat}.[17]

$$G = G_0 \exp\left[-\frac{G-1}{G} \frac{P_{\text{out}}}{P_{\text{sat}}} \right] \tag{13.11}$$

Where G_0 is the small-signal gain as discussed earlier. The saturation power, P_{sat} at a specific wavelength is the power required to invert a slice of erbium-doped fiber sufficiently to obtain optical transparency in other words zero gain.

P_{sat} is written as:

$$P_{\text{sat}} = \frac{Ahv}{\sigma_a \tau_{sp}} \tag{13.12}$$

where A is the mode-field area, σ_a is the absorption coefficient as discussed previously, and $\tau_{sp} \sim 10$ ms, is the spontaneous lifetime of the ion in the metastable state.

The saturation power can be modified by increasing the fiber mode-field area A. The amplifier 3 dB compression point is a figure of merit describing the output power capabilities of the amplifier. This is the output power at which the amplifier gain is reduced to 50% of its small signal value. From Equation 13.11, the 3 dB compression power is proportional to the saturation power: $P_{\text{out}}^{-3\text{dB}} = \ln(2)\, P_{\text{sat}}$.[26] High-power amplifiers tend to have active fibers with larger mode-field diameters to increase the saturation power and hence the 3 dB compression point.

13.2.3 Polarization Hole-Burning

In an experiment where a single wavelength channel was passed through a link employing a large number of optical amplifiers, it was discovered that the small-signal optical gain in the polarization orthogonal to the large-signal polarization was greater than the large signal gain.[5] This polarization-dependent gain, (PDG), occurred even when the large-signal polarization was changed to various states, to differentiate it from the usual polarization-dependent loss. Subsequent studies provided confirmation to this effect whose origin is due to polarization dependence of the emission cross-section of the erbium ions in the silica host. This effect leads to polarization hole-burning with a hole depth which depends on the degree of amplifier compression C_p of :[27]

$$PHB \approx 0.027C_p - 0.001C_p^2 \text{ [dB]} \tag{13.13}$$

for $C_p < 8$ dB. The amplifier compression is in units of decibels. PDG induced by polarized pump light was also observed, with a magnitude of 0.07 dB for the particular amplifier studied.[27] Since the PHB effect within each amplifier is small (~0.2 dB), its impact is more important in large concatenations of amplifiers. Fortunately, the gain recovery for the PHB is slow, and rapid polarization modulation of the input signal has been shown to effectively suppress the effect of PDG.[28,29]

13.2.4 Spectral Hole-Burning

A localized signal power-dependent spectral gain depression is referred to as spectral hole-burning, (SHB).[30] SHB occurs in EDFAs when a strong signal reduces the average ion population contributing to gain at a particular wavelength in excess of the global reduction.

SHB is relatively small in EDFAs since these amplifiers are predominantly homogeneously broadened. A homogeneously broadened amplifier has the property that an input signal at any wavelength in the amplification band can equally access the total energy stored within the amplifier. Homogeneous broadening in EDFAs is caused by the rapid transport of energy across the different Stark-broadened lines within a specific manifold (in other words, $^4I_{15/2}$ or $^4I_{13/2}$ in Figure 13.4).[31] This tends to reduce the extent of the SHB. The presence of phonons (heat exchange) is responsible for the EDFA homogeneous broadening.

Research has shown that at room temperature, SHB is relatively small for EDFAs with a dependency of ~ 0.3 dB per dB increase in gain compression.[32] The effect of SHB tends to be more significant in the 1530 nm wavelength region than the 1550 nm region. A plot of the inhomogeneous gain saturation caused by SHB is shown in Figure 13.10. This measurement was performed using an edge-emitting LED (EELED) probe in combination with a time-domain extinction technique to accurately measure gain as discussed in Section 13.5. The full-width half-maximum of SHB hole-widths are typically in the range of ~ 3 to ~ 10 nm in the EDFA gain spectrum, the narrowest hole-widths occurring near the 1530 nm region.

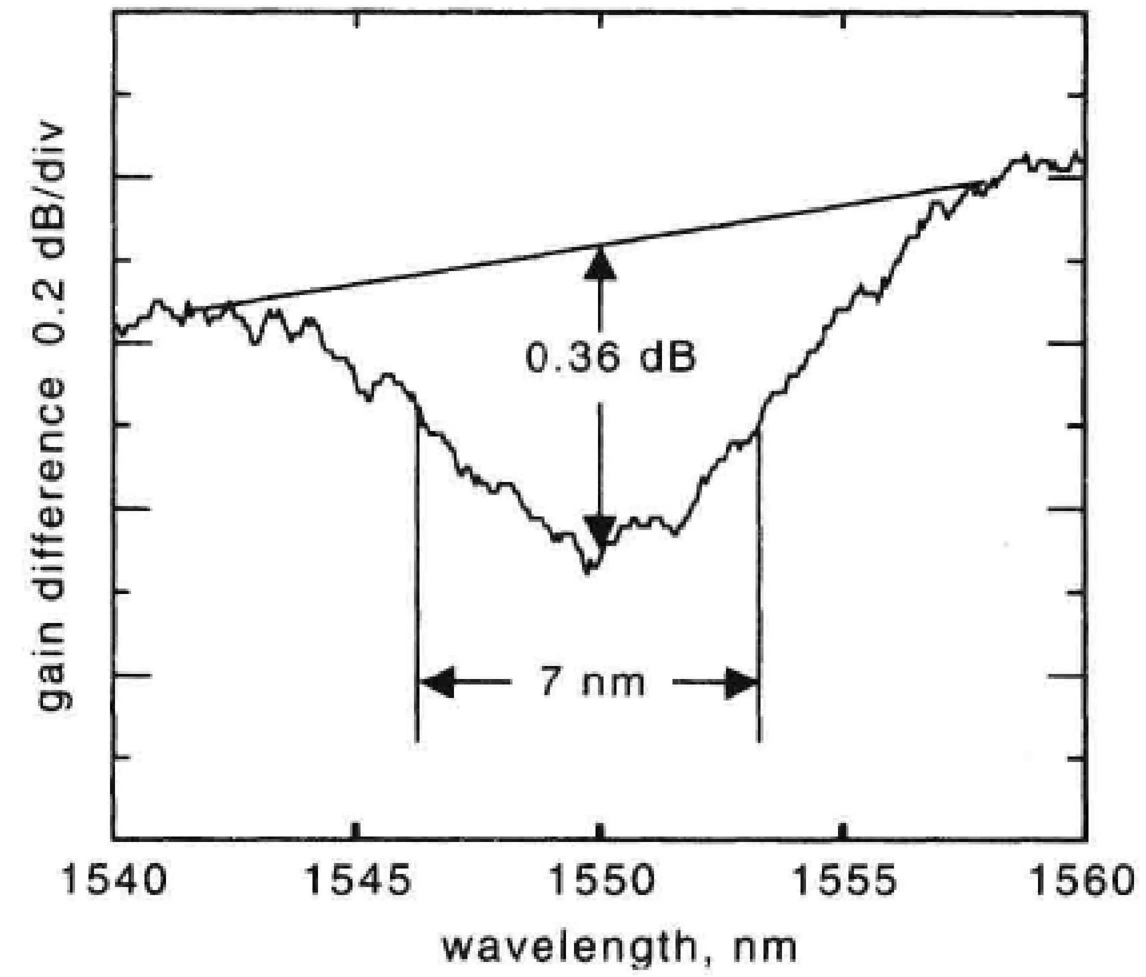

Figure 13.10 EDFA spectral hole-burning at a wavelength of 1550 nm.

13.2.5 Gain Tilt, Gain Slope

The amplifier gain tilt has important implications in systems sensitive to distortion brought on by the combination of laser chirp and amplifier gain slope.[33] In long-haul WDM systems, the amplifier gain spectrum must remain flat to avoid dominance of the power of one channel over the rest. The change or tilt in the amplifier gain spectrum that occurs when wavelength channels are added or dropped to the WDM data stream degrades performance of long-haul telecommunications systems. Gain tilt is defined here as the ratio of the gain change at a test wavelength to the change in gain at a reference wavelength where the gain changes are caused by a change in input conditions. For a homogeneously broadened amplifier, gain tilt is invariant with input power. Once the gain tilt is characterized for one set of input conditions, it can be applied to predict the amplifier gain tilt for other input conditions.

A related concept is the amplifier gain slope. It is important to distinguish between the static gain slope (see Figure 13.11) and the dynamic gain slope. The differences between the static and dynamic gain slopes are due to the change in the amplifier inversion level that results from a change in the wavelength of the strong saturating input signal.

The static gain slope, m_s is defined by

$$m_s(\lambda_o) = \frac{G_s(\lambda_o + \Delta\lambda) - G_s(\lambda_o - \Delta\lambda)}{2\Delta\lambda} \tag{13.14}$$

where $G_s(\lambda_o \pm \Delta\lambda)$ is the gain at the saturating signal wavelength as the saturation signal wavelength is tuned to $\lambda_o \pm \Delta\lambda$.

The dynamic gain slope, m_d is defined as

$$m_d(\lambda_o) = \frac{G_p(\lambda_o + \Delta\lambda) - G_p(\lambda_o - \Delta\lambda)}{2\Delta\lambda} \tag{13.15}$$

where $G_p(\lambda_o \pm \Delta\lambda)$ is the gain of a small signal probe at the wavelength of $\lambda_o \pm \Delta\lambda$. A large input signal maybe present to set the amplifier gain saturation for the gain slope

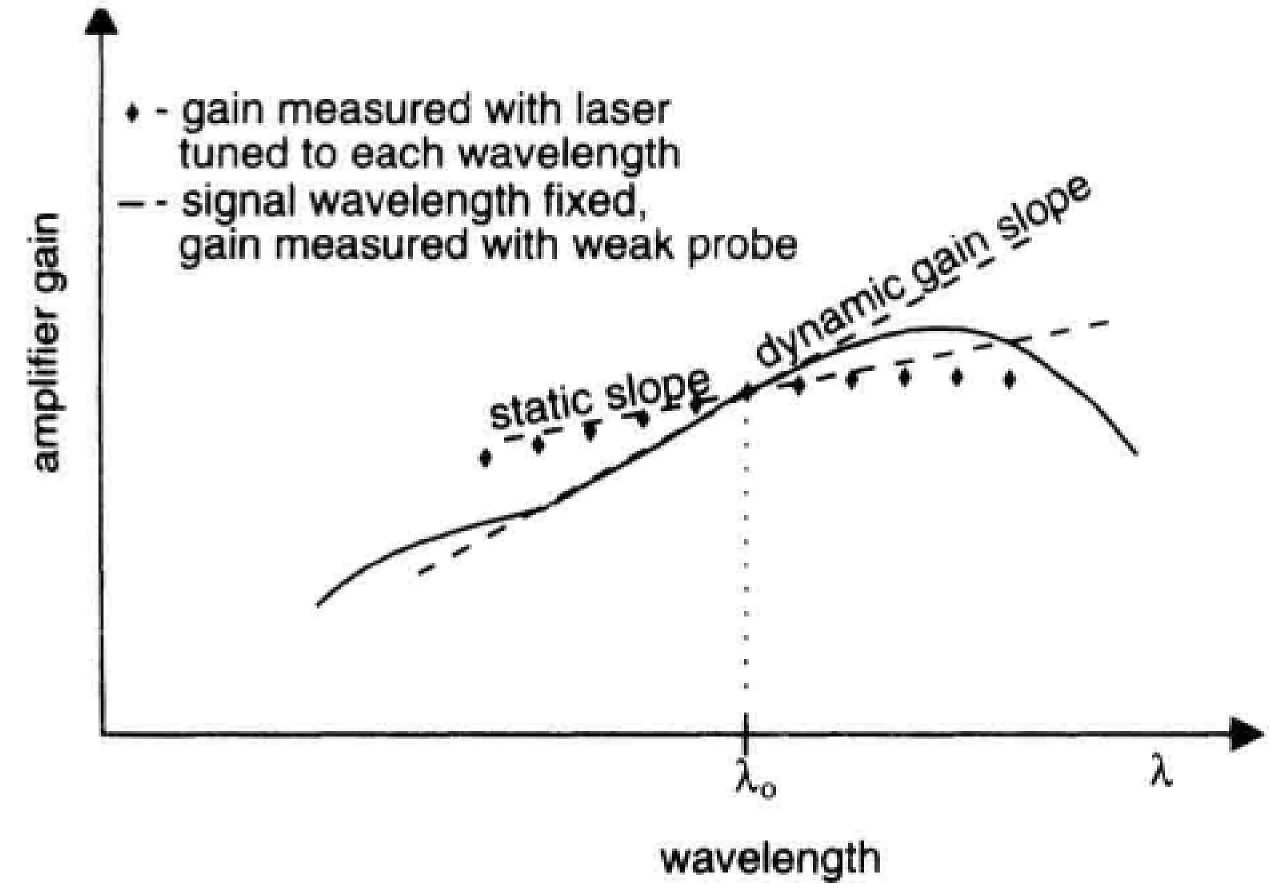

Figure 13.11 Illustration of static and dynamic gain slope.

measurement. The probe for characterizing the dynamic gain slope may be a continuously tunable laser set to low output power, or a broadband light source such as an EELED.

13.3 NOISE

In this section, the noise associated with an amplified optical signal is discussed. Noise in two domains will be considered: optical field noise, and intensity/photocurrent noise. Optical field noise refers to the optical noise spectrum measured with the typical tuning-filter-based (for example, grating) OSA. This type of noise is usually characterized over the EDFA spectral window. ASE from an optical amplifier is the main contributor to this noise. Intensity/photocurrent noise refers to the power or current fluctuations associated with the optical beam. This noise is typically characterized up to tens of GHz in bandwidth. The intensity noise spectrum refers to the power spectrum of the optical intensity prior to detection. The intensity noise spectrum is different than the photocurrent spectrum in subtle ways when shot noise is considered. For this reason, special attention has been applied in the discussion on shot noise in view of its representation in both the intensity noise and photocurrent noise domains. The concepts of power spectral densities, relative intensity noise, and SNR will be used in this section.

13.3.1 Optical Noise

Within the amplifying section of optical fiber, the excited erbium ion can decay to its ground state through stimulated emission caused by a signal photon, or, spontaneously. The spontaneously emitted photon has random direction and phase. Some of the spontaneously emitted photons are captured by the propagating mode of the optical fiber. These captured photons will be amplified as they travel inside the doped fiber. This results in ASE. The total ASE power is summed over all the spatial modes that the optical fiber supports in an optical bandwidth, B_o. In the typical erbium-doped fiber there are two propagating modes of polarization with a total ASE power equal to:

$$P_{\mathrm{ASE}} = 2n_{sp}\, h\nu\, (G-1)B_o \tag{13.16}$$

where $h\nu$ is the photon energy and G is the amplifier gain.

The spontaneous emission factor, n_{sp}, is given by

$$n_{sp} = \frac{\sigma_e N_2}{\sigma_e N_2 - \sigma_a N_1} \tag{13.17}$$

with σ_e, σ_a, N_1, and N_2 as defined in Section 13.2. The SE factor, n_{sp} is a measure of the quality of the inversion of the optical amplifier. An n_{sp} value near unity is possible with strong pumping in the 980 nm band. This is the lowest value of n_{sp} that can be attained. It corresponds to nearly complete inversion ($N_1 \sim 0$) of the amplifier. Complete inversion, where $N_2 = N_t$ results in the lowest optical noise figure (discussed in Section 13.4).

Depletion of pump power along the erbium-doped fiber causes the N_2 population to vary as well. According to Equation 13.17, the SE factor depends on N_2 and it will vary with length along the active fiber. Usually n_{sp} is defined as the effective or integrated value for the amplifier. When the 1480 nm pump wavelength is used, complete inversion is not possible since the pump and signal share the same ground and excited states. Pump photons are not only absorbed but also contribute to stimulated emission since the emission cross-section is nonzero at this wavelength. The result is an amplifier with incomplete inversion and a higher SE factor, n_{sp}. This translates to a direct increase in the noise figure of the amplifier. The effective values for n_{sp} typically range from 1 (980 pumping) to 4.

In noise figure calculations it is sometimes useful to work with the ASE spectral density (W/Hz) in a single polarization:

$$\rho_{\text{ASE}} \overset{\Delta}{=} n_{sp}\, hv(G-1) \tag{13.18}$$

Given a large enough amplifier gain, the ASE can become significant, resulting in saturation of the amplifier gain by the generated ASE. For this reason EDFAs can be applied as ASE sources for a variety of applications ranging from gyroscopes to "white light" interferometry (Chapter 10).

Example

Find the ASE power generated by an amplifier supporting two polarizations with 20 dB gain, 30 nm bandwidth, a 1.55 μm center wavelength and an n_{sp} factor of 1.5.

Solution

Referring to Equation 13.16, the bandwidth in Hertz is calculated:

$$B_o \approx \frac{c\Delta\lambda}{(\lambda_o)^2} \tag{13.19}$$

This yields a bandwidth B_o of 3.75 THz. The photon energy was computed to be 1.28×10^{-19} *J*. Using $G = 100$ and Equation 13.16 the total ASE power is 143 μW. The ASE power produced in a 1 nm bandwidth is plotted as a function of optical gain in Figure 13.12 for various effective values of n_{sp}.

13.3.2 Intensity/Photocurrent Noise

Before embarking into the discussion on noise, the basic conversion of light intensity into electrical current by an optical receiver is discussed in terms of the receiver responsivity. The average photocurrent, i_{dc} generated in a photodetector by an optical source of average power $<P>$ is:

$$i_{dc} = \mathfrak{R} < P > \tag{13.20}$$

where the detector responsivity is defined as:

$$\mathfrak{R} = \frac{\eta q}{hv} \quad [A/W] \tag{13.21}$$

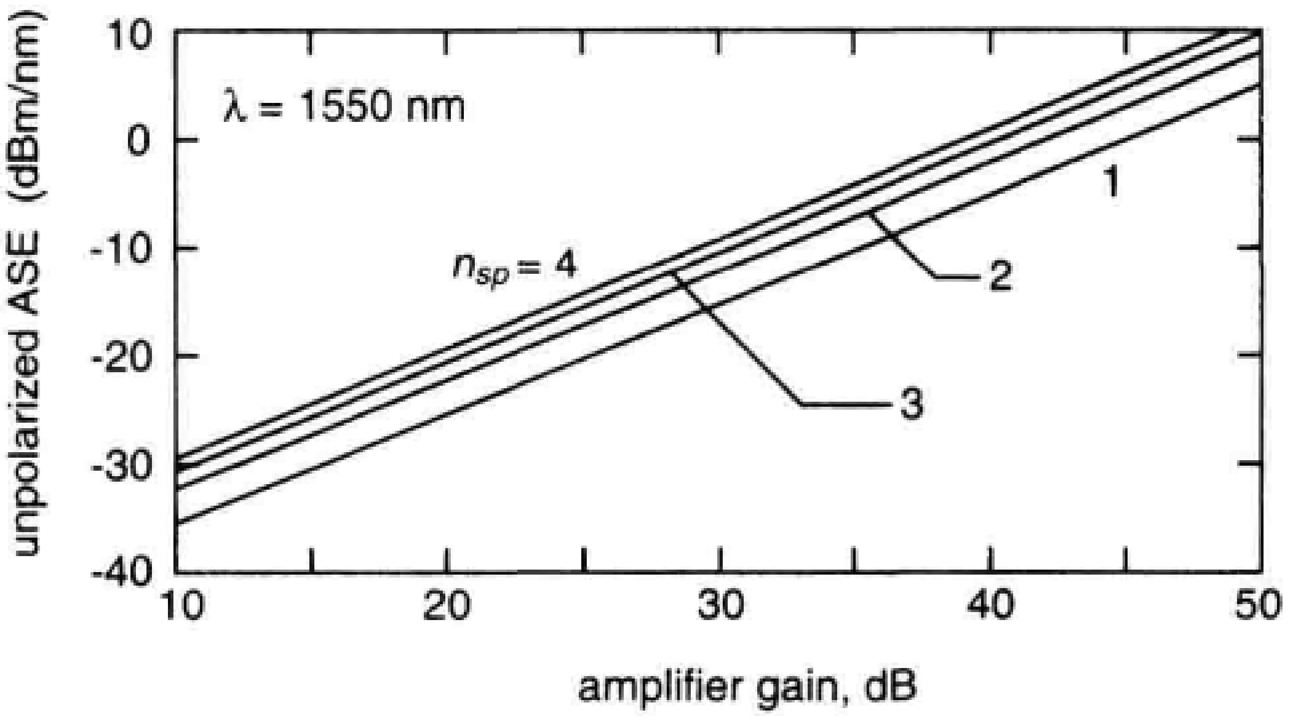

Figure 13.12 ASE power produced in 1 nm bandwidth as a function of length for various spontaneous emission factors. Add 2.3 dB to compute power at a wavelength of 1300 nm.

The light collection quantum efficiency of the receiver is denoted by η. The electronic charge, q is equal to 1.602×10^{-19} coul. At a wavelength of 1.55 μm, the photon energy $h\nu$, is 1.283×10^{-19} J. The light collection quantum efficiency η includes all optical losses that are part of the optical receiver. This can include optical coupling loss as well as the quantum efficiency of the receiver photodetector.

In addition to the average optical power, intensity noise is also present. Intensity noise is a significant limiting factor in optical communications systems. Photodetectors convert intensity noise directly into electrical noise. While the optical field noise can have both amplitude or phase noise, photodetectors do not directly respond to the phase noise. However, phase noise can be converted to intensity noise by interference effects. The following intensity noise types are commonly encountered in optical systems:

- Shot noise,
- Signal-spontaneous beat noise,
- Spontaneous-spontaneous beat noise, and
- Interference noise.

The two beat noises and the interference noise fall in the category of excess noise. It is important to differentiate between shot noise and the excess noise since the resulting photocurrent noise they generate depends differently on the responsivity of the receiver detector. Intensity noise is defined in terms of a power spectral density, $S_p(f)$ of the light intensity fluctuations. The power spectral density of the optical intensity variations is related to the power spectral density of the electrical current $S_i(f)$ variations according to:

$$\begin{aligned} S_P(f) &= \frac{1}{\mathcal{R}^2} S_i(f) && \text{for excess noise} \\ S_P(f) &= \frac{1}{\mathcal{R}} \frac{h\nu}{q} S_i(f) && \text{for shot noise} \end{aligned} \tag{13.22}$$

$S_i(f)$ is measured with an electrical spectrum analyzer. When $S_p(f)$ is integrated over a bandwidth, it yields the mean-square optical noise power in the integration bandwidth.

It is useful to refer the noise density to the average optical power by way of the relative intensity noise (RIN_o). RIN_o is defined with respect to the power spectral density of the optical intensity as:

$$\mathrm{RIN}_o\,(f) = \frac{S_P\,(f)}{< P >^2} \quad [\mathrm{Hz}^{-1}] \tag{13.23}$$

where $<P>$ is the average optical power. This is indicated in Figure 13.13 which illustrates the spectral density of the optical intensity variations with frequency as well as the average dc intensity. Sometimes the RIN concept is used to describe the fluctuations on the electrical current instead of the light intensity. To avoid confusing the two RINs, the electrical relative intensity noise will be referred to here as RIN_e. RIN_e is defined as:

$$\mathrm{RIN}_e\,(f) = \frac{S_i(f)}{[i_{dc}]^2} \quad [\mathrm{Hz}^{-1}] \tag{13.24}$$

Shot Noise. Shot noise has its origins in the uncertainty of the time of arrival of electrons or photons at a detector. When the dominant noise is due to shot noise it is referred to as shot-noise-limited or quantum-limited. Both the laser signal and ASE contribute shot noise. In this discussion, the shot noise will be examined in both the intensity and electrical domains. This will avoid confusion with respect to the impact of the quantum efficiency η of the optical detection. The shot-noise spectral densities are given by:

$$\begin{aligned} S_i(f)\big|_{\mathrm{shot}} &= 2q\, i_{dc} \quad [A^2/\mathrm{Hz}] \\ S_P(f)\big|_{\mathrm{shot}} &= \frac{2\,h\nu i_{dc}}{\mathcal{R}} = 2h\nu < P > \quad [W^2/\mathrm{Hz}] \end{aligned} \tag{13.25}$$

where i_{dc} and $<P>$ are the average values for the electrical current and optical power respectively.

The RIN for the intensity and electrical domains are derived using Equations 13.23, 13.24, and 13.25:

$$\begin{aligned} \mathrm{RIN}_e\big|_{\mathrm{shot}} &= \frac{2q}{i_{dc}} \qquad [\mathrm{Hz}^{-1}] \\ \mathrm{RIN}_o\big|_{\mathrm{shot}} &= \frac{2\eta\, q}{i_{dc}} = \frac{2h\nu}{< P >} \end{aligned} \tag{13.26}$$

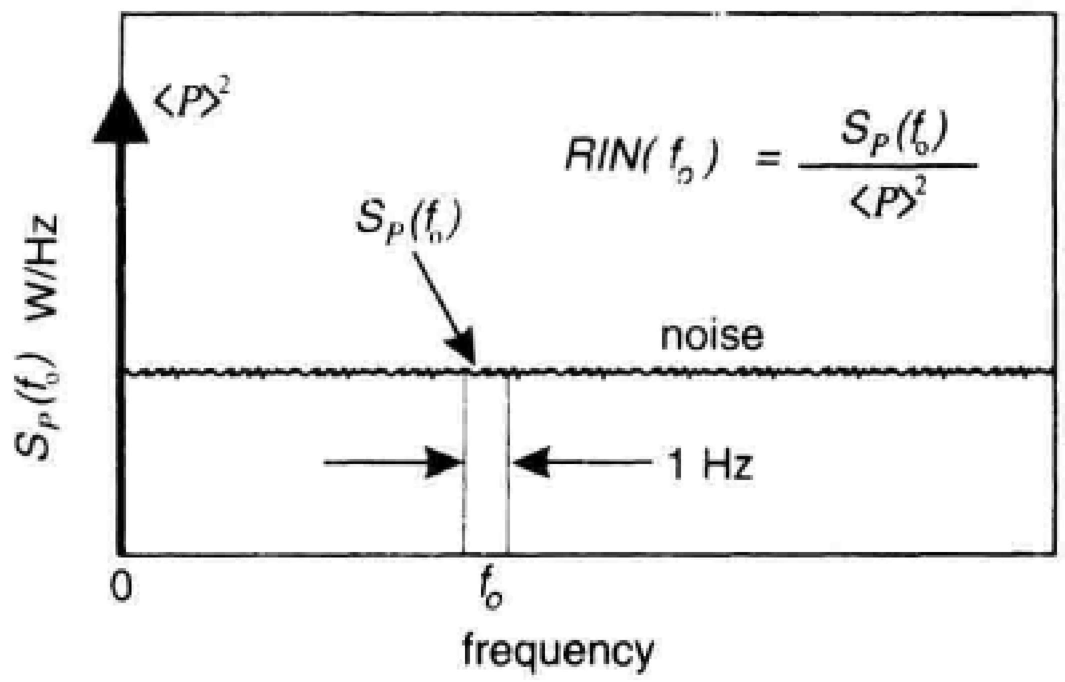

Figure 13.13 Quantification of noise in terms of spectral density and RIN.

$\text{RIN}_e|_{\text{shot}}$ is larger than $\text{RIN}_o|_{\text{shot}}$ when the quantum efficiency of the optical detection is less than unity. $\text{RIN}_o|_{\text{shot}}$ improves (gets smaller) with an increase in optical power. Any optical signal can be made to be shot-noise limited. By attenuating the optical signal (decreasing η), the excess noise sources (discussed later) reduce in magnitude faster than the shot noise, and the shot noise will eventually dominate. The $\text{RIN}_e|_{\text{shot}}$ is plotted in Figure 13.14 as a function of photodetector current. From Figure 13.14, the RIN produced by a 1 mW shot-noise-limited laser source is approximately −155 dB/Hz.

A special class of light, known as squeezed-light has an associated intensity noise content below the conventional shot noise level. The intensity noise is compressed or squeezed at the expense of an increase in phase noise. The degree of squeezing is rapidly lost when the squeezed light passes through an optical amplifier or a lossy medium.

Signal-Spontaneous Beat Noise. Interference between signal light and ASE causes intensity fluctuations known as signal-spontaneous beat noise.[34] This noise is unavoidable in EDFA-based systems and is one of the primary noise contributions in optically amplified communications systems. This beat noise is analogous to the case of two frequencies beating in a heterodyne mixer to generate a difference frequency. Recall that the mixing product is polarization dependent, so the signal will beat only with those ASE components in the same polarization as the signal. Since the ASE is typically unpolarized, only one-half will contribute to the sig-sp beat noise density. This mixing process is illustrated in Figure 13.15. The bandwidth of optical receivers is typically less than 50 GHz, (~ 0.4 nm @ $\lambda = 1.55\ \mu\text{m}$) so only those ASE spectral components within 0.4 nm of the signal wavelength contribute to the detected signal-spontaneous beat noise.

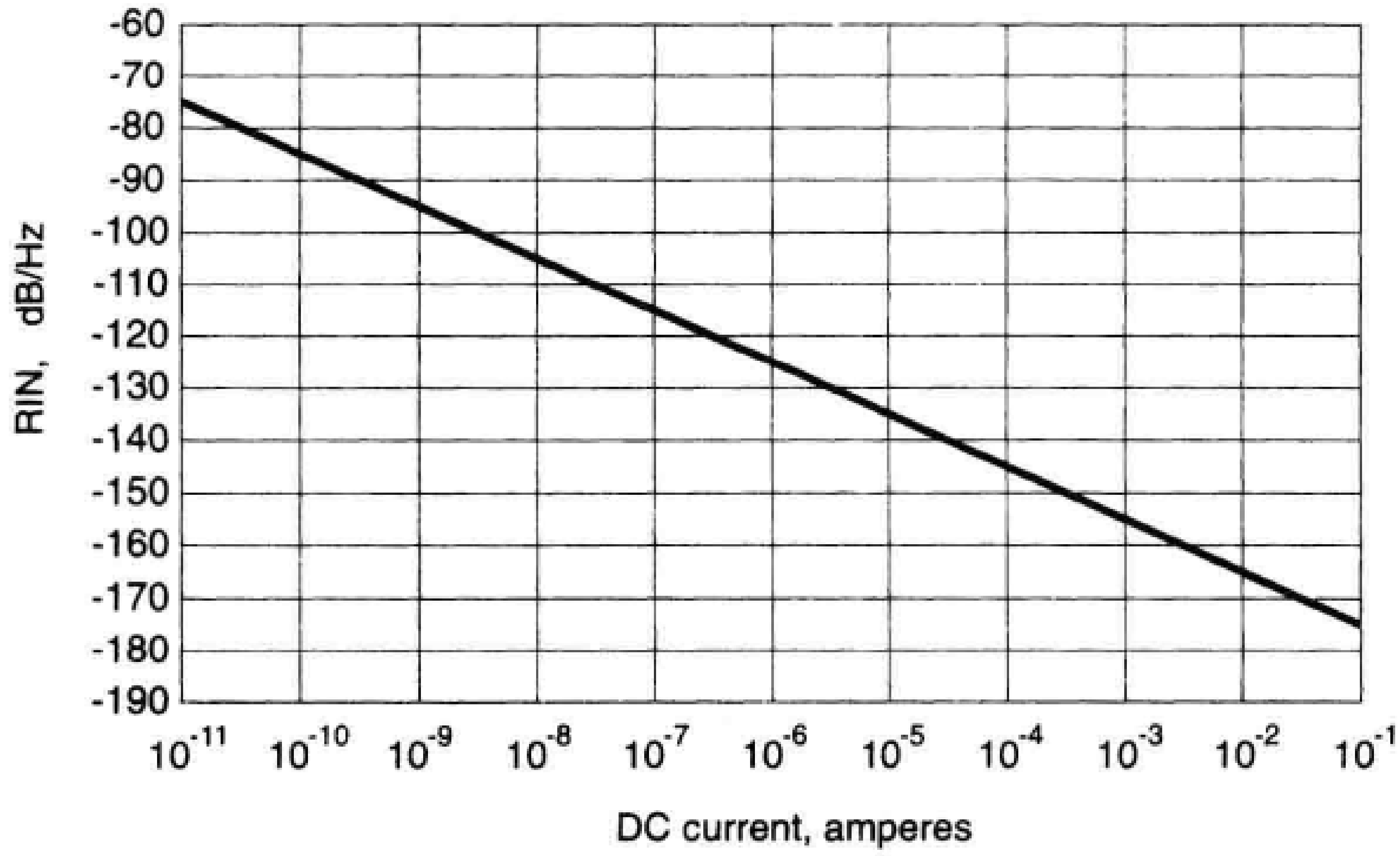

Figure 13.14 Shot-noise RIN dependency on average current.

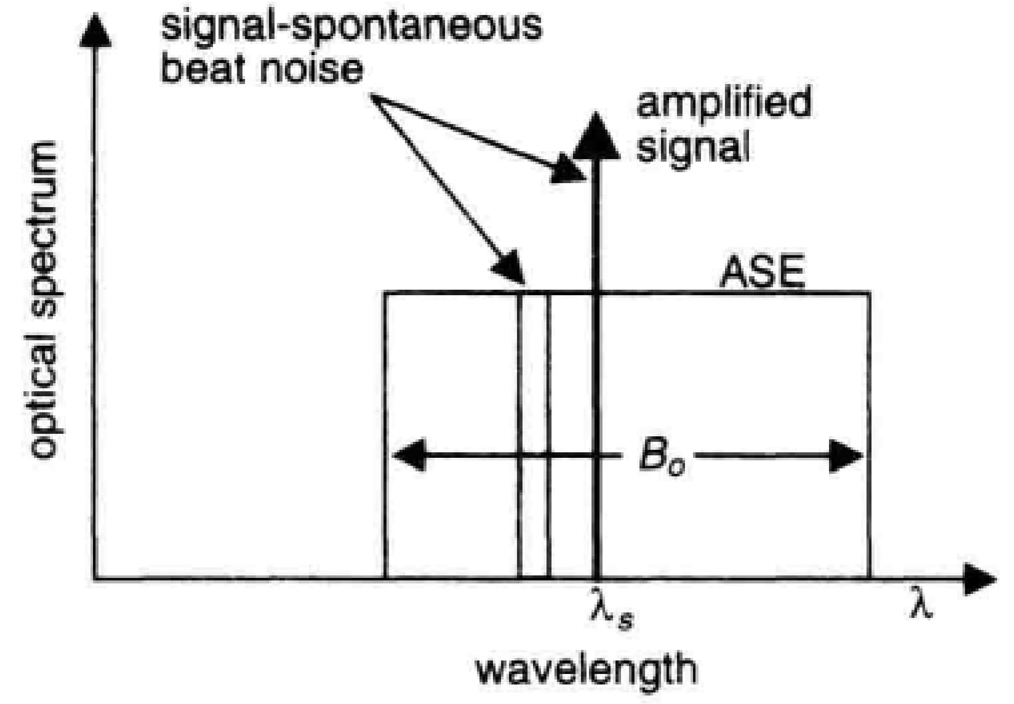

Figure 13.15 Signal-spontaneous beat noise between amplified signal and the spectral components of the ASE.

The detected current noise density measured with an electrical spectrum analyzer has a low-frequency ($f < B_o/2$) value of:

$$S_{i_{sig-sp}}(f) = 4\Re^2 G P_s \rho_{\text{ASE}} \quad [A^2/\text{Hz}] \tag{13.27}$$

According to Equations 13.18 and 13.27, the signal-spontaneous beat noise varies as the square of the optical gain and linearly with input signal power. The use of the RIN concept with signal-spontaneous beat noise has the complication due to the average power contribution of the ASE. Taking the average unpolarized ASE power as P_{ASE}, the signal-spontaneous beat noise RIN is given by:

$$\text{RIN}_{sig-sp} = \frac{4GP_s\rho_{\text{ASE}}}{(GP_s + P_{\text{ASE}})^2} \quad [\text{Hz}^{-1}] \tag{13.28}$$

The following observations can be made about sig-sp beat noise:

- $S_{i_{sig-sp}}(f)$ increases linearly with the input signal.
- $S_{i_{sig-sp}}(f)$ does not depend on the ASE spectral width, B_o ($f_o << B_o$).
- $S_{i_{sig-sp}}(f)$ can not be reduced by placing a polarizer at the amplifier output.
- RIN_{sig-sp} is approximately independent of gain when $G > 10$.

Spontaneous-Spontaneous Beat Noise. The beating between the different spectral components of the SE results in intensity noise known as spontaneous-spontaneous, (sp-sp) beat noise.[34] This is illustrated in Figure 13.16. Each pair of ASE spectral components generates an intensity beat tone at their difference frequency. Thus, the entire ASE spectrum contributes to the sp-sp intensity beat noise. If the ASE is unpolarized, the ASE in each of two orthogonal polarizations will contribute to the total sp-sp beat noise. From Figure 13.16, the maximum frequency extent of the beat noise is equal to the maximum width of the ASE spectrum. Thus the beat noise could well have an intensity spectrum beyond 1000 GHz, and certainly beyond the bandwidth of electronic receivers. The frequency content of the photocurrent noise generated by sp-sp beating can be significantly reduced by placing an optical filter before the photodetector. This is easily understood from Figure 13.16 where the total number of possible beating pairs decreases as the opti-

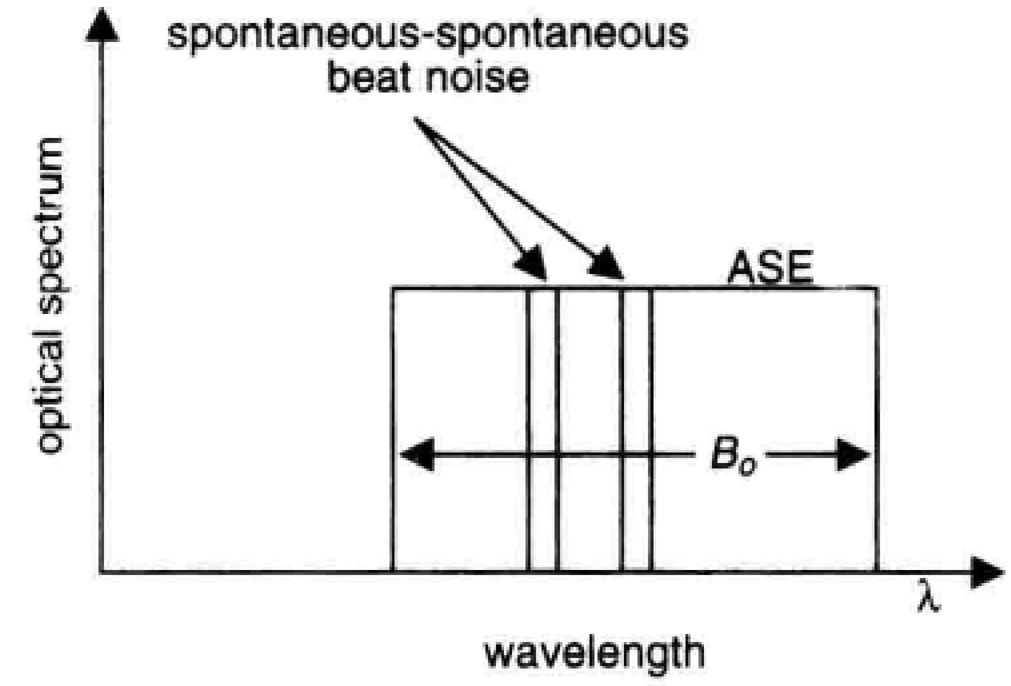

Figure 13.16 Spontaneous-spontaneous beat noise between ASE spectral components.

cal bandwidth decreases. The photocurrent spectrum for the case of an unpolarized ASE spectrum with a rectangular shape is:

$$S_i(f) = 4\mathfrak{R}^2\rho_{\text{ASE}}^2\, B_o\Lambda(f/B_o) \quad [A^2/Hz] \tag{13.29}$$

where $\Lambda(f/B_o)$ is the triangle function which has a value of unity at 0 Hz and linearly decreases to 0 at $f = B_o$.

In general, the peak magnitude of the RIN is dependent on the actual shape of ASE spectrum. This is discussed also in Section 13.5.2. When the signal power is small or absent, the RIN caused by sp-sp beat noise varies inversely with the spectral width of the ASE source. A rectangle-shaped ASE spectrum delivers the most RIN of any optical shape[35] with a value equal to:

$$\text{RIN}_{\text{rect}} = \frac{1}{B_o} \quad \text{(for unpolarized light)} \tag{13.30}$$

Reducing the optical bandwidth increases the RIN. This simple relation can also be remembered as follows: RIN is related to the inverse of the number of degrees of freedom the system supports. In the case of ordinary telecom-grade optical fiber, and intensity detection, there are two spatial orientations for polarization, and $B_o/(1\text{ Hz})$ possibilities for bandwidth. For polarized light, the RIN increases by a factor of two since one degree of freedom is absent.

Table 13.2 gives the analytical relations for the frequency dependent sp-sp RIN for several different ASE spectral shapes. The optical field shape refers to the ASE spectral shape as measured with an OSA.

To provide a comparison of the way the different noise types discussed vary with signal power, the shot, sig-sp and sp-sp beat noises are plotted in Figure 13.17. The noise levels are plotted versus amplified signal power for an amplifier having a 5 nm passband and 37 dB gain. Thermal noise is also shown for an electrical system noise figure of 8 dB and a 50 ohm impedance. At low signal levels, the noise is dominated by sp-sp beat noise. Eventually, sig-sp beat noise dominates, increasing linearly with signal power. At low

Table 13.2 Relationship Between Unpolarized Optical Field Spectrum and RIN.

Optical field shape	Normalized $S_E(\nu)$	RIN(f)	RIN$(f=0)$
Rectangle	$\Pi\left(\frac{\nu-\nu_o}{B_o}\right)$	$\frac{1}{B_o}\Lambda\left(\frac{f}{B_o}\right)$	$\frac{1}{B_o}$
Gaussian	$\exp\left\{-(4\ln 2)\left(\frac{\nu-\nu_o}{B_o}\right)^2\right\}$	$\frac{1}{B_o}\frac{\sqrt{2ln2}}{\sqrt{\pi}}\exp\left\{-(2\ln 2)\left(\frac{f}{B_o}\right)^2\right\}$	$\frac{0.66}{B_o}$
Lorentzian	$\frac{B_o^2}{B_o^2+(2(\nu-\nu_o))^2}$	$\frac{B_o/\pi}{B_o^2+f^2}$	$\frac{0.32}{B_o}$

signal powers the shot noise is actually dominated by the ASE average power contribution.

Reflection Noise/Multipath Interference. The presence of optical reflections within the optical amplifier, such as those shown in Figure 13.18 will cause an interferometric conversion of laser phase noise into intensity noise. This intensity noise degrades the SNR at the optical receiver.[6,7] The converted noise is known as multipath interference noise or MPI. Important parameters determining the magnitude of MPI are the reflection levels, the optical gain, the signal linewidth and the time delay between the reflectors. The presence of optical gain can greatly increase the impact of small reflections. The worst-case RIN occurs when the polarizations of the delayed and non-delayed beams are aligned and the average interference phase is near quadrature. The interferometer is said to be in quadrature when the output power is halfway between its minimum and maximum values.

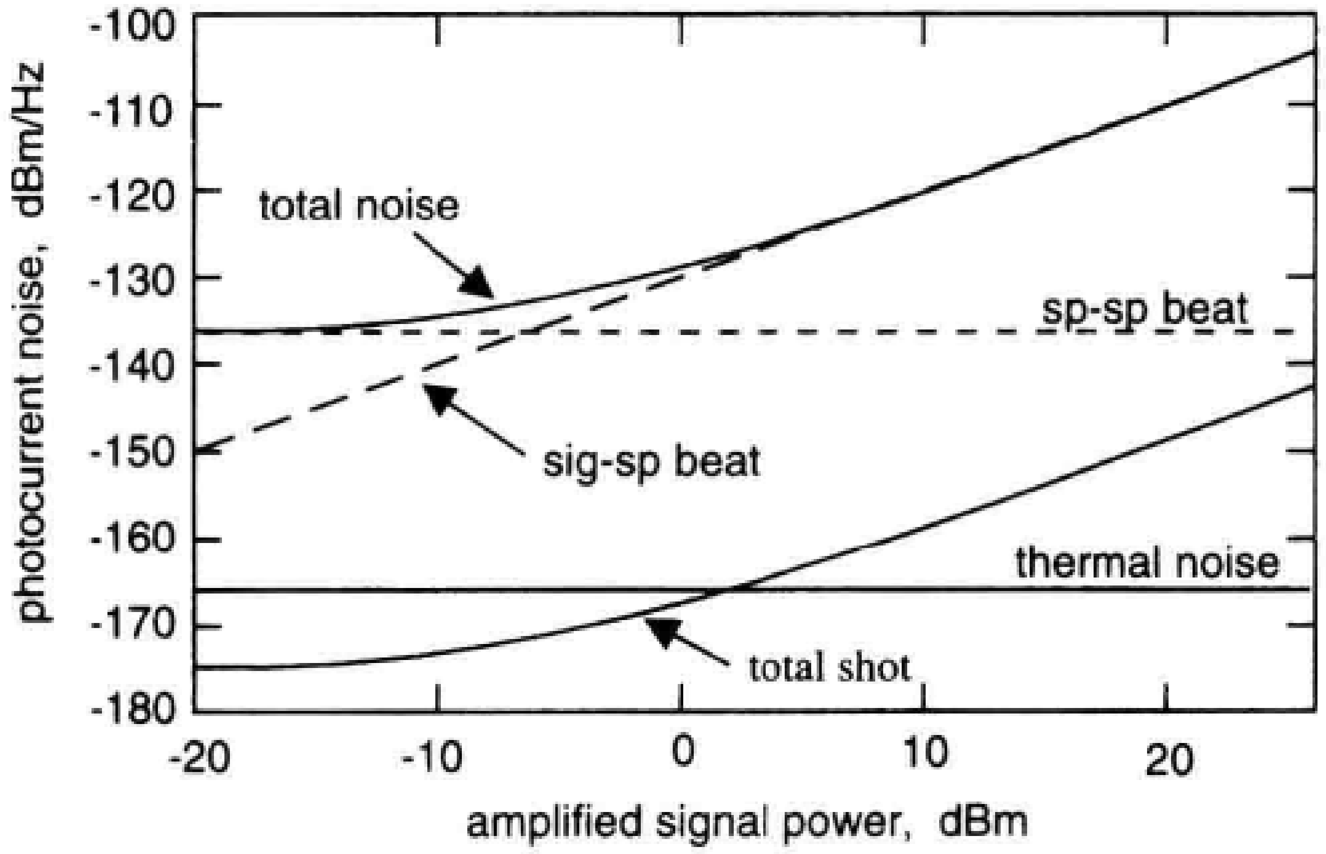

Figure 13.17 Total and individual noise contributions from an EDFA as a function of the amplified signal power.

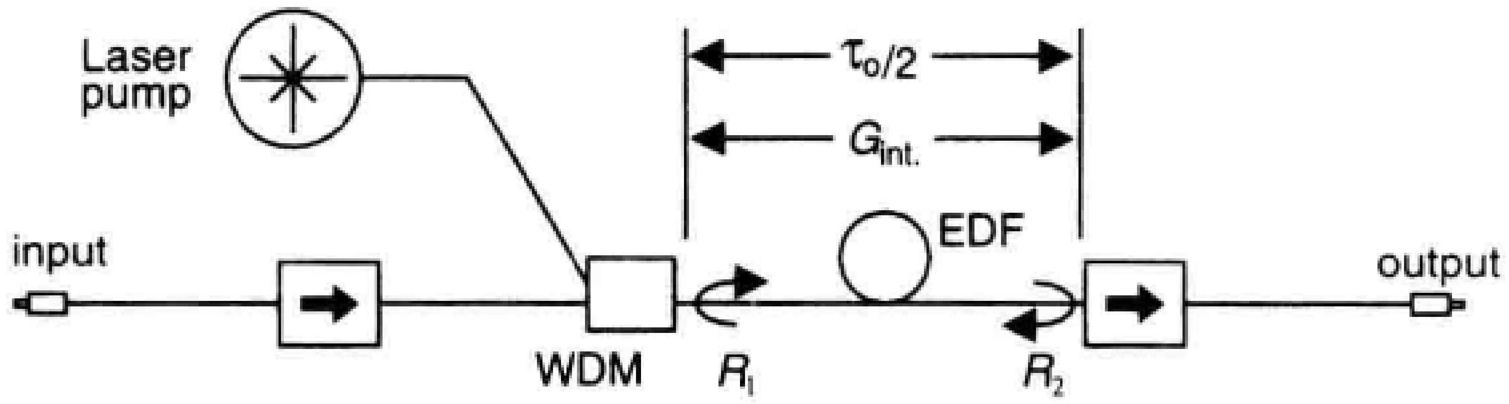

Figure 13.18 Fiber optic amplifier showing optical reflections contributing to multi-path interference noise.

The following relations can be used to estimate the RIN generated by a pair of small optical reflections when illuminated by a laser with a Lorentzian-shaped optical spectrum. The two reflections, denoted by R_1 and R_2 are assumed to satisfy: R_1, $R_2 << 1$. The expected RIN for three regimes of coherence (see Chapter 5) and with the interferometer in quadrature is:

any coherence

$$\mathrm{RIN}_{\Delta\phi_{\max}}(f) = \frac{4G_{\mathrm{int}}^2 R_1 R_2}{\pi} \frac{\Delta\nu}{\Delta\nu^2 + f^2} [1 + e^{-4\pi\Delta\nu\tau_o} - 2\cos(2\pi f\tau_o)e^{-2\pi\Delta\nu\tau o}] \tag{13.31}$$

coherent case

$$\Delta\nu\tau_o < 0.1, \quad f < 1/2\pi\tau_o, \text{ maximum RIN}$$

$$\mathrm{RIN}_{\Delta\phi_{\max}}(f = 0) = 16\pi\Delta\nu\, \tau_o^2 G_{\mathrm{int}} R_1 R_2 \tag{13.32}$$

incoherent case

$$\Delta\nu\, \tau_o > 1$$

$$\mathrm{RIN}_{\Delta\phi_{\max}} = \frac{4G_{\mathrm{int}}^2 R_1 R_2}{\pi} \frac{\Delta\nu}{\Delta\nu^2 + f^2} \tag{13.33}$$

where $\Delta\nu$ is the laser FWHM linewidth, f is the baseband frequency, τ_o is the delay time of the reflected light and G_{int} is the optical gain of the medium separating the reflections. The gain-reflection product is assumed to be small (in other words, $G_{\mathrm{int}} R_1 R_2 <<1$) for the above equations to hold.

In the coherent case, the conversion of phase noise into intensity noise increases as the square of the distance separation between the reflections. Therefore, when using highly coherent lasers in test systems, the lead lengths should be kept as short as possible to reduce the phase noise to intensity noise conversion. As the product of the laser linewidth and the delay τ_o increases, the noise spectrum tends toward a Lorentzian function as defined by Equation 13.33. The gain, G_{int} causes a significant increase in the MPI-induced RIN. Thus reflections must be kept small when optical gain is present. An understanding of the parameters affecting the MPI process can be applied to improve the optical amplifier design or the amplifier test system to limit the effects of this unwanted noise.

Example

Calculate and plot the maximum MPI-induced RIN for a 1.55 μm optical amplifier with a fiber gain section 1.71 m in length. Assume –45 dB optical reflections at each end of the 30 dB gain section and laser linewidths (Lorentzian approximation) varying from 10 MHz to 1 GHz.

Solution

The linewidth-delay time product is calculated first. A fiber refractive index of $n = 1.46$ is assumed. The delay time is calculated ($\tau_o = 2nL/c$) to be 16.6 ns. Thus the smallest and largest $\Delta\nu\tau_o$ products are 0.166 and 166 for linewidths of 1 MHz and 1 GHz respectively. Equation 13.31 is valid for this wide range of the $\Delta\nu\tau$ product. The estimated MPI RIN is shown in Figure 13.19.

From the above discussion, it is interesting to note that the RIN generated by the reflections internal to the amplifier depends on the linewidth of the source. Therefore, the noise generated by the amplifier is a function not only of the laser wavelength and power, but the signal linewidth as well.

13.4 NOISE FIGURE

The amplifier noise figure is a figure of merit quantifying the SNR (related also to the carrier-to-noise ratio, CNR) degradation after passage through the amplifier. Large-noise figures are detrimental to system performance, it causes poor received SNRs, increased jitter in soliton-based systems and ASE accumulation in long-haul amplified links. The main contributors to the noise figure are the effects of amplified spontaneous emission generated within the amplifier and importantly for analog communications, the phase-noise to intensity noise conversion due to internal optical reflections. The ASE manifests

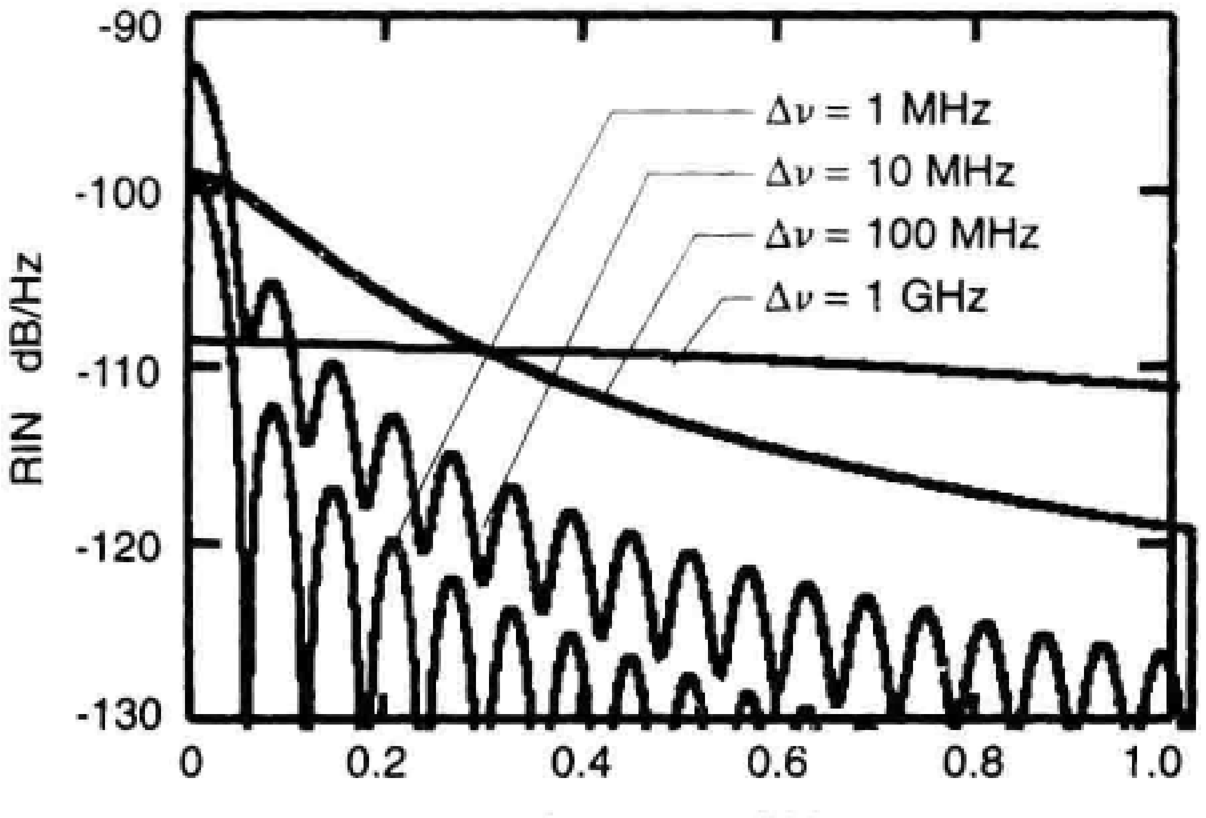

Figure 13.19 Optical amplifier MPI-induced relative intensity noise versus frequency for various signal laser linewidths.

itself through the generation of beat noise. In this section, the noise figure is defined, and later cast in a form that can be readily applied from a measurement standpoint.

13.4.1 Noise-Figure Definition

The degradation of the SNR after passage through an optical amplifier is quantified in terms of the noise figure, F, defined as

$$F = \frac{\text{SNR}_{\text{in}}}{\text{SNR}_{\text{out}}} \tag{13.34}$$

In the discussions that follow, the noise figure in decibels is determined according to: $F = 10\log(F)$. The SNRs are referred to the output of an ideal photodetector which is capable of converting each photon of incident light into electrical current (in other words, 100% quantum efficiency). The input SNR is defined to be that from a shot-noise-limited source. The shot-noise-limited input reference is critical to the definition. If an optical source with a large amount of intensity noise were used to measure the noise figure of an amplifier, the amplified source noise would dominate over the amplifiers own noise contribution and lead to an erroneous noise figure of 0 dB, in other words, no observed SNR degradation caused by the amplifier.

The noise figure concept is illustrated in Figure 13.20. The input SNR is determined with the amplifier bypassed using an idealized source and receiver. The amplifier is inserted and the output SNR is determined. Equation 13.34 is next used to calculate the amplifier noise figure. The idealized source is shot-noise-limited and set to the appropriate

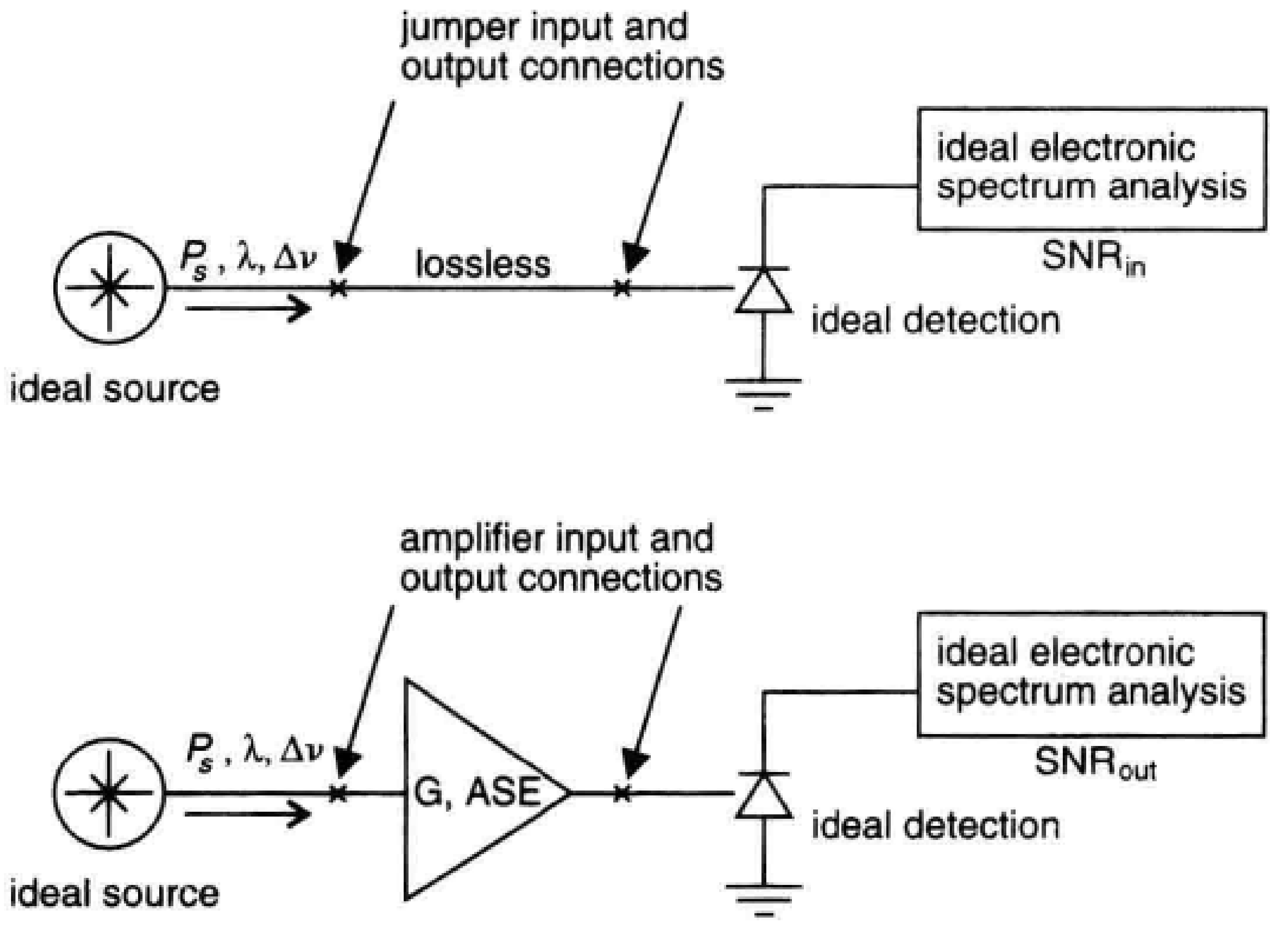

Figure 13.20 Noise figure concept in terms of idealized source and receiver.

power, wavelength, and linewidth. The idealized receiver has a calibrated frequency response and contributes no excess noise of its own. Obviously the real world is not yet ideal and much of the work involving noise figure measurements is in dealing with the source and the receiver non-idealities.

Signal-Spontaneous Beat-Noise-Limited Noise Figure. A commonly used definition of noise figure is the quantum-beat-noise-limited noise figure, sometimes referred to as the sig-sp beat-noise-limited noise figure. This noise figure is more restricted than the general definition defined by Equation 13.34. It doesn't include, for example, the output SNR degradation due to sp-sp beat noise, or MPI. The quantum-beat-noise-limited noise figure is advantageous in simplifying measurement procedures. It is measured with both optical and electrical techniques which are discussed later.

The quantum-beat-noise-limited noise figure is derived using Equations 13.18, 13.25, and 13.27 in Equation 13.34:

$$\mathrm{NF} = \underset{\text{sig}-\text{sp}}{\frac{2\rho_{ASE}}{G\,hV}} + \underset{\text{shot}}{\frac{1}{G}} \tag{13.35}$$

where ρ_{ASE} is the amplifier ASE output density in the same polarization and wavelength as the signal as defined in Equation 13.18. This noise-figure definition is useful because of the ease with which it can be implemented. The ability to correlate noise figure measurement results between different laboratories is improved when this definition is used. The shot noise effect on the noise figure is sometimes excluded for noise calculations involving concatenated amplifiers.

Example

Calculate the quantum beat-noise-limited noise figure for an amplifier with 30 dB of gain, producing 12 μW of ASE in a 0.5 nm optical bandwidth at the signal wavelength of 1.55 μm.

Solution

Using Equation 13.19, the gain, ASE density, and photon energy are 1000, 0.19 f W/Hz, and 1.28×10^{-19} J respectively. Substituting into Equation 13.35 yields a noise figure of 3.0 or 4.8 dB. Notice that the shot noise contributed little to the noise figure because of the high gain of the amplifier.

The 3 dB Noise-Figure Myth. A minimum 3 dB (actually, $\log_{10}(2) = 3.01$ dB) amplifier noise figure is sometimes attributed to the EDFA. If taken out of context this can result in a considerable misunderstanding of the EDFA noise performance. To better understand where the 3 dB limit originates, let us examine the noise figure under moderate signal conditions as the amplifier gain varies. Moderate signal conditions imply that the signal power is much greater than the ASE power in the optical bandwidth of interest. This ensures that the sig-sp beat noise dominates over that of the sp-sp beat noise as indicated by Figure 13.17. Consider the case of a fiber amplifier where initially there are no erbium ions in the "active" optical fiber. Discounting any loss in the optical fiber, the noise figure is unity, in other words, no SNR degradation since the signal passes from amplifier input to output unchanged. As the erbium-ion-doping increases, so does the optical gain, the ASE level, and the signal level. The noise figure increases from 0 dB to 3 dB, or beyond, if other noise sources or optical losses are present. This can be seen from the equation for sig-sp beat noise and shot-noise-limited noise figure derived by substituting Equation 13.18 into Equation 13.35:

$$F = 2n_{sp}\frac{(G-1)}{G} + \frac{1}{G} \tag{13.36}$$

which for large gains yields: $F \approx 2n_{sp}$ where the SE factor, $n_{sp} \geq 1$. A fully inverted amplifier can be achieved with 980 nm pumping resulting in an effective SE factor of unity which leads to a noise figure of 3 dB. Equation 13.36 is plotted versus gain in Figure 13.21. From the figure, a fully inverted amplifier (in other words, $n_{sp} = 1$) with 4 dB of gain and zero input coupling loss has a noise figure near 2 dB. The 3 dB value is the limit for a high-gain amplifier with zero input coupling loss and a fully inverted amplifying fiber. Any loss near the amplifier input, or departure from complete inversion will cause the noise figure to exceed 3 dB.

A special class of amplifiers, referred to as phase-sensitive amplifiers, can achieve a noise figure less than 3 dB. Most optical amplifiers in use, such as EDFAs are phase insensitive, which means that the amplifier gain does not depend on the optical phase of the input signal. Thus the noise generated by the amplifier is amplified in both the in-phase and quadrature phase components. This is the physical origin of the 3 dB limit in high

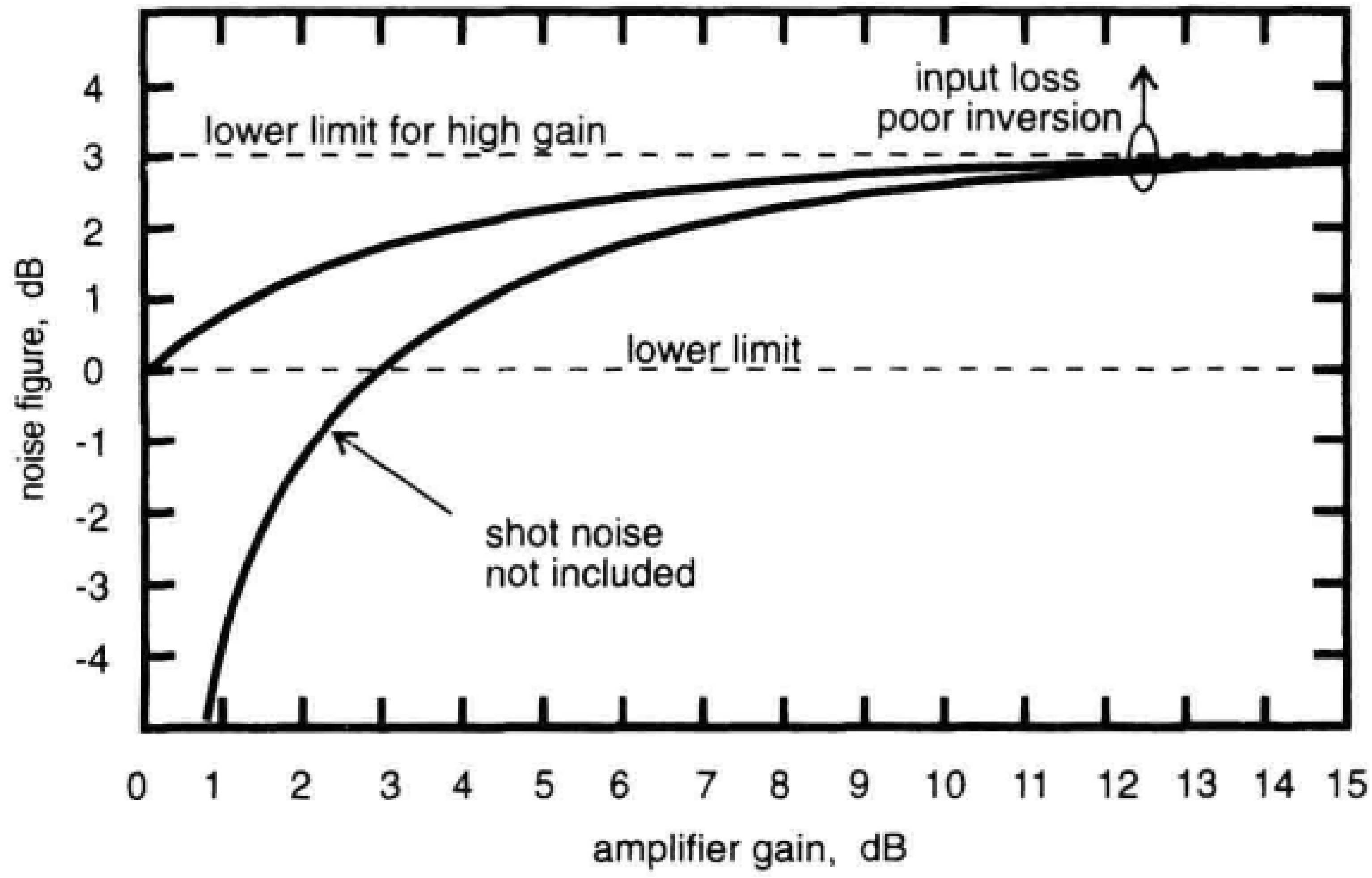

Figure 13.21 Noise figure dependence on optical amplifier gain with and without the shot-noise contribution.

gain amplifiers such as the EDFA. In calculations with concatenations of amplifiers, it is convenient to suppress the shot noise until the signals are analyzed at the detector. In the calculation of noise figure for a single amplifier, failure to include the shot noise will result in significant error in the gain regime below 15 dB.

13.5 CHARACTERIZATION OF GAIN AND NOISE FIGURE

The amplifier gain and noise figure are the fundamental parameters concerning their application to an optical communications link. By measuring these parameters over wavelength, power, input signal polarization, and temperature, the characterization of the amplifier is nearly complete. The measurement of noise figure requires the measurement of gain according to Equations 13.34 and 13.35. The noise-figure measurement techniques are classified into two groups:

- Optical method: optical spectrum analyzer-based,
- Electrical method: electrical spectrum analyzer-based.

Both methods have their merits. The selection of which to use depends on the application of the measurement result and the available instrumentation. Sometimes both electrical and optical methods are used.

The electrical method is often used in optical-amplifier characterization for analog-optical communications. It can be argued that this method provides a more complete noise figure since it directly measures the complete photocurrent noise at the receiver. Hence it provides characterization of amplifier nonidealities such as multipath interference (MPI) caused by reflections internal to the amplifier. This method, however, requires stringent control over measurement system effects that would otherwise be difficult to separate out from the amplifier characteristics.

Optical methods, on the other hand, are often used for amplifier characterization for long-haul digital communications systems. Accurate measurements of amplifier ASE spectra and gain are performed with OSAs. Based on these measurements, Equation 13.35 is used to compute the noise figure. This method is more tolerant of test system reflections and is capable of rejecting the effects of optical source nonidealities.

The optical and electrical methods have demonstrated their ability to perform single-channel EDFA characterization. Another area of EDFA characterization is for multichannel or WDM amplifiers. WDM is an obvious method to more fully utilize the available transport bandwidth that optical fiber provides. In WDM systems, multiple optical carriers are used to transport information. Multiplexers and demultiplexers are used to combine or separate the various wavelength channels to and from the fiber. WDM systems present similar measurement challenges for the EDFA but at multiple optical carrier frequencies. The suitability of the different measurement techniques for the WDM environment are considered separately in this chapter. At the risk of overgeneralization, Table 13.3 is provided to help compare the level of measurement difficulty, as well as the ap-

Table 13.3 Test Method Comparisons

Method	Measure MPI	Applicability for WDM	Difficulty: scale 1 to 5
optical: source subtraction	no	moderate	2
optical: polarization extinction	no	poor	3
optical: time-domain extinction	no	excellent	3
electrical	yes	moderate	4

plicability of the various techniques to WDM measurements. The relative merits of the different methods may change as the measurement art advances.

13.5.1 Amplifier Gain

Several methods of measuring the gain of an optical amplifier are discussed here. While not necessarily a complete list of all possible methods, it covers the most commonly used methods. In the discussions on noise figure measurement that follow, the issue of gain measurement with respect to the specific noise figure measurement techniques is also addressed.

Optical Power Meter: Optical Gain. Measurement of optical gain can be performed using the simple approach shown in Figure 13.22. In this approach, the incident source power is measured along with the filtered amplifier output using an optical power meter. The system is calibrated by replacing the amplifier with a lossless connection. An important source of measurement error is the presence of ASE incident on the optical power meter. This is reduced significantly by filtering. Filtering the source reduces the effect of source spontaneous emission (SSE) on the amplifier saturation. The combined effects of ASE and amplified SSE contribute to a net gain measurement error. The gain measurement error, defined here as the ratio of the measured gain to the actual gain is given by:

$$\frac{G_m}{G} = 1 + B_o \frac{F h\nu}{P_s} \tag{13.37}$$

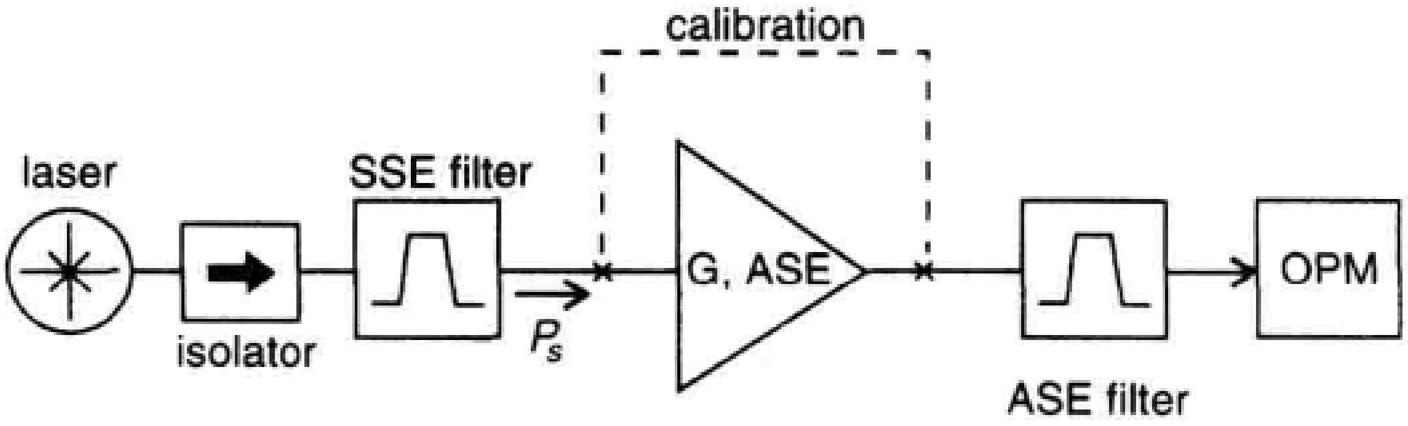

Figure 13.22 Optical amplifier gain measurement with an optical power meter and bandpass filters. OPM: optical power meter.

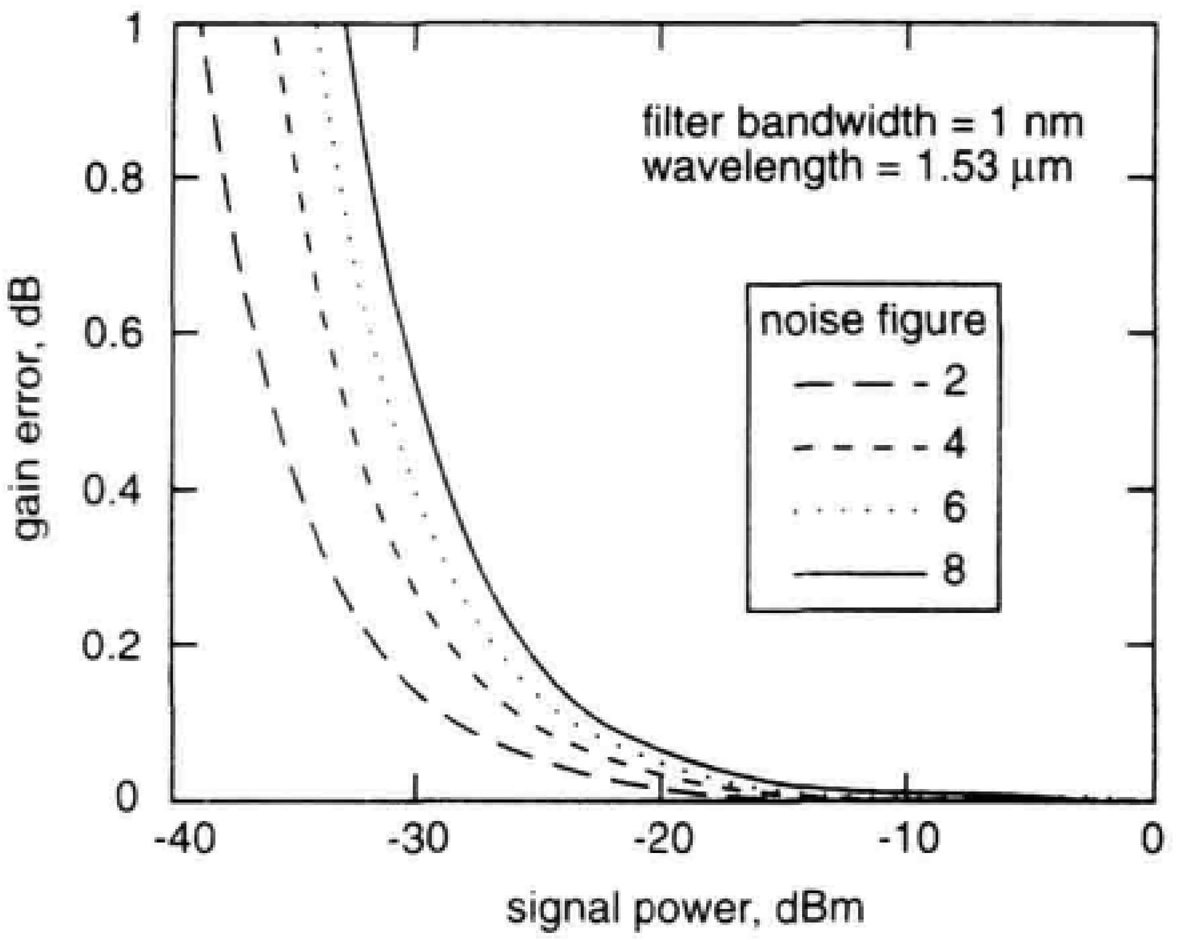

Figure 13.23 Gain measurement error due to additive effect of ASE.

where F is the noise figure, B_o the filter bandwidth, and P_s is the input power. This is plotted in Figure 13.23 for different noise figures assuming a 1 nm filter bandwidth. Input powers below approximately −20 dBm result in appreciable errors for the 1 nm filter bandwidth.

Electrical Spectrum Analyzer: Optical Gain. One method to measure gain at lower input powers is to use source modulation in conjunction with a frequency selective receiver. An electrical spectrum analyzer can be used to measure a small intensity modulation index imparted onto the optical source. By performing measurements of the photocurrent spectrum at the modulation frequency with and without the optical amplifier, the gain can be determined. The advantage of this approach is that the signal is separated from the ASE by the modulation. The modulation frequency is set to be significantly faster than the inverse of the EDFA gain recovery time (~ 300 μs) so as not to modulate the ASE. The measurement set-up, using an electrical spectrum analyzer, is shown in Figure 13.24a. A measurement using this setup is shown in Figure 13.24b. The laser source (a DFB with an electroabsorption modulator) was sinusoidally modulated at a 10 MHz frequency and passed on to the receiver directly for gain calibration. Next the amplifier was inserted for the gain measurement. The measurement results are shown Figure 13.24b. The input and amplified output spectrums are shown with spectral peaks at the 10 MHz modulation rate. The difference in amplitudes of the 10 MHz modulation tone corresponds to the optical gain squared. An electrical lock-in amplifier may also be used to measure the gain where the synchronous detection of the lock-in amplifier improves the measurement sensitivity.[36]

Optical Spectrum Analyzer: Optical Gain. Measurement of the amplifier gain using an OSA provides a more general evaluation of the amplifier. Information concerning the ASE spectral shape, source characteristics, and the presence of spurious signals such as pump laser feedthrough is obtained as well. The basic measurement setup is

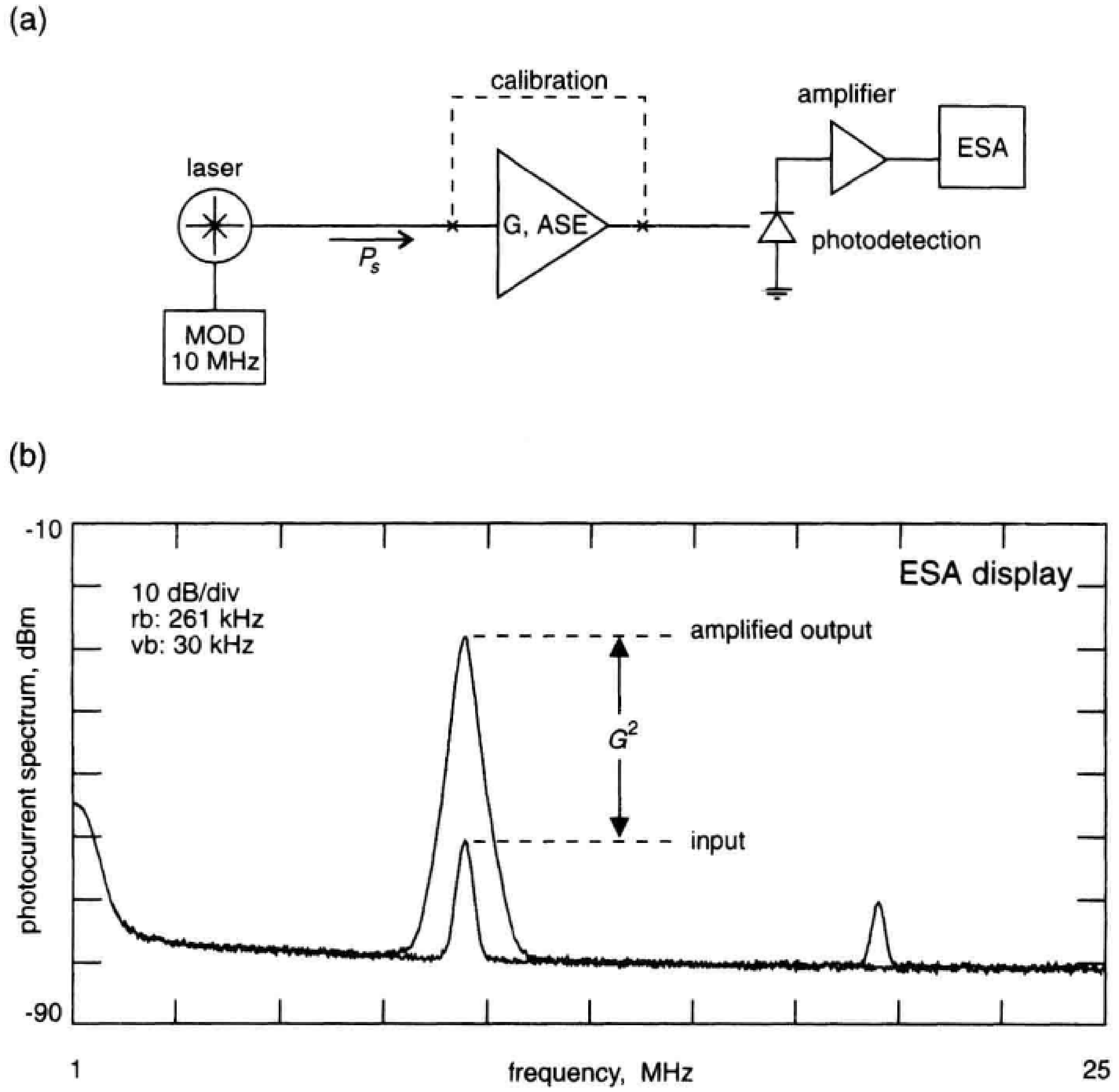

Figure 13.24 Optical amplifier gain measurement. (a) Measurement setup using modulated source. (b) Displayed ESA data. ESA: electrical spectrum analyzer.

shown in Figure 13.25a. A gain measurement of an EDFA under the same input signal conditions as in Figure 13.24b is shown in Figure 13.25b.

The amplifier dynamic gain spectrum can be readily measured by combining a small-probe signal with the laser that sets the EDFA saturation level. This is illustrated in Figure 13.26. The probe signal could be a broadband noise source such as an EELED or a tunable laser.[30,36,37] The EELED approach is more rapid if the tunable laser is not capable of sweeping synchronously in wavelength with the OSA. The tunable laser probe power has less of an impact on the amplifier saturation level for a given measurement SNR as compared with the EELED approach. The effect of the probe on the saturation level of the amplifier should be monitored closely. Preferably the probe power is set to a value less than the effective input noise of the amplifier as given by Equation 13.10, but this is not

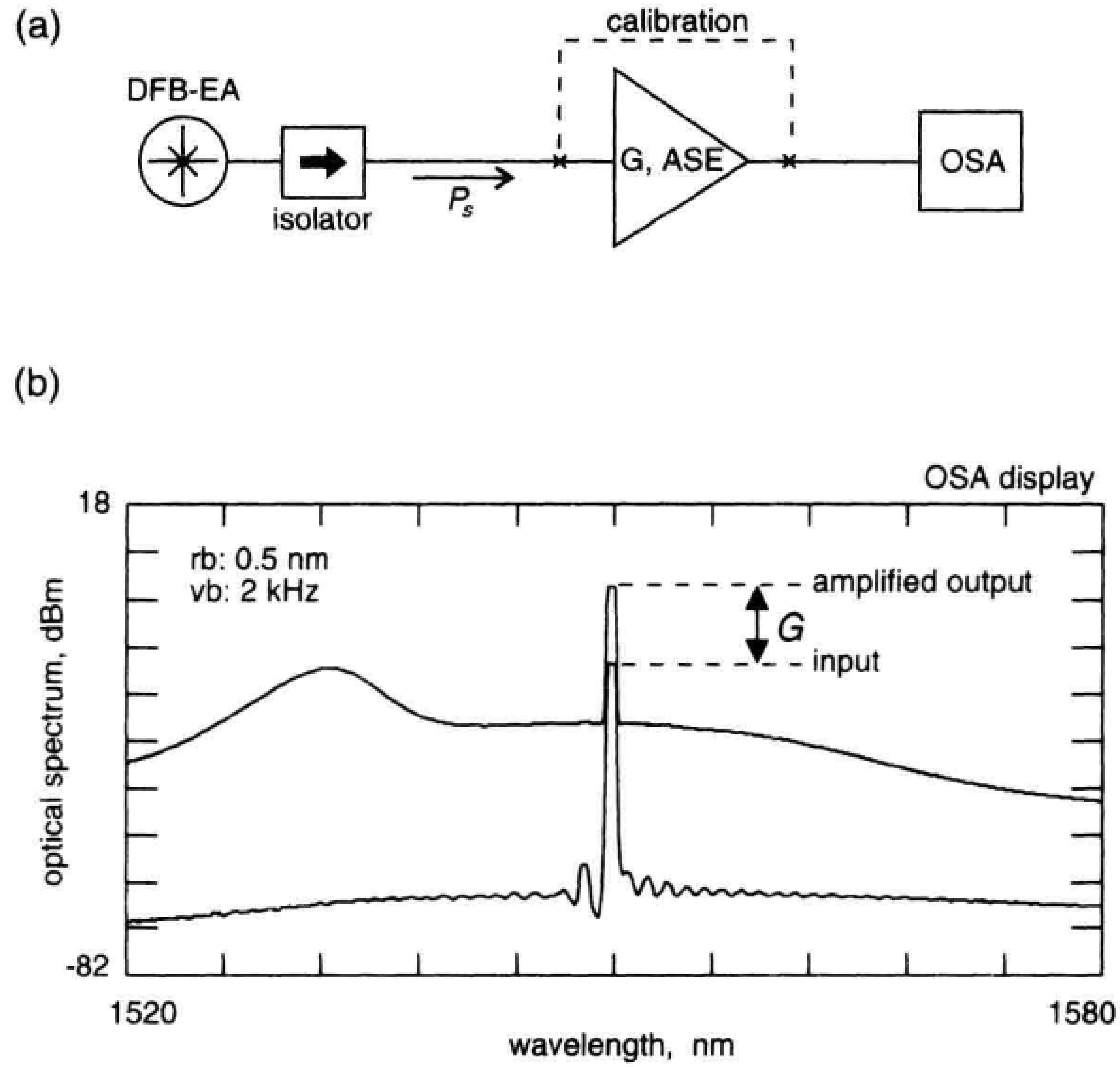

Figure 13.25 Amplifier gain measurement using optical spectrum analyzer. (a) Measurement setup. (b) OSA display. OSA: optical spectrum analyzer.

always practical in view of measurement speed and sensitivity considerations. Actual measurements using the EELED probe technique are presented in the discussion on the time-domain extinction method for noise figure measurement.

13.5.2 Measurement of Noise Figure

Generally, noise figure measurements involve two activities: (1) making noise and gain measurements, (2) removing the test-system noise contribution. Before discussing some of the various techniques available to measure amplifier noise figure, it is worth discussing one of the villains that manifests its presence in electrical and optical methods: laser noise.

Source Spontaneous Emission. One of the challenges that the various noise figure characterization techniques have had to address in their evolution was how to deal with the excess noise present with optical sources. The excellent noise performance of the EDFA allows laser noise to mask the observed amplifier noise. Recall that the noise fig-

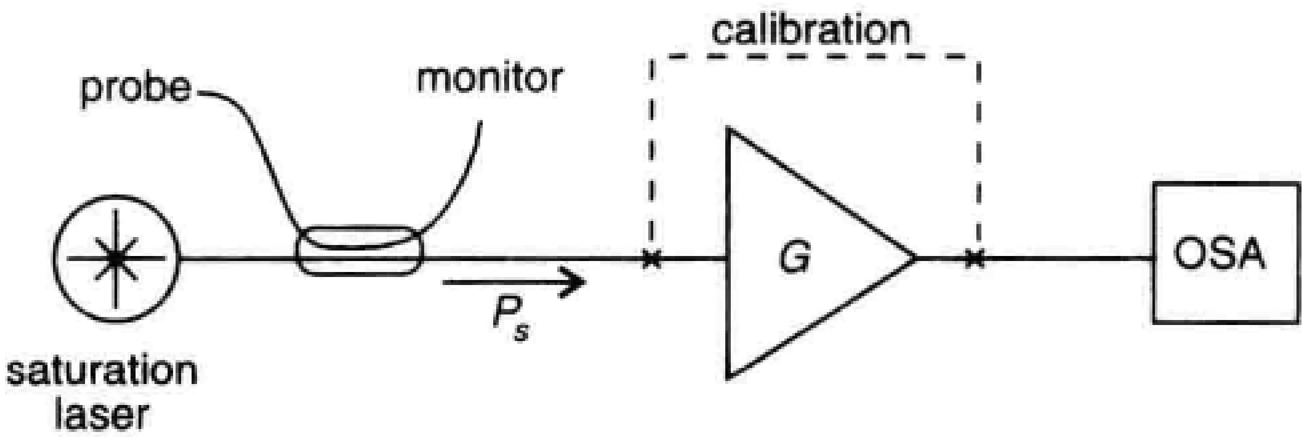

Figure 13.26 Optical amplifier gain measurement with small-signal probe combined with strong signal laser.

ure was defined in terms of a shot-noise limited source. A typical laser source, such as a DFB-LD, consists of an optical amplifier made from semiconductor material with distributed mirrors providing feedback for the lasing process. The DFB-LD internal optical gain generates ASE in the same way as the EDFA. This source noise is referred to as SSE. The SSE is broad in bandwidth, as shown in the measured DFB-LD optical spectrum shown in Figure 13.27. In addition to SSE, laser side-modes are also observed adjacent to the coherent signal. A telltale sign of imminent SSE problems is the observation of source spectral structure in the amplifier output.

Impact on Optical Methods. The optical methods of noise figure measurement rely on a measurement of the ASE density at the EDFA output. Therefore, steps must be taken to insure that SSE doesn't cause an overestimate of the amplifier noise figure. The effect of SSE on the noise figure is shown in Figure 13.28. The measured noise figure (in linear units) will be the numerical error shown in Figure 13.28 added to the actual noise

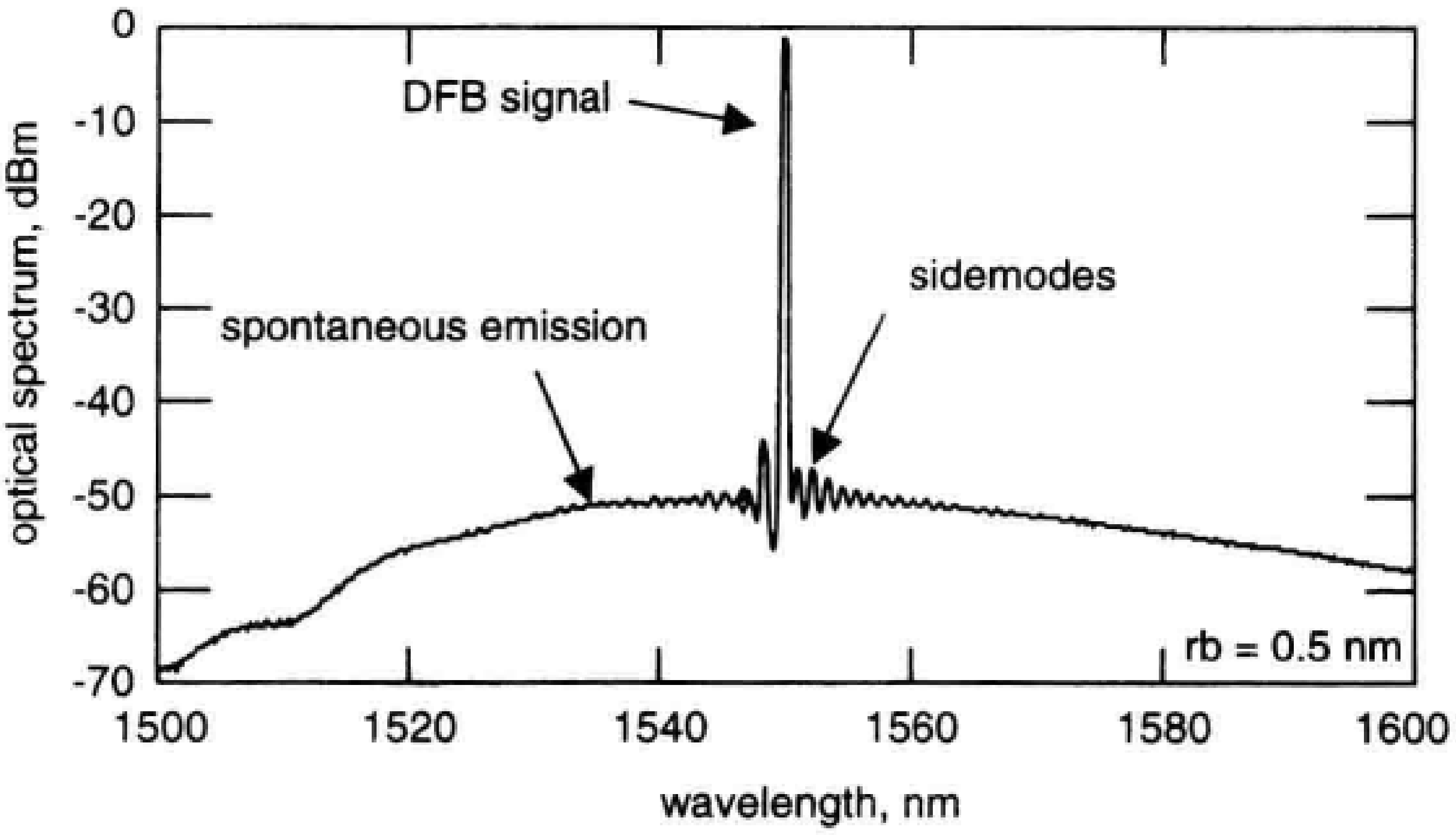

Figure 13.27 Optical spectrum of a DFB laser showing sidemodes and spontaneous emission.

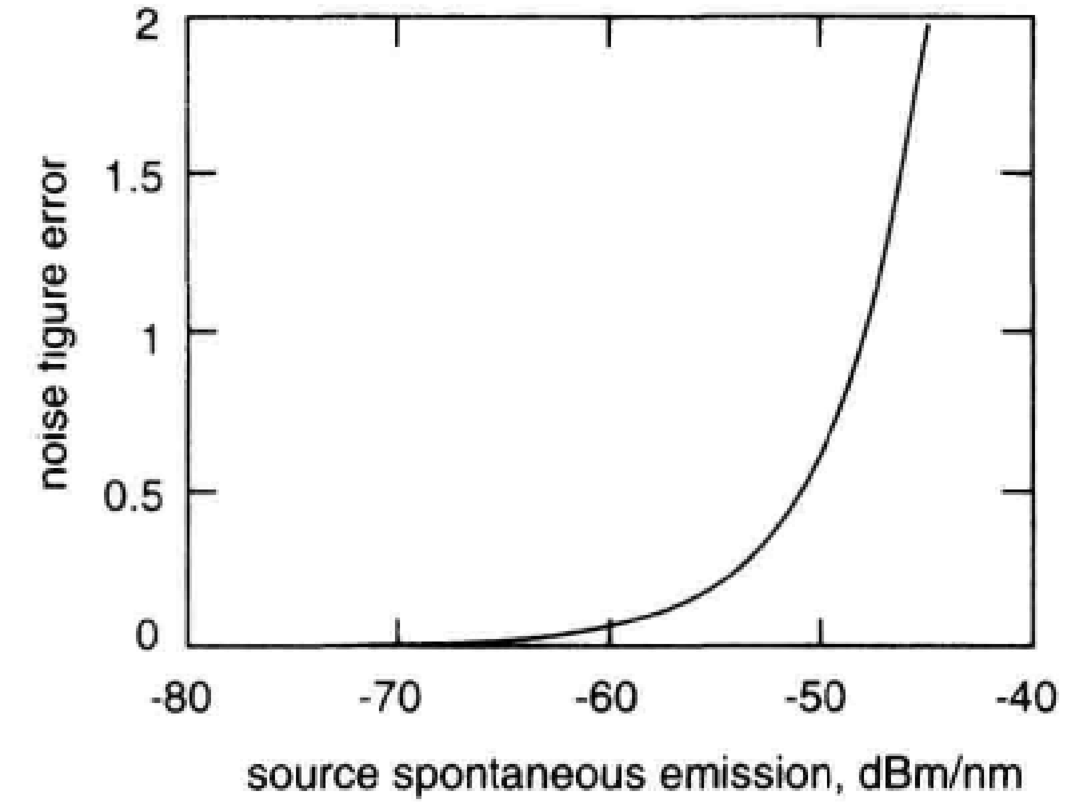

Figure 13.28 Increase in measured noise figure due to source spontaneous emission at amplifier input.

figure. An SSE density of −50 dBm/nm will add approximately 0.6 to the actual noise figure in linear units. It is apparent that to make accurate measurements, the absolute SSE level at the input to a low-noise amplifier should be below approximately −65 dBm/nm. The −50 dBm/nm SSE level of the DFB laser shown in Figure 13.27 would create a large measurement error, if unaccounted for. The simplest method to reduce the SSE is to attenuate the source to achieve the specified measurement accuracy. The short-coming of this approach is the need to measure the amplifier response at relatively high input levels. Reducing the bias current through a semiconductor laser to lower its output power does not alter significantly the SSE generation. An optical attenuator is preferred for setting power levels because it reduces both signal and noise power.

Impact on Electrical Methods. The electrical methods calculate noise figure based on measurements of photocurrent noise. If the optical source illuminating the amplifier is not shot-noise limited, there may be an increase in the measured noise. The error caused by this noise depends on the absolute level of the noise generated by the source at the amplifier input terminals. This error can be plotted in terms of relative intensity noise, (RIN) for various values of input signal power as shown in Figure 13.29. The figure indicates that lowering the input signal power relaxes the requirement for the laser RIN. As an example, an input signal power of −10 dBm from a laser with a RIN of −144 dB/Hz will cause a measurement error of 0.3 if unaccounted for. An amplifier with a noise figure of 2 would measure 2.3 (3.6 dB) with this laser source.

Optical Methods. To measure gain and noise figure, the optical methods must be able to determine the following:

- Gain,
- ASE spectral density,
- Wavelength.

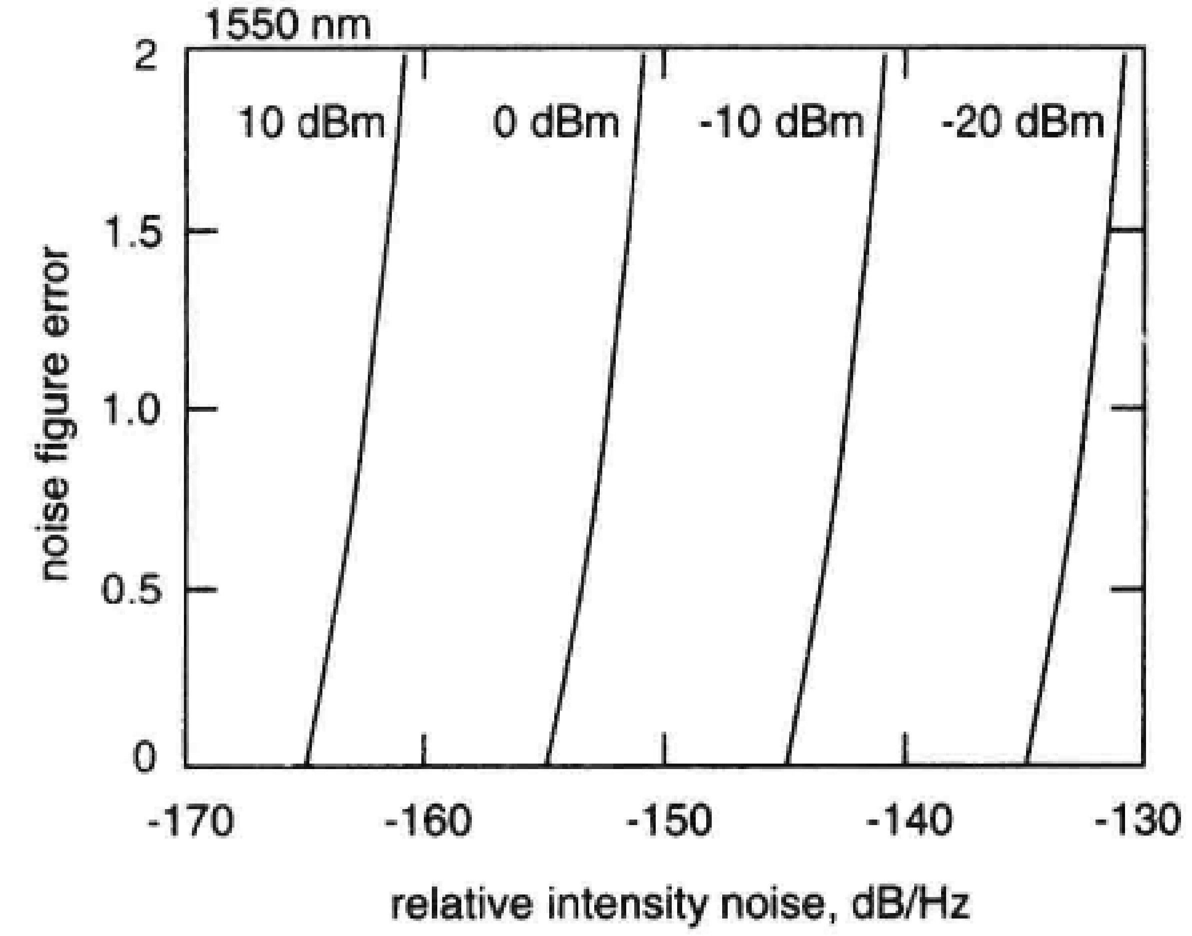

Figure 13.29 Noise figure error due to excess source noise in terms of RIN for different input signal power levels.

Three basic optical methods are used for noise figure measurement:[38] (1) source subtraction technique; (2) polarization nulling; (3) time-domain extinction or pulse method. The differences in these methods are in the ways the source SSE is accounted for and how the noise and gain are measured. The source subtraction method has the simplest setup and allows for rapid measurement of amplifier noise figure. It is best suited for single-channel environments but can be applied in WDM environments. Limitations on the spectral selectivity of OSAs make it difficult to measure close to the channel wavelength with this technique. The polarization extinction method has a more complicated setup with polarization synthesis requirements and longer measurement time. It is useful for single-channel amplifier characterization and allows for noise figure measurements close-in to the actual signal wavelength. The time-domain extinction method is useful for both single or multichannel testing of EDFAs. This method allows for noise figure measurement close-in to the actual signal wavelength and offers very rapid measurement through-put. In all the optical techniques, the amplifier ASE and gain are measured. From these measurements the noise figure is calculated according to Equation 13.35.

In the following discussions on noise figure measurement, the OSA bandwidth, B_o refers to the effective noise bandwidth of the OSA in units of Hertz. It may vary, by up to ~ 20%, from the nominal displayed resolution bandwidth. The reader is referred to Chapter 3 for more detail on this. In the next three sections, the three optical techniques are described in detail.

Optical Source-Subtraction Method. The optical source subtraction method provides for straightforward characterization of the gain and noise figure performance of optical amplifiers. In its simplest form, the measurement setup consists of a laser to provide the input signal, and an amplitude calibrated OSA as shown in Figure 13.30. As discussed above, the SSE causes an error in the noise figure measurement. With the optical source subtraction approach, the SSE is carefully measured during calibration and later

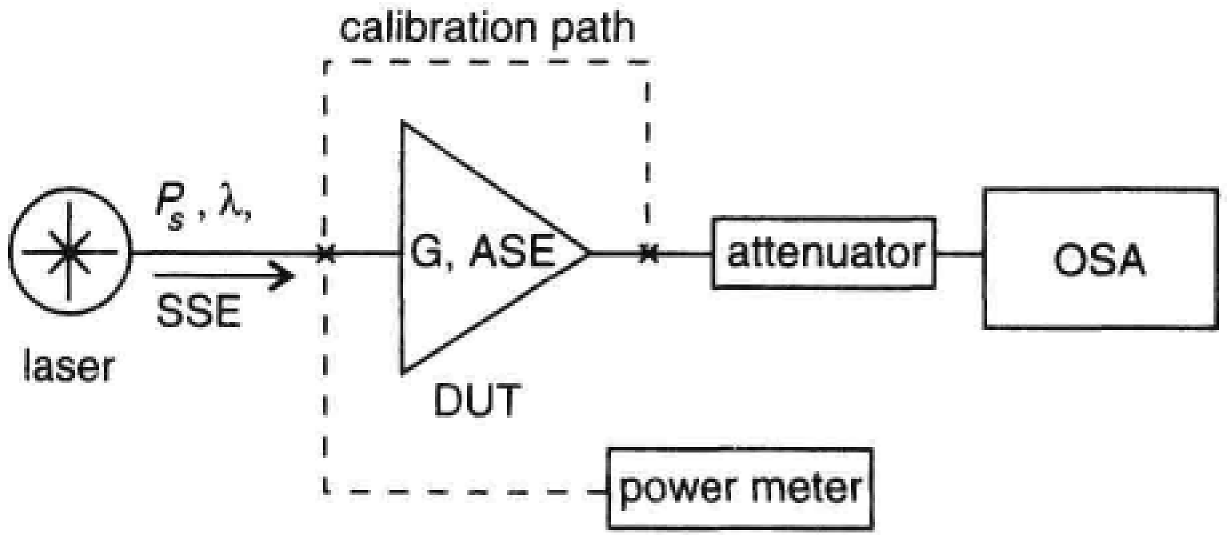

Figure 13.30 Gain and noise figure measurement setup using the optical source subtraction method.

subtracted from the total noise emitted by the amplifier to obtain the true amplifier ASE. In the calibration sequence, the power delivered to the amplifier input connector must be determined as well as the loss from the amplifier output to the OSA.

To measure amplifier noise figure, the following quantities must be obtained:

- ν — optical signal frequency
- P_s — signal power incident at the amplifier input
- P_{out} — total amplifier output power within the OSA resolution bandwidth measured at the signal wavelength including ASE and amplified SSE.
- P_{ASE}—total noise spectral density from the EDFA, including SSE, at the signal wavelength due to both polarizations
- P_{SSE}— SSE spectral density at the signal wavelength caused by both polarizations

From these quantities, the gain and quantum-limited noise figure are calculated according to Equation 13.1 and:

$$NF = \frac{P_{\text{ASE}}}{G\,h\nu\,B_o} + \frac{1}{G} - \frac{P_{\text{SSE}}}{h\nu\,B_o} \tag{13.38}$$

noise figure – SSE correction

The last term performs the subtraction of the amplified SSE. The presence of the amplified signal prohibits the measurement of P_{ASE} and P_{SSE} at the signal wavelength. Interpolation is required to estimate these noise powers at the signal wavelength.

Experiment: Interpolation-Source Subtraction. The noise figure and gain of an EDFA was measured at a wavelength of 1.55 μm using an interpolation technique with source subtraction to remove the effects of SSE. The setup is shown in Figure 13.30. The input signal, P_{in}, was provided by a tunable external cavity laser (HP 8168). An optical attenuator (HP 8157) reduced the high powers from the EDFA to an acceptable level for the OSA (HP 71450). The input signal, was first measured with an optical power meter (HP 8153/HP 81532A). Next the OSA and attenuator were calibrated as an ensemble by comparison with the power meter reading. The correction was +1.4 dB. The SSE was measured at the ±1 nm offset interpolation wavelengths using the built-in noise marker func-

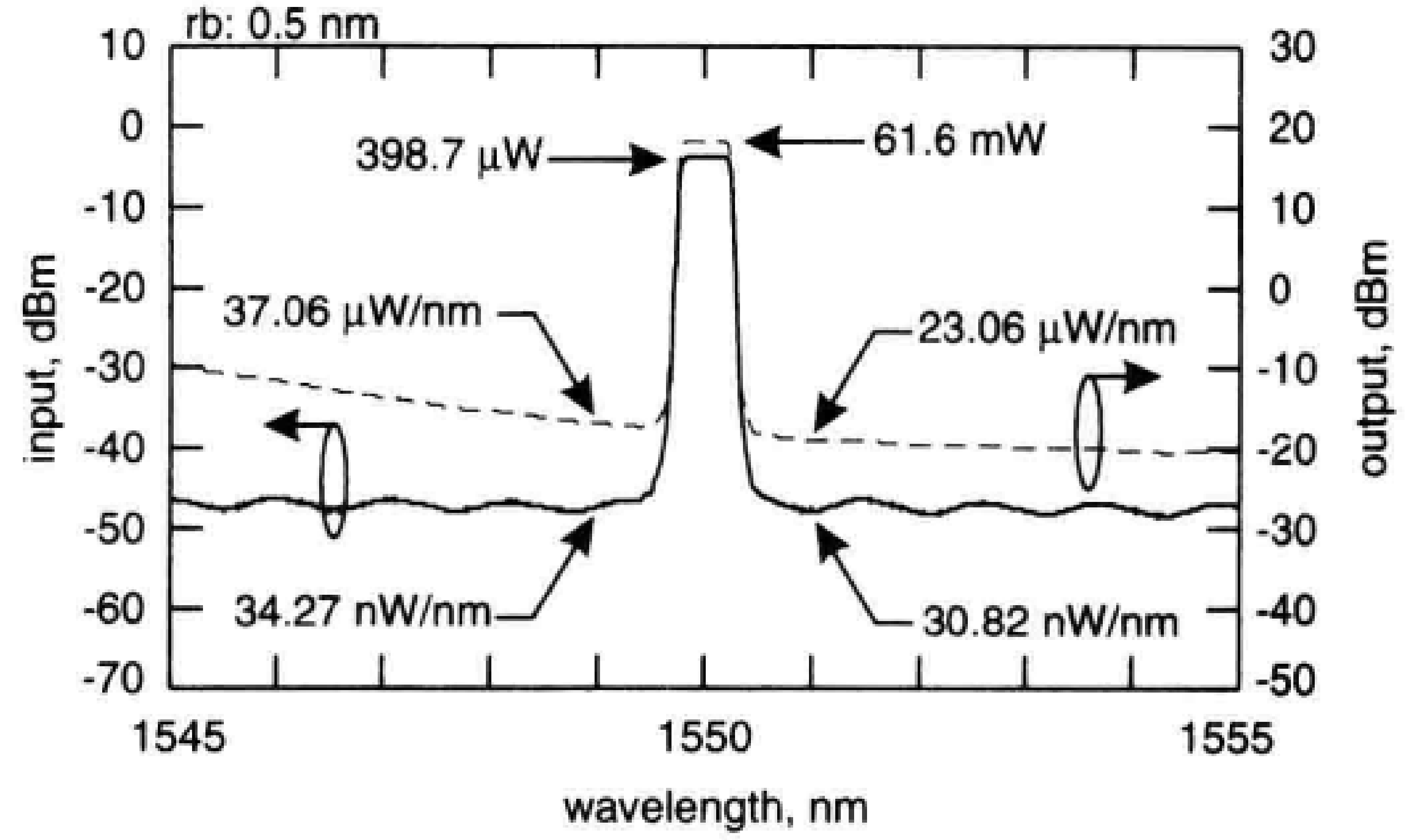

Figure 13.31 Noise figure and gain measurement of an EDFA using the optical source subtraction method combined with ASE interpolation.

tion which refers the measured noise to a 1 nm equivalent noise bandwidth. The corrected signal input and EDFA output spectrums are shown in Figure 13.31. The attenuator was set to 20 dB when the amplifier was inserted into the measurement setup. The EDFA output ASE measurements were made at the interpolation wavelengths and the amplified signal power was measured. The resulting data is tabulated in Table 13.4 along with the noise figure computed according to Equation 13.38.

Polarization Extinction. The polarization extinction method offers an alternative way to reduce the error in the noise figure measurement due to SSE. An additional benefit offered by this method is that for a given OSA wavelength resolution, measurement of ASE can be performed closer to the optical carrier than with the source subtraction tech-

Table 13.4 Noise Figure Measurement Data

Parameter	Value	Units
P_s: power meter	398.7	μW
P_s: OSA	306.2	μW
P_{SSE}*	32.5	nW/nm
P_{out}*	61.6	mW
Gain	21.9	dB
P_{ASE}	30.1	μW/nm
ASE density	25.1	μW/nm
Noise Figure	10.1	dB

*With power meter correction.

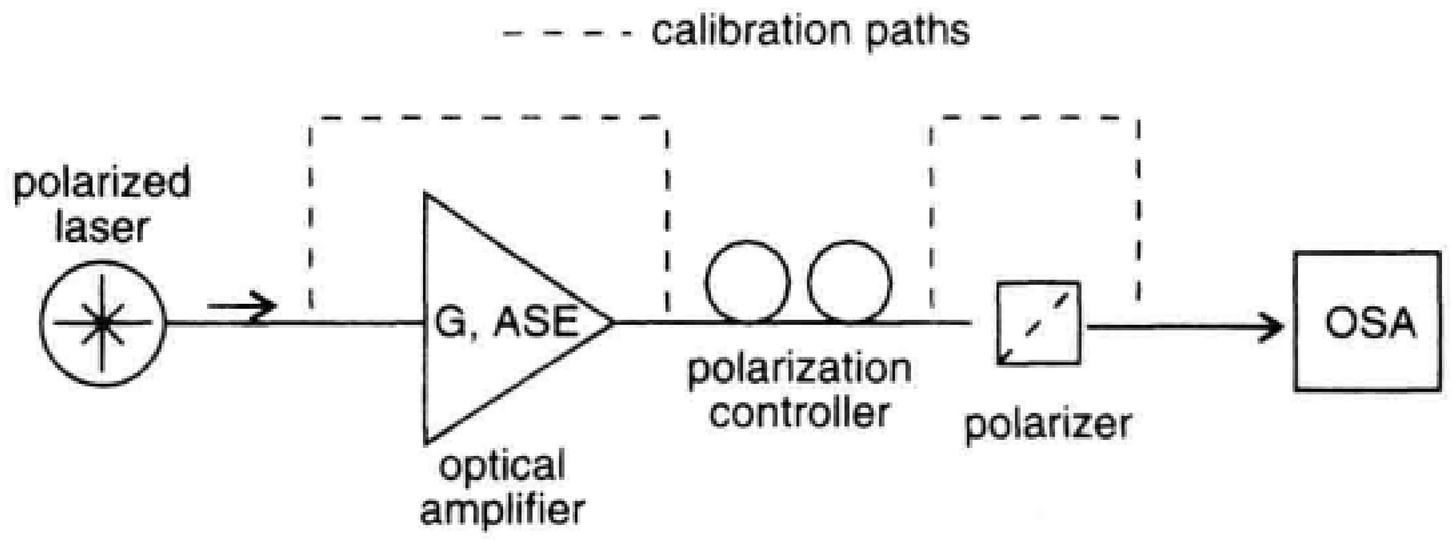

Figure 13.32 ASE measurement setup using polarization nulling technique.

nique. A simple measurement setup to implement this technique is shown in Figure 13.32. For this technique to work, the EDFA ASE should be unpolarized and the SSE must be polarized in the same polarization state as the laser signal. The polarizer in Figure 13.32 allows separation of signal and SE according to polarization states. When the polarization controller is set to suppress the laser signal at the OSA, the SSE will also be suppressed, or extinguished over a certain optical bandwidth. Under these conditions, the OSA measures half the EDFA-produced ASE with reduced measurement corruption by SSE. To obtain the total ASE, the amplitude of the measured spectrum is multiplied by two.

The measurement is calibrated by measuring the loss from the laser to the OSA display as well as characterizing the loss of the polarizer to a signal aligned to the transmitted polarization state. With the system calibrated, the following quantities are determined:

- ν — optical signal frequency
- P_s — signal power incident at the amplifier input
- P_{out} — output power measured at the signal wavelength (polarizer bypassed)
- P_{ASE} —total noise at the signal wavelength (polarizer bypassed)
- P_N — ASE power at the signal wavelength (signal nulled)

The OSA amplitude response is calibrated with an average optical power meter. OSAs with noise marker capability simplify the measurement of noise densities by automatically referring the measured noise to a 1 nm effective noise bandwidth. Often it is not practical to completely suppress the amplified signal and so some residual signal may be observed with the OSA. Thus interpolation may be required to estimate P_N, at the signal wavelength.

Once the signal and ASE powers at the signal wavelength are determined, the optical gain and noise figure is calculated according to Equations 13.1 and 13.35 where $\rho_{\text{ASE}} = P_N/B_o$.

Impact of Polarization Hole-Burning. Polarization hole-burning as discussed in Section 13.2.3 results in a lower amplifier gain in the same polarization as the saturating signal.[5] The gain and ASE will be larger in the polarization orthogonal to the saturating signal polarization. Therefore a measurement of the ASE when the signal is nulled will actually be larger than the ASE in the same polarization as the signal laser. Recall that the noise figure depends strictly on the ASE in the same polarization as the signal. If polarization hole-burning is significant, noise figure measurement by polarization extinction will yield an overestimate of the actual noise figure of the amplifier.

Impact of Polarization Mode Dispersion. Polarization mode dispersion (see Chapter 12) will affect the ability of the measurement systems to reject the SSE over a broad spectral bandwidth. This is caused by the wavelength-dependent birefringence in the measurement system and test amplifier. While the polarization controller in Figure 13.32 can be set to null the signal at one wavelength, the SSE, with its large spectral extent will not be nulled across all wavelengths. A measurement of the null width of the measurement setup of Figure 13.32 is shown in Figure 13.33. In Figure 13.33a the amplifier of Figure 13.32 was bypassed and the laser was set to 1555 nm while the polarization controller was adjusted to obtain a null of approximately 60 dB at the laser wavelength. Next the laser wavelength was tuned from a wavelength of 1520 nm to 1570 nm while the OSA was set to record the maximum observed signal level (bottom trace of Figure 13.33a. Next the polarization controller was adjusted for maximum signal transmission and the laser wavelength was tuned across the band (top trace of Figure 13.33a). It is apparent that PMD in the test system limited the null-width resulting in a null depth in excess of 35 dB across most of the band.

Next the EDFA was inserted and the measurement procedure was repeated. The measured null width was considerably reduced as shown by the bottom trace in Figure 13.33b. The null width for 30 dB extinction was reduced to about 1 nm for this EDFA.

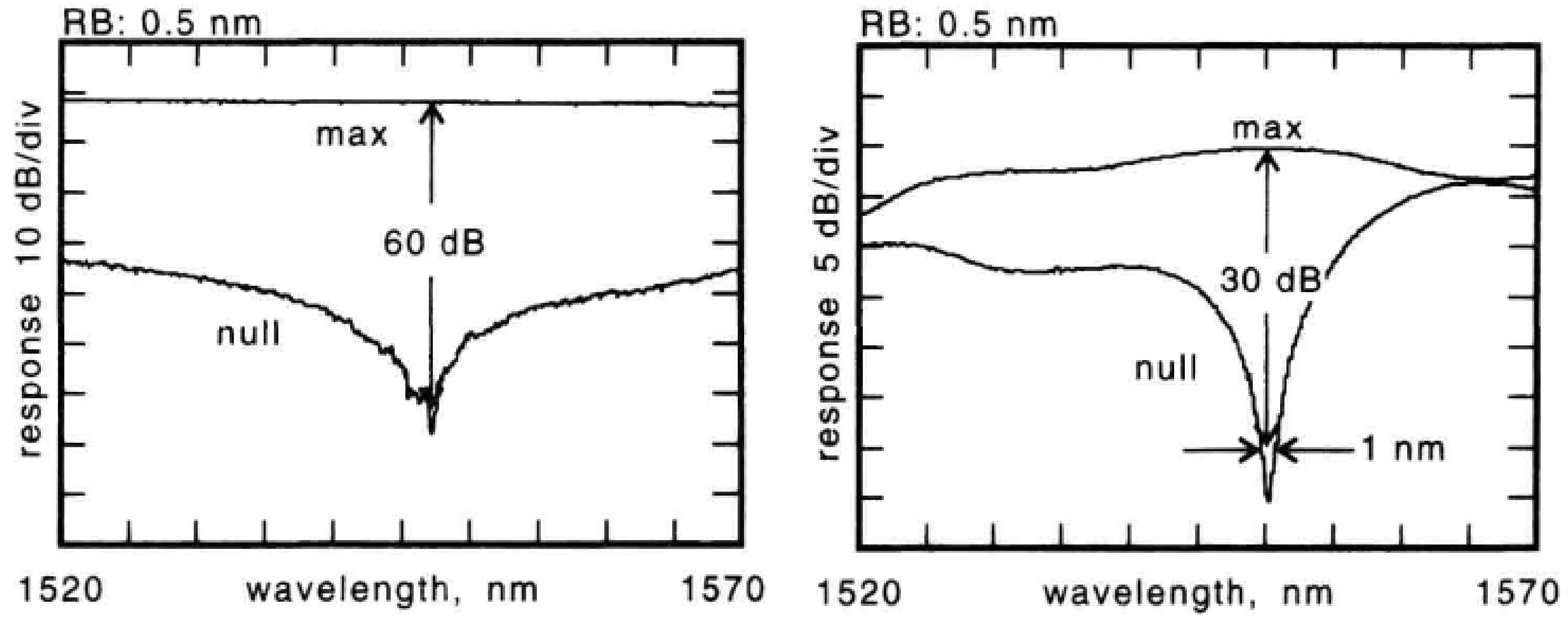

(a) (b)

Figure 13.33 Measurement of signal rejection using polarization extinction at a wavelength of 1550 nm (a) EDFA bypassed; (b) EDFA inserted.

The top trace corresponds to the case where the polarization controller was set for maximum signal transmission at a wavelength of 1555 nm. From the figure, it is apparent that the degree of suppression of the SSE in the noise figure measurement depends heavily on the PMD in the test system and importantly, on the EDFA. Therefore the null width and depth should be characterized to insure adequate extinction of SSE is obtained prior to the measurement of ASE.

Example: Noise Figure and Gain Measurement

The noise figure and gain of an EDFA was measured using the setup shown in Figure 13.32. The loss through the polarizer was calibrated using the unpolarized ASE from the EDFA as a signal source. The polarizer loss was measured to be 1.1 dB. Next the input signal to the amplifier was characterized by connecting it directly to the OSA, the measurement result is shown in the lower trace of Figure 13.34a. Comparison with a calibrated power meter indicated a correction of 0.47 dB to the OSA readings was required.

The SSE was found to be approximately –53 dBm in a 1 nm noise bandwidth. From Figure 13.28, at an SSE density of –50 dBm/nm (add 3 dB to the SSE since the measured ASE is multiplied by 2) the SSE will add approximately 0.6 to the measured noise figure if not rejected. The gain was measured by connecting the amplifier output directly to the OSA (polarizer was bypassed) as shown by the top trace in Figure 13.34a.

With the polarizer and EDFA in place, the polarization controller was set to maximize the signal displayed on the OSA (Figure 13.34b). This measurement provides a reference to determine the degree of polarization extinguishing achieved by the measurement setup. Next the polarization controller was set to null the signal as indicated by the lower trace in Figure 13.34b. Here the signal could not be completely nulled, thereby requiring the ASE to be estimated by interpolation. With the signal nulled, the ASE was measured at a 0.3 nm spacing from the signal wavelength as shown. While the signal null obtained was approximately

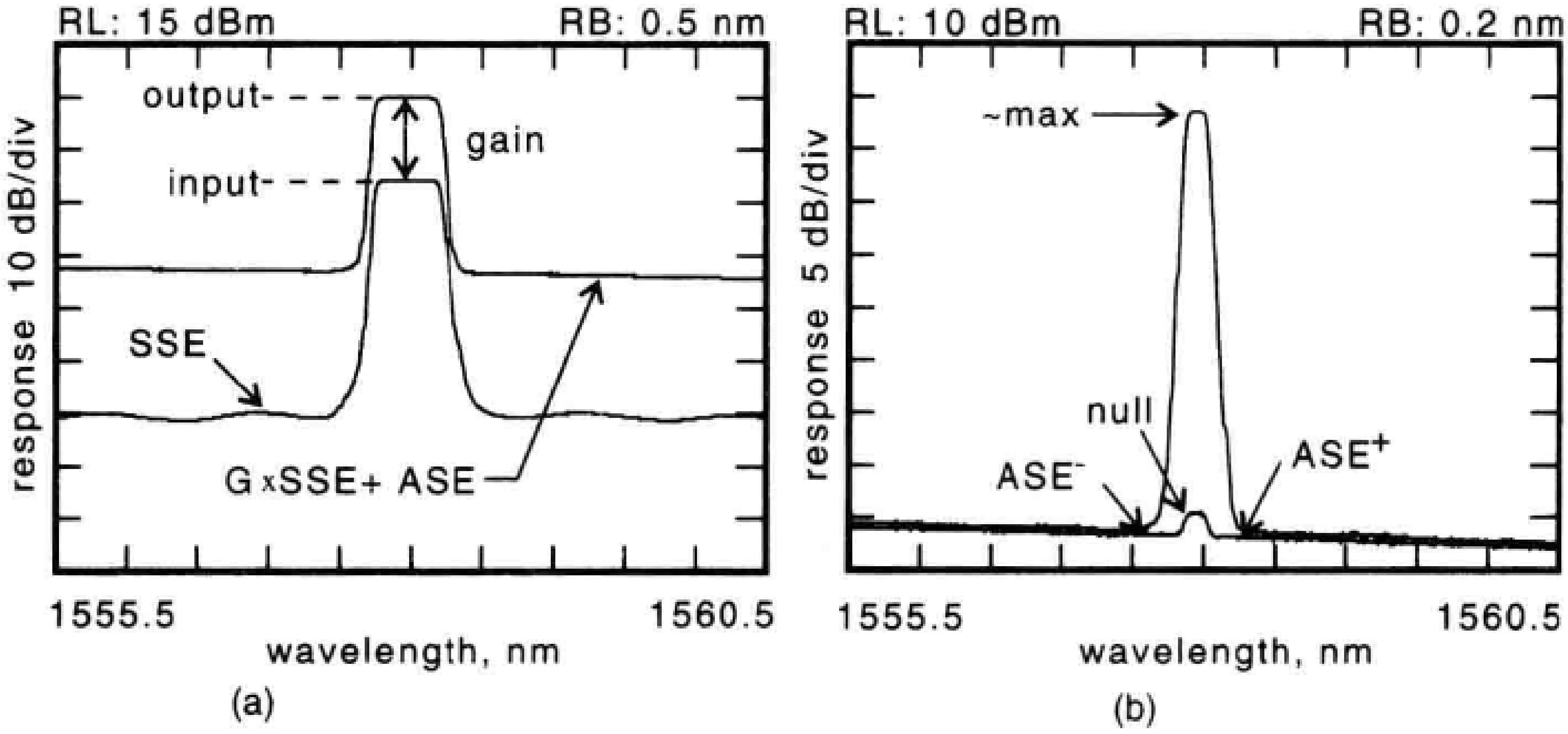

(a) (b)

Figure 13.34 Measurement of EDFA gain and noise performance at a wavelength of 1558 nm using polarization extinction. (a) gain (b) ASE generation.

38 dB, the finite null width limited the extinction of SSE to approximately 26 dB at the ASE measurement frequencies. According to Figure 13.28, the 26 dB rejection will make the error due to the presence of SSE negligible. Some of the measurement data and results are shown in Table 13.5.

The noise figure is calculated using the data in Table 13.6 after conversion to MKS units. The ASE density is converted to watts/Hz using Equation 13.19. The noise figure is calculated according to Equation 13.35 yielding 6.1 dB for this amplifier.

Time-Domain Extinction/Pulse Techniques. The slow gain dynamics of the EDFA may be used advantageously for the measurement of amplifier gain and noise figure using the time-domain extinction (TDE) technique.[39] In this section, the basic TDE concept will be discussed. A discussion of the transient response of the EDFA and its impact on the measurement is also given. Next the TDE method is extended to cover the measurement of dynamic gain (see Section 13.2.5) using an incoherent probe. This extended method has also been referred to as noise gain profiling.[37] TDE with dynamic gain-spectrum measurement enables the user to rapidly characterize the wavelength-dependent gain profile for a particular amplifier saturation condition.

Time-Domain Extinction. In the TDE method, the input signals, that would otherwise interfere with the measurement, are momentarily gated off.[39,40] The gated light is usually the signal or signals that affect the saturation level of the amplifier. By temporarily blocking the signals, several measurements can be performed: (1) measure the amplifier-generated ASE, (2) probe the amplifier with a small signal to measure the dynamic gain (noise-gain profiling).[37]

The basic measurement setup is shown in Figure 13.35. The cw optical saturating source leading to the amplifier is gated at frequency, f_{TDE}. When the input switch (SW1 in the figure) is opened, the output switch (SW2) is closed allowing the OSA to sample the amplifier ASE output. The switching may be performed either electronically (within the laser source and the OSA) or optically (for example, using acousto-optic modulators). Since the signal is extinguished during the measurement, it does not corrupt the measure-

Table 13.5 Noise Figure Measurement Data

Symbol	Parameter	Value	Units
λ_s	wavelength	1558	nm
P_s	input power	70.4	μW
G	gain	38.2	linear
$\Delta\lambda$	interpolation offset	0.3	nm
ρ^+_{ASE}	ASE density at $\lambda_s + \Delta\lambda$	1.18	μW/nm
ρ^+_{ASE}	ASE density at $\lambda_s - \Delta\lambda$	1.25	μW/nm
$\rho^+_{\mathrm{ASE}} = P_N/B_o$	interpolated ASE density	1.22	μW/nm

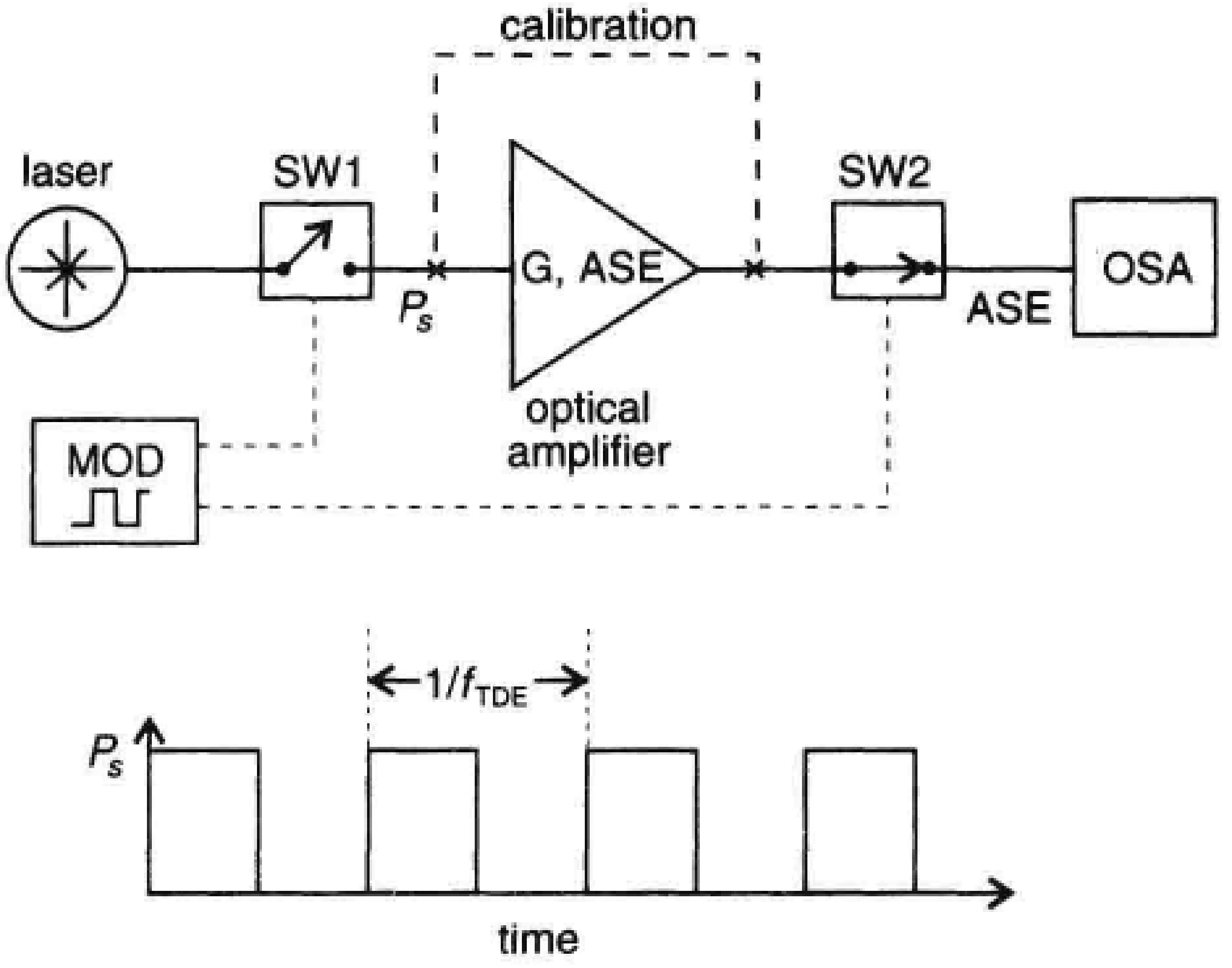

Figure 13.35 Optical amplifier ASE measurement setup for the time-domain extinction technique. OSA measures when signal is gated off. Gain measurement is performed with switches operating in unison.

ment of ASE required for noise figure calculations. This is illustrated for slow gating in Figure 13.36. Spiking in the amplifier output is observed because of the increased energy storage in the amplifier when the signal was gated off. Stimulated emission of the input signal quickly reduces the energy stored (causing spiking) to achieve a steady-state value towards the end of the gated-on period. At low repetition rates (below ~ 1 kHz) and high input powers, spiking may actually cause self-destruction of the EDFA.

When the source is gated at higher frequencies, the spiking is no longer present and the ASE follows a triangle-shaped waveform as shown in Figure 13.37. Increasing the gate frequency reduces the ASE peak-to-peak variation. In the limit of an infinite gate frequency, the triangle waveform converges to its average value. For gate frequencies above

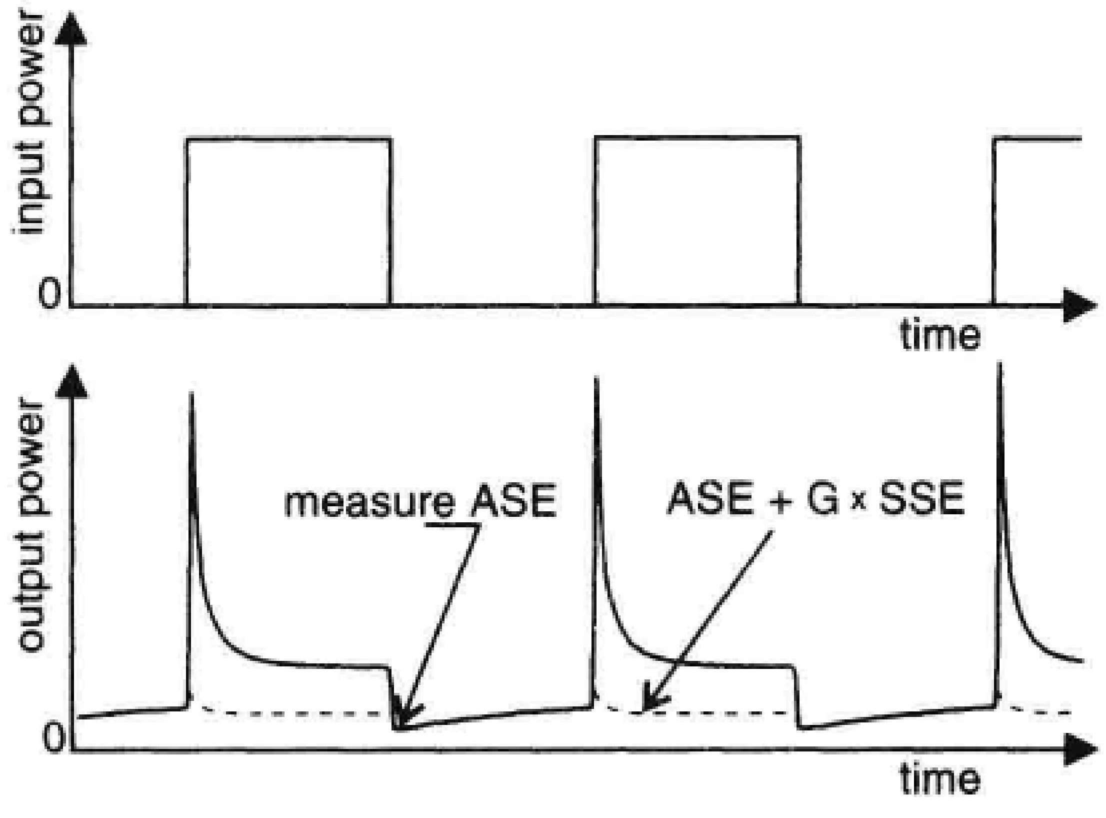

Figure 13.36 Input and output waveforms for low frequency time-domain extinction measurement.

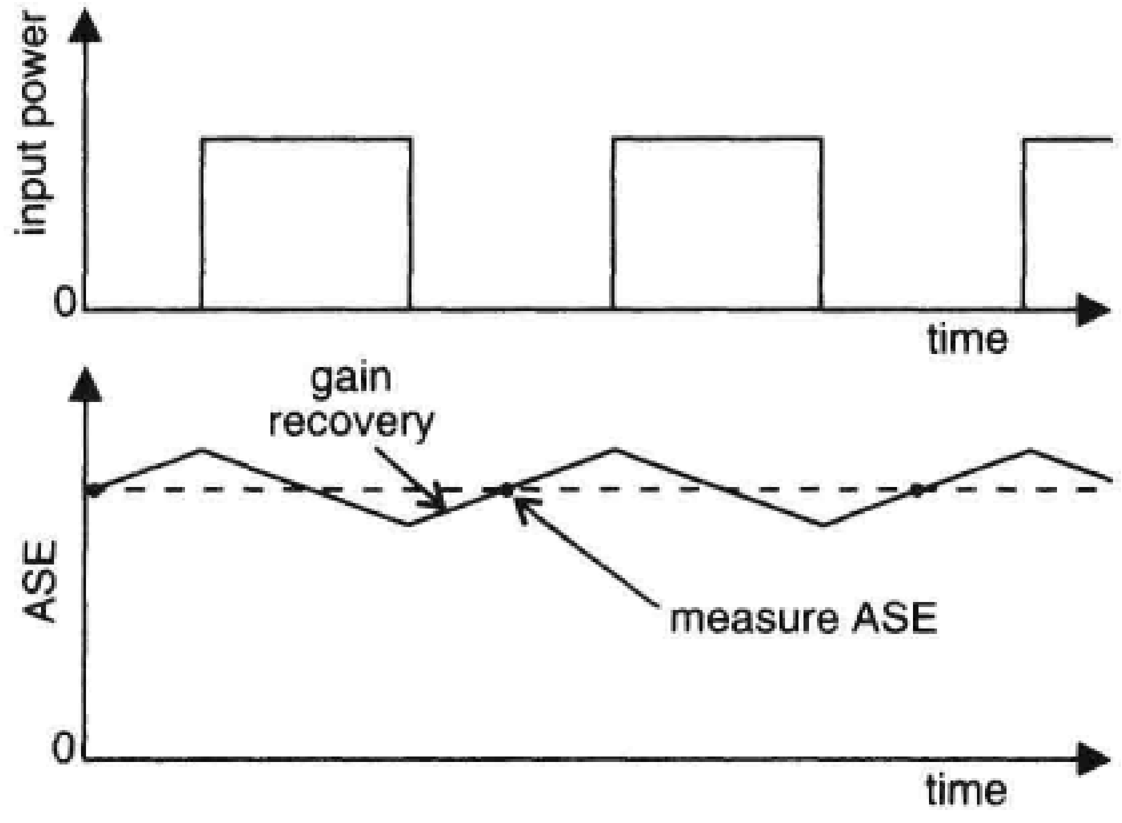

Figure 13.37 Input and output waveforms for high frequency time-domain extinction technique.

approximately ~ 20 kHz *the ASE sampled at the midpoint through the gain recovery time corresponds to the average ASE.* The actual low frequency limit depends on factors such as the applied pump power to the EDFA and the presence of active control circuits for output power leveling. The effective input signal power to the amplifier is the average power of the gated signal as measured with an optical power meter. Once the ASE is determined, the amplifier noise figure is calculated according to Equation 13.35. The amplifier gain can be characterized by a variety of techniques. A broadband EELED probe technique (discussed further on) may be included in the measurement setup to provide a rapid gain measurement across many wavelengths.

EDFA Transient Response. The mechanisms of pump absorption, energy storage, stimulated emission, and fluorescent decay all contribute to determine the response of the EDFA to changes in signal level.[4] When the signal level is abruptly changed, the EDFA will slowly stabilize to a new level of gain. The recovery time after the signal is gated-off is of the order of 100 μs but depends strongly on the EDFA pump power. In general, the recovery characteristic, measured in terms of the transient response of a small probe signal, varies approximately exponentially with time. Using the approximation: $e^{at} \approx 1 + at$, for small time t, the recovery will follow a linear recovery immediately after the signal is gated off. In the method discussed here, the data sampling must be made in the regime where the gain recovery varies linearly with time to obtain accurate measurements.

Characterizing the EDFA gain recovery is straightforward. The measurement setup used in the following experiment is shown in Figure 13.38. In the measurement, the counter-propagating-pumped EDFA delivered 32 mW of 1480 nm pump light to the erbium-doped amplifying fiber. Isolators at the amplifier ports shielded the unit from reflections. The saturating signal wavelength was set to 1533 nm and the input signal power was square-wave modulated. This caused gain modulation at all wavelengths in the erbium band. The gain modulation was measured with a small signal laser probe tuned to a wavelength of 1552 nm. The magnitude of the gain variation depended strongly on modulation rate as shown in Figure 13.39 where the amplified saturating signal, and the small signal probe are plotted. Where the gain perturbation is small, an expanded scale with off-

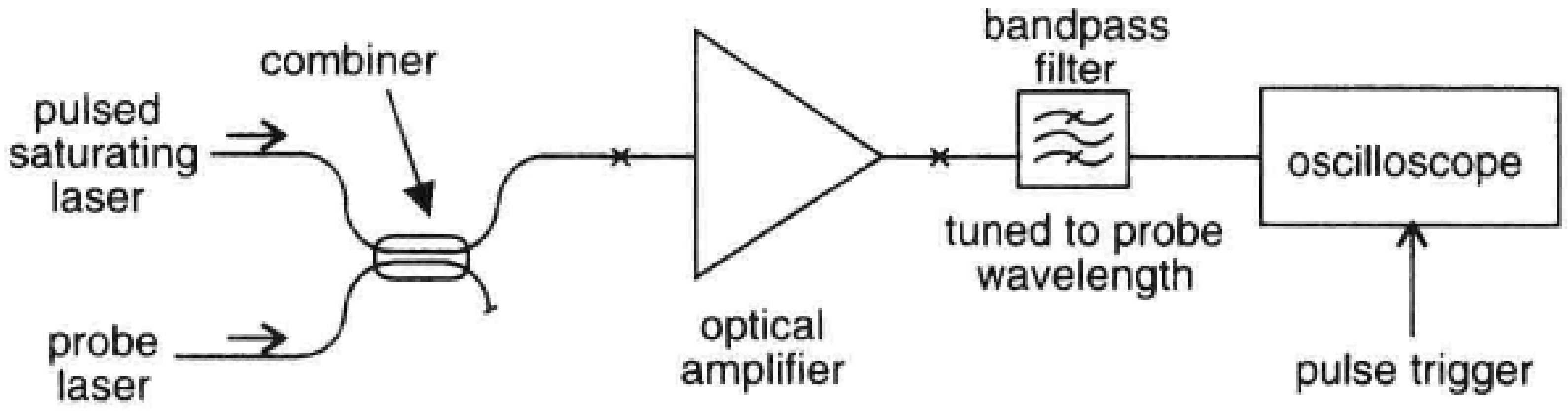

Figure 13.38 Measurement of EDFA transient gain recovery using a pulsed saturating source and a small signal probe.

set is used to show the probe variations. As discussed above, the initial peak in the saturating signal output power at signal turn-on was caused by the higher level of inversion realized after gain recovery. The signal transient can be quite rapid, with amplifier dependent decay-time constants on the order of ~ 10 μs. The reduction of the probe signal gain is evident as the saturating signal depletes the erbium inversion level. As the rate of modulation is increased, the amplifier recovery is truncated, the maximum instantaneous amplifier inversion level decreases, and the gain modulation at the probe wavelength of 1552 nm decreases. With further increases in modulation rate, the gain modulation takes on a triangle waveform profile with a peak-to-peak variation decreasing with modulation rate.

Gain Recovery Errors. Proper use of the TDE method requires setting the signal gate frequency to the appropriate value. The gate frequency should be set such that the gain recovery has a linear response. If the gate frequency is set too low, the recovery is not linear as indicated by the probe gain recovery in Figure 13.39a. Deviation from a linear response leads to measurement error since the measurement at the midpoint of the gain recovery characteristic is no longer representative of the average high-frequency value.

The error caused by nonlinear gain recovery was measured for an EDFA. The results are shown in Figure 13.40 The error is defined as the ratio of the measured probe gain at the test frequency divided by the probe gain measured at 300 kHz. Below a gate-rate of 10 kHz, the error significantly increases. This was performed for several different values of 1480 nm pump power incident on the erbium-doped fiber. From the data, it can be shown that the error due to nonlinear gain recovery increases linearly with pump power.

Transient Gain Saturation. Transient gain saturation is responsible for the spiking observed in Figures 13.36 and 13.39. This spiking does not affect the probe gain measurement, but it can impact the measured output signal power, which in turn affects the accuracy of the gain calculation. The error in the determination of output power occurs when the power is measured midway through the non-linear transient gain saturation recovery. This problem is solved by increasing the gate frequency and making an average power measurement. In practice, the gate frequency may be set appropriately by increasing it from ~ 20 kHz, until the transient gain saturation recovery becomes approximately

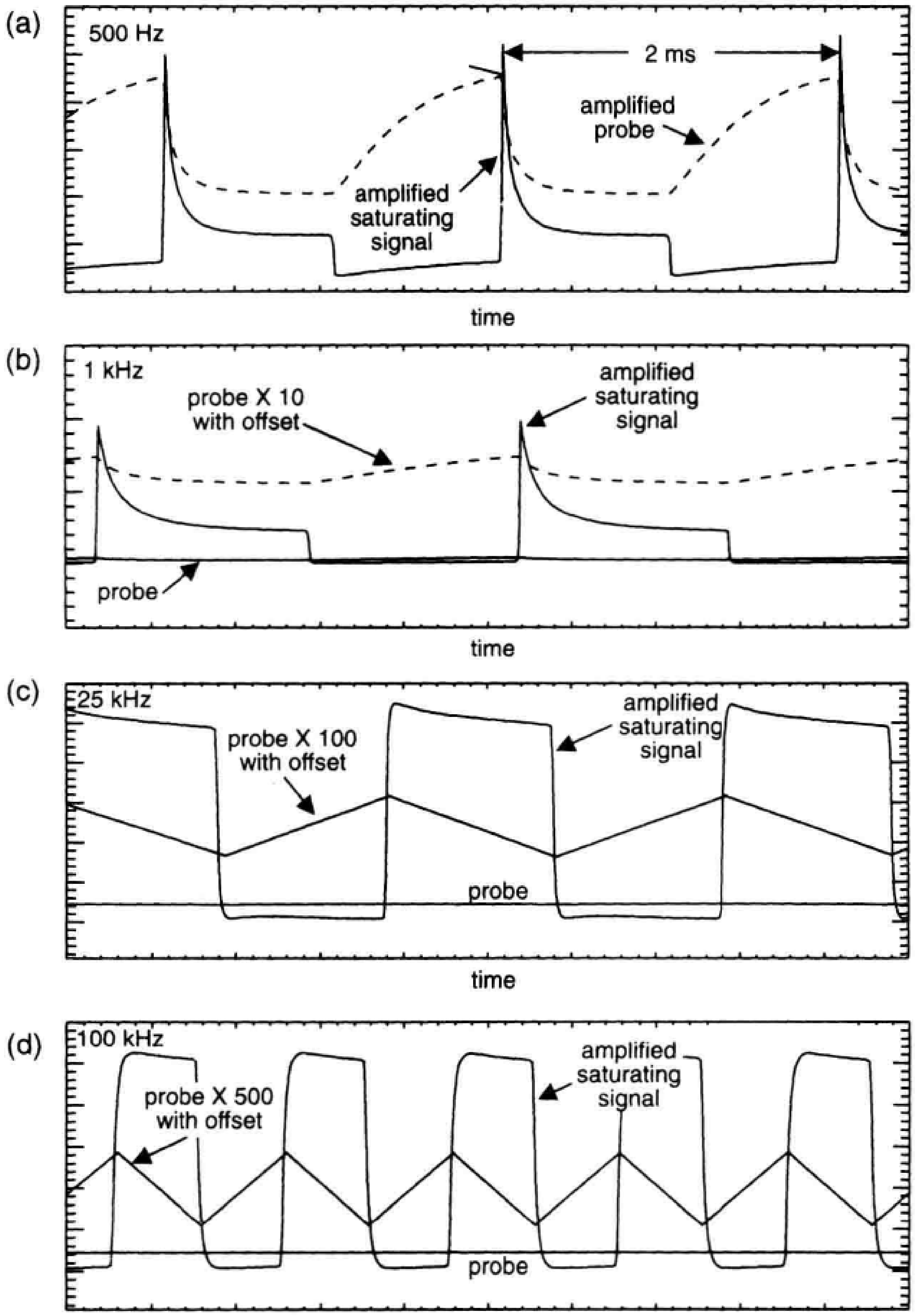

Figure 13.39 Measurement of EDFA transient response for different gate rates. (a) 500 Hz. (b) 1 kHz. (c) 25 kHz. (d) 100 kHz.

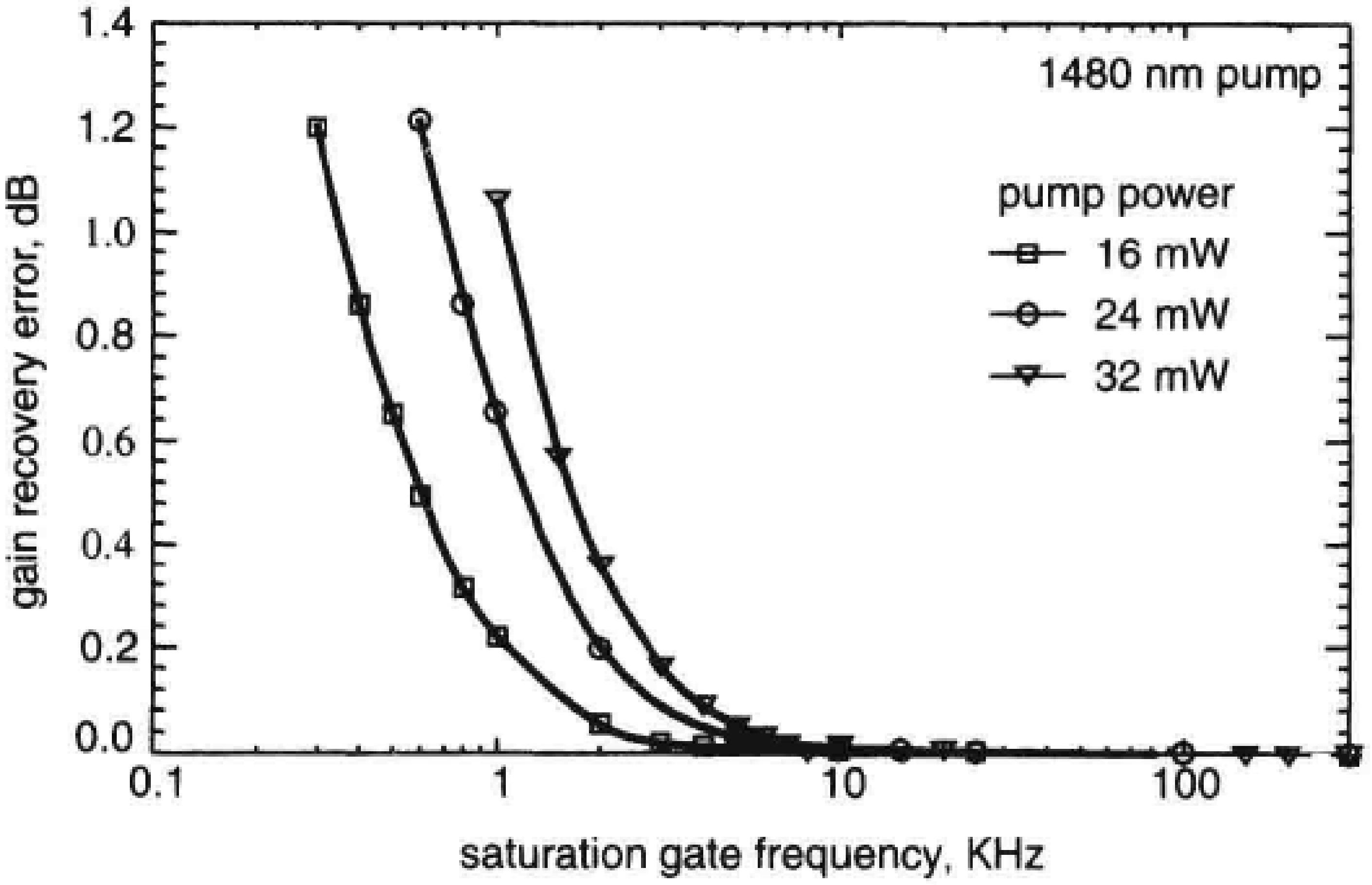

Figure 13.40 Measured error in gain as a function of gate frequency for various EDFA pump powers.

linear. This may require an optical receiver and an oscilloscope as part of the measurement setup.

Experiment: Time-Domain Extinction with Dynamic Gain Measurement. The noise figure and the dynamic gain spectrum of an EDFA were measured for various lengths of erbium-doped fiber. The dynamic gain spectrum refers to the gain of a small signal probe, measured versus wavelength, with the EDFA saturation set by a saturating signal. The slope of the dynamic gain spectrum is the dynamic gain slope as discussed in Section 13.2.5. The measurement setup is shown in Figure 13.41a. The saturating signal wavelength and power were 1554.4 nm and 40 μW respectively. The saturating signal laser had internal pulse capability allowing its output power to be pulsed at a 25 KHz rate. The laser source (HP 8168) trigger output (synchronized with the pulse modulation) was passed to the OSA (HP 71450) to trigger the OSA's internal time-domain detection capability. This allowed the OSA to sample the optical power 10 μs after the saturating signal was extinguished. The time-domain capability of the OSA was used in place of the second switch shown in Figure 13.35. The control input to the EELED (HP 83437) allowed it to be pulsed on when the falling edge of the gated signal was detected by the OSA. By operating the EELED output in pulsed mode, the EELED average output power is reduced. This reduces the effect of the EELED power on the amplifier saturation. The timing diagram for the measurement is shown in Figure 13.41b. Initially, the measurement was calibrated by bypassing the EDFA as shown in the figure. The EELED was pulsed on by a command from the OSA and its power was measured by the OSA 10 μs after the falling edge of the saturating signal laser. This yielded the wavelength-dependent calibration $P_{\text{cal}}(\lambda)$:

$$P_{\text{cal}}(\lambda) = P_{\text{LED}}(\lambda) \tag{13.39}$$

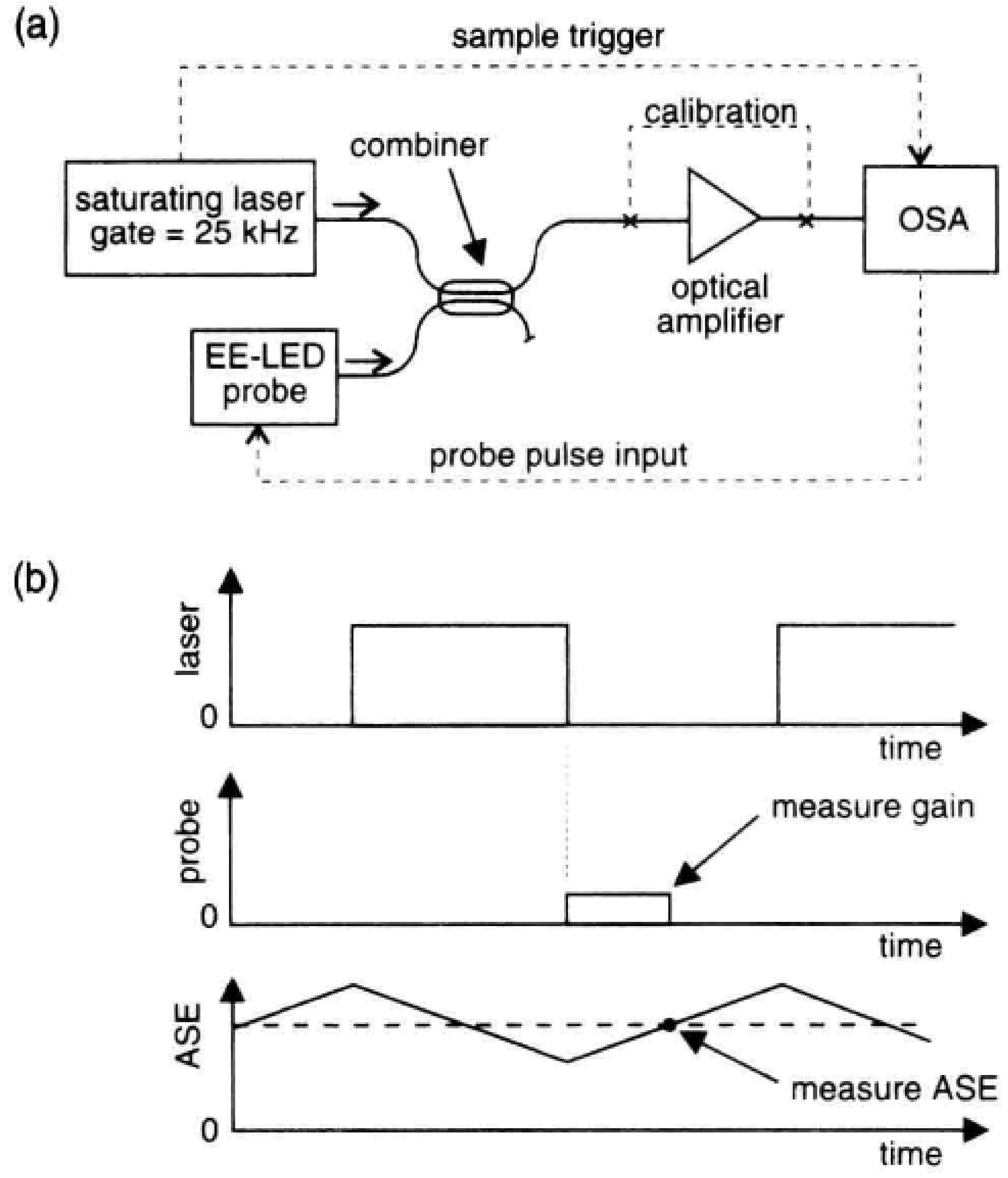

Figure 13.41 Time-domain extinction measurement with dynamic gain spectrum measurement. (a) Measurement setup; (b) optical waveforms for saturating laser, EE-LED probe and EDFA ASE.

Next the EDFA was inserted into the test setup and the OSA measured the output spectrum ($P_1(\lambda)$) 10 μs after the saturating laser was gated off, with the EELED pulsed on. This measurement yielded:

$$P_1(\lambda) = G(\lambda) \times P_{\mathrm{LED}}(\lambda) + P_{\mathrm{ASE}}(\lambda) \tag{13.40}$$

To solve for gain $G(\lambda)$, the ASE spectrum ($P_2(\lambda)$) is measured with the EELED output off, 10 μs after the saturating signal was gated off, yielding:

$$P_2(\lambda) = P_{\mathrm{ASE}}(\lambda) \tag{13.41}$$

The dynamic gain spectrum is calculated according to:

$$G(\lambda) = \frac{P_1(\lambda) - P_2(\lambda)}{P_{\mathrm{cal}}(\lambda)} \tag{13.42}$$

The noise figure is computed according to Equation 13.35 using Equation 13.19 and $\rho_{\mathrm{ASE}}(\lambda) = P_2(\lambda)/2B_o$.

After each gain and noise figure measurement, the erbium-doped fiber in the amplifier was reduced in length. The results of the noise figure and dynamic gain spectrum for

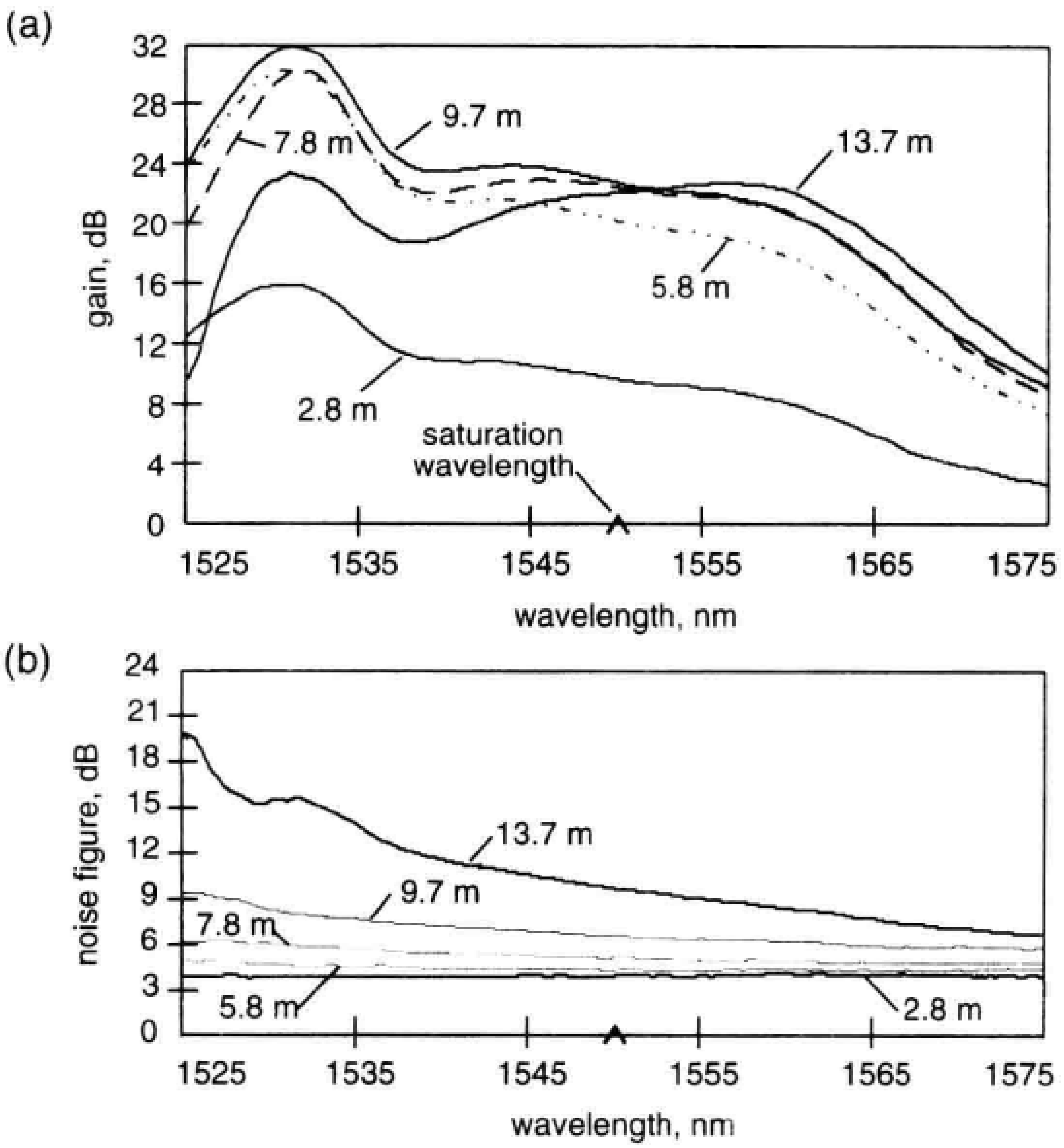

Figure 13.42 EDFA dynamic gain and noise figure measurement for various lengths of erbium-doped fiber. (a) Gain. (b) Noise figure.

the various lengths are shown in Figure 13.42. From the curves, it is apparent that the amplifier can be optimized separately in terms of maximum gain, lowest noise figure, and gain flatness. The gain and noise figure results are plotted, in Figure 13.43, versus length for the two wavelengths of 1530 nm and 1550 nm. From the figure, it is clear that the optimum gain length does not correspond to the lowest noise figure. The erbium-doped fiber length is particularly critical for low noise operation in counter-pumped amplifiers, such as the one measured here, since the noise figure depends heavily on the inversion level near the input. The sensitivity of the amplifier performance at 1530 nm to fiber length (and inversion level near the input) is a reflection of the fact that the absorption cross-section of the erbium-doped fiber peaks near this wavelength (see Figure 13.7).

WDM Characterization. Wavelength division multiplexed (WDM) transmission is a versatile method to increase the transmission capacity of singlemode optical fiber. Laboratory experiments using WDM have demonstrated over 2.6 Tb/s transmission capacity along a single fiber. In Figure 13.44, the input and output spectrums are shown for a very dense 1.1 Tb/s WDM transmission experiment using a transmitter composed of

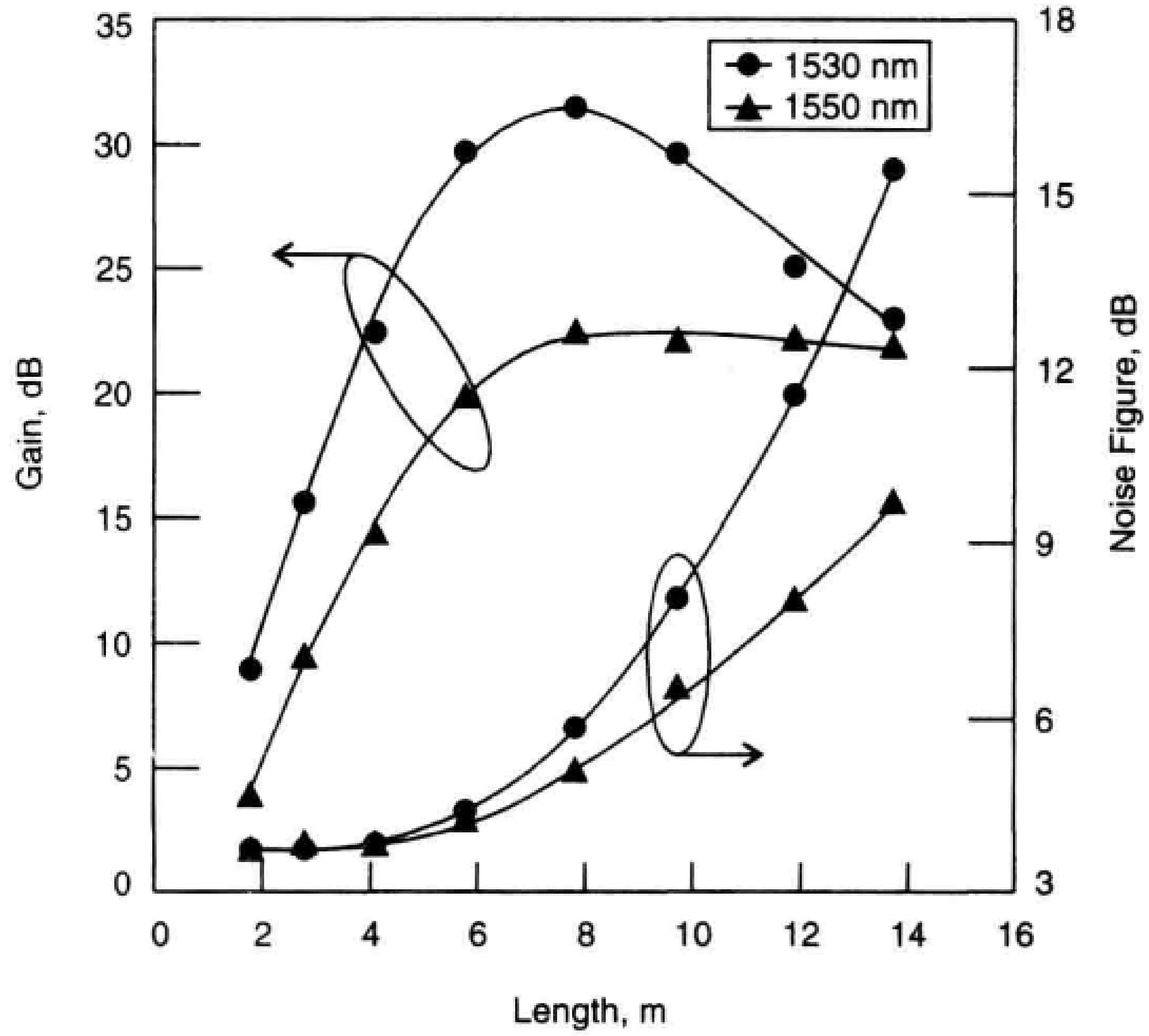

Figure 13.43 Gain and noise figure versus erbium-doped fiber length at the wavelengths of 1530 nm and 1550 nm.

55 lasers, each modulated at a 20 Gb/s rate.[41] The wavelength range of the lasers spanned most of the EDFA gain range from 1529 nm to 1565 nm as shown in the figure. Qualification of EDFAs for WDM applications will require measurement of gain and noise figure over a broad range of wavelengths. In principle, characterization of EDFAs for the WDM environment is an extension of the techniques used for single wavelength test. In WDM gain characterization, the optical gain is measured at each channel wavelength for a set of input conditions. The input conditions include the channel powers and wavelengths or "events" such as an added or dropped channel.

One of the principle challenges for making WDM noise figure and gain measurements is the required assembly of the large numbers of lasers. This process can be complex and costly to maintain. Measurement of the ASE generation at a specific wavelength also becomes more difficult as channel spacings become narrow.

In this section, the TDE method combined with dynamic gain-spectrum measurement is discussed for characterization of WDM gain and noise figure. The polarization extinction method is not covered since polarization nulling of a large number of wavelength channels is time-consuming and not practical due to the polarization-mode dispersion (PMD) effects discussed in Section 13.5.2.

The source-subtraction technique may be used for WDM characterization of EDFAs. Careful attention to the stability of the WDM lasers, and the effects of overlap-

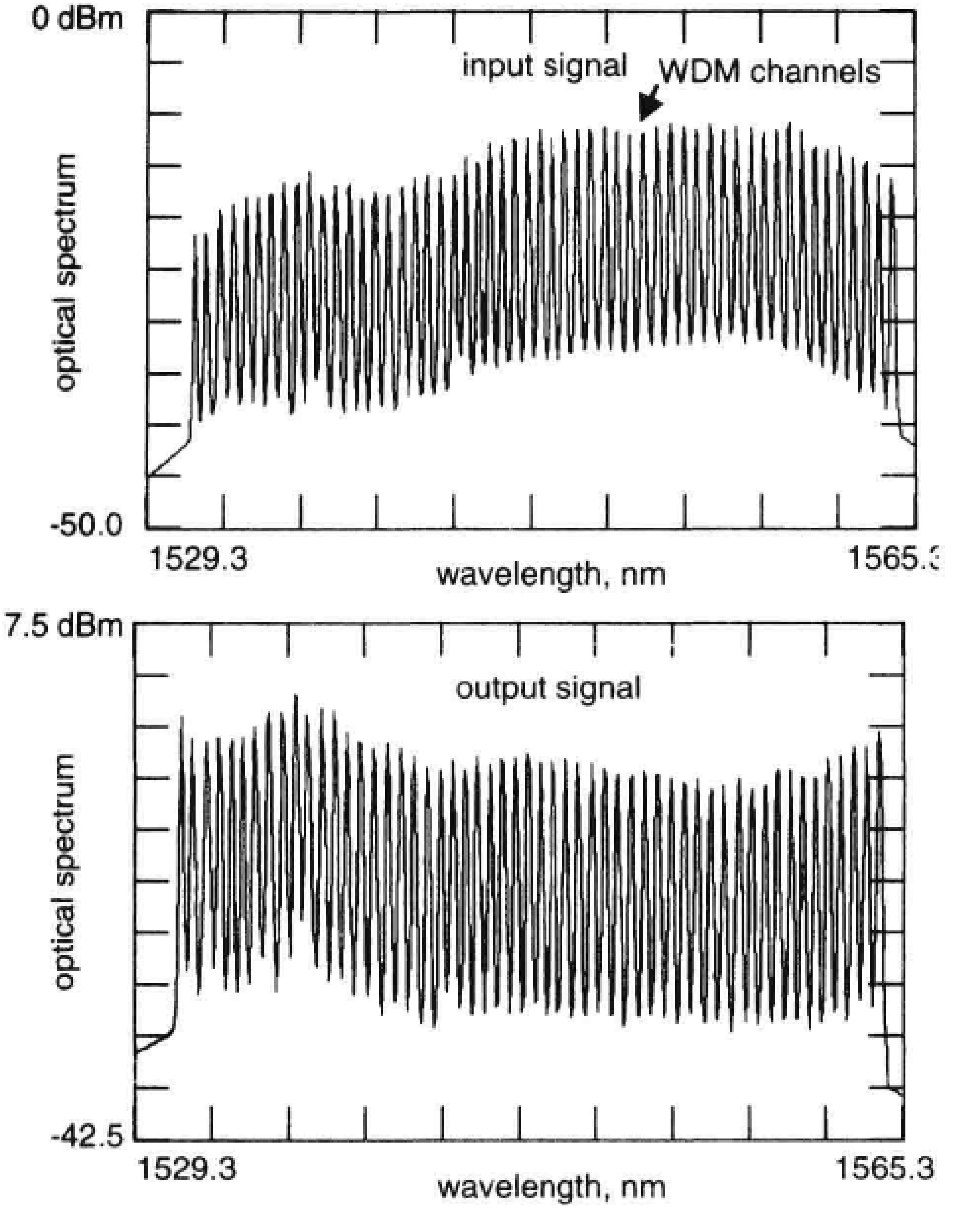

Figure 13.44 Optical spectrums for a 1.1 Tb/s 55 channel WDM transmission experiment: (a) input signal (b) output signal after passage through 150 km optical fiber containing two EDFAs. (With permission, after ref [41] ©1996, Optical Society of America.)

ping SSE from the WDM lasers at the measurement wavelength are required. Because of the similarities with the single-channel method, the reader is referred to the discussion on source-subtraction in Section 13.5.2.

A method allowing the same EDFA saturation effects due to multiple WDM channels while using fewer saturating signal lasers will be presented. This allows a significant simplification of the test system while maintaining amplifier conditions similar to those encountered with the actual number of channels.

Multichannel Method. The EDFA gain is measured by comparing the input and output powers at each channel wavelength. This is similar to the methods used for the single channel case discussed earlier. Instead of gating a single laser, for multichannel TDE test, all the lasers in the WDM transmitter are synchronously gated. The addition of the small signal probe, as discussed in Section 13.5.2 permits measurement of the dynamic gain spectrum allowing gain shape measurement between the WDM channels. The multichannel TDE method with the small-signal gain probe will be compared to the multichannel spot gain measurement method in an experiment with a four channel WDM source.

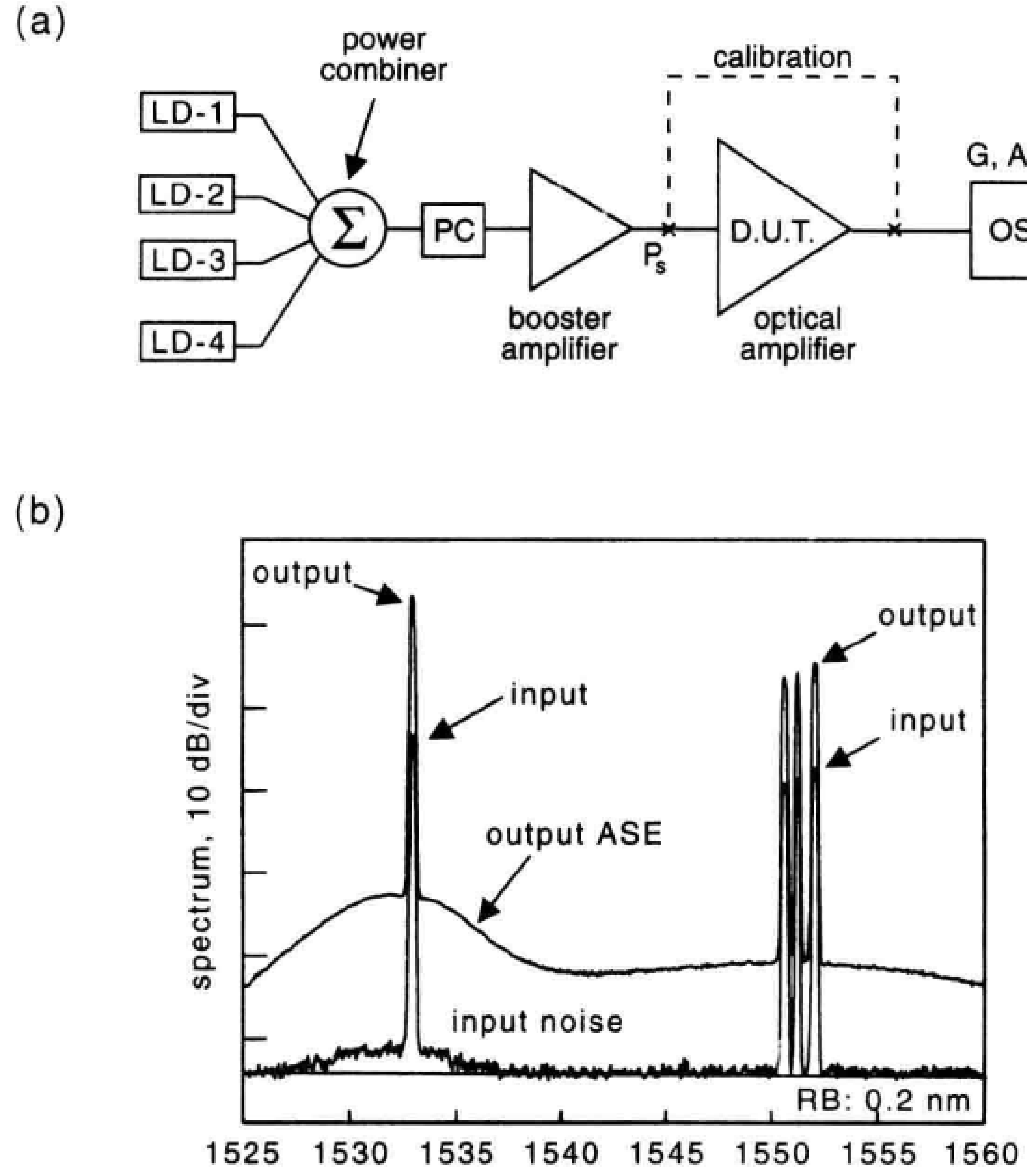

Figure 13.45 Multichannel gain measurement of an EDFA: (a) measurement setup, (b) optical spectrums of input and output signals.

Experiment: WDM Multichannel Gain. The gain of an EDFA was measured two ways. The setup shown in Figure 13.45a was used in the first experiment to measure the EDFA spot gains at each channel wavelength. Four lasers were combined using fused-fiber directional couplers. The polarization controller (HP 11896A) was set to randomly vary the light-combined lasers. The EDFA booster amplifier compensated for the optical loss (~8 dB) incurred in the power combiner. An OSA measured the optical power spectrums of the input signal to the EDFA and the amplified output spectrum. The input and output spectrums are shown in Figure 13.45b. The EDFA gains at the signal laser wavelengths of 1533.0 nm, 1550.5 nm, 1551.1 nm, and 1552.0 nm were measured to be 16.65 dB, 12.79 dB, 12.70 dB, and 12.65 dB respectively.

In the next experiment, the EDFA gain is measured with a multichannel TDE method using a small-signal probe. The experiment setup is shown in Figure 13.46a. FC/PC connectors were used to connect to the EDFA. The input signal powers and wavelengths were the same as with the previous measurement. An EELED was used as a small

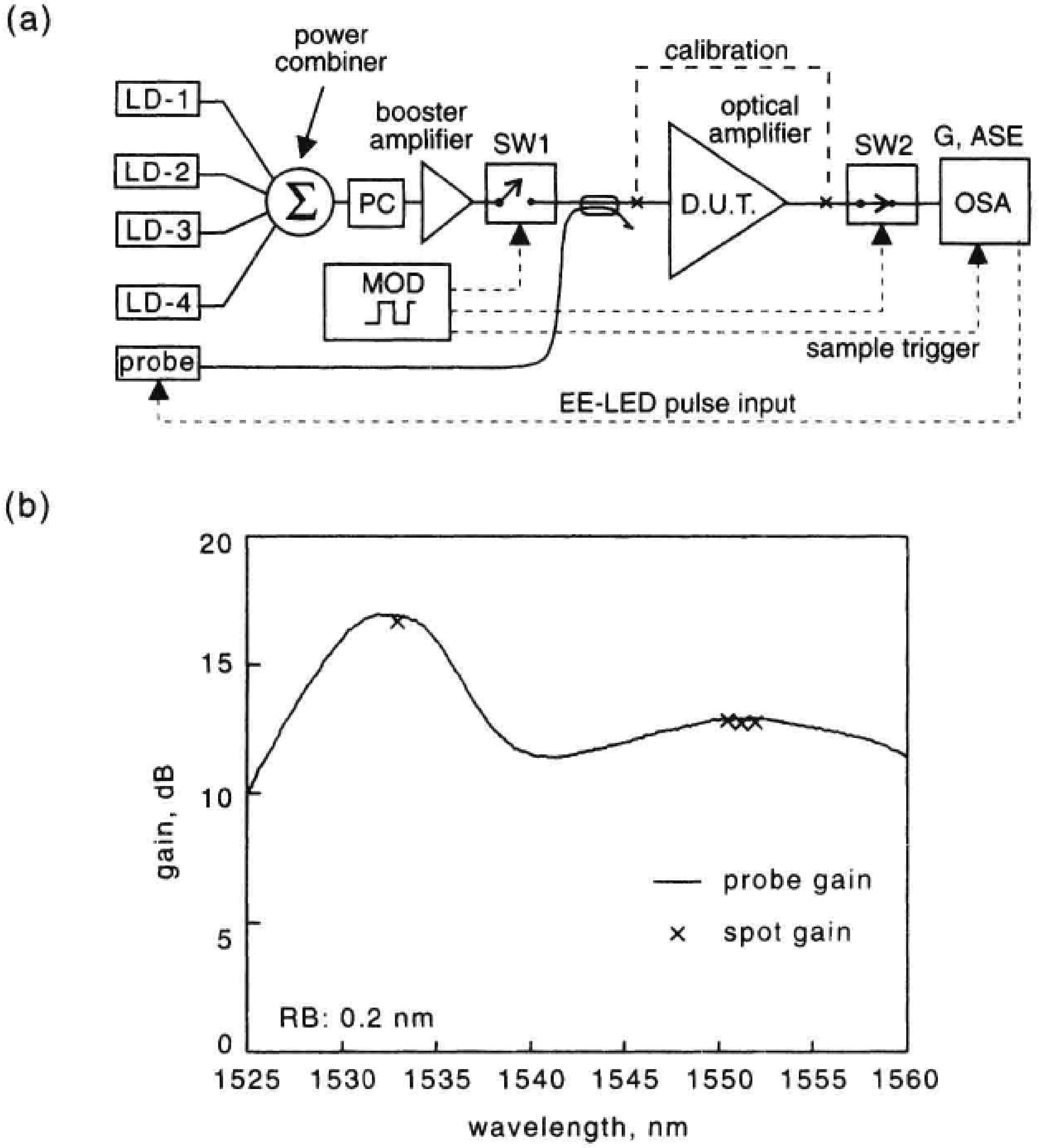

Figure 13.46 Four-channel WDM gain using time-domain extinction with a multichannel stimulus and small signal probe: (a) measurement setup, (b) dynamic gain measurement.

signal probe to measure the wavelength-dependent dynamic gain. The optical switches (acoustooptic modulators) were driven by two pulse generators. One pulse generator provided the trigger for the second pulse generator and the sampling trigger of the OSA (HP 71450). The OSA provided a signal to pulse the EELED output power as discussed in Section (13.5.2). The combination of the optical switch at the EDFA output and the time-domain capability of the OSA resulted in complete extinction of the amplified four-channel WDM source. This permitted a continuous measurement of the EDFA gain across the measurement range as shown in Figure 13.46b. The spot gains measured in the first experiment are plotted in Figure 13.46b for comparison. The two measurement techniques agreed to ~ 0.2 dB. This agreement is within the uncertainty of the connector insertion loss.

Multisource Approximations. For multichannel measurements, such as those required for WDM applications, the cost and complexity increases with the number of channels. In situations where the test cost/complexity are excessive, an approximate method may be considered. The reduced-source approximation can be considered for testing EDFAs in WDM applications.[42] The assumption behind this method is that the amplifier gain spectrum, or at least some portion of it, is homogeneously broadened. In EDFAs, homogeneous broadening has been shown to be predominant.[30] This is another way of saying that the gain saturation caused by a signal at any wavelength in the EDFA gain band reduces the amplifier inversion (common energy reservoir) responsible for gain at all other wavelengths.

It has been shown that spectral hole-burning (SHB) exists in EDFAs to a small degree.[31] To the extent that within a given bandwidth, SHB is insignificant, a single source can represent the ensemble of signals found in the spectral interval. This concept is shown in Figure 13.47. Recall from Equation 13.9 that the gain depends on the metastable state population, N_2. The N_2 population level defines the operating state of the amplifier. To mimic the effects of several channels, the representative source method must place the amplifier in the same state that would exist if the channels were actually present. This yields a requirement on the amplifier inversion level for the two cases

$$N_{2,rs} = N_{2,wdm} \tag{13.43}$$

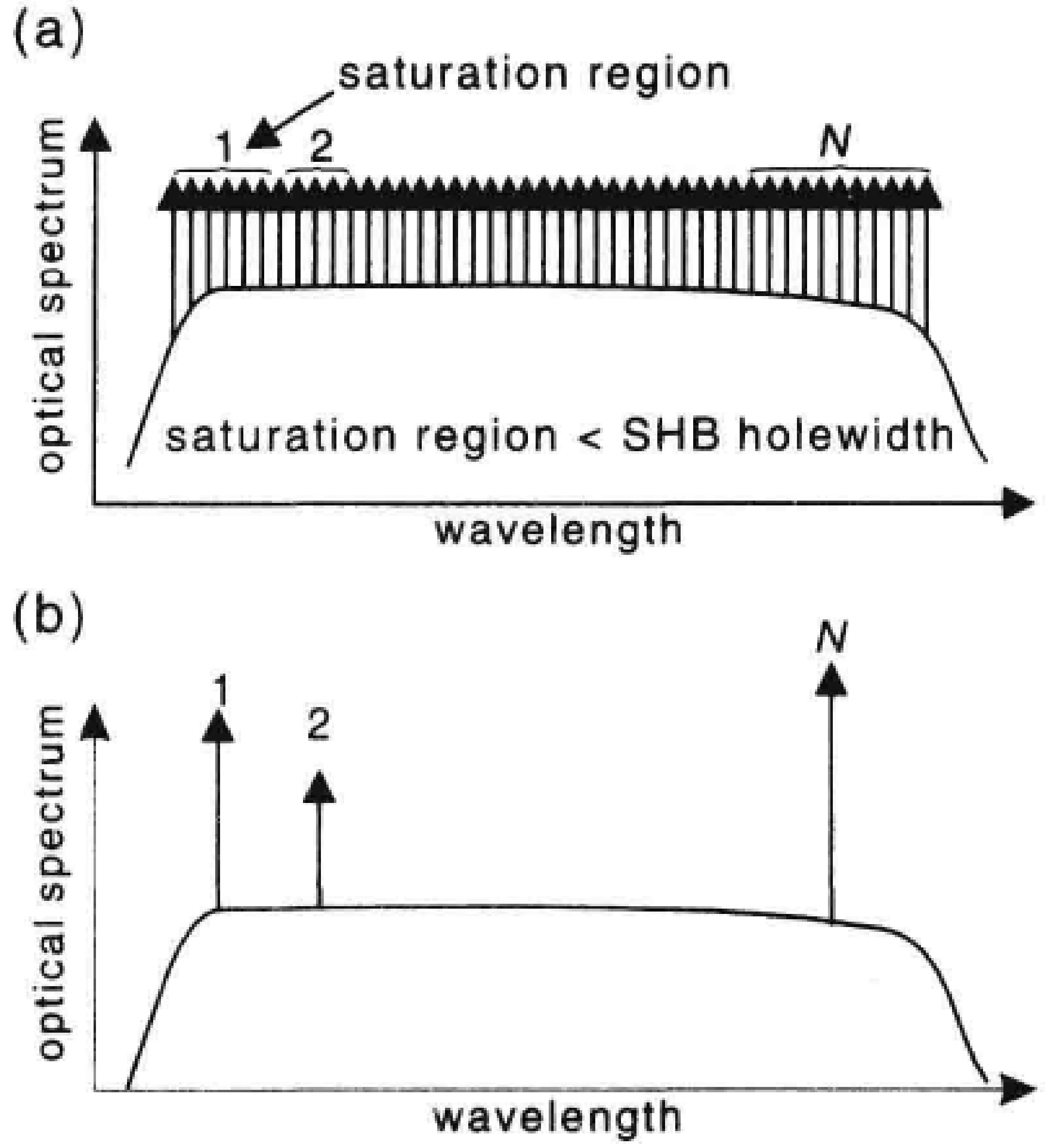

Figure 13.47 Reduced source concept for multichannel gain characterization. Homogeneous broadening across an interval permits representation of multiple signals with a single source.

where $N_{2,rs}$ is the inversion level established with the reduced set of saturating signal sources and $N_{2,wdm}$ is the inversion level established in the presence of all the WDM channels. The steady-state population $N_{2,wdm}$ is derived from a generalization of Equation 13.5 to include multiple signal beams. Equating the excited state populations in the two experiments places conditions on the reduced-source power and wavelength to achieve the best simulation of WDM amplifier performance. This leads to the following requirements for the optical power from a single source to simulate the effects of a cluster of WDM sources about the single source wavelength.[42]

$$P_s = \frac{1}{\lambda_s G_s} \sum_n P_n \lambda_n G_n \tag{13.44}$$

where P_s and P_n are the input single-source and WDM-input channel powers, respectively. The single-source wavelength can be set on the basis of the weighted wavelength

$$\lambda_s = \frac{1}{G_s P_s} \sum_n P_n \lambda_n G_n \tag{13.45}$$

In Equations 13.44 and 13.45, the channel gains are not known initially. Therefore G_n may be set equal to G_s as a starting guess to set the initial values for P_s and λ_s. After the dynamic gain spectrum is measured, better estimates of G_s and G_n are obtained. The measurement procedure converges in about two iterations.

Experiment: Single-Source WDM Gain. The single-source and multichannel WDM gain methods are compared for a four-channel WDM system.[42] The WDM gain measurement was performed with four independent channels combined through a power combiner as shown in Figure 13.46. The channel powers and wavelengths were: 41.1 μW, 1549.6 nm; 39.9 μW, 1553.0 nm; 35.1 μW, 1555.9 nm; and 33.9 μW, 1558.2 nm. Calibration was performed by bypassing the EDFA. In the reduced-source method, a single saturating source was combined with an EELED-ASE source as shown in Figure 13.48. Both the saturating laser (HP 8168) and the OSA (HP 71450) detection circuitry had gating capability which eliminated the need for external optical switches. The EELED (HP 83437) and saturating laser were pulsed using the noise-gain probe

Figure 13.48 Measurement setup using a single laser to represent four channels. P. R.: polarization randomizer.

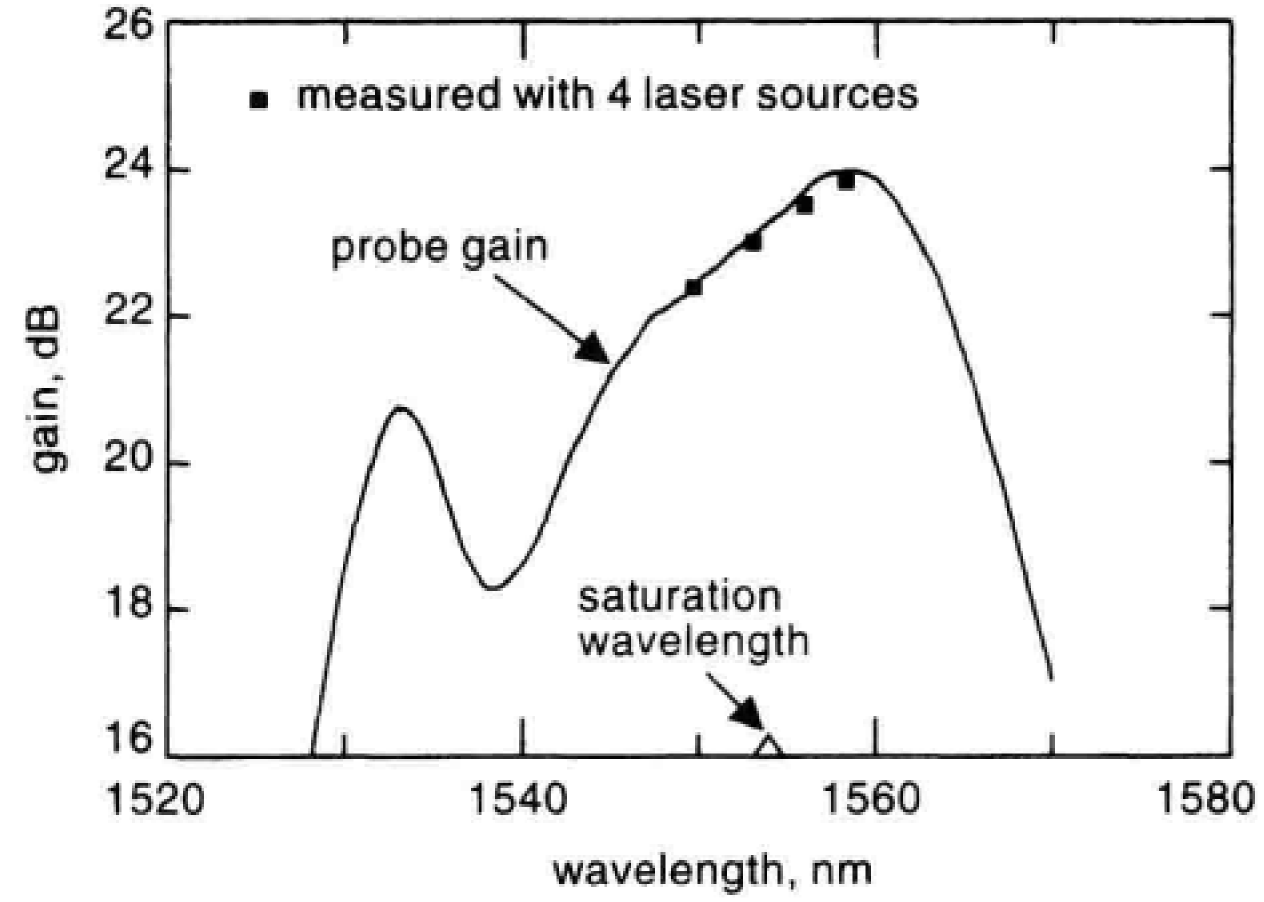

Figure 13.49 Comparison of four-channel WDM gain measurement using four lasers and a single laser with an EE-LED probe.

method described for the TDE technique (Section 13.5.2). The measurement results comparing the four-channel stimulus to the reduced source method with a noise-gain probe are shown in Figure 13.49. The two measurements agree well. There was a maximum of 0.2 dB difference at the third-channel wavelength.

In choosing the number of channels for the reduced source method, the following factors will come to bear:

- Degree of inhomogeneity in the amplifier saturation,
- Total power represented by each reduced-source channel,
- WDM channel spacings.

If the amplifier gain is determined to be completely homogeneously broadened, then a single channel will be sufficient to set the saturation. If inhomogeneous broadening (SHB) is significant and the reduced-source stimulus power becomes large to accommodate the ensemble of WDM channels, a spectral hole will reduce the probe gain in the vicinity of the saturation wavelength. In the wavelength band near 1.55 μm, the FWHM SHB hole-widths in EDFAs are ~ 8 nm which allows the use of fewer saturating signals than at a wavelength of 1.53 μm where the hole-width is ~ 4 nm. Finally, the combination of amplifier inhomogeneity and wide WDM-channel spacings may necessitate multiple sources for the reduced source set to best replicate the amplifier saturation. Ultimately, prior to the application of this technique, a comparison must be made with a complete WDM source to authenticate the measurement. Any significant difference between the measurements could serve as a correction factor for the reduced source method.

Electrical Methods. Noise figure measured by the electrical method is generally perceived to be a more complete measure of the intensity noise generated by the optical amplifier. It includes effects such as sig-sp beat noise, sp-sp beat noise, and multipath interference noise. In the electrical method, the gain and noise figure are derived from a spectral analysis of the optical receiver photocurrent. The amplifier noise figure is calculated with the general relation defined by Equation 13.34. Because of the effect of source noise, laser power, wavelength, coherence, and beat noise, the following system parameters must be specified with respect to the measured noise figure:

- Source power,
- Source wavelength,
- Source linewidth, and
- Receiver optical bandwidth.

The influence of the source power and wavelength on noise figure can be understood from their influence on the inversion level of the amplifier as discussed in Sections 13.2, and 13.3.1. The source linewidth is important in the effect it will have on the phase-to-intensity noise conversion, or multipath interference (MPI) caused by optical reflections within the EDFA as discussed in Section 13.3.2. Equations 13.31 through 13.33 indicate that the MPI-induced noise varies with the source linewidth, the reflection magnitudes as well as the time delay between the optical reflections. The source linewidth is specified as a stimulus parameter. The receiver optical bandwidth determines the spectral width of the ASE incident on the photodetector. This affects the contribution that the sp-sp beat noise will make to the measured noise. Additionally, the optical filter bandwidth determines the ASE shot noise and the spectral extent of the sig-sp beat noise in the photocurrent power spectrum. Normally this is not observed unless wide bandwidth optoelectronic detection (> 50 GHz) is used along with narrow optical filtering (< 1 nm).

Accurate noise figure measurements require that careful attention is placed on the effect of excess source laser noise, test system MPI noise, and receiver thermal noise. The amplifier noise figure should not depend on these noise contributions. Effects such as the source optical linewidth and the receiver optical bandwidth can result in measurement ambiguities which must be fully specified in the actual measurement. The power levels measured on the electrical spectrum analyzer must be calibrated to an absolute standard to obtain meaningful results. Two methods for this purpose are discussed: the RIN transfer technique and the IM index transfer technique.

To measure the amplifier noise figure the following must be determined:

- Gain,
- Input power,
- Intensity noise density produced by the amplifier: $S_P(f)$, and
- Photon energy.

The gain, input power and photon energy (or wavelength) are assumed to be known according to the methods discussed in Section 13.5.1 and Chapter 3. The principal task is to determine the spectral density of the amplifier intensity noise, $S_P(f)$. Low-noise optical amplifiers are designed to minimize $S_P(f)$.

Measurement of Optical Amplifier Noise. In this section, a method is discussed to separate the optical amplifier excess noise, $S_P(f)$, from the total noise spectrum given by an electrical spectrum analyzer. The corrupted noise spectrum refers to the optical-amplifier-generated noise, plus the other noise sources or effects that originate from the test system. The basic steps in the noise measurement procedure are[43]:

- Calibrate receiver,
- Measure the corrupted amplifier noise spectrum,
- Remove thermal noise,
- Remove measured shot noise, and
- Calculate $S_P(f)$.

A test system for measuring optical amplifier noise is shown in Figure 13.50. There are a number of factors affecting the measured data as shown in the figure. The receiver thermal noise, detected shot noise, and frequency response of the system will contribute to measurement error. The amplifier noise must be separated from the total measured noise.

The electrical spectrum analyzer display is proportional, by way of $|k(f)|^2$ to the power spectrum of the photocurrent. The bandwidth limitations of the photodetector and electronics are included in $|k(f)|^2$.

With the amplifier under test illuminated by the an optical source with the required wavelength, power and linewidth, the measured photocurrent power spectrum $S_{\mathrm{ESA}}(f)|_{\mathrm{mea.}}$ is described by:

$$S_{\mathrm{ESA}}(f)|_{\mathrm{mea.}} = |k(f)|^2[\mathcal{R}^2 S_P(f) + S_i(f)|_{\mathrm{shot}}] + S_{\mathrm{ESA}}(f)|_{th} \ \text{[W/Hz]} \quad (13.46)$$

(measured noise = excess noise + shot noise + thermal noise)

The terms on the right-hand-side correspond to the excess noise contributions of the optical amplifier, the photocurrent shot noise, and the thermal noise. In an ideal measure-

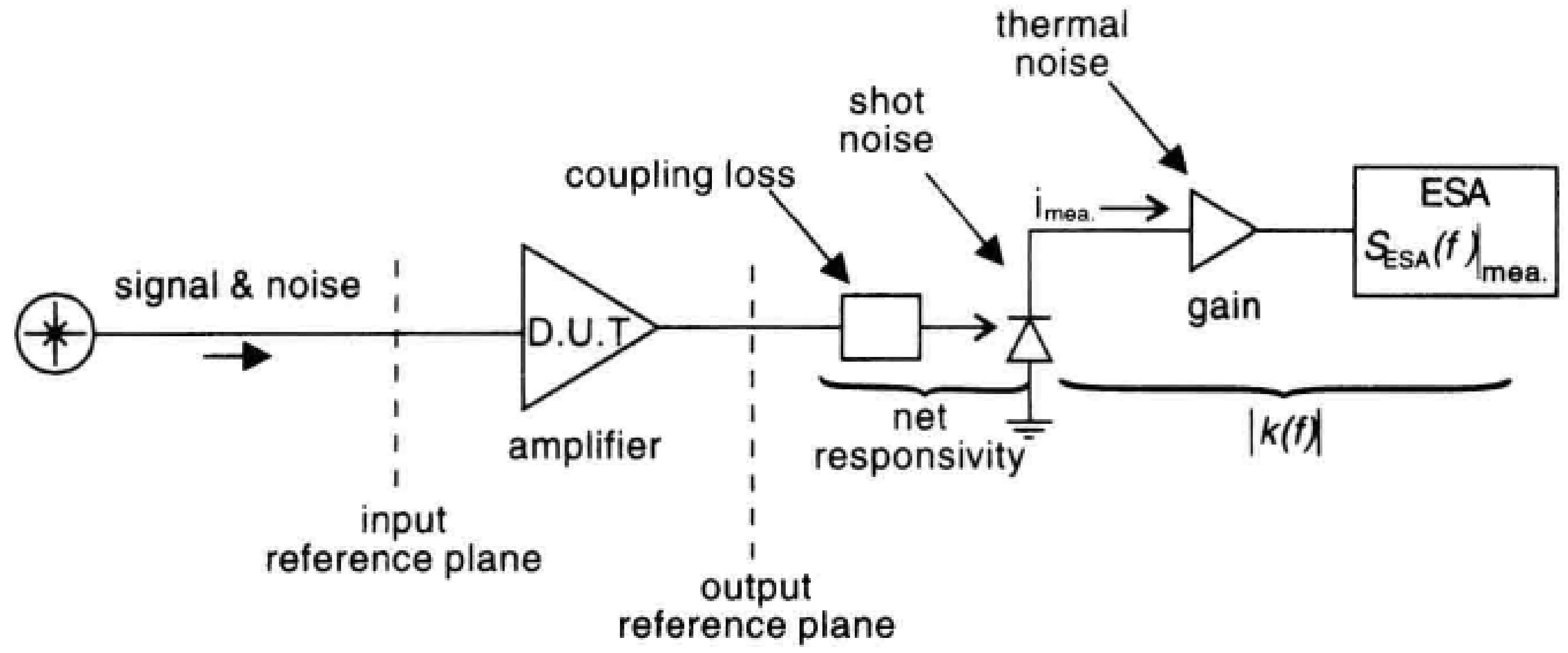

Figure 13.50 Basic measurement setup for measuring optical amplifier noise using the electrical method. ESA: electrical spectrum analyzer.

ment, the thermal noise would be negligeable and $|k(f)|^2$ would be the reference resistance, R_{ESA}, of the electrical spectrum analyzer, which is typically 50 Ω.

Thermal Noise Correction. The thermal noise density, $S_{\mathrm{ESA}}(f)|_{th}$ is measured with the input light blocked as shown in Figure 13.51. Under the assumption that the thermal noise density is independent of the magnitude of the optical signal, it is measured by completely blocking the light from the photodetector. The measured thermal noise spectrum is denoted by $S_{\mathrm{ESA}}(f)|_{th}$. Subtracting the density $S_{\mathrm{ESA}}(f)|_{th}$ from $S_{\mathrm{ESA}}(f)|_{\mathrm{mea}}$ performs the thermal noise correction.

RIN Transfer: System Transfer Function Correction. The frequency dependent system transfer function, $|\mathcal{R}k(f)|^2$ is measured next. A calibrated source of excess optical noise replaces our source (for example, amplifier) under test. The setup with the calibration source is shown in Figure 13.52. This step is referred to as a RIN transfer calibration since the optical noise source is characterized by a RIN which is very stable over time. A practical way to implement the noise source is to optically filter the ASE from an EDFA. A typical filter bandwidth is of the order of 1 nm. This will yield a flat intensity noise spectrum up to ~ 2 GHz. The RIN associated with the filtered ASE source is not required to be flat for the calibration to be valid. The only requirements are that the RIN caused by the standard is large compared to the receiver thermal and shot noise, and that the frequency dependence of the RIN is known.

The RIN associated with the filtered source can be derived from an analysis of the optical intensity associated with the filtered optical field spectrum. For an arbitrarily shaped, bandwidth-limited unpolarized ASE source, the frequency-dependent RIN is given by:

$$\mathrm{RIN}_{\mathrm{cal}}(f) = \frac{FT\left[\left|FT^{-1}\{S_E(\nu)\}\right|^2\right]}{\left[\int S_E(\nu)\,d\nu\right]^2} \quad [Hz^{-1}] \tag{13.47}$$

where $S_E(\nu)$ is the single-sided optical field power spectrum, and FT denotes the Fourier transform. The denominator corresponds to the average optical power-squared and the nu-

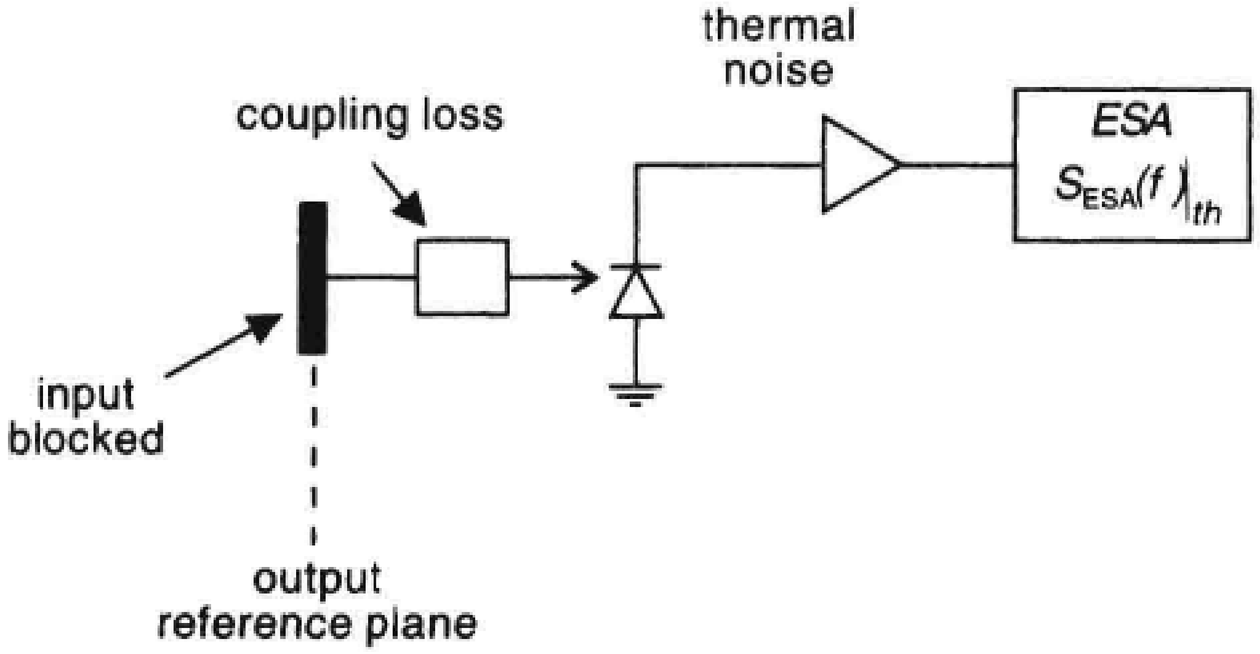

Figure 13.51 Measurement of receiver system thermal noise.

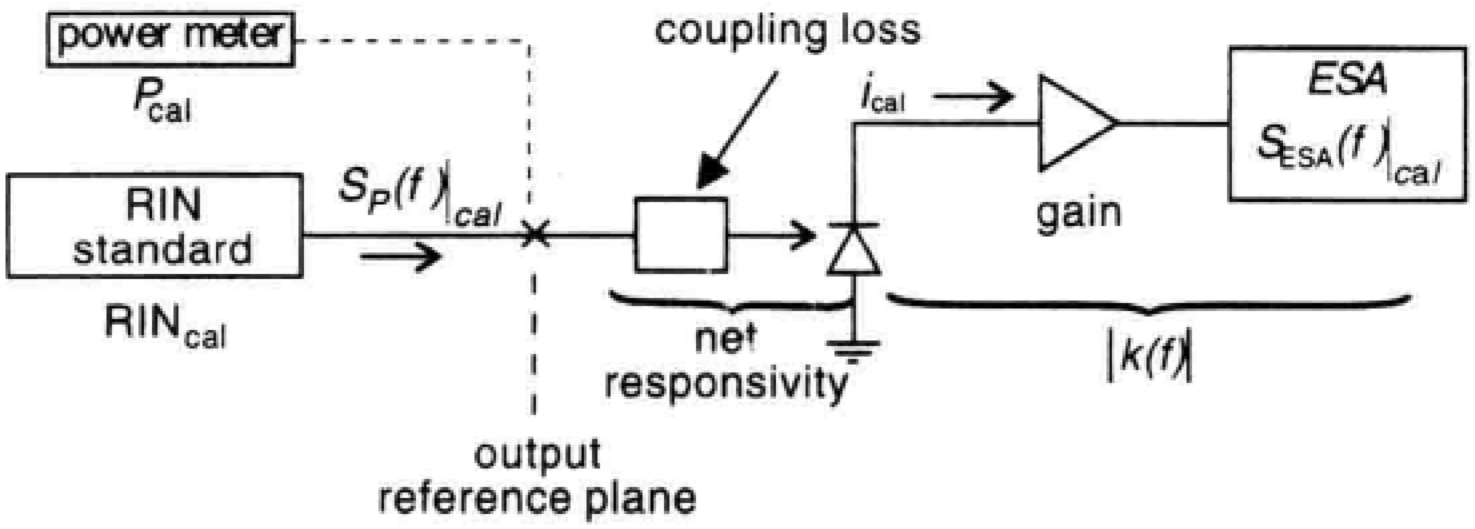

Figure 13.52 RIN transfer technique for receiver calibration.

merator corresponds to the expected spontaneous-spontaneous intensity beat noise. The absolute RIN is determined from a simple measurement of the optical field spectrum using an OSA. The RIN must be calculated numerically, except when the filtered ASE shape follows simple functional forms such as those given in Table 13.2. The RIN depends only on the shape of the ASE spectrum and not on the absolute amplitude. This results in a very stable RIN transfer standard since the bandwidth of the optical filter is fixed.

When the RIN transfer standard is combined with a calibrated optical power meter, the filtered ASE source provides an *absolute spectral noise power reference* according to Equation 13.23. The two fundamental quantities for the reference are the RIN of the filtered ASE source and the average power. The average power measurement is performed accurately with an optical power meter. Thus, according to Equation 13.23, the absolute optical noise reference density is:

$$S_P(f)|_{\text{cal}} = \text{RIN}_{\text{cal}}(f) \times P_{\text{cal}}^2 \quad [W^2/\text{Hz}] \tag{13.48}$$

Where P_{cal} is the RIN standard average output power measured with an optical power meter.

The electrical spectrum analyzer measures the photocurrent noise spectrum $S_{\text{ESA}}(f)|_{\text{cal}}$ due to the RIN transfer standard. Using Equation 13.46, the spectral density is:

$$S_{\text{ESA}}(f)|_{\text{cal}} = |\Re k(f)|^2 \, S_P(f)|_{\text{cal}} \tag{13.49}$$

The thermal and shot noise are not included in the above expression since the photocurrent noise is dominated by the detection of the intensity noise from the RIN transfer standard. The excess noise from the RIN standard dominates over any other noises present.

The unknown calibration constant is found according to:

$$|\Re k(f)|^2 = \frac{S_{\text{ESA}}(f)|_{\text{cal}}}{S_P(f)|_{\text{cal}}} \tag{13.50}$$

With this second calibration step, the system transfer function is now known across the frequency range of interest.

Correcting the Shot Noise. The actual receiver shot noise must be corrected to obtain the shot noise that would be produced by an ideal receiver according to the noise figure definition given in Equation 13.34. The differences between the actual receiver shot noise and the shot noise obtained with an ideal receiver are caused by the optical coupling loss to the receiver and the limited quantum efficiency of the actual receiver photodetector. The correction procedure subtracts out the measurement system shot noise from the measured noise and adds the shot noise generated by an ideal receiver to the amplifier noise measurement.

The photocurrent spectrum of the shot noise in the measurement receiver is given by Equation 13.25. The DC responsivity $\mathcal{R}$ must be found to complete the shot noise subtraction. Two measurements are required to determine $\mathcal{R}$. The setup for the system transfer function measurement shown in Figure 13.52 is used. The average photodetector current, i_{cal}, is measured. The other required measurement, P_{cal}, was already performed (see Equation 13.48). This data permits determination of the net DC responsivity according to:

$$\mathcal{R} = \frac{i_{\text{cal}}}{P_{\text{cal}}} \tag{13.51}$$

At this point, the calibration process is complete. The next step is to use the calibration data to determine the optical amplifier noise.

Corrected Amplifier Noise. Equation 13.46 can be solved for the unknown intensity noise $S_P(f)$:

$$S_P(f) = \frac{S_{\text{ESA}}(f)|_{\text{mea}} - S_{\text{ESA}}(f)|_{th}}{|\mathcal{R}k(f)|^2} - \frac{2qi_{\text{mea}}}{\mathcal{R}^2} \tag{13.52}$$

Equation 13.52 indicates the need for the three operations discussed: thermal noise correction, amplitude frequency response correction, and shot-noise subtraction.

Inserting the calibration coefficients given by Equations 13.50 and 13.51 into 13.52, the excess amplifier noise is found in terms of measured parameters:

$$S_P(f) = \frac{S_{\text{ESA}}(f)|_{\text{mea}} - S_{\text{ESA}}(f)|_{th}}{\dfrac{S_{\text{ESA}}(f)|_{\text{cal}}}{RIN_{\text{cal}}(f)\, P_{\text{cal}}^2}} - \frac{2qi_{\text{mea}}}{\left(\dfrac{i_{\text{cal}}}{P_{\text{cal}}}\right)^2} \quad [W^2/\text{Hz}] \tag{13.53}$$

This equation is one of the principle results of this section. It shows how the intensity noise $S_P(f)$ (excluding shot noise) from the optical amplifier under test is found by making measurements of: (1) the uncalibrated measurement of the amplifier noise $S_{\text{ESA}}(f)|_{\text{mea}}$ and photocurrent i_{mea}; (2) the thermal noise; and (3) the average optical power P_{cal} and DC photodetector current i_{cal} when the receiver is connected to the calibrated noise standard. The measurement data and calibration coefficients are summarized in Table 13.6

In the preceding analysis, the effective system quantum efficiency $\mathcal{R}$ was frequency independent. All frequency-dependent system effects have been confined to the electronics which includes transit time effects in the photodetector and bandwidth limitations in

Table 13.6 Variable Definitions for Equation 13.53.

Symbol	Description	Units
$S_P(f)$	Spectral density of optical intensity noise	W^2/Hz
$S_{ESA}(f)\|_{mea}$	Uncorrected amplifier noise spectrum	W/Hz
$S_{ESA}(f)\|_{th}$	Electrical spectrum analyzer noise with input light to photodetector blocked	W/Hz
$S_{ESA}(f)\|_{cal}$	Electrical spectrum analyzer noise data with RIN-transfer source applied to measurement system input	W/Hz
$RIN_{cal}(f)$	RIN-transfer standard	Hz^{-1}
P_{cal}	Average power of RIN-transfer standard	W
P_{dc}	Average amplifier output power	W
i_{cal}	Average photocurrent produced by RIN-calibration standard	A
q	Elementary electronic charge: 1.602×10^{-19}	coul.

the electronics. Therefore, the test system must be free from optical reflections which could create significant amplitude ripple, otherwise the measurement technique should be modified to account for the system interference effects. The effect of the reflections between the amplifier and receiver will be to impart a frequency ripple onto the intensity-noise spectrum and to convert source laser phase noise to amplitude noise. Therefore, it is wise to use low-reflection connections and an optical receiver with a low optical back-reflection.

Calculation of Noise Figure. The amplifier noise figure defined in Equation 13.34 requires the determination of the amplifier input and output SNRs. The input SNR is calculated on a shot-noise basis. The output SNR is computed based on the photocurrent signal and noise created in an ideal receiver illuminated by the amplified signal GP_s, and the amplifier excess noise $S_P(f)$ obtained from Equation 13.53. The ideal receiver has a flat frequency response, no thermal noise, and unity quantum detection efficiency ($\mathcal{R}_{\text{ideal}} = q/h\nu$).

Input SNR. The shot-noise density given by Equation 13.25 is multiplied by the detection bandwidth B_e to obtain the mean-squared shot noise. The input SNR is calculated by taking the ratio of the signal-to-noise powers at the ideal receiver electrical output:

$$\text{SNR}_{\text{in}} = \frac{\mathcal{R}_{\text{ideal}}^2 P_s^2}{2qi_{dc}B_e} = \frac{P_s}{2h\nu\, B_e} \qquad (13.54)$$

Output SNR. The output noise density of the ideal receiver is the sum of the contributions from the amplifier generated noise $S_P(f)$, and the shot noise:

$$S_i(f) = S_i(f)\big|_{\text{excess}} + S_i(f)\big|_{\text{shot}} \qquad (13.55)$$

The amplifier contribution to the ideal photocurrent noise is determined by computing the photocurrent spectral density (see Equation 13.22) corresponding to the excess noise in Equation 13.53:

$$S_i(f)\big|_{\text{excess}} = S_P(f) \times \mathcal{R}^2_{\text{ideal}} \tag{13.56}$$

Integrating the excess and shot noises given by Equations 13.56 and 13.25 over the detection bandwidth B_e yields the output SNR:

$$\text{SNR}_{\text{out}} = \frac{< GP_s >^2}{S_P(f)B_e + 2 < GP_s > h\nu\, B_e} \tag{13.57}$$

The noise figure is calculated by taking the ratios of Equations 13.54 and 13.57 with B_e set to 1 Hz:

$$F = \frac{P_s\, S_P(f)\, B_e + 2 < GP_s > h\nu\, B_e}{2h\nu \quad < GP_s >^2} \tag{13.58}$$

Equation 13.58 reduces to:

$$F = \frac{S_P(f)}{2h\nu\, G^2 P_s} + \frac{1}{G} \tag{13.59}$$

$$\text{noise figure} = \text{excess noise factor} + \text{shot-noise factor}$$

This equation is the main result of the electrical noise figure section. This general relation is composed of two parts. One part contains all the excess-noise contributions to the net-noise figure. The second part is the shot-noise contribution. This result is very general since it does not specify or constrain the type of noises that contributes to the amplifier excess noise. It is valid with sig-sp, sp-sp beat noises as well as MPI-induced phase-to-intensity converted noise. The amplifier excess noise, $S_P(f)$, is measured according to Equation 13.53, P_s is determined using a calibrated optical power meter, and the amplifier gain G is measured using the techniques described in Section 13.5.

As a check for Equation 13.59, the limiting form of this expression is found where sig-sp beat and shot noise are the dominant noise processes. Substituting into Equation 13.59 the sig-sp beat noise from Equation 13.27 and applying the conversion indicated in Equation 13.22, the noise figure obtained is:

$$F = \frac{2\rho_{\text{ASE}}}{G\, h\nu} + \frac{1}{G} \tag{13.60}$$

which is the same relation as defined in Equation 13.35 for the optical method for noise-figure measurement.

Laser Sources with Excess Noise. Any excess noise (in excess of the usual shot noise) from the source illuminating the amplifier under test must be taken into account in order to make an accurate noise characterization of the amplifier. The effect of the source noise on the accuracy of the electrical method is shown in Figure 13.29. One difficulty with the electrical method is there are not many options available to correct for the excess source noise. If the excess noise from the laser is stable over time, it can be measured and later subtracted from the result obtained when the amplifier is in place.[44] This method will be the focus of the following discussion.

Let the excess source noise be designated by: $S_p(f)|_{\text{source}}$. Measurement of the source excess noise is accomplished using the same procedures outlined earlier for characterizing the amplifier excess noise. Any optical attenuation between the source and the receiver should be minimized to obtain the best measurement of the source excess noise. Let T denote the variable optical transmission factor ($0 < T < 1$) between the source and the amplifier under test. T does not include any losses present when the excess source noise $S_P(f)|_{\text{source}}$ was measured. T originates from unavoidable optical-coupling losses as well as deliberate optical attenuation provided to control the input signal level P_s to the amplifier. Taking the transmission factor T into account, effective noise power at the amplifier input terminals is:

$$S_P(f)|_s = T^2\, S_P(f)|_{\text{source}} \tag{13.61}$$

The noise at the amplifier output is a combination of internally generated noise and the amplified excess noise from the source:

$$S_P(f) = S_P(f)|_{\text{amp}} + G^2T^2S_P(f)|_{\text{source}} \tag{13.62}$$

The amplifier noise figure is corrected for the excess source noise according to:

$$F = \frac{S_P(f) - G^2T^2S_P(f)|_{\text{source}}}{2h\nu\, G^2P_s} + \frac{1}{G} \tag{13.63}$$

Alternate Receiver Calibration Method: IM Index Transfer. An alternative method to the RIN transfer technique for calibrating the optical receiver is the IM index-transfer technique. This technique offers calibration at a single frequency or point by point through multiple calibrations. In this method, the modulation index m_I of a fixed-frequency sinusoidally intensity modulated light is first accurately measured. Let $P(t)$ designate the output intensity versus time of the modulated optical source

$$P(t) = P_{\text{cal}}\left(1 + \frac{\Delta P}{P_{\text{cal}}}\cos 2\pi f_m t\right) \tag{13.64}$$

where P_{cal} is the average power detected by the optical receiver. By measuring the DC and modulation strength, the intensity modulation index m_I is obtained at the frequency f_m.

$$\Delta P(f_m) = \langle P_{\text{cal}} \rangle\ m_I(f_m) \tag{13.65}$$

The corresponding power spectral density at the frequency f_m is:

$$S_P(f_m)|_{\text{cal}} = m_I^2(f_m) \times P_{\text{cal}}^2 \quad [\text{W}^2/\text{Hz}] \tag{13.66}$$

When this source of intensity modulation is applied to the optical receiver, the electrical spectrum analyzer will measure:

$$S_{\mathrm{ESA}}(f_m)\big|_{\mathrm{cal}} = (\mathfrak{R}k(f_m))^2\, S_P(f_m)\big|_{\mathrm{cal}} \tag{13.67}$$

The unknown multiplicative constants are next calculated:

$$[\mathfrak{R}k(f_m)]^2 = \frac{S_{\mathrm{ESA}}(f_m)\big|_{\mathrm{cal}}}{S_{\Delta P}\,(f_m)\big|_{\mathrm{cal}}} \tag{13.68}$$

With the IM index-transfer method, the optoelectronic detection chain as well as the electrical spectrum analyzer is calibrated for a deterministic modulation. Note that with this method, the electrical noise bandwidth of the receiver is not calibrated. The electrical spectrum analyzer IF filter noise bandwidth must be calibrated separately.

Noise Figure Experiment. Using the RIN-transfer calibration technique, the noise figure of an EDFA was measured at a wavelength of 1550 nm with an amplifier input power of −20 dBm. The experiment setup is similar to that shown in Figure 13.50. With the source attenuator set to 0 dB, the source RIN was approximately −149.2 dB/Hz at a power level of −3.6 dBm. The addition of 16.4 dB of attenuation to bring the input signal level to −20 dBm results in an input RIN of −135 dB/Hz. This RIN level according to Figure 13.29 will have no significant impact on the noise figure measurement, the attenuated source is essentially shot-noise-limited.

In the first step, the transfer function from the optical amplifier to the electrical spectrum analyzer display was calibrated. An optically filtered ASE source with an FWHM spectrum of approximately 2.5 nm served as the RIN transfer standard. The optical spectrum of the transfer standard is shown in Figure 13.53a. The RIN for this source was calculated according to Equation 13.47 yielding a low frequency RIN of −116.18 dB/Hz. The calculated RIN spectrum is shown Figure 13.53b. Across the frequency range of interest, the frequency roll-off of the RIN transfer standard is small, and the noise power it generates dominates over all other noise sources.

The gain of the EDFA was measured with an OSA. The optical spectrums of the input and amplified output signals are shown in Figure 13.54a. The EDFA was equipped with an optical filter with an FWHM of approximately 1.6 nm. This filter served to reduce the sp-sp beat noise contribution to the amplifier noise figure. The EDFA produced 15.05 dB of gain as seen from the figure. The three lower traces in Figure 13.54b correspond to the RIN standard, the EDFA, and the thermal noise powers. The thermal noise, $S_{\mathrm{ESA}}(f)|_{th}$ was subtracted from the EDFA noise $S_{\mathrm{ESA}}(f)|_{\mathrm{mea.}}$ as indicated by Equation 13.53. A measurement of the average power generated by the RIN-transfer standard along with the calibration noise data, $S_{\mathrm{ESA}}(f)|_{\mathrm{cal}}$, shown in Figure 13.54b, permitted absolute amplitude calibration of the display according to Equation 13.53. The shot-noise correction required measurement of the electrical currents produced by the transfer standard and the amplified signal which resulted in an effective responsivity, $\mathfrak{R}$, of 0.428. The shot-noise correction for the coupling loss to the detector was small in this experiment, contributing less than 0.1 dB to the noise figure. Using the values for the gain and excess noise, the noise figure was approximately 7.8 dB as shown in Figure 13.54b.

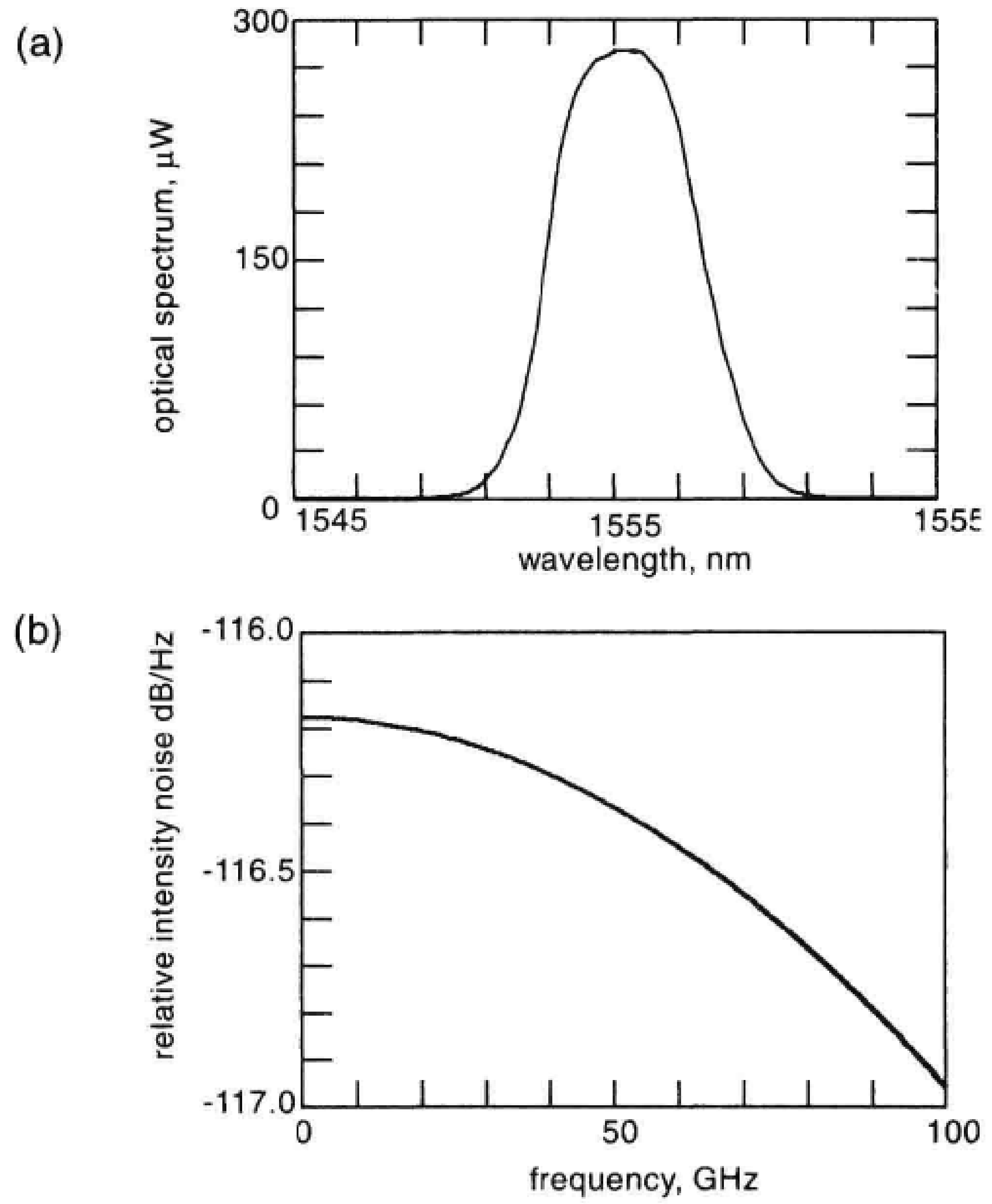

Figure 13.53 RIN transfer standard spectrums. (a) Measured optical power spectrum. (b) Calculated RIN spectrum.

13.6 OTHER TYPES OF OPTICAL AMPLIFIERS

13.6.1 Rare-Earth Doped Fiber Amplifiers

Amplification at a variety of wavelengths has been demonstrated in rare-earth doped optical fibers. The mechanism for gain is similar to that of the EDFA: excitation of the rare-earth ion with pump light causes population inversion between a pair of energy levels. This produces gain at a wavelength corresponding to the energy difference between the inverted levels. A partial energy diagram for the rare-earths in a $LaCl_3$ host is shown in Figure 13.55. This diagram is also useful for other glass hosts since the electronic structure of the trivalent ions provides some shielding of the transitions from the host crystalline fields.

1.3 μm Amplifiers. When praseodymium ions are doped in a low-phonon energy glass host such as a fluorozirconate fiber, optical gain can be achieved at a number of different wavelengths. Indeed, with this ion, practical demonstrations of amplification or lasing has been achieved from the visible to the infrared.[45–55] The transition responsible for gain near the important 1.3 μm telecom window is designated by 'a' in Figure 13.55. This